Performance Investigation and Optimization Studies on a Solar-Assisted Liquid Desiccant Air Conditioning System

A thesis submitted in fulfilment of the requirements for the degree of

Doctor of Philosophy

by

Mrinal Bhowmik

(Roll No: 166151103)

School of Energy Science and Engineering

Indian Institute of Technology Guwahati

Guwahati – 781039, India

August 2021

School of Energy Science and Engineering
Indian Institute of Technology Guwahati
Assam – 781039
India

STATEMENT

The present thesis entitled, "**Performance Investigation and Optimization Studies on a Solar-Assisted Liquid Desiccant Air Conditioning System**" has been carried out by me under the supervision of Prof P. Muthukumar, Department of Mechanical Engineering, Indian Institute of Technology Guwahati and Dr. R. Anandalakshmi, Department of Chemical Engineering, Indian Institute of Technology Guwahati. This work has not been submitted elsewhere for the award of any degree.

(Mrinal Bhowmik)
School of Energy Science and Engineering
Indian Institute of Technology Guwahati
Assam – 781039, India

School of Energy Science and Engineering
Indian Institute of Technology Guwahati
Assam – 781039
India

THESIS CERTIFICATE

It is certified that the work described in this thesis, entitled "**Performance Investigation and Optimization Studies on a Solar-Assisted Liquid Desiccant Air Conditioning System**", done by Mr. **Mrinal Bhowmik**, a Ph.D. student of 'School of Energy Science and Engineering', Indian Institute of Technology Guwahati, for the award of degree of ***Doctor of Philosophy*** has been carried out under our supervision. This work has not been submitted elsewhere for the award of any degree.

Signature of Supervisor(s)

Dr. R. Anandalakshmi
Associate Professor,
Thesis Co-supervisor
Department of Chemical Engineering,
Indian Institute of Technology Guwahati,
Assam – 781 039, India

Dr. P. Muthukumar
Professor,
Thesis Supervisor
Department of Mechanical Engineering
Indian Institute of Technology Guwahati
Assam – 781039, India

Dedicated

to

my Ph.D. Thesis Supervisors

Prof. P. Muthukumar

&

Dr. R. Anandalakshmi

ACKNOWLEDGEMENTS

I express my sincere gratitude to my Ph.D. research supervisors **Dr. P. Muthukumar**, **Professor**, Department of Mechanical Engineering, IIT Guwahati and **Dr. R. Anandalakshmi**, **Associate Professor**, Department of Chemical Engineering, IIT Guwahati, for their constant support, guidance, motivation, encouragement, valuable advice and discussions. This has helped me to improve an understanding of the subject and research skills for my thesis work. Working under them has been an excellent experience for me. I am very thankful to them for building up my confidence and having faith in me during the Ph.D. period. Their suggestions broadened my views on engineering subjects and practical life. I have been deeply inspired by their rich experience, knowledge, and way of approaching a problem, immense patience and utmost care. I must acknowledge their unconditional freedom that allowed me to explore the research possibility, think creatively, and accept me for straightforward technical discussions. I enjoyed each moment working under their supervision and learned many things from them, which will be an asset for my future research.

I would like to thank Engineering Section, IIT Guwahati, to approve financial support (Project No.: IITG/ENGG/AEE/EL81). I also thank the people of the Engineering and Maintenance section of IIT Guwahati, especially Mr. S. Senapati, Mr. K. Barman and Mr. T. J. Singh to provide the necessary support during the installation of experimental setup.

I am highly thankful to my doctoral committee members, **Prof. Tapas Kumar Mandal** (Chairman), **Dr. Pankaj Kalita** and **Dr. S Senthilmurugan,** for their continuous academic guidance, checking my Ph.D. work progress and seminars during my Ph.D. I would like to express my sincere thanks to Dr. Ganesh Natarajan, Department of Mechanical Engineering, for being my doctoral committee member for the first two years. I am grateful to Emeritus Dr. -Ing. Manfred Groll, IKE, University of Stuttgart, Germany, for providing valuable suggestions and ideas during the initial stage of my research work, which significantly forwarded my research progress.

I would like to express my sincere gratitude to the head of the School of Energy Science and Engineering for providing me the departmental facilities. I am also grateful to all the faculty members and staff of the Chemical Engineering Department and Mechanical Engineering Department. I also thank Mr. Nip Borah, scientific officer, for providing the necessary equipment throughout my research study. Further, I thank workers Mr. Atanu, Mr. Dipankar,

Mr. Bimal of A/C plant and 'cycle shop' workers for their support and kind cooperation, which helped me to accomplish my research work. My special thanks to all scientific officers and staff members of 'School of Energy Science and Engineering' and 'Central Instruments Facility'.

I am thankful to my seniors Dr. B. Satya Sekhar, Dr. S. Anbarasu, Dr. Hakeem Niyas, Dr. Chilaka Ravi Chandra Rao, Dr. D. V. N Lakshmi, Dr. Gyan Sagar Sinha, Dr. Debakanta Rabha, Dr. Lav Kumar Kaushik, Dr. Jasinta Poonam Ekka, Dr. Vigneshwaran, Dr. K. Dharmalingam, Dr. Pankaj Jha, Dr. Sanjukta Devi, Dr. Sanchari Deb and Dr. P. S. Balaji for their career guidance and support. They have also constantly motivated me in various aspects of my research work.

The financial support for this thesis provided by the Indian Institute of Technology Guwahati and Ministry of Human Resource and Development, India, is highly acknowledged.

I would like to thank my research team members and colleagues, Dr. Kiran Naik Bukke, Ms. Juri Sonowal, Mr. Praveen Thakur, Mr. Mullapudi Joshi, Mr. Ankit, Mr. Sayan , Mr. Kamesh Singh and Mr. Siddhartha for their help, suggestions and enjoyable company.

I am also thankful to my lab colleagues, Mr. Sunku Prasad, Mr. Sayanthan Jana, Mr. Alok Kumar, Mr. G. Surendhar, Mr. Nithin Narmada, Mr. Vivek Selvan, Mr. Viswanth, Miss. Sunita Deb, Mr. Malleswara Rao, Mr. G. Sodhi, Miss. Pratibha Muriya, Mr. R. Abhishek, and other colleagues of IITG for their friendly behaviour, which makes my stay at IIT Guwahati a memorable experience. I wish to express my deepest gratitude to all those who have helped me in various ways during my PhD work at IIT Guwahati.

I would like to thank Prof. Tamal Banerjee, Prof. Vimal Katiyar, Dr. Partho Sarathi Gooh Pattader and Dr. R. Prasanna Venkatesh, Department of Chemical Engineering, IIT Guwahati, for their kind support during material characterization.

I am deeply indebted to my M. Tech supervisor Dr. G R K Sastry, Professors, Department of Mechanical Engineering, National Institute of Technology Andhra Pradesh and Dr. Madhujit Deb, Assistant Professors, Department of Mechanical Engineering, National Institute of Technology Agartala, India for their motivation towards the research that encourages me to pursue Ph.D.

I am very much thankful to my parents Mr. M.K. Bhowmik (surveyor) and Mrs. D. Bhowmik, my brothers Er. Manish Bhowmik (Computer), Er. Manik Bhowmik (Civil), Er. Manoj Kumar Bhowmik (Civil) and my one & only younger sister Er. Manidipa Bhowmik (Electrical) and

my brother in law Er. Ashish Banik (Electrical) for their support, which inspires me to do my best. I especially thank my parents, who have encouraged me to pursue higher studies, and their never-ending sacrifices helped me to reach my career goals. I also thank my best friends, Mr. Kishor Kumar Sutradhar, Er. Arunava Das, Er. Subrajit Sen, Dr. Biswajit Das, Mr. Rupak Mujumdar, for their support and motivation to pursue higher studies in premier institute IIT Guwahati.

I would like to thank my best friends in IIT Guwahati Er. Ojing, Er. Sunku, Er. Samar, Er. Nabendhu, Er. Anil, Er. Tippa and my wall partner Mr. Manvendra, for their support in every step of my life.

Finally, I would like to thank Prof. T G Sitharam, Director, IIT Guwahati and Prof. Gautam Biswas, former Director, IIT Guwahati, for their constant encouragement and motivation throughout my doctoral studies at IIT Guwahati.

It is not possible to acknowledge the contributions of all who have helped directly or indirectly in carrying out the present research work, and those are unnamed and appreciated nonetheless. Several individuals and organizations deserve special mention.

Mrinal Bhowmik

Abstract

Air-conditioning systems are used to control the air dry-bulb temperature and humidity level for achieving human thermal comfort conditions. In order to control the humidity level, air dry-bulb temperature needs to be brought down below its dew point temperature to condense the moisture from the air. This eventually consumes a significant amount of energy in terms of electricity. In order to minimize energy consumption, researchers have been given more attention towards an alternative latent heat load (humidity) control system. In this regard, desiccant based sorption technologies are more effective compared to the conventional vapour compression system. Recently, sorption technology has taken significant attention as an alternative process to standardise mechanical air conditioning systems for dehumidification of air without cooling below its dew point temperature. Liquid desiccant dehumidification systems are one of the sorption technologies, where a synthetic or natural desiccant is used as a hygroscopic material to absorb the moisture of the surrounding air. Desiccant based ACs is classified as solid desiccant and liquid desiccant based ACs. Generally, the liquid desiccant-based ACs are advantageous over solid desiccant systems due to less air side pressure drop, less maintenance, operational flexibility, and utilisation of low-grade thermal energy sources such as solar or waste heat reactivation of desiccant. However, in the liquid desiccant system, the selection of proper desiccant solution has a greater significance on the performance of a dehumidifier. The major objectives chosen for the present thesis work are:

- To numerically investigate the performance of various single desiccant solution systems to compare the cross and counter flow dehumidifier performance, and to select the desiccant for the present study.
- To experimentally investigate the performance of solar evacuated tube collectors and develop a numerical model based on experimental results for desiccant regenerator system.
- Experimentally and numerically study the coupled heat and mass transfer phenomena between air and desiccant in a solar-assisted thermal liquid desiccant dehumidifier-regenerator system.
- To develop heat and mass transfer correlation based on experimental results to optimize the input process parameters for better performance of the dehumidifier-regenerator system.
- To study the performance of combined dehumidifier-regenerator system at the optimum conditions.

- To prepare, characterize and analyze the liquid desiccant doped novel hydrogel films for potential air-dehumidification applications.

The governing equations of energy, mass and species balance are solved to study the performance of a dehumidifier/regenerator. These equations are solved using the finite difference method. The variation in thermodynamic properties (air temperature, humidity, desiccant temperature and desiccant concentration) inside the dehumidifier module is visualized in terms of contour plots. Furthermore, the irreversibility in heat and mass transfer operation for the optimal blend is investigated in terms of the physical and chemical exergy destruction paradigm. It is found that LiCl is the most stable liquid desiccant and has many favourable properties for dehumidification, such as low vapour pressure, and it does not vapourize into the air at ambient conditions. However, it is relatively more corrosive, expensive and crystallizes at low temperatures. Therefore, it is necessary to analyze the different desiccants' individual properties and their physical behaviour from a material perspective. In this thesis, efforts are devoted to explore the thermo-kinetic properties of pure LiBr, $CaCl_2$ as well as their mixtures (LiBr: $CaCl_2$ of 90:10; 85:15; 80:20 and 75:25) by X-ray diffraction (XRD), thermo-gravimetric (TG) and absorption rate, analyzes through numerous control experiments. The XRD study confirmed that peaks of $CaCl_2$ and LiBr were shifted slightly for LiBr and $CaCl_2$ mixtures due to interaction effects. The mixtures of LiBr and $CaCl_2$ showed a less moisture regeneration cost than pure $CaCl_2$, and all the mixtures revealed higher rate of moisture absorption than pure LiBr and $CaCl_2$. Further, 85:15 mixture of LiBr: $CaCl_2$ showed higher rate of moisture absorption when compared to other prepared samples.

Subsequently, in this thesis, a hybrid method is proposed by combining the solar evacuated tube collectors as a regeneration source to drive liquid desiccant system in a close-loop. Solar collectors are efficient in utilising solar thermal energy for heating applications as their efficiency is quite high even in the medium temperature range, which motivated to design a high efficient collector system. An experimental investigation was carried out by developing a series of evacuated tube solar collectors with U-tube configuration using water as a working fluid. The performance of the collector system was continuously measured throughout the day. A trade-off study was carried out considering all the performance parameters. On the basis of experimental datasets, a multilayer perceptron (MLP) architecture is developed to predict thermal efficiency, useful heat gain and water outlet temperature of the evacuated tube collector as a function of solar irradiation, mass flow rate of water and water inlet temperature. It is

demonstrated that the MLP model has an excellent agreement with experimental data as the mean square error is very low (<0.001). Test results showed that the MLP architecture gives a precise prediction of the actual collector performance parameters for different operating conditions. Test results also indicate that MLP model is a robust prediction platform for evaluating the solar collector performance.

In order to assess the performance of the overall air conditioning system using a novel desiccant mixture, an experimental setup of liquid desiccant dehumidification has been fabricated. The overall energy balance between the ambient air and the liquid desiccant was estimated. Effects of independent parameters such as the solution to air flow rate, solution concentration and temperature on the dehumidifier-regenerator performance parameters such as latent heat ratio, condensation rate, desiccant mass fraction index, evaporation rate and latent and enthalpy effectiveness were analyzed. The results obtained from the present investigation showed that high solution to airflow (L/G) ratio enhanced the dehumidification and low L/G ratio enhanced the liquid desiccant regeneration rate. For tested liquid desiccant dehumidifier, condensation rate and latent effectiveness lie in the range of 2.2 to 4.6 g/m^2-s and 36 to 68%, respectively. Whereas the evaporation rate, sensible and the latent effectiveness of the regenerator lies in the range of 0.1 – 11.2 g/m^2-s, 25.9 – 63% and 10 – 92% depending on the operating conditions. The maximum latent heat ratio for the dehumidifier at the design condition was 0.62, and the thermal coefficient of performance of the system was found as 1.1. The airside pressure drop in the dehumidifier/regenerator was also estimated at different flow rates of desiccant. Finally, the variation of thermodynamic properties (air temperature, humidity, desiccant temperature and desiccant concentration) inside the dehumidifier module is visualized in terms of contour plots.

Over the last few decades, a substantial advancement has been observed in dehumidifier modules for their energy-conservative and environment-friendly nature; however, still, uncertainty in decision-making is of concern in selection of optimum input parameters to attain an effective performance. The sensitivity analysis of independent variables on performance parameters is carried out using the cosine amplitude method. It is observed that air mass flux rate (F_a), solution concentration (ζ) and air specific humidity (ω_a) have significant impact on condensation rate (CR), whereas, air mass flux rate (F_a) and solution temperature (T_s) are the most effective parameters for moisture effectiveness and latent heat factor, respectively. Further, developed the relationships between the performance parameters and control variables through the application of various well-known artificial intelligence-based methods such as

artificial neural network (ANN), adaptive neuro-fuzzy inference system (ANFIS), and gene expression program (GEP). The GEP model results exhibited a good agreement with the experimental outcomes. The proficiency of developed GEP meta-models is provided by statistical parameters and Theil uncertainty. Subsequently, GEP meta-model based fuzzy logic is developed for optimising dehumidifier/regenerator inlet process parameters in terms of multi-responsive performance characteristics using genetic algorithm. The optimisation results showed that the performance characteristics have a tendency to become optimal at F_a = 0.766 kg/m^2-s, T_a = 30.745°C, ω_a = 0.023 kg_{wv}/kg_{da}, F_s = 1.812 kg/m^2-s, T_s = 24.01°C, and ζ = 48.1%. GEP meta-model predicted that the CR, ε_m and LHR values are 5.875 g/m^2-s, 48.65% and 0.82, respectively at this optimum inlet conditions. At near optimum point (F_a = 0.76 kg/m^2-s, T_a = 30.1°C, ω_a = 0.024 kg_{wv}/kg_{da}, Fs = 1.8 kg/m^2-s, T_s = 24°C, and ζ = 48%), the experimental results CR of 5.584 g/m^2-s, ε_m of 42% and LHR of 0.83, respectively were obtained. The experimental and predicted results for the optimum dehumidifier performance parameters (CR, ε_m, LHR) showed a very good agreement to each other (>8%) and that endorses the great reproducibility of the experimental inferences.

Keeping in mind that the temperature-independent humidity control through desiccant material provides a substantial impact on minimizing energy shortages and reduces the environmental problems without compromising human thermal comfort. An effort has been given to develop a novel desiccant doped sodium carboxymethyl cellulose (NaCMC) films using citric acid as a crosslinker to explore the dehumidification and regeneration capability of films. Films were prepared at various desiccant concentrations (5%, 10%, and 20%), and it was characterized using X-ray powder diffraction (XRD), thermo-gravimetric (TG), moisture absorption (ΔW) and water vapour permeability (WVP) analysis. XRD analysis revealed that there were no characteristic peaks of desiccants in the film samples, which indicated that the mixing of desiccants was homogeneous in the films. ΔW and TG analysis revealed that films contained 10% desiccant showed an effective instantaneous moisture-holding capacity and faster regeneration rate, respectively, compared to 5% and 20% desiccant doped hydrogel films. It was found from WVP test that an increasing amount of desiccant decreased the WVP due to a reduction in intermolecular space in the prepared films. Further, a comprehensive comparison was made to visualize the effectiveness of developed desiccant films. All these data recommend that the prepared desiccant doped films can be used for potential air dehumidification applications.

Nomenclature

ABS	Acrylonitrile Butadiene Styrene
A_c	Collector area (m^2)
AC	Air Conditioning
ACO	Ant Colony Optimization
AEH	Auxiliary Electric Heater
AI	Artificial Intelligence
a_i	Average ionic activity coefficient of the solute
Al_2O_3	Aluminium oxide
ANFIS	Adaptive Neuro-Fuzzy Inference System
ANN	Artificial Neural Network
a_s	Specific surface area of packing material (m^2/m^3)
ASHRAE	American Society of Heating, Refrigerating and Air-Conditioning Engineers
ASTM	American Society for Testing and Materials
a_w	Activity of water
A_ϕ	Debye-Huckel constant
B	Blower
$CaCl_2$	Calcium chloride
CFM	Cubic Feet per Minute
CHO_2Na	Sodium formate
CO_2	Carbon dioxide
COP	Coefficient of Performance
COP_{sys}	System Coefficient of Performance
Cp_a	Specific heat capacities of dry air (kJ/kg-K)
Cp_v	Specific heat capacities of vapour (kJ/kg-K)
CR	Condensation Rate (kg/m^2-s)
C_s	Water concentration in solution (wt.%)
d	Index of agreement
D	Dehumidifier
da	Dry air
D_a	Diffusion coefficient (m^2/s)
DAQ	Data Acquisition

DBT	Dry Bulb Temperature (°C)
d_e	Equivalent diameter (mm)
DMFI	Desiccant Mass Fraction Index
D_ϕ	De-normalization value
$d\omega$	Change in specific humidity (kg/kg_{da})
EAs	Evolutionary Algorithms
$E_{ch,des}$	Destroyed chemical exergy (kW)
ECOP	Electrical Coefficient of Performance
ED	Electro-Dialysis
EFDM	Explicit Finite Difference Method
$E_{ph,des}$	Destroyed physical exergy (kW)
ER	Evaporation Rate (g/m^2-s)
ETCs	Evacuated Tube Collectors
ETs	Expression Trees
Ex_{che}	Chemical exergy (kJ/kg)
Ex_{des}	Exergy destruction (kJ/kg)
Ex_{in}	Exergy in (kJ/kg)
Ex_{out}	Exergy out (kJ/kg)
Ex_{tot}	Exergy total (kJ/kg)
Ex_{tph}	Thermomechanical/physical Exergy (kJ/kg)
ε_h	Enthalpy effectiveness
ε_{lat}	Latent/ Moisture effectiveness
ε_{sen}	Sensible effectiveness
F	Mass flux rate of fluid (kg/m^2-s)
f_i	Fitness function
FIS	Fuzzy Inference System
FPC	Flat plate collector
F_s	Mass flux rate of solution (kg/m^2-s)
f_w	Activity coefficient of water
GA	Genetic Algorithm
GUI	Graphical User Interface
GWP	Global Warming Potential
H	Height of dehumidifier (m)

h	Enthalpy of fluid (kJ/kg)
HCOOK	Potassium formate
h_{fg}	Latent heat of condensation (kJ/kg)
HNO_3	Nitric acid
HP	Horsepower
h_e	Equilibrium enthalpy of humid air with the desiccant solution (kJ/kg)
HVAC	Heating, Ventilation, and Air Conditioning
HX	Heat exchanger
IIR	International Institute of Refrigeration
IST	Indian standard time
I_T	Solar irradiation (W/m^2)
KGE	Kling–Gupta Efficiency
L	Length of dehumidifier (m)
L/G	Liquid to Gas flow rate (solution to air)
LDCS	Liquid Desiccant Cooling System
Le	Lewis number
LHR	Latent Heat Ratio
LiBr	Lithium bromide
LiCl	Lithium chloride
$LiCO_3$	Lithium carbonate
$LiNO_3$	Lithium nitrate
LPH	Litre per hour
M	Molecular weight (kg/kmol)
$\dot{m}$	Mass flow rate (kg/s)
M1,M2,M3	Manifolds
MAE	Mean Absolute Error
MAPE	Mean Absolute Percentage Error (%)
$\dot{m}_{deh}$	Dehumidification rate (g/m^2-s)
m_i	Molality
MLP	Multi-Layer Perceptron
MLR	Multiple Linear Regression
MPCI	Multiple Performance Criteria Index
MSE	Mean Square Error

MSRE	Mean Square Relative Error
$\dot{m}_w$	Mass flow rate of water (kg/s)
MWh	Megawatt-hour
MWNTs	Multi-walled carbon nanotubes
N	Normalised data
NARX	Nonlinear auto-regressive model with exogenous inputs
NRMSE	Normalised Root Mean Square Error
NSE	Nash–Sutcliffe coefficient of efficiency
NTU	Number of transfer unit
N_ϕ	Normalized value
ODP	Ozone Depletion Potential
P	Pump
P^0	Pure substance vapour pressure (kPa)
P_{atm}	Atmospheric pressure (kPa)
PCM	Phase Change Material
P_{sol}	Vapour pressure of solution (kPa)
P_V	Vapour pressure (kPa)
PVP	Polyvinylpyrrolidone
Q	Heat gain (W)
Q_B	Energy consumption for blower(kW)
Q_d	Dehumidification energy output (kW)
Q_E	Energy consumption for electric heater (kW)
Q_{lat}	Latent heat (kW)
Q_P	Energy consumption for pump (kW)
Q_{ph}	Heat transfer rate (kW)
Q_s	Energy consumption for the sun (kW)
Q_{sen}	Sensible heat (kW)
Q_u	Useful heat flux (W/m^2)
R	Pearson correlation coefficient
R_a	Gas constant (8.314 kJ/mol.K)
Re	Reynold number
RH	Relative Humidity (%)
RMSE	Root Mean Square Error

RSM	Response Surface Method
R-square / R^2	Coefficient of determination / Statistical correlation
R_u	Universal gas constant (J/mol.K)
SADE	Self-Adaptive Differential Evolutionary
Sc	Schmidt number
$SD_{\lambda e}$	Standard deviation of experimental data
$SD_{\lambda p}$	Standard deviation of model predicted data
Sh	Sherwood number
sMAPE	symmetric Mean Absolute Percentage Error
SOTA	State-of-the-art
SRM	Stepwise Regression Model
SS	Stainless steel
T	Temperature (K)
T_0	Outlet temperature (K)
T_1,T_2,T_3,T_4	Water temperature (°C)
T_a	Ambient temperature (°C)
$T_{a,o}$	Dehumidifier outlet air temperature (°C)
TCOP	Thermal Coefficient of Performance
TEG	Tri-Ethylene Glycol
T_f	Mean fluid temperature (K)
Theil U2	Theil Uncertainty
$T_i=T_1$	Water inlet temperature (°C)
$T_o=T_4$	Water outlet temperature (°C)
TR	Ton of Refrigeration
T_{red}	Reduced temperature difference (m^2-K/W)
T_s	Solution inlet temperature (°C)
$T_{s,o}$	Solution outlet temperature (°C)
U_h	Heat transfer coefficient (W/m^2 -K)
U_m	Mass transfer coefficient (kg/m^2 -s)
V	Volume of dehumidifier (m^3)
V_1,V_2,…,Vn	Independent variables
V_1,V_2…V_n	Independent variables
VCAs	Vapour compression air conditioning systems

WO_3	Tungsten trioxide
WT	Water Tank
wt.%	Weight percentage
wv	Water vapour
y	Fuzzy element value
y*	Centroid of each membership function
z	No of test cases
α	Absorptivity
ΔT	Temperature difference (°C)
ΔU	Total uncertainty (%)
ΔV_1, ΔV_1..., ΔV_n	Error of individual independent variables
Δω	Specific humidity difference (kg/kg_{da})
ζ	Total desiccant concentration
λ_e	Experimental value
λ_p	Model-predicted data
μ	Ratio of standard deviation
μ°	Standard chemical potential (kJ/kg)
μ_F	Membership function value
ξ	Concentration (wt.%)
ρ	Density (kg/m^3)
σ	Standard deviation
τ	Transitivity
ψ	Ratio of experimental data to predicted data
ψ_i	i^{th} experimental data
ψ_{max}	Maximum data corresponding to respective parameter
ψ_{min}	Minimum data corresponding to respective parameter
ω	Specific humidity (kg/kg_{da})
ω_a	Air inlet humidity (kg_{wv}/kg_{da})
ω_a	Air specific humidity (g_{wv}/kg_{da})
$\omega_{a,o}$	Air outlet humidity (kg_{wv}/kg_{da})
ω_e	Equilibrium air inlet humidity (kg_{wv}/kg_{da})
η	Thermal efficiency

$\bar{\lambda}_e$	Average of experimental data
$\bar{\lambda}_p$	Average of model-predicted data
P_v^e	Equilibrium vapour pressure (kPa)

CONTENTS

List of Figures

List of Tables

CHAPTER 1

Introduction

1.1. Overview

Energy is the primary resource needed for fulfilling human necessities such as cooking, lighting, mobility, thermal comfort, and communication. However, the rapid depletion of conventional energy resources and the rise in demand for creating comfortable human thermal conditions are becoming a vital global environmental concern. The use of fossil fuels has a huge negative impact on the environment, increasing carbon footprint and global warming. It has been observed that the increased global temperature, numerous climatic and weather disruptions, such as flooding and hurricanes, are the consequence of global warming (Barrios et al., 2006). Since the standard of living and the population growth are directly influencing energy consumption, the demand for energy generation is also expected to increase accordingly. Hence an immediate action is needed to minimize the consumption of fossil fuels. The world energy consumption reported in different sectors is presented in Fig. 1.1.

Global energy consumption is expected to increase by 50% between 2010 and 2040, as shown in Fig. 1.1 (British Petroleum, 2019). It has been found that the energy required to create human thermal comfort conditions is around 50% of the building total energy consumption (British Petroleum, 2019). The International Institute of Refrigeration has projected that almost 15% of all electricity generated worldwide has been utilized for air-conditioning (ACs) and refrigeration processes of several kinds (Lucas, 1988). Most of the building's energy consumption is spent on dehumidifying, cooling or heating loads. The electrical energy consumption for indoor environments is expected to increase by 120% between 2002 to 2030 (Radhwan et al., 1993). Also building sector contributes to carbon dioxide (CO_2) as well as chlorofluorocarbons (CFC) emissions. The resulting CO_2 emission from such an upsurge in global energy consumption is also expected to hike by 10% between 2017 and 2040, as seen in Fig. 1.2. The aforementioned statistics also confirm a dual challenge in addressing any potential energy system (i.e., effectively meeting the energy demand with a reduced carbon footprint). Therefore, to reduce CO_2 and CFC emissions into the environment, there is an urgent need for alternatives to traditional cooling systems that can be efficiently driven by renewables. Renewable energy sources that are not utilized adequately have been gaining focus because of their affordability, commercial acceptance, easy maintenance, ease of use, and environmental friendliness.

Further, the increase in demand for human thermal comfort is becoming a major global environmental issue. In order to meet this demand, an air conditioning device plays a vital role. In 1902, Willis Carrier in Buffalo, New York, introduced the first modern electrical air conditioning unit (Basavaraja et al., 2019). The initial prime function of the air conditioning device was to control the temperature and humidity, as mentioned in Fig. 1.3. The leading electrical-based refrigeration systems are based on the vapour compression refrigeration cycle. As seen in Fig. 1.4, this cycle comprises four essential elements: the compressor, evaporator, expansion valve, and condenser.

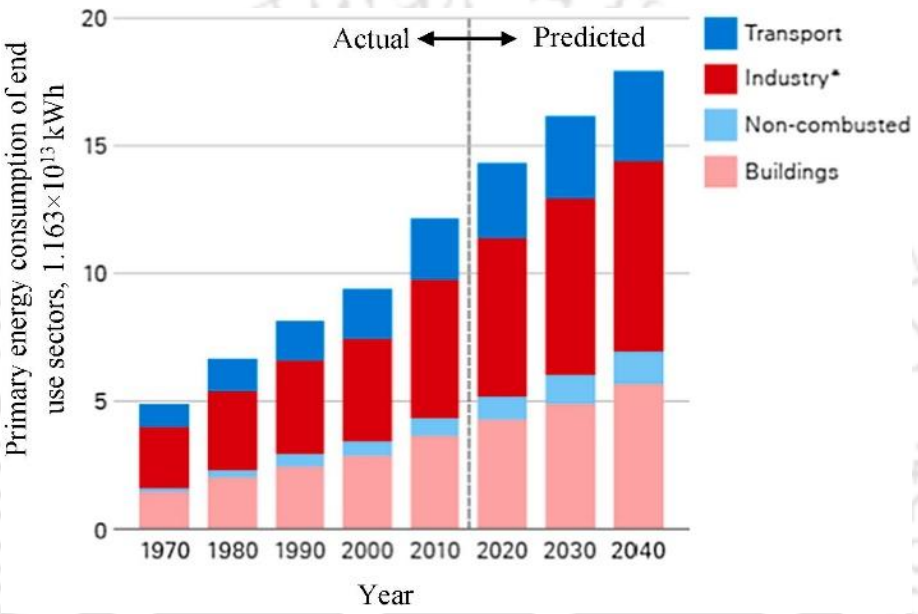

Fig. 1.1: World energy consumption (British Petroleum, 2019)

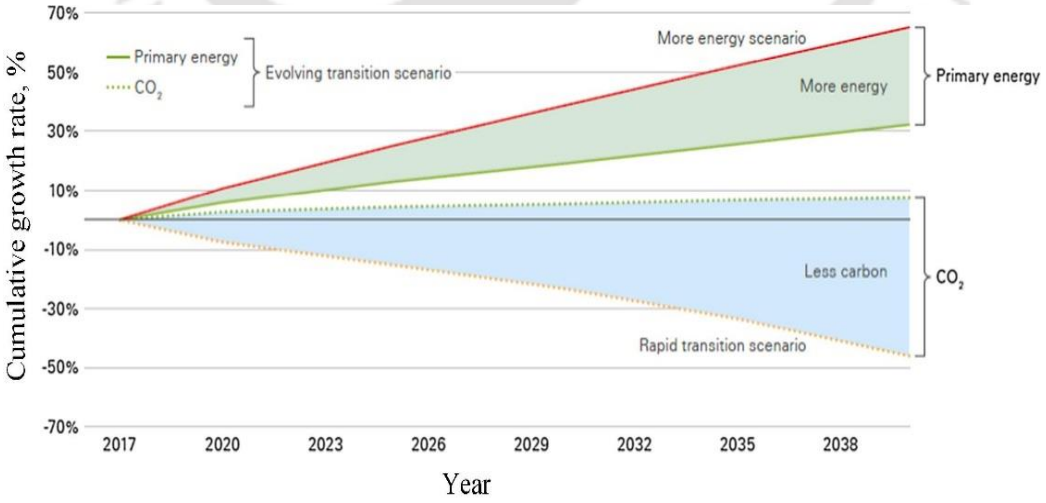

Fig. 1.2: Cumulative growth rate of primary energy demand and CO_2 emissions (British Petroleum, 2019)

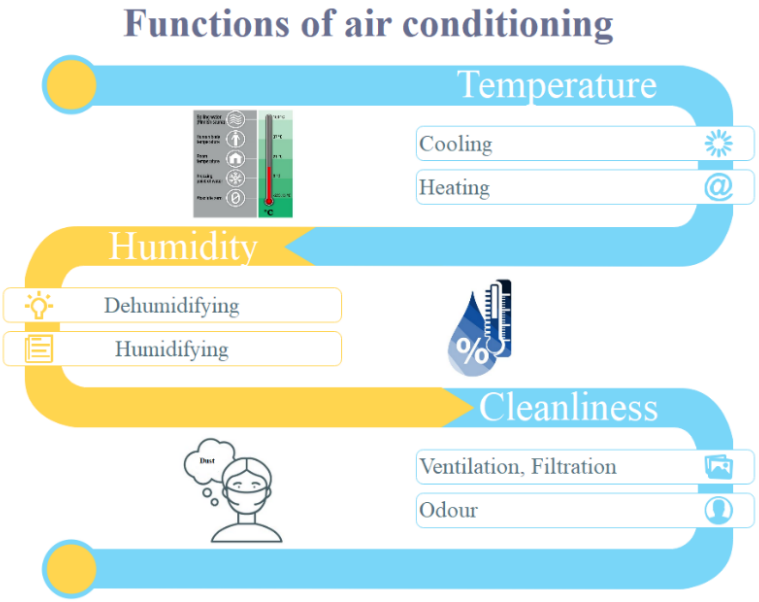

Fig. 1.3: Function of air conditioning unit

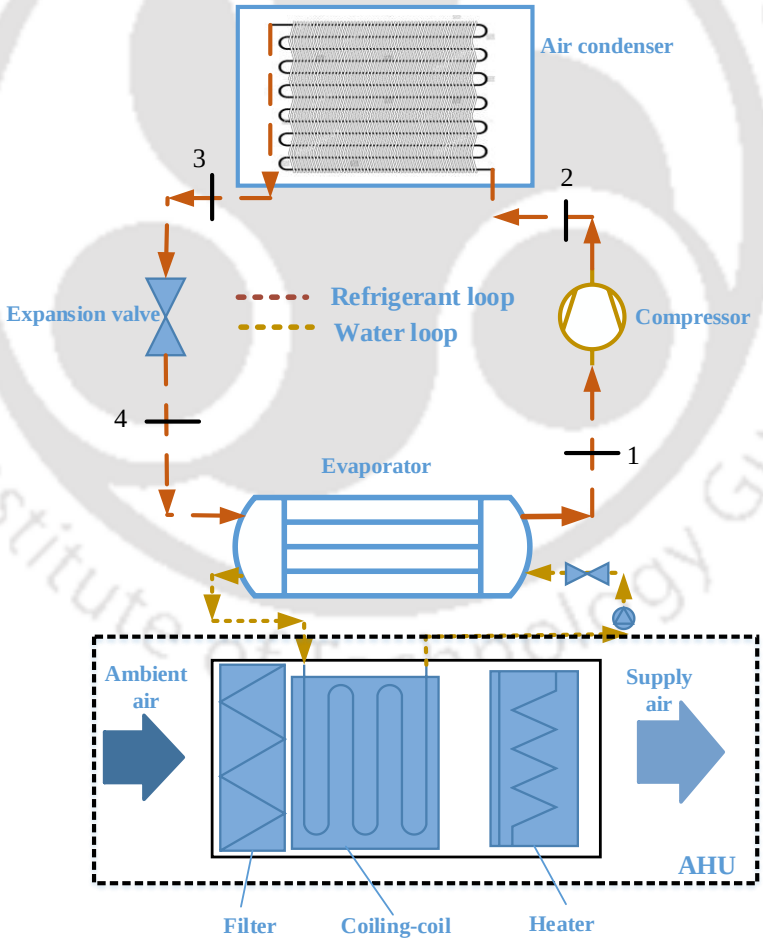

Fig. 1.4 (a): Basic components of vapour compression system

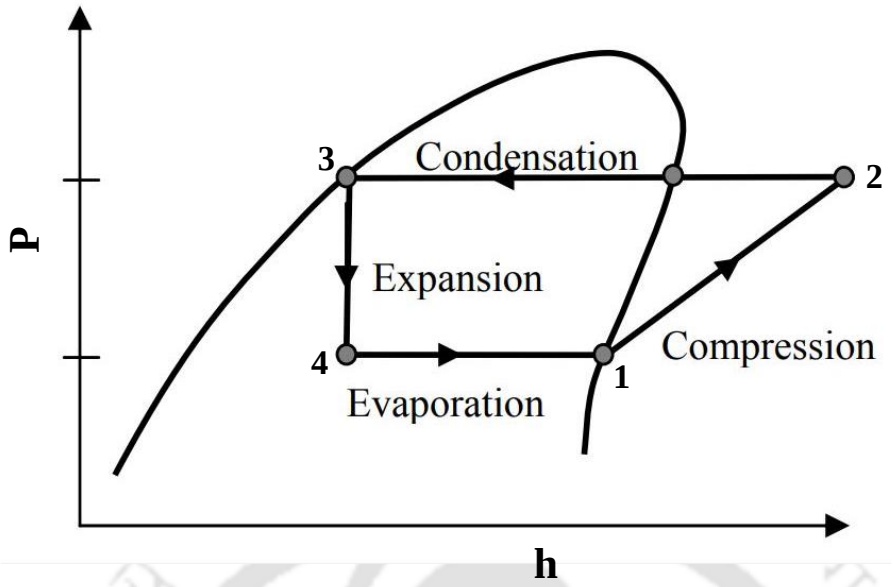

Fig. 1.4 (b): Vapour compression refrigeration cycle on a p-h diagram

It is necessary to apply the first law of thermodynamics to the entire cycle and its components to explain the system, where the potential and kinetic energy changes are considered to be neglected (Afonso, 2006). The $\dot{m}_r$ represents the mass flow rate of refrigerant in the system. The following set of equations can be used to determine the different energy fluxes of the cycle:

- Evaporator- refrigeration effect : $\dot{Q}_{evap} = \dot{m}_r (h_1 - h_2)$ (1.1)
- Compressor- compression power: $\dot{W} = \dot{m}_r (h_2 - h_1)$ (1.2)
- Condenser-condensation heat: $\dot{Q}_{evap} = \dot{m}_r (h_2 - h_1)$ (1.3)
- Expansion valve: $h_4 = h_3$ (1.4)

Then the coefficient of performance (COP) can be written as:

$$COP = \frac{\dot{Q}_{evap}}{\dot{W}} = \frac{h_1 - h_4}{h_2 - h_1} \quad (1.5)$$

where h_i is enthalpy (kJ/kg), $\dot{Q}_{evap}$ is the heat power that has been extracted from the evaporator (kW), $\dot{Q}_{cond}$ is the heat released from the condenser (kW), and $\dot{W}$ is the compressor mechanical power (kW). COP values are constantly positive and generally exceed one since the refrigeration effect is larger than compressor power. Typical values for the vapour compression system's COP range between 2-3 (Afonso, 2006).

Researchers have since developed several advanced models based on the different applications to enhance the COP of the system. One very common method is the usage of multistage compression, which utilises more than one compressor in conjunction with the refrigerant intercooling between each pair of compressors. This subsequently results in the reduction of the total system work input. Multistage systems generally possess higher COP values than traditional compression systems. This is because there is a reduction in compression work and a rise in the refrigerant effect. There are three degrees of pressure: the low in the evaporator, the intermediate between the two compressors, and the high at the condenser. Different methods can also be utilised to implement this method (e.g., coupling the system with a number of evaporators, each with a typical operating temperature). Other modifications can similarly be implemented in the whole system. For example, a basic radiation shield can be positioned in the conditioning chamber's rear side and freezers to prevent heat transfer by radiation on these surfaces from the condenser and compressor. It can reduce the refrigerator's internal air temperature by up to 2ºC (Afonso, 2006).

1.2. Real-time challenges of conventional air conditioning system

In order to provide indoor human thermal comfort, the cooling load requirement should not be considered solely in terms of the sensible cooling capacity (temperature control). Latent load capacity (humidity control) should also be considered, particularly in humid and hot regions. The range of requirements of human thermal comfort conditions is illustrated in Fig. 1.5. Two types of thermal load connected to the sensible heat ratio (SHR) are (i) sensible load and (ii) total load which includes both sensible and latent loads. Therefore, a larger value of the sensible heat ratio specifies a smaller value of the latent load and vice-versa. Common traditional vapour compression air-conditioning system generally handle an average SHR of 0.75, which means that 75% of the system's capacity is utilized to control the sensible load, and the remaining 25% controls the latent load. Therefore, conventional systems can only deliver optimal comfort conditions when the sensible heat ratio exceeds 0.75 (Davanagere et al., 1999). In hot and humid climates, the designed sensible heat ratio's value is often lesser than 0.75. Further, traditional vapour-compression air-conditioning systems typically manage air processing in two steps. In the first step, the air is cooled below its dew point temperature during which the moisture present in the air gets condensed. In the second step, cold dehumidified air is reheated to a required indoor temperature. Due to reheating process, the system becomes energy-

intensive. Overcooling also provides ideal conditions for certain molds and bacteria's growth over the condenser coil. The resulting mold and bacteria growth can potentially cause health issues and affect the indoor air quality as well (Pérez-Lombard et al., 2008). The incoming air may carry the condensate into the conditioned space, causing increased humidity levels in the comfort zone. Temperature-independent humidity controls (TIHC) reduced the size of cooling machines and the amount of required refrigerant fluid. TIHC is eco-friendly since it reduces the amount of electric energy usages and lessened greenhouse gases. This, thereby, allows the system to become more energy efficient. Various industries and humidity-sensitive applications require controlled environments (e.g., pharmaceutical, food, and chemical industries). Conventional air conditioning systems find it challenging to achieve the necessary air humidity level. Even if such conditions are met, these systems are energy inefficient while doing so. Using conventional systems, the dew point temperature does not dip lower than approximately 4.0°C. Over 60 years, traditional air conditioning systems have used chlorofluorocarbons (CFCs) as the refrigerant. However, these refrigerants have been linked to the depletion of the ozone layer as well as a significant contributor to global warming (Afonso, 2006). Environmental concerns regarding CFCs, hydrochlorofluorocarbons (HCFCs), and some of their substitutes have triggered further research to discover new technologies that could provide an alternative. In order to address all of these issues, a sorption based desiccant system can be used as a potential alternative to conventional AC systems.

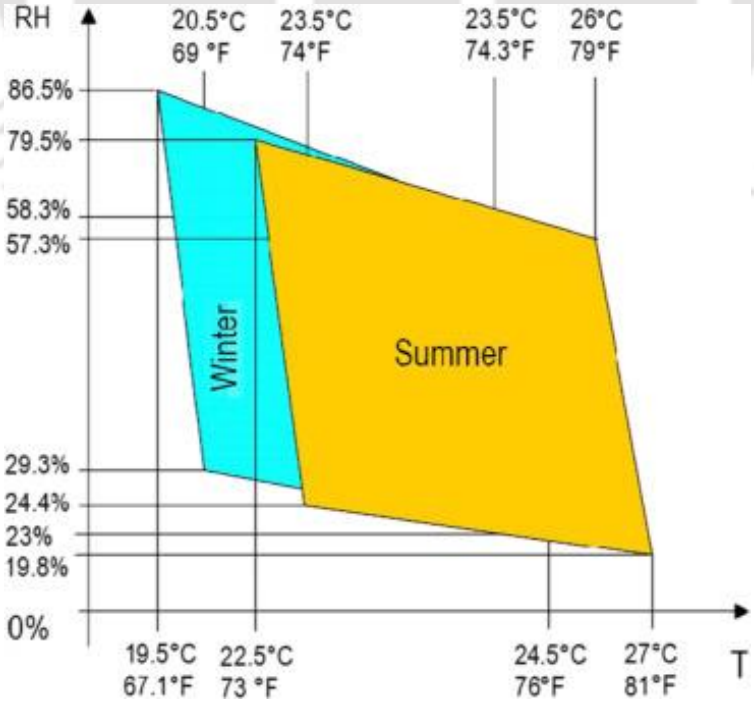

Fig. 1.5: Thermal comfort zone according to ASHRAE55 (NSI/ASHRAE55, 1992)

1.3. Desiccant air-conditioning systems

Desiccant is the substance, either solid or liquid, that attracts moisture at different capacities. A desiccant draws water molecules from the surrounding air onto its surface; thereby, the air gets dried. Once the desiccant becomes saturated, it is consequently heated to release the moisture, which will be absorbed by the air. This process is referred to as 'reactivating' the desiccant. Depending on their physical state, these materials can be categorized by their state, whether it is solid or liquid. Further, the commercial desiccants can hold moisture from 10% to 1100% from its specific weight (Enteria and Mizutani, 2011). These commercial desiccants attract moisture until an equilibrium condition is reached in relation to the surrounding air. Absorbed moisture can be removed from the desiccant by either applying heat or reducing the pressure. For commercial purposes, the application of heat is the most commonly utilized method for desiccant reactivation, while reduction in pressure is the most common one for industrial purposes. The process of moisture intake by desiccants is based on two distinct physical methods – adsorption and absorption. Fig. 1.6 illustrates the physical contrast between these two processes.

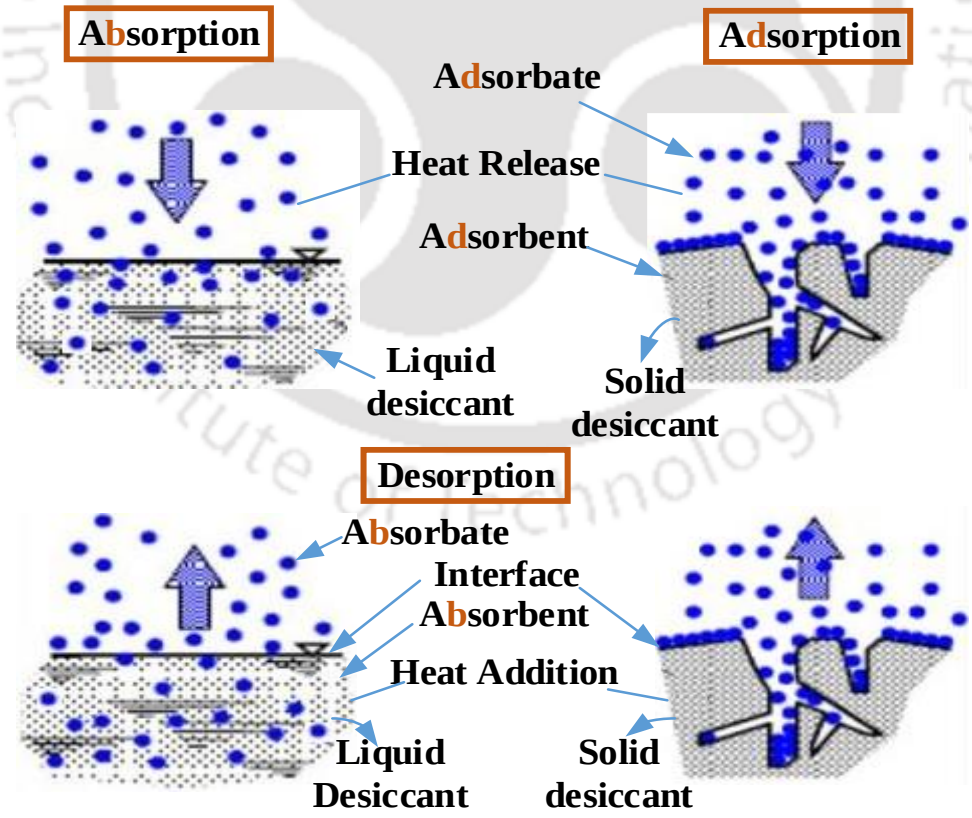

Fig. 1.6: Conceptual representation of adsorption and absorption process

As a surface phenomenon, adsorption occurs at the boundary of two phases, in which cohesive forces, such as the Van der Waals forces, and hydrogen bonding act between the molecules of all the elements, regardless of their state of aggregation. This process is also referred as 'physisorption'. In contrast, absorption is a chemical process and it is a volumetric phenomenon triggered by chemisorption (i.e., due to valency forces) (Low, 1960). Overall, solid desiccant followed the adsorption principle. Conversely, the liquid desiccant absorbs moisture from the surrounding air through the absorption principle. Both of these desiccant systems have been broadly applied for the purposes of dehumidification, cooling, and drying. Silica gel, activated alumina, and zeolites are the most commonly used solid desiccants, and triethylene glycol (TEG), lithium chloride (LiCl), calcium chloride ($CaCl_2$), and lithium bromide (LiBr) solutions are the most commonly used liquid desiccants. The selection of the liquid desiccant is essential in view of the overall dehumidification system performance. Its selection depends on various properties, which are listed in Table 1.1.

Table 1.1: Framework for the selection of liquid desiccant

Sorption/ desorption properties	**Economic and environmental properties**	**Thermodynamic properties**
• Dehumidification capacity • Heat of absorption	• Availability • Low initial and operating cost • Non-hazardous (flammability and toxicity) • Low corrosivity • High durability	• Low vapour pressure • Hold large quantity of water vapour • Low crystallization point • Low regeneration temperature • High density • Low surface tension • Stability (non-volatile) • A high rate of mass transfer

1.3.1. Working principle of desiccant air-conditioning systems

The liquid desiccant air-conditioning system generally consists of two units: the dehumidifier and regenerator. The function of the dehumidifier unit is to remove the water vapour from the ambient/process air by bringing in contact with liquid desiccant. The regenerator unit regenerates the diluted desiccant solution flowing from the dehumidifier unit to an acceptable concentration (near the desiccant's inlet concentration of dehumidifier) by utilizing low-grade

energy sources. Thus, continuous operation of the dehumidifier–regenerator can be maintained. Further, the sensible heat handling unit (Air-handling unit; AHU) handles the sensible heat load of the process air flowing from the dehumidifier unit as per indoor thermal comfort. The working principle of a conventional vapour compression system is shown in Fig. 1.7. To achieve total heat load requirements of the incoming air, a basic liquid-desiccant system combined with a vapour compression air-conditioning system proposed is shown in Fig. 1.8.

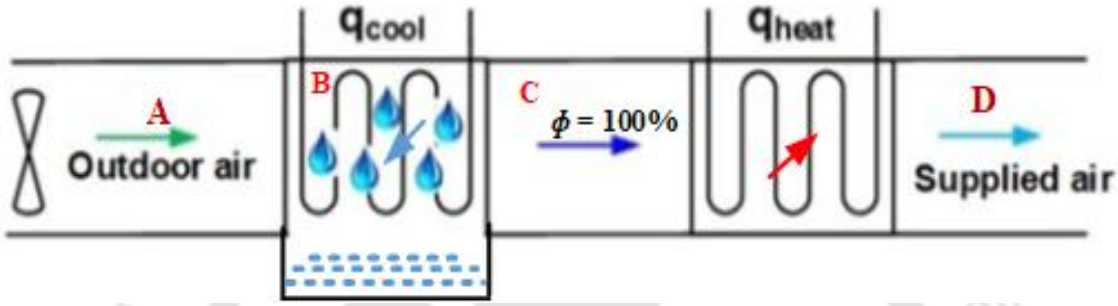

Fig. 1.7: Schematic of conventional vapour compression air conditioning system

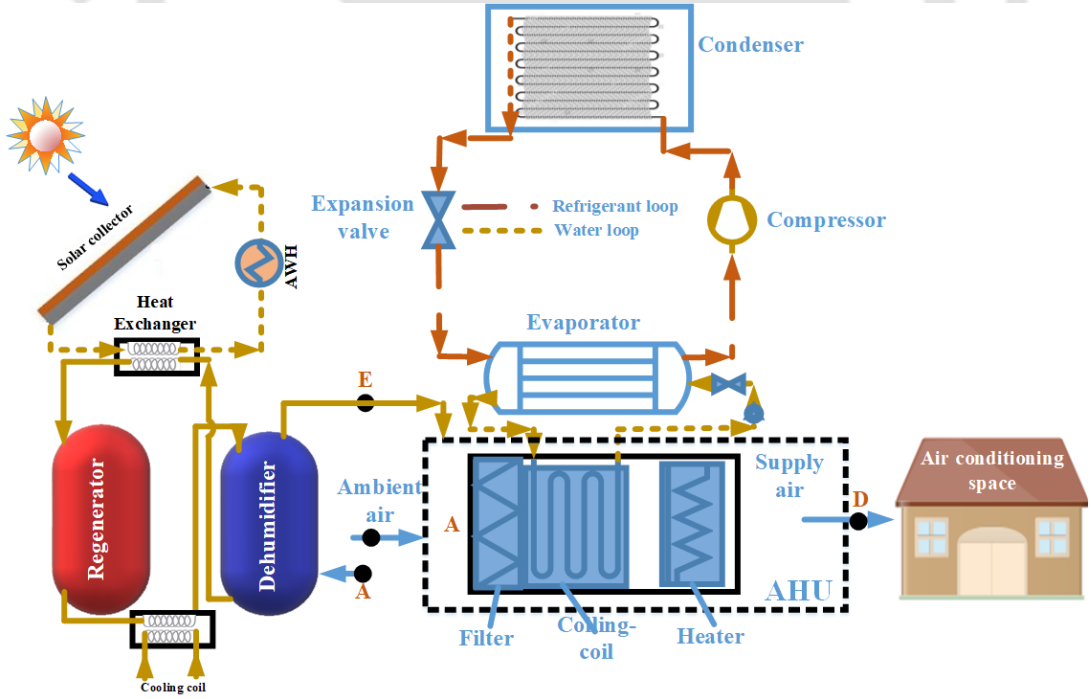

Fig. 1.8: Schematic of the liquid desiccant cooling system combined with vapour compression system (A: Humid air; B: Dehumidifier air; C: Ambient air; D: Cooled and dehumidified air; AHU: air handling unit; AWH: auxiliary water heater)

In the dehumidification system, the difference in vapour pressure between the desiccant and humid air is the driving force for moisture transfer. When the vapour pressure of humid air is higher than the vapour pressure of the desiccant solution (dehumidifier), moisture present in humid is transferred to the desiccant solution and make the desiccant solution more aqueous (air dehumidification). Similarly, when the vapour pressure of humid air is lower than the vapour pressure of the desiccant solution (regenerator), the moisture present in the desiccant solution is transferred to supply air and make the air more humid (regeneration). These processes are graphically represented in Fig. 1.9.

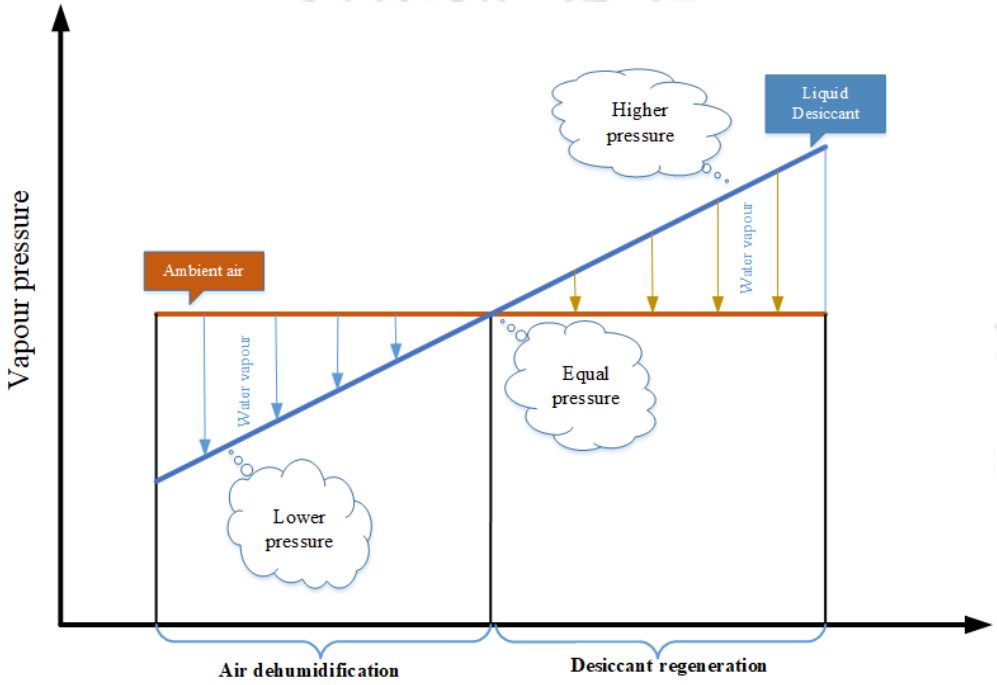

Fig. 1.9: Variation of vapour pressure in liquid desiccant system

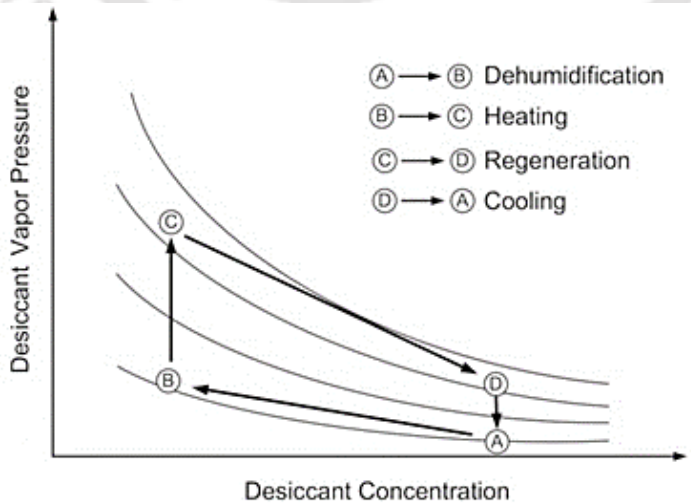

Fig. 1.10: Vapour pressure change in the desiccant dehumidification system

Therefore, to enhance the regeneration performance, the vapour pressure of the desiccant needs to be raised by heating the desiccant solution. Similarly, the desiccant solution needs to be cooled to lower the vapour pressure for better dehumidification. The process of heating and cooling can be accomplished with the help of heat exchangers. The change in vapour pressure of the air stream and desiccant solution throughout the dehumidification and regeneration process is illustrated in Fig. 1.10. In state A, the desiccant solution enters the dehumidifier with high concentration and a lower vapour pressure than the humid air. The solution draws the moisture from the air during the dehumidification process and reaches State B with a decreased concentration and increased vapour pressure. Vapour pressure is further adjusted when the solution is heated before entering the regenerator in State C. At stage C, the solution's vapour pressure exceeds that of the process air and releases the retained moisture into the air. Subsequently, vapour pressure decreases, and concentration increases as it enters State D. Finally, it is further cooled to lower its vapour pressure. The desiccant and conventional air conditioning processes are represented in the psychometric chart, as shown in Fig. 1.11.

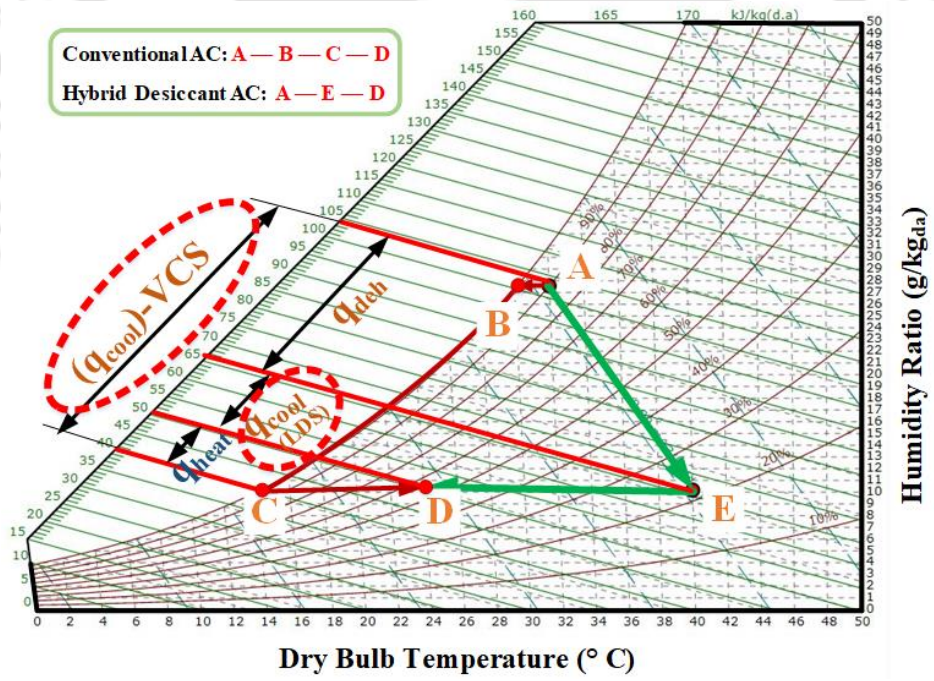

Fig. 1.11: Psychometric chart for space air conditioning process

For the conventional air conditioning system (Fig. 1.7), the dehumidification process from outdoor air (state A) to supplied air (state D) is depicted in a psychometric chart (A-B-C-D), as shown in Fig. 1.11. First, the outdoor air (state A) is cooled down to its dew point temperature (state B). Line A-B represents this process in a simple and straightforward manner. In order to condense extra water from the outdoor air, the cooling process continues and follows

the line B-C. Further, to meet the comfort requirement, the air is reheated by following line C-D. Conversely, in the case of hybrid desiccant air conditioning system (Fig. 1.8), the dehumidification process from outdoor air (state A) to outlet dehumidifier (state E) can be achieved by chemical dehumidification. Subsequently, to meet the comfort requirement, the air is cooled by following the line E-D, as shown in Fig. 1.11. It is clearly observed from the Psychometric chart that the need of cooling load for the desiccant air conditioning system is significantly reduced compared to the conventional air conditioning system.

1.3.2. Categories of desiccant air-conditioning systems

The desiccant ACs are classified as

- **Solid desiccant air-conditioning systems**

In the solid desiccant system, the ambient air is passed through the wheel. Due to the vapour pressure difference between the air and the desiccant surface, the desiccant surface adsorbs the water vapour from the processed ambient air. Ambient air and desiccant material get heated during the adsorption processes due to the latent heat of condensation, exothermic reaction, and sensible heat exchange. Hence, hot and dehumidified air exits from the solid desiccant wheel, and the wetted desiccant material can be regenerated using low-grade thermal energy sources. The operation of the desiccant wheel is shown in Fig 1.12.

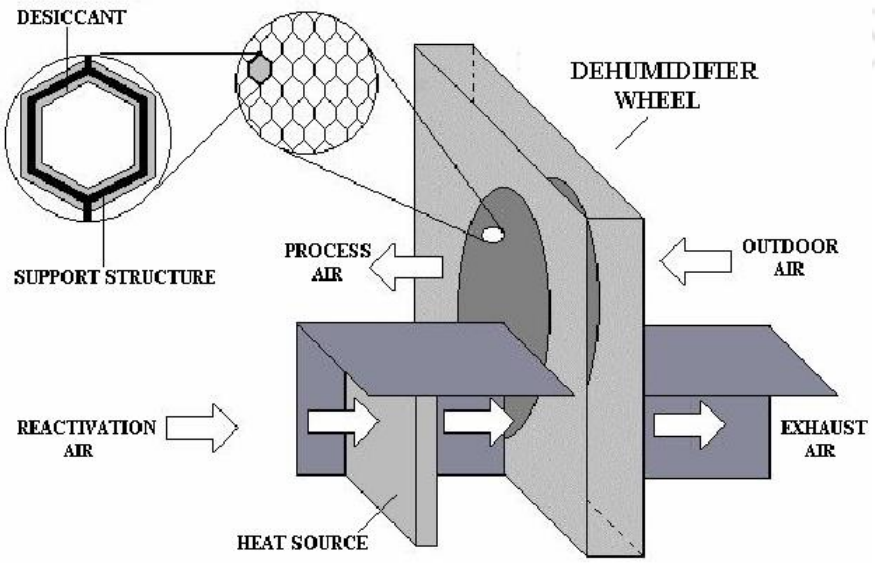

Fig. 1.12: Schematic of a solid desiccant wheel (Camargo et al., 2005)

In the solid desiccant wheel, the area of regeneration is typically between 25% to 50%. Air passes through the wheel, as shown in Fig 1.12 (Camargo et al., 2005). The desiccant material absorbs moisture from the air in the wheel's dehumidification region because of the vapour pressure difference. Generally, 75% of the wheel is considered the dehumidification area. As the wheel rotates, the area that has absorbed moisture from the air will reach the wheel's regeneration section. In the regeneration section, the ambient air absorbs the previously absorbed moisture from the wheel. Thus, the dehumidification and regeneration process occurs in a cycle in the solid desiccant wheel. Solid desiccant dehumidifiers have different configurations, especially for the wheel's flutes through which the air passes, such as sinusoidal, honeycomb, triangular, etc. A solid desiccant wheel is typically composed of hygroscopic materials such as silica gel, activated carbon, zeolites, LiCl, charcoal, etc. Out of all of the desiccant materials, silica gel is the most widely preferred since silica gel is affordable and readily available.

- **Liquid desiccant air-conditioning systems**

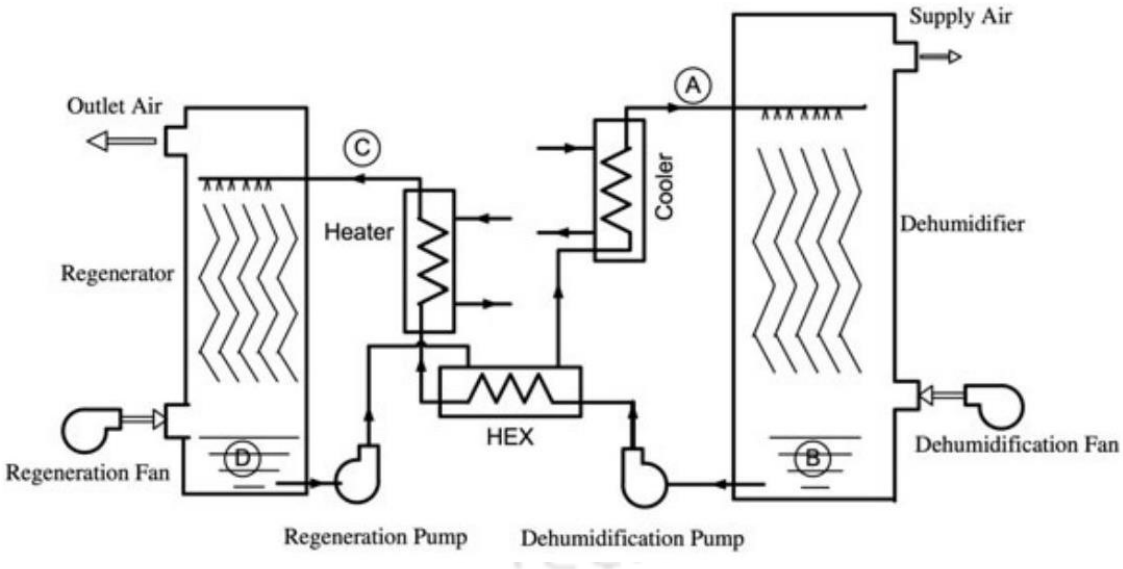

Fig. 1.13: Liquid desiccant dehumidification system (Wang et al., 2013a)

Ambient air is dehumidified when it comes into contact with a strong liquid desiccant solution. In order to provide sensible cooling to the dehumidified air, traditional vapour compression/vapour absorption/ direct or indirect evaporative cooler units can be used. Subsequently, the dehumidified air is forwarded to the conditioned space (Fig. 1.13). Due to

the absorption of moisture weakens the solution concentration; therefore, it is directly sent to the regeneration process to release the moisture using external heat sources like solar energy. This process is called "reactivating" the desiccant.

1.3.3. Comparison of liquid and solid desiccant based air-conditioning systems

Table 1.2 show that the liquid desiccant-based ACs is a promising alternative for handling high-latent loads compared to solid desiccant-based ACs. Liquid desiccants can absorb moisture at a higher rate than that of solid desiccants. Liquid desiccants require lower regenerating temperatures, usually in the range of 50–80°C. In contrast, the solid desiccant system requires regenerating temperature in the range of 60–115°C (Hamed et al., 2013). Another benefit of liquid desiccants is that it can be stored in a concentrated solution for use during periods when solar energy is absent and offers more flexible operational characteristics. These systems are attractive because of their operational flexibility and capability to absorb airborne pollutants and bacteria (Oberg and Goswami, 2016, 1998). Compared to solid desiccants, the liquid desiccant system generally causes lower airside pressure drops (Mei and Dai, 2008). Moreover, the latest developments are focused on liquid sorption applications.

Table 1.2: Comparison between liquid and solid desiccant ACs (Deng et al., 2011; Ghafoor and Munir, 2015)

Characteristics	**Liquid desiccant ACs**	**Solid desiccant ACs**
Materials	Liquid desiccant material	Solid desiccant material
Regeneration temperature	60-90°C	60-150°C
Capacity range	50-500 kW, 3000-140,000 $m^3 h^{-1}$	5-350 kW, 500-50,000 $m^3 h^{-1}$
Cooling method	Cooling water or air-cooled	Cooling water
COP	0.5-1.3	0.3-1.0+
Applications		
	1) Large capacity industrial deep drying dehumidification applications.	1) Industrial process or storage.

2) Building comfort and indoor air quality control.	2) Cold footprint buildings, building comfort and indoor air quality control.
3) Especially the site for removing airborne contaminants.	

The liquid sorption materials possess the advantages of higher air dehumidification at the same driving temperature and the possibility of high energy storage through hygroscopic solutions (Hwang et al., 2008). The liquid desiccant-assisted ACs can achieve up to 40% of energy savings over traditional ACs. Those savings become even more significant when the required energy needed for regeneration is drawn from solar energy (Ali and Vafai, 2004). During dim sunlight, the weak liquid desiccant can be stored until required regeneration heat is not available. These systems can handle large heat loads (> 50 TR or 176 kW) and minimise the overall energy demand. Furthermore, they can be employed in large capacity industrial deep drying applications.

1.4. Desiccant system with sensible cooling system

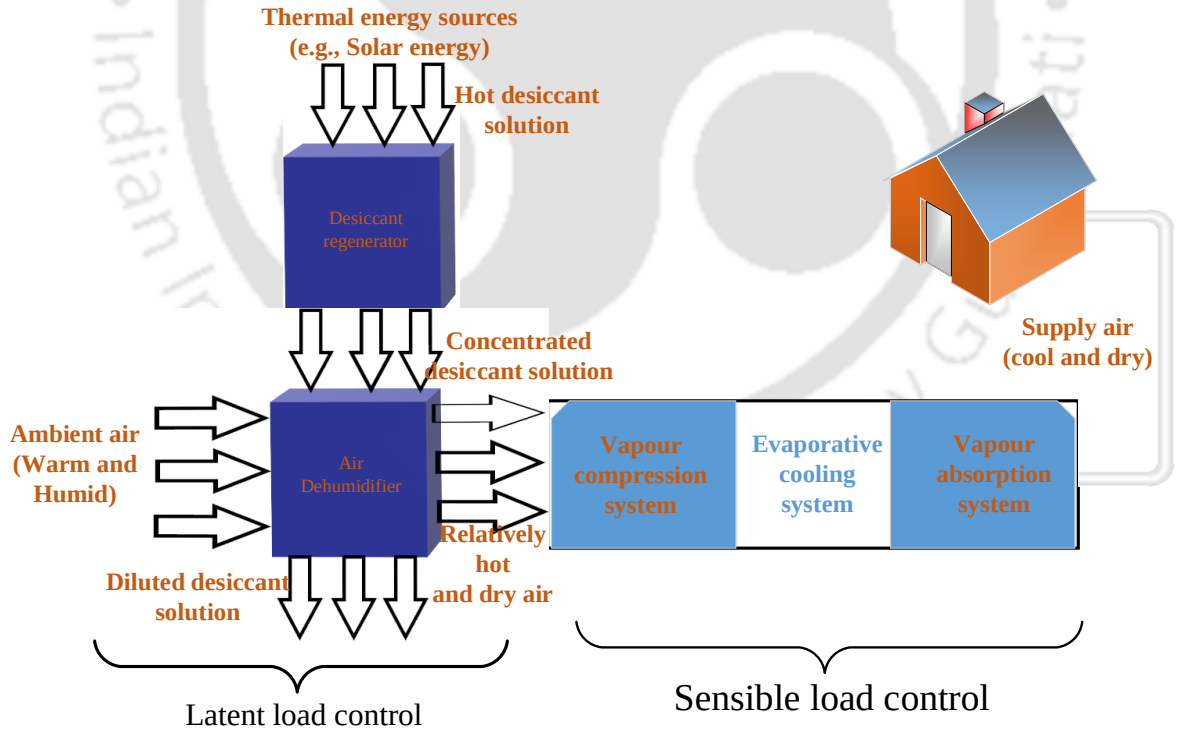

Fig. 1.14: Desiccant system with sensible cooling system

Thermal energy must be applied to reactivate the desiccant material by desorbing moisture from the desiccant materials. This concept of a thermally-driven desiccant dehumidification

technique is illustrated in Fig. 1.14. In the first stage, the air is dehumidified by condensing moisture out of the air via the desiccant. During the second stage, the dehumidified air is cooled by the adsorption heat exchanger/evaporative cooling (direct or indirect)/vapour compression system until it reaches a comfortable temperature, as seen in Fig. 1.14. Subsequently, the dry, cooled air send to the air-conditioned space.

1.5. Desiccant film based air dehumidification

Hydrogels are a three-dimensional network consisting of hydrophilic polymers, which can swell in water and absorb a substantial amount of water without changing its structure due to either physical or chemical crosslinking (Matsumoto et al., 2018). The hydrophilic parts of the polymer cater to the water-absorbing ability, while the crosslinks between the polymeric chains maintain the structure, ensuring the molecules not disintegrating in the solution. A broad range of hydrogels has been utilized largely in the food processing industry, disposal diaper industry as well as contact lenses industry because of their thermo-physical properties of water absorption, permeability, transparency, viscoelasticity, swelling, and biocompatibility. Some hydrogels have a unique property that it changes its volume abruptly in response to certain environmental changes, such as temperature (Chen and Hoffman, 1995; Yoshida et al., 1995), pH (Siegel, 1993), light (Suzuki and Tanaka, 1990), electric field (Osada et al., 1992), and biomolecules (Miyata et al., 2006, 1999). Such stimuli-responsive hydrogels can be potentially used as a smart material as well as soft materials in an aqueous state or in their dry form. Hydrogels can be tailor-made for various applications in different forms such as films, pellets, powders and membranes. These unique properties make the hydrogel films as energy-efficient materials for air dehumidifying applications. Additionally, the incorporation of desiccant in those stimuli-responsive hydrogel films would be a great research interest for potential air dehumidification applications.

1.6. Motivation of present work

National Oceanic and Atmospheric Administration (NOAA) had prescribed the year 2015 as the warmest year from the time when records began in 1880 (ASHRAE, 2016). The increased number of scorching hot summer days are record-breaking in various zones of the globe. Therefore, the demand for heating, ventilation and air conditioning systems are annually expected to hike by 6.2% (Rafique et al., 2015). The requirements of human comfort indoor conditions are elucidated in terms of regulated temperature (sensible load capacity) and also

by control of humidity (latent load), especially for hot and humid geographic regions. In order to control the required humidity level, the conventional refrigerant aided vapour compression systems (VCS) are condensed out the water vapour present in air by lowering the air dry-bulb temperature below its dew point temperature. Subsequently, the dehumidified air is subjected to reheat for reaching the desired indoor temperature range that eventually consumes more power in terms of electricity. For example, in order to extract the air specific humidity of ~0.07 kg_{wv}/kg_{da}, the air needs to be cooled to nearly 9°C (Ahmed et al., 1997). The electricity generation often involves the fossil-fuelled driven power plant that is having a resultant emission of CO_2 into the lower atmosphere. Emerging nations like China and India are still relying on refrigerants (those are not fully environmental friendly) based for air conditioning. However, European Commission Regulation 2037/2000, articulates the usage of all HFCs would be phasing out from the year of 2015 (Sarbu and Sebarchievici, 2013). Even so, environmental concern seems to revoke when the level of comfort, luxury and standard of living associated with humans. Many convenient protocols, such as Montreal Protocol are directed to some significant changes in the production of refrigerants and their control consumption. Since then, different initiatives have been considered to minimise the use of HFCs. In this perspective, a holistic approach needs to be adopted to maintain the energy-intensive humidity level. Recently, sorption technology has taken significant attention as an alternative process to standardise the mechanical air conditioning system for dehumidification of air without cooling below its dew point temperature. Liquid desiccant dehumidification systems (LDAC) are one of the sorption technologies, where a synthetic or natural desiccant is used as a hygroscopic material to absorb the moisture of the surrounding air. Desiccant based ACs is classified as solid desiccant based ACs and liquid desiccant based ACs. As discussed earlier, compared to solid desiccant based ACs, liquid desiccant based ACs is advantageous due to less air side pressure drop, less maintenance, operational flexibility and utilisation of low- grade thermal energy sources such as solar or waste heat for the regeneration of liquid desiccant. Therefore, solar-driven liquid desiccant based ACs is considered for the present investigation. Key components of solar driven liquid desiccant ACs are dehumidifier, regenerator and solar collector. In this thesis, experimental and numerical analyses of the solar collector based dehumidifier-regenerator system are presented. Further, a major importance is given for analysing the heat and mass transfer characteristics along the structured packing chamber of a liquid desiccant dehumidifier/regenerator and the heat transfer characteristics of the U–tube evacuated solar tube collector system.

1.7. Structure of the thesis

The performance of the solar-driven liquid desiccant ACs mainly depends on the dehumidifier/regenerator's heat and mass transfer characteristics. The desiccant dehumidifier/regenerator and U–tube solar evacuated tube collector module is fabricated, and the performance is investigated at different operating conditions.

This thesis is organised in eight chapters. A brief description of the content of each of the chapters is discussed below:

Chapter 1 starts with a brief introduction of conventional air conditioning systems. The drawback of conventional air conditioning systems and the advantages of sorption based air conditioning systems are discussed. The advantages of liquid desiccant based ACs is explained over the solid desiccant ACs. The working procedure of desiccant based dehumidification system and motivation of the present work are presented.

Chapter 2 discusses the state-of-the-art on various aspects of the liquid desiccant dehumidification/regeneration systems and the solar evacuated U–tube collector system. The literature on the developed experimental study and numerical models are reviewed. Based on the literature survey, the objectives of the present thesis work are formulated.

Chapter 3 covers the performance investigations of various single desiccant solution systems numerically to compare the cross and counter flow dehumidifier performance. The selection of desiccant is discussed briefly.

Chapter 4 depicts solar evacuated tube collectors' performance investigation experimentally and develops a numerical model based on experimental results for desiccant regenerator system.

Chapter 5 outlines the experimentally and numerically studies on coupled heat and mass transfer phenomena between air and desiccant in a solar-assisted thermal liquid desiccant dehumidifier-regenerator system.

Chapter 6 covers the development of heat and mass transfer correlation based on experimental datasets to optimise the input process parameters for the dehumidifier-regenerator system's better performance. To study the performance of combined dehumidifier-regenerator study at the optimum condition.

Chapter 7 introduces the preparation, characterization and analysis of liquid desiccant doped novel hydrogel films for potential air-dehumidification applications.

Chapter 8 outlines the major conclusions arrived from numerical, experimental and optimisation analyses of the solar-assisted liquid desiccant dehumidification systems. Further, a future scope on the present field is also mentioned in detail.

1.8. Closure

This chapter presents the introduction of conventional air conditioning systems. The drawback of conventional air conditioning systems and the advantages of sorption based air conditioning systems are discussed. The advantages of liquid desiccant based ACs is explained over the solid desiccant ACs. The working procedure of desiccant based dehumidification system and motivation of the present work are presented. In the next chapter (Chapter 2), the literature review related to desiccant air conditioning is presented comprehensively.

CHAPTER 2
State of the Art

2.1. Introduction

The concept of liquid desiccant ACs was initially explored by 'Lof' in 1955 using tri ethylene glycol as a desiccant (Gommed and Grossman, 2004). During the 1970s, many investigators further improved this technique to save energy consumption in conventional ACs by shifting the major part of the air conditioning load to the more energy-efficient desiccant systems (Oberg and Goswami, 2016, 1998). In the late 1970s, public concern on energy issues led investigators to focus on desiccant dehumidification for commercial and residential AC applications. However, to study the recent advancement in the liquid desiccant system, a thorough literature review is needed. In this chapter, a detailed review of liquid desiccant materials and key characteristics are presented. Subsequently, the literature review on desiccant dehumidification is carried out in two sections: experimental work and analytical work. A brief discussion of different significant research findings is presented in this chapter. At the end of this chapter, based on the literature closure, the core objectives are fixed. The flow chat of the current chapter is shown in Fig. 2.1.

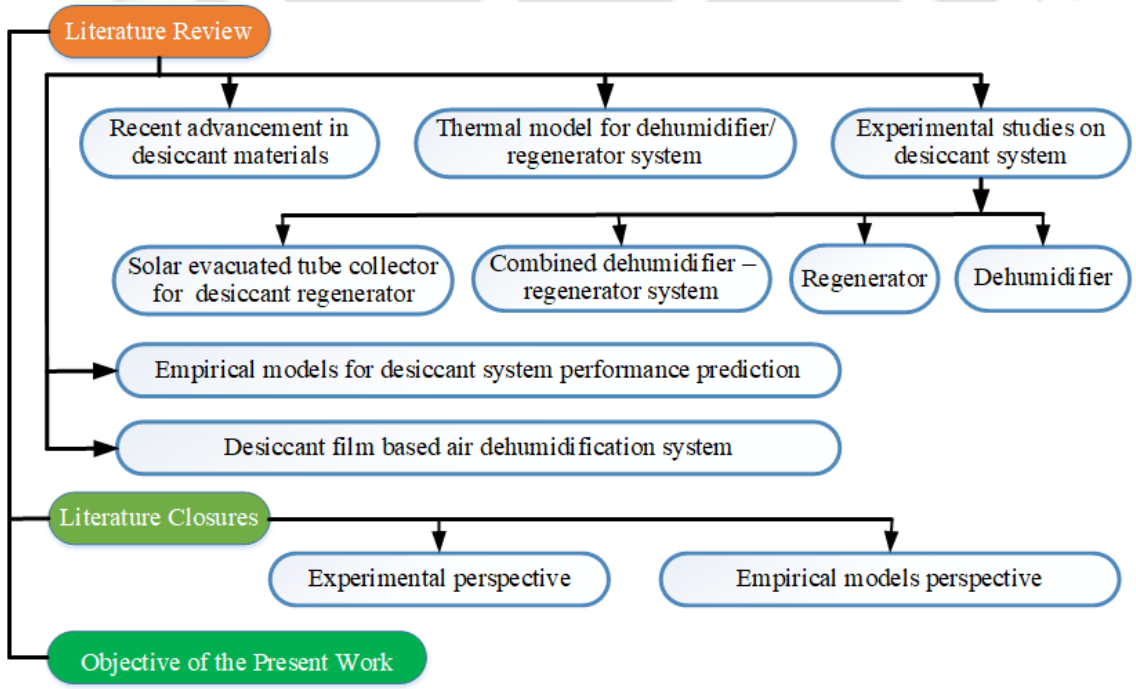

Fig. 2.1: Flowchart of state of the art chapter

2.2. Recent progress in liquid desiccant materials

Desiccant material can hold a large amount of water vapours and can also desorb easily. Liquid desiccants are generally in liquid form having high affinity of water vapour. In general, for choosing a suitable desiccant, the equilibrium vapour pressure and other physical properties should be comprehensively considered. The selection of a desiccant material will have a direct effect on the desiccant dehumidifier design. An ideal liquid desiccant should possess the following properties: large saturation absorption capacity, low regeneration temperature, high heat transfer, non-volatile, non-corrosive, odourless, non-toxic, non-flammable, stable and inexpensive. There are many ways to classify desiccant materials (Rafique et al., 2016). On the other hand, worldwide researchers have made a significant contribution in investigating the effectiveness of adiabatic dehumidification/regeneration systems employing different kind of liquid desiccant materials (Buker et al., 2015; Jain et al., 2011; Katejanekarn et al., 2009; Liu et al., 2020). Lof (1955) carried out experimental studies using tri-ethylene glycol (TEG) as a liquid desiccant and concluded that the desiccant system could be an energy-saving system for hot and humid locations. Chau and Worek (2009) and Zurigat et al. (2004) also conducted a study using TEG desiccant. Similarly, Fumo and Goswami (2002), Gommed et al. (2004a), Yin et al. (2007a), Katejanekarn et al. (2009), Das and Jain (2015) and Naik and Muthukumar (2019) presented experimental investigations on dehumidification/regeneration systems using aqueous LiCl desiccant material. Further, few investigators also experimentally investigated the performances of LiBr, $CaCl_2$ and HCOOK liquid desiccants (Buker et al., 2015; Jain et al., 2011; Liu et al., 2020). Moreover, the recent desiccants and the unique desiccant combinations are listed in Table 2.1.

Table 2.1: Summary of advanced desiccant proportions of liquid desiccant

Procedure	Author (s)	Desiccant	Additions (Concentration)	Novel contribution/ key remarks
Addition of surfactant	Rivera and Cerezo (2005)	$LiBr/H_2O$	1-octanol, 2-ethyl-l-hexanol (400 ppm)	It was found that COP with 1-octanol additive increases slightly compared to the use of a 2-ethyl-1-hexanol additive. The COP increases up to 40% with the addition of 2-ethyl-1-hexanol additive in the LiBr mixture. This increment is due to an increase in the interfacial convection (Marangoni convection)

	Yao et al. (1991)	LiBr/H_2O	2-ethyl-1-hexanol (400 ppm)	It was found that the surface tension of LiBr aqueous solution (50 wt.%) was reduced from 88.10 mN/m to 35.52 mN/m with the addition of surfactant at 25 °C.
	Lin and Shigang, (2011)	LiBr/H_2O	2-ethyl-l-hexanol (2EH) (90 ppm)	The mass transfer coefficient with 2EH was about twice compared to the without 2EH that was mainly lead by the strong Marangoni convection.
	Wen et al. (2018a)	LiCl/H_2O	Polyvinyl pyrrolidone (PVP-K30)(0.4%)	PVP-K30 surfactant improved the dehumidification rate and effectiveness of 22.7% and 19.9%, respectively, compared to the pure LiCl operation.
	Cosenza, F. (1990)	LiBr/H_2O	2-ethyl-1-hexanol	It was found that the absorption rate was increased up to 4 times with the adding of surfactant.
	Cihan et al. (2017)	LiCl/H_2O	Polyether modified siloxane (0.05% to 0.3%)	Higher amount of surfactant (0.05% to 0.3%) reduced the surface tension of desiccant solution. The minimum surface tension was obtained with the addition of 0.3% surfactant into desiccant solution.
Addition of nanoparticles	Ali et al. (2004); Ali and Vafai, (2004)	$CaCl_2$/H_2O	Cu nanoparticles (0-0.2%)	Nanoparticles suspensions were added to the desiccant to enhance the heat and mass transfer process of the system. It was also found that the dehumidification and cooling rates of air were improved with an increase in the volume fraction of nanoparticles and dispersion factor.
	Kang et al. (2008)	LiBr/H_2O	Fe nanoparticles, Carbon nanotubes (CNT) (0.01%,0.1%)	The vapour absorption rate was found to increase with increasing the solution mass flow rate and the concentration of Fe and CNT nanoparticles. It was found that the mass transfer enhancement was much more significant than the heat transfer enhancement in

				the binary nanofluids with Fe and CNT. Further, it was concluded that the mass transfer enhancement from the CNT nanoparticles becomes higher than that from Fe nanoparticles.
	Kim et al. (2011)	LiBr/H_2O	SiO_2 nanoparticle	It was stated that the distribution stabilizer was required for the stable dispersion of nanofluid when the concentration of SiO_2 nanoparticle was greater than 0.01 %vol. Experimentally studied the vapour absorption rate of the solution with 0.005 % vol SiO_2 nanoparticles and 18% absorption enhancement was detected.
	Shoaib et al. (2020)	$CaCl_2$/H_2O (48 wt.%)	CuO nanoparticles (0.35 vol.%)	Results revealed that the addition of nanoparticles could hike the dehumidification rate up to 11 g/s- m^2 as compared to pure desiccant operation.
	Wen et al. (2018b)	LiC1/H_2O	multi-walled carbon nanotubes (MWNTs) 0.1%	It was experimentally showed that LiCl/H_2O-PVP solution and nanofluid can enhance the dehumidification rate by up to 26.1% and 25.9%. Therefore, the nanoparticles (MWNTs) can improve dehumidification rate more compared to surfactant (LiCl/H_2O-PVP).
Compound liquid desiccants	Wen et al. (2019)	LiC1/ hydroxyethyl urea/ H_2O	25:39:36	Examined a new kind of mixed liquid desiccant to reduce the corrodibility, and as well as the dehumidification performance. The experimental results indicated that the corrodibility of mixed solution was far smaller than that of pure LiCl solution. The absolute moisture change and effectiveness has a significantly improved of 8.7–14.3% and 5.8–15.2% for the newly mixed

			solution compared with LiCl solution
Ertas et al. (1992)	LiC1/$CaCl_2$ / H_2O	21.5:21.5:57	Developed a new Cost Effective Liquid Desiccant (CELD, comprised of 50% each of LiCI and $CaCl_2$ salt content). It was shown that the vapour pressure of the CELD solution was lower than that of pure calcium chloride.
Wei et al. (2008)	LiC1/$CaCl_2$ / H_2O	31.2:20:48.8	The dehumidification effect could be raised by more than 20% with mixed LiCl and $CaCl_2$ solution compared to pure LiCl solution.
Chen et al. (2009)	Gycol/desiccant (LiBr or LiCl)/ H_2O	Gloycol varied (4–25) mass% with desiccant (16–25) mass% .	DEG/H_2O/LiCl, T_4EG/H_2O/LiCl, DPG/H_2O/LiCl, DEG/H_2O/LiBr, T_4EG/H_2O/LiBr, and DPG/H_2O/LiBr were studied, where gloycol varied (4–25) mass% with desiccant (16–25) mass%. Compared to the conventionally use liquid desiccants, the vapour pressures of the aqueous-organic systems with salt yield smaller values of vapour pressures. Thus, the aqueous-organic with salt systems may well be treated as the potential absorbents for liquid desiccants.
Zhao et al. (2016)	(LiBr/LiCl+ $CaCl_2$/$MgCl_2$ +water/methanol)	31.7:16.7:51.6	Results showed that the dehumidification efficiency of mixed liquid desiccant was higher than that of a single solution. The LiBr–$CaCl_2$–water system can

				obtain higher COP compared with other systems under the condition of the same dehumidification performance in summer.
Ionic liquid desiccants	Luo et al. (2011)	1-Ethyl-3-methyl-imidazolium Tetrafluoroborate ([EMIM]BF_4)/ H_2O	83%	Compared with traditional desiccants, [EMIM]BF_4 solution has considerably lower corrosion rate and does not crystallize at high mass concentration. Therefore, it is a possible substitute of existed desiccants in liquid desiccant air-conditioning system.
	Qu et al. (2017)	1-Ethyl-3-methylimidazolium acetate, [EMIM][OAc/ H_2O	30%-75%	Investigation was carried out to reduce the corrodibility with higher dehumidification performance.

2.3. Thermal models reported on liquid desiccant dehumidification/regeneration system

Treybal (1980) was the first person to describe the complex heat and mass transfer process during air dehumidification by proposing a simple mathematical model. Merkel (1925) came up with an analytical model to describe the heat and mass interactions between air and the working fluid for evaporative cooling purposes, whereas the developed model did not accounted the evaporation loss. Nottage (1941) and Yadigraoglu and Pastor (1974) modified the Merkel model by considering evaporation loss and achieved higher accuracy compared to Merkel's model. Zhang et al. (2012) proposed an analytical model for analyzing the simultaneous heat and mass transfer processes involved in a counter – flow cooling tower and validated with the experimental data available in the literature. Peng and Howell (1981) developed mathematical models for two liquid desiccant systems powered by solar or geothermal energy and using triethylene glycol as the desiccant solution. Their parametric analysis showed that the optimum absorber height for the process recirculation mode is 1.2 m, while for the exhaust recirculation mode, it is 0.9 m. The exhaust recirculation mode has better thermal performance and lower fan power requirements at full capacity, whereas the process recirculation mode produces cooler and drier air. Factor and Grossman (1980), Fumo and

Goswami (2002b), and Khan and Ball (1992) developed finite difference based thermodynamic models to evaluate the liquid desiccant dehumidifier and regenerator. In contrast, Stevens et al. (1989) provided analytical expressions of the air and desiccant parameters for the counter-flow dehumidifier. Jain et al. (1994) attempted to evaluate seven liquid desiccant cycles for hot and humid climates. A simulation model was developed based on the constant effectiveness of heat exchangers and evaporative coolers. The effect of various outdoor conditions and the effectiveness of heat exchangers on the cooling capacity has been investigated. It was found that a combination of dehumidifier and wet surface heat exchanger has a better performance for a wide range of outdoor conditions. Oberg and Goswami (2016) introduced NTU method to analyse the performance of the aforementioned systems.

Babakhani and Soleymani (2010) and Liu et al. (2007) compared their mathematical models based on finite difference/NTU method with the experimental findings. It was found that their models were in good agreement with the experimental datasets. Chengqin et al. (2006) developed a model for heat and mass transfer interactions in a liquid desiccant dehumidifier/regenerator. Patil et al. (2016) developed an empirical correlation for estimating the actual gas-liquid contact area and found more accurate than other correlations with a maximum deviation of ±15%. Zalewski and Gryglaszewski (1997) developed a mathematical model by introducing a correction factor for the mass transfer coefficient. Gandhidasan (2004; 2005) presented a simplified model using dimensionless parameters such as moisture and thermal effectiveness and formulated the correlations for predicting the evaporation and condensation rates in terms of heat and mass exchange effectiveness. The proposed model has been compared with Fumo and Goswami's experimental data, and the error has been found to be within ±13%. Peng et al., 2017 studied the heat and mass transfer characteristics of a packed tower by proposing a thermodynamic model. They compared the developed model with Fumo and Goswami's experimental data and observed a maximum error of ±18%. Lu et al. (2001) and Chengqin et al. (2006) reported a method for finding the analytical solution of the coupled heat and mass transfer performance for the dehumidifier and regenerator. Analytical solutions of the air enthalpy and desiccant equivalent enthalpy field within the cross-flow dehumidifier/regenerator were given by Liu et al. (2007) where the air and desiccant are not mixed breadthwise (which means the transfer processes of the air and desiccant are both two dimensional). The enthalpy field gained from the analytical solutions compares well with numerical solutions, and the analytical enthalpy efficiency compares well with experimental results of the cross-flow dehumidifier. Researchers (Dai and Zhang, 2004; Khan and Martinez,

1998; Liu et al., 2007) have developed mathematical models of the coupled heat and mass transfer processes in the dehumidifier or regenerator, and most of the models were solved numerically. Babakhani and Soleymani (2009) presented a new analytical solution of heat and mass transfer processes in a packed bed liquid desiccant dehumidifier. Their results revealed that design variables such as desiccant concentration, desiccant temperature, air flow rate, and air humidity ratio have the most significant impact on the dehumidifier's performance. The liquid flow rate and the air temperature did not have a significant effect. Furthermore, the effects of air and liquid desiccant flow rate have been reported on the humidity effectiveness of the column. Langroudi et al. (2014) statistically evaluated the performance of the liquid desiccant dehumidification system using response surface methodology (RSM) and studied the heat and mass transfer processes occurring in the liquid desiccant dehumidification system. It was observed that the proposed model with the NTU model were in good agreement with an accuracy of ±13%. Yin et al. (2009) investigated the heat and mass transfer interactions along the liquid desiccant dehumidifier and regenerator using a mathematical model validated by the experimental data.

Several thermodynamic models have been developed for predicting the heat and mass exchange processes in the adiabatic dehumidification/regeneration system, which includes finite difference model (Factor and Grossman, 1980; Liu et al., 2007), ε – NTU model (Babakhani and Soleymani, 2010, 2009; Stevens et al., 1989) and simplified models (Gandhidasan, 2005; 2004). Further, a comparison is made with the notable contributions presented in the literature for highlighting the importance of different thermodynamic models (Table 2.2).

Table 2.2: State of the art on the dehumidifier/ regenerator model for operational behaviour studies

Author (s)	**Model addressed**	**Notable contribution**
Stevens et al. (1989)	Effectiveness-NTU model	The performance of dehumidifier was predicted by considering the analogy of heat exchanger effectiveness-NTU method. Good agreement with experimental results was found for the single solution system.

Diaz (2010)	Transient model	Flow dynamics of liquid desiccant ($CaCl_2$) in a parallel flow dehumidifier prototype was analyzed using transient model.
Koronaki et al. (2013)	Runge-kutta five-order model	The performance of a dehumidifier was predicted under different operating conditions with single aqueous desiccant solutions, i.e., $CaCl_2$, LiBr and LiCl.
Li et al. (2013)	Kinetic mass transfer model (based on kinetic theory of gases)	The dehumidification mechanism was described and the dehumidification performance was predicted for a single solution system.
Wang et al. (2013b)	Hybrid Levenberg–Marquardt model	Dehumidifier performance was predicted over a wide range of operational settings and was verified with experimental results.
Luo et al. (2014)	CFD analysis	The temperature profile of working fluids (aqueous LiCl and air) inside the dehumidifier was predicted.
Naik et al. (2018)	Finite difference method combined with recursive model	The effectiveness value was initially guessed, and dehumidifier governing equations were solved using a recursive method for a single solution desiccant (LiCl, LiBr) dehumidification system.

2.4. State of the art on experimental studies

Researchers around the globe have made a significant contribution in investigating the performance of adiabatic dehumidification/regeneration systems by employing different (a) liquid desiccant materials (Buker et al., 2015; Jain et al., 2011; Katejanekarn et al., 2009; Liu et al., 2020), (b) flow configurations (Cho et al., 2019; Liu et al., 2006; Naik and Muthukumar, 2019), (c) geometry of packing materials (Fumo and Goswami, 2002; Naik and Muthukumar, 2019; Rafique et al., 2016) and (e) operating conditions (Cho et al., 2019; Lun et al., 2018; Wen et al., 2018b). Lof (1955) carried out experimental studies using tri-ethylene glycol (TEG) as a liquid desiccant and concluded that the implementation of desiccant system could be feasible for hot and humid locations. Öberg (1998), Chau and Worek (2009) and Zurigat et al.

(2004) also conducted a study using TEG desiccant. Similarly, Fumo and Goswami (2002), Gommed et al. (2004a), Yin et al. (2007a), Katejanekarn et al. (2009), Das and Jain (2015) and Naik and Muthukumar (2019) have focused on the experimental investigations on dehumidification/regeneration systems using aqueous LiCl desiccant material. Further, few investigators also experimentally studied the performances of LiBr, $CaCl_2$ and HCOOK liquid desiccants (Buker et al., 2015; Jain et al., 2011; Liu et al., 2020).

2.4.1. State of the art on dehumidifier

Different dehumidifier designs have been studied by researchers. Elsarrag et al. (2006) performed theoretical and experimental research on structured packed dehumidifier using triethylene glycol (TEG) as a liquid desiccant. Their research sets a design guideline for the structured packed based desiccant centred air dehumidifier. Further, the experimental outcomes were compared with the theoretical model for the confirmation of experimental results. Subsequently, it was observed that the effectiveness of such dehumidifier ranging from 0.72 to 0.91 at different operating conditions. Wen et al. (2020) carried out an investigation on liquid desiccant dehumidification using potassium formate (HCOOK) desiccant solution. The vapour pressure of HCOOK solution was measured at different concentrations and temperatures. It was found that the vapour pressure of HCOOK solution with concentration of 64.3% to 73.3% was similar to that of lithium chloride (LiCl) solution with concentration of 33% to 38% when the solution temperature ranged from 45°C to 65°C. Lychnos and Davies (2012) conducted experiments and theoretical modelling to investigate the performance of a liquid desiccant system using magnesium chloride ($MgCl_2$) desiccant. It was shown that the moisture absorption rate was ranged from 154 to 194 $g.h^{-1}.m^{-3}$ at different operating conditions. Due to these advantages, the liquid dehumidifier is widely adopted in many developed countries. However, the dehumidifier suffers from a disadvantage in providing effective performance compared to VCAs due to the poor thermo-physical properties of desiccant materials. This shortcoming in the desiccant systems can be improved by introducing an effective desiccant mixture. Recently, many research efforts have been dedicated towards the exploration of desiccant mixtures, which will provide better dehumidification performance.

Wen et al. (2018) carried out an experimental study in the liquid desiccant system by adding polyvinyl pyrrolidone (PVP) surfactant. It was observed that the mass transfer performance was improved and the dehumidification rate was increased with an average of 26.1% compared

to the pure LiCl operation. Qu et al. (2017) tested 1-Ethyl-3-methylimidazolium acetate [EMIM][OAc] for adsorption and desorption process. The test results indicated that [EMIM][OAc] solution has comparable vapour pressure with LiBr or LiCl solution at a higher mass fraction of [EMIM][OAc]. Luo et al. (2011) investigated the counter-flow dehumidifier to study the performance of 1-Ethyl-3-methylimidazolium Tetrafluoroborate ([EMIM]BF_4) aqueous solution. The results showed that the dehumidification performances using [EMIM]BF_4 was a little lower than that of LiBr and subsequently, mentioned that this performance difference could be compensated by increasing the mass concentration of [EMIM]BF_4. Ren et al. (2019) introduced a new working solution of phase change materials (PCM) into aqueous LiCl desiccant to analyse the dehumidification intensity. The results showed that the dehumidification efficiency was improved. Ameel et al. (1995) conducted experiments by mixing zinc chloride and lithium chloride desiccants with a proportion of 1:1.63. It was observed that dehumidification efficiency was improved at the expense of high cost. The LiCl based desiccant mixtures are more corrosive, expensive and crystallise at low temperature. Alternatively, Donate et al. (2006) studied the mixture of organic salts (sodium formate/methanol) with LiBr desiccant and observed that the moisture absorption capability of such mixtures was high compared to pure LiBr. Lucas et al. (2008) investigated the water vapour absorption capacity of LiBr and sodium formates (CHO_2Na) based desiccants with n-octanol. The results showed that such mixtures increase the water vapour absorption capability in the presence of n-octanol. The LiBr + CHO_2Na at 45% by mass with 1000 ppm of n-octanol solution showed a better water vapour absorption capacity than a single LiBr solution. However, LiBr possesses a demerit of solubility and is responsible for uneven performance profile throughout the operation, which can be minimised by introducing calcium chloride ($CaCl_2$), an inorganic salt (typically synthesised from calcium carbonate ($CaCO_3$) (Abdullah et al., 2014). Moreover, $CaCl_2$ is the most easily available and cheapest desiccant for dehumidification, whereas its dehumidification performance greatly depends on operating conditions (Xiong et al., 2009; Ahmed et al., 1998).

2.4.2. State of the art on regenerator

Different regenerator designs have been studied by researchers. For falling film, Jain et al. (1999) studied experimentally a falling film plate regenerator. The results were compared with the predictions from theoretical model. Howell (1987) modelled a regeneration chamber

containing a finned heating coil, where hot water flowing through the coil to provide the heat of regeneration. It was found that by increasing the air to desiccant flow rate and the hot water flow rate gave a stronger desiccant leaving the chamber. For spray towers, Scalabrin and Scaltri (1990) analyzed a spray tower in which a stream of scavenging air comes into direct contact with the weak LiCl solution sprinkled over a tube bank heated internally by warm water. Chung et al. (1999) designed a U-shaped spray tower to prevent carry over and developed a mass transfer correlation for the air stripping process using TEG. Packed tower configurations have received more attention. Many researchers worked on packed regenerators and compared the results with theoretical models. Although random packed towers facilitate more mass transfer by providing larger area in a relatively smaller volume, the air pressure drop through the packing is generally high. Factor and Grossman (1980) compared the experimental and theoretical model of a packed regenerator using LiBr and pre-heated air. Etras et al. (1994) investigated the influence of the performance variables on a packed regenerator performance. Potniz and Lenz (1996) tested a packed regenerator using random polypropylene and structured packings. Experiments showed that the evaporation rate was 130–300% greater in the randomly packed bed than the structured packing bed. Oberg and Goswami (2000) developed two novel performance correlations for the effectiveness of a packed bed liquid desiccant dehumidification/regeneration. A comparison to experimental results showed that the correlations presented correctly predict the influence of the design variables on the performance within 15% error. Fumo and Goswami (2002) assessed the regeneration process under the effect of the design variables of a packed regenerator using LiCl. Longo and Gasparella (2004) reported experimental tests on sorption/desorption liquid desiccant system using H_2O/LiBr and H_2O/HCOOK. They compared between experimental and calculated values within 20% error. Gandhidsan (2005) investigated the influence of the heating source on the evaporation rate of a packed bed regenerator. Apart from that Kim et al. (2015) gave a statistical analysis based simple numerical model for packed bed regenerator performance prediction using LiCl as desiccant solution. The effect of operating parameters on regeneration characteristics was analyzed using response surface methodology. The model is suitable for determining the optimal regeneration temperature or flow rate of the desiccant solution for energy-efficient systems. Peng and Luo (2017) developed mathematical models to investigate the performance of liquid desiccant regenerator considering parallel, counter and cross-flow configurations. It was reported that the ratios of flow-rate of solution to air ($\dot{m}_s/\dot{m}_a$) and water to air ($\dot{m}_w/\dot{m}_a$) greatly influenced regeneration behaviour. The counter flow direction of heating water to desiccant solution was found to have the best effects on systems performance. Huang

et al. (2018) proposed a packing bed heating tower for dilute desiccant reactivation using PVC structured packing material and glycol as liquid desiccant with 18.2% to 31.1% of desiccant concentration. The lower solution equivalent humidity ratio and air humidity ratio drastically reduces the regeneration temperature enabling the use of low-grade heat. Inlet parameters on both air and desiccant side showed similar behaviour as in literature. Further, empirical correlations were proposed and it was in good agreement with experimental data. Dong et al. (2019) conducted a series of experimental tests using a cross-flow packed bed regenerator using lithium chloride desiccant solution to measure the regeneration effectiveness and energy performance. The investigation was aimed at reducing the heating energy consumption for the proposed package unit of liquid desiccant and an indirect and a direct evaporative cooling-assisted 100% outdoor air system compared to conventional air handling units. For balanced regeneration performance with lower energy consumption, regeneration temperature of 65°C for LiCl was suggested for optimized operation. Gu and Zhang (2020) investigated the regeneration performance of a counter flow packed bed regenerator. Comparative analysis of regeneration effectiveness with the conventional regenerator was made by observing the effects of the air flux, solution flux, air inlet parameters, and solution inlet parameters. The distributor introduces fine elements of desiccant solution from the top into the central static housing. Mass transfer of the suggested regenerator was found to be higher than the conventional type. Table 2.3 shows other relevant research literature on reported on dehumidifier/ regenerator performance studies.

Table 2.3: State of the art on experimental studies reported on dehumidifier/ regenerator

Author(s)	Type of system	Notable contribution
Chung et al. (1996)	Dehumidifier	Compared the performance of the random and structured packing dehumidifiers and developed empirical correlations for heat and mass transfer coefficients of the random and structured packing liquid desiccant dehumidifiers.
Fumo and Goswami (2002b)	Dehumidifier/regenerator	Studied the influences of ambient and operating parameters on evaporation and condensation rates. Further, analysed the

		performances of the liquid desiccant dehumidifier and regenerator in accordance with hot and humid climate.
Longo and Gasparella (2005)	Dehumidifier/regenerator	Studied the mass transfer characteristics of the randomly packed column dehumidifier and regenerator. Also, investigated the performance of the dehumidifier and the regenerator using LiCl, LiBr and HCOOK as a liquid desiccant materials.
Zhang et al. (2010)	Dehumidifier/regenerator	Developed dimensionless correlations for mass transfer coefficient of the liquid desiccant dehumidifier and regenerator. Further, investigated the performance of the structured packing dehumidifier/regenerator for summer and winter climatic conditions.
Wang et al. (2010)	Dehumidifier	Developed empirical correlations for enthalpy and moisture effectiveness. Further, experimentally investigated the influence of packing height for different desiccant flow fluctuations and consequently, optimized the packing height of the liquid desiccant dehumidifier.
Li et al. (2016)	Dehumidifier	Studied the heat and mass transfer characteristics of the liquid desiccant dehumidifier and compared the developed dynamic model with the results obtained from the experimental analysis.
Peng and Zhang (2009)	Solar based liquid regeneration system.	The regeneration efficiency obtained was 45.7%, while the effective solution proportion decreased from 100% to 62%.

Alosaimy and Hamed (2011)	Regenerator coupled with solar water heater for liquid desiccant regeneration.	Desiccant concentration of 30% was concentrated up to 50% by solar energy. ANN model was built to pattern the overall performance of the system.
Yang et al. (2019)	Ultrasonic atomized liquid desiccant regeneration system (UARS) was combined with the ultrasonic atomization aided dehumidifier.	Regeneration temperature and energy consumption for regenerating the desiccant were reduced to 4.4°C and 60.4%, respectively, for UARS.
Cheng et al. (2012)	Double-stage photovoltaic/thermal ED for liquid desiccant regeneration system.	With optimized working conditions, double-stage system showed 90.5% better energy-efficient than a single-stage system.
Wu et al. (2017)	Dehumidifier	Developed a desiccant solution regulation strategy for the liquid desiccant dehumidifier and studied the effectiveness of this strategy in different working conditions.

2.4.3. State of the art on combined dehumidifier - regenerator system

The combined study on dehumidifier-regenerator systems are very limited. In this regard, Zhang et al. (2010) presented an experimental study of air dehumidification and desiccant regeneration in a packed bed dehumidifier with structured packing material. LiCl was considered as desiccant. The heat and mass transfer phenomena between desiccant solution and air is carried were studied. For the air velocity of 0.5 to 1.5 m/s, the overall mass-transfer coefficient was found to lie in the range 4.0 to 8.5 g/m^2 s for dehumidifier and 2.0 to 4.5 g/m^2 s for regenerator. Further, it is noticed that increase in solution temperature cause reduction in mass-transfer coefficient value for regenerator. Finally, dimensionless overall mass-transfer

coefficient correlations were proposed. Mohaisen and Ma (2015) conducted an extensive numerical study of a counter flow packed bed dehumidifier and regenerator system integrated with evaporative cooler to cool the process air. A full-scale MATLAB Simulink simulation study was carried out for Sydney weather conditions. The average daily thermal coefficient of performance in the range of 0.5-0.55. Liu et al. (2015) experimentally investigated the performance of thermally conductive plastic material (polypropylene) with 16.5 W/mK conductivity, as compared to metal in an internally cooled and heated dehumidifier and regenerator system. Fin coil structure was used for providing the cooling and heating water. Superior corrosion resistive properties were observed when tested using LiBr solution at different working conditions. Park et al. (2016) conducted experimental investigations aiming to propose an empirical correlation for prediction of dehumidification effectiveness in a liquid desiccant dehumidification system. A packed bed dehumidifier and regenerator were used using LiCl desiccant solution. Finally, a linear model for dehumidification effectiveness prediction as a function of six operating parameter sets was developed. Applicability of the model was found to be valid within the given operating range and accurately predicting dehumidification effectiveness of liquid desiccant system using conventional packed bed type dehumidifier and regenerator columns. Asati, (2016) tested performance of a liquid desiccant system using Celdek structured packing material and $CaCl_2$ as desiccant solution. The variation of mass flow rate of air, desiccant solution flow rate, inlet air temperature, inlet solution temperature, inlet specific humidity and concentration of desiccant solution were studied for the counter flow configuration at different operating conditions. In case of the dehumidifier, increase of inlet specific humidity, solution flow rate improved the system performance, while degrading the system performance with increase of air mass flow rate, inlet temperature of air and desiccant. Further, it was observed that the regenerator effectiveness was influenced by increase in solution flow rate, inlet desiccant concentration.

2.4.4. State of the art on solar energy for regenerator system

Solar collectors have been used for desiccant regeneration purposes in a liquid desiccant dehumidification system. As energy shortages continue to rise and become a worldwide concern, solar energy utilisation can minimize the energy shortages; as it is abundant in nature and environmentally friendly. Kakabaev et al. (1969) were among the first to propose the idea of a system powered by solar energy in which the solar collector could be applied both indirectly and directly for desiccant regeneration. In direct contact mode, the fluid collecting

the heat in the solar collector is the weak desiccant. In the indirect contact mode, water is utilized as the fluid that collected the heat in the solar collector. Subsequently, this heated water is utilized to preheat the diluted desiccant solution before sending it into the regenerator. The direct contact mode has a better solar energy utilization ratio because the regeneration temperature can reach equivalent to the temperature of the solar collector plate; besides, the regeneration chamber can be eliminated. The problem with the direct contact mode is that liquid desiccant would directly contact the solar collector system that has a significant chance to corrode the solar collector material. Due to the intermittent nature of solar energy, continuous regeneration of desiccant may not be possible. For example, on days with an overcast sky, the solar collector cannot perform the process of regeneration. For this reason, the solar collector needs to be equipped with an auxiliary heater for continuous operation of the system.

It is also worth noting that in order for uninterrupted dehumidification to be achieved, reactivation of the desiccant solution is necessary. There are two methods that can be used to regenerate the solution: directly heating the desiccant or utilizing hot air as the medium for regeneration. Liu et al. (2009) experimentally showed that the hot desiccant driven regeneration is more effective than hot air driven regeneration in the packed bed regenerator due to its better mass transfer potential. Various hot desiccant driven regenerator techniques have been studied over few decades (Misha et al., 2012), which broadly categorized as thermal (Qi et al., 2013) and non-thermal techniques (Li and Zhang, 2009). The non-thermal regeneration techniques are widely explored in desalination, electro-dialysis (ED) and wastewater treatment processes. On the other hand, thermal regeneration methods are promising for diluted desiccant reactivation, as it allows the use of various low-grade energy sources for regenerating the desiccant. In this perspective, Alosaimy and Hamed (2011), Katejanekarn et al. (2009) and Alizadeh (2008) used a flat plate solar water heater for the regeneration of liquid desiccant. Further, Li et al. (2011) performed experimental studies on both single as well as double stage photovoltaic (PV) assisted regeneration for reactivation of diluted desiccant. It was concluded that the double stage system is more economical than a single-stage system, as double stage systems can save above 70% energy.

On the other hand, Zambolin and Del (2010) performed a comparative study on the performance of ETC and FPC using mixture of water and propylene glycol as working fluid. It was observed that the ETC shows better efficiency than FPC for intensity of 1000 W/m^2. Liang et al. (2011) investigated the thermal performance of U-tube based filled-type ETC both

theoretically and experimentally. Investigation showed that filled type ETC exhibits higher thermal efficiency than copper fin (Liang et al., 2011). Kim and Seo (2007) carried out a comparative study on ETC performance using different designs of absorber plates with air as working fluid. It was observed that absorber with U- tube welded on the plate shows a better performance. Mehla and Yadav (2017a) studied ETCs using phase change material in the header and air as working fluid. A significant enhancement in performance was observed when the system employed a coil and a circular fin in the header (Mehla and Yadav, 2017b). Harding et al. (1985) studied a special type of solar collector made of evacuated glass tubes filled with water (thermosiphon) and compared the performance of collectors with and without a fin. Such thermosiphon collector can provide higher efficiency, but the temperature rise of the working fluid is less (8ºC), whereas in the metal U-tube configuration temperature rise is higher (20ºC), but the efficiency is less (Harding et al., 1985). In order to enhance the thermal performance of solar collectors, nanoparticle-based working fluid was proposed by Kang et al. (2006) and Liu et al. (2005) in order to increase the thermal conductivity of the working fluid. Ghaderian and Sidik (2017) experimentally studied the performance of ETC with passive circulation using Al_2O_3-water (nanofluid) and Trixton X100 (surfactant). It was found that the efficiency of the system increased significantly with flow rate and volume fraction of nanoparticles (Ghaderian and Sidik, 2017). Mahbubul et al. (2018) performed an experimental analysis to investigate the thermal performance of ETC using nanofluid (carbon nanotubes in water) as a working fluid. Results showed that 0.2 vol.% of nanoparticles could increase the efficiency by around 9% (Mahbubul et al., 2018). Kaya and Arslan (2018) also studied the performance of U-tube ETC with different nanofluids such as silver, zinc oxide and magnesium oxide in water-ethylene glycol mixture. It was demonstrated that high thermal conductivity nanofluids increase efficiency significantly. The summary of state of art on solar evacuated tube collector studies are presented in Table 2.4.

Table 2.4: State of art on ETC performance studies

Author(s)	**Research Methodology (Experimental / Theoretical)**	**Contribution**
Fischer et al. (2012)	NARX model (Nonlinear Auto-Regressive model) and neural network model	The performance of water in glass ETC system was predicted.

Dikmen et al. (2014)	Experimental and ANN model	Thermal performance of water-in-glass ETCs was predicted experimentally and developed ANN architecture. The comparison between experimental results and ANN architecture yielded R^2 value of 0.8.
Gao et al. (2014)	Experimental and simplified mathematical model	Outlet parameters of ETCs were analysed and the collector design was optimized.
Ma et al. (2016)	Heat transfer model	Heat transfer model was established. The temperature distribution and heat transfer characteristics of filled U-type ETC system were analyzed.
Naik et al. (2019)	Experimental and RSM model	Experimentally studied the thermal performance of U-type ETC system and developed empirical correlation between input and output parameters.
Essa et al. (2018)	Experimental	An experimental study was carried out and the effect of PCM (phase change material: paraffin wax) in a U-tube ETC system was visualized.
Wannagosit et al. (2018)	Experimental and Explicit Finite Difference Method model (EFDM), Thermal resistance method model	Experimentally investigated the thermal efficiency of ETC and validated with thermal resistance network model and EFDM model.
Sharafeldin and Gróf (2019)	Experimental	Effect of WO_3 (tungsten trioxide) nanoparticles on the performance of the evacuated tube solar collector were studied and the collector outlet temperature, efficiency and heat gain were analyzed.
Saikia et al. (2019)	1-D steady-state model	Thermal performance of ETCs was analyzed using MATLAB as simulation platform.

Korres et al. (2019)	Experimental and time-dependent computational fluid dynamic model	Outlet water temperature and thermal efficiency of U-type ETC system were experimentally investigated.

2.5. State of the art on empirical model for dehumidifier/regenerator system

Numerical models are quite complicated, less accurate and use too many simplifying assumptions. Therefore, an extendable model that can be used in a wide range of system operations with low computation cost and simple in practice is very much essential. A feasible solution for any process/system can be obtained using soft computing techniques with statistical analysis. Soft computing models seem to be more powerful and very simpler as compared to an assumption based numerical models. Generally, three categories of empirical models are available for modeling the experimental data that can statistically predict the performance of the systems with very good accuracy. Those are multiple linear regression (MLR) model, stepwise regression model (SRM) and artificial intelligent (AI) model. These models can be effectively used for estimating the air and the desiccant outlet conditions and overall performances of the system. Naik and Muthukumar (2019) proposed an MLR model for predicting the change in specific humidity in both dehumidifier and regenerator systems as a function of operational parameters, i.e., inlet desiccant concentrations and temperature, inlet air temperature (dry-bulb), humidity ratio and flow ratio. Langroudi et al. (2014) developed an SRM model as a function of air specific humidity, air temperature, solution to airflow rate and solution concentration for predicting the dehumidifier's effectiveness with R^2 value of 0.98. Wang et al. (2016) also developed a SRM model for predicting the enthalpy and moisture effectiveness in terms of air temperature, air specific humidity, air mass-flow rate, solution temperature and solution of mass-flow rate.

2.6. State of art on desiccant film based air dehumidification system

Amongst many polymers, cellulose is a non-toxic, natural, abundant, renewable and biodegradable polymer. As a result, it has been widely used to produce different hydrogels for broad applications (Dharmalingam et al., 2020; Dharmalingam and Anandalakshmi, 2019; Raucci et al., 2015; Weng et al., 2004). In addition, amongst various celluloses, sodium carboxymethyl cellulose (NaCMC) is having a high-molecular-weight water-soluble hetero-

polysaccharide, which is also biodegradable and biocompatible cellulose. It is highly hydrophilic substance due to the presence of abundant carboxyl (—COOH) and hydroxyl (—OH) groups, which further leads to strong electronic repulsion, resulting in enhanced pore size (Dharmalingam et al., 2020). Though various cellulose-derivative polymers have been utilized to fabricate hydrogels, NaCMC-based hydrogels stand out in swelling rate, water and equilibrium water uptake (Ghorpade et al., 2017; Ma et al., 2015). It has excellent film-forming property. Extensive studies have also been performed on the preparation of NaCMC-based hydrogels using chemical or physical crosslinking methods for different applications (Arica, 2000; Fei et al., 2000; Kök et al., 1999; Koneru et al., 2020; Wach et al., 2003). In recent times, stimuli-responsive hydrogel films are showing great interest in various fields. It can undergo a drastic change in volume in response to ambient conditions (i.e., by absorbing moisture from the air). It can also be found that the NaCMC films undergo a drastic change in its hydrophilic property with respect to temperature. Those unique properties make the hydrogel films as energy-efficient materials for air dehumidifying applications.

Sängerlaub et al. (2019) developed a low-density polyethylene (PE-LD) monolayer films with a nominal silica gel concentration of 0.2, 0.4, and 0.6 g dispersed silica gel per 1 g film (PE-LD). It was found that the moisture absorbed up to 0.15 g/g of the dried film. Further, the regeneration temperature of silica gel dispersed PE-LD monolayer films has not been studied yet.

2.7. Literature closure

From the literature survey, the following conclusions are made.

2.7.1. Shortcoming from experimental studies

Pure TEG has low surface vapour pressure that makes the TEG evaporate into the air. Generally, the viscosity of the TEG is high, due to which the system operations turn out to be unstable and sometimes it becomes unsupportable for air- conditioning applications (Rafique et al., 2016). On the other hand, LiCl is the most stable liquid desiccant and has many favourable properties for dehumidification, such as low vapour pressure and it does not vaporize into the air at ambient conditions. However, it is relatively more corrosive, expensive and crystallizes at low temperatures. Liu et al. (2011a) experimentally showed that the LiBr solution has a higher mass transfer potential than LiCl solution. However, LiBr possesses a

demerit of solubility and is responsible for uneven performance profile throughout the operation.

Besides, the literature also reveals that more research studies have been reported on investigating the effectiveness of dehumidifier/regenerator systems by employing a single desiccant material. On the other hand, it can be noticed that the solar collector performance significantly depends on the collector design configuration. However, to the best of authors knowledge, no experimental studies attempted to predict the performances of structured packed bed liquid desiccant dehumidifier/regenerator system, which is driven by low-grade thermal energy harvested from evacuated tube solar collector using mixed desiccant as a working fluid. Further, there is also a lack of comprehensive experimental study on the combined dehumidifier-regenerator cycle.

On the other hand, although NaCMC hydrogel films have been investigated as a potential candidate for various applications, to best of the authors' knowledge, no research has been carried out to observe the unique stimuli-responsive behaviour of the NaCMC films in air dehumidification and regeneration applications.

2.7.2. Shortcoming from empirical models

Several investigations have been performed to pattern the system performance with inlet conditions. It is well known that heat and mass transfer processes occur simultaneously in the dehumidifier/regenerator. This coupled phenomenon is quite complicated in nature, and it is difficult to obtain accurate correlations to forecast outlet conditions of the system. Therefore, the outlet parameters can be easily predicted based on experimental data patterns. However, the statistical-based empirical correlations are not efficient to provide precision in the predicted results. Generally, experimentally obtained datasets are limited due to the man-material and money factor.

In recent years, soft computing techniques grab more attention and be broadly implanted in different paradigms of energy systems. Artificial Intelligence (AI) based computational methods (ANFIS, ANN, ACO, Fuzzy etc.) have been proved as robust design tools for various technical systems. Artificial Neural Network (ANN) methodology has been found in wide range of applications as a fast, accurate, robust, practical, and easy-to-practice analysis and design tool. A well-trained ANN model is faster than conventional mathematical models. Moreover, very few research works were published using AI-ANN algorithms to forecast the thermal performance of solar collector systems. Fischer et al., 2012 carried out a comparative

study between neural network model and state-of-the-art (SOTA) model for solar collectors (FPC and conventional water-in-glass ETC) by constructing a 5-4-1 NARX model (Nonlinear Auto-Regressive model with exogenous inputs) and a 5-5-1 neural model. Results indicated an acceptable performance of an ANN architecture compared with SOTA modeling. Dikmen et al. (2014) conducted experiments and collected 567 data to predict thermal performance of water-in-glass type ETCs using ANN model, where 80% of datasets were randomly chosen for training and 20% of datasets were used for testing. It was found that R^2 (absolute fraction of variance) value of selected model architecture is 0.8, which shows that the model has not achieved its desired accuracy. It is noticed that there is a research gap in solar energy domain in utilizing ANN model to get the desired accuracy of predicted outputs. On the other hand, the prediction models based on the artificial intelligent (AI) models for dehumidifier/regenerator performance parameters prediction are still categorically lacking. The recent advanced AI models such as gene expression programming (GEP), Adaptive neuro-fuzzy inference system (ANFIS) can be used for accurate prediction.

2.8. Objectives of the present work

Based on the literature closure, the following core objectives are chosen for the present thesis work:

- To numerically investigate the performance of various single desiccant solution systems to compare the cross and counter flow dehumidifier performance, and to select the desiccant for the present study.
- To experimentally investigate the performance of solar evacuated tube collectors and develop a numerical model based on experimental results for desiccant regenerator system.
- Experimentally and numerically study the coupled heat and mass transfer phenomena between air and desiccant in a solar-assisted thermal liquid desiccant dehumidifier-regenerator system.
- To develop heat and mass transfer correlation based on experimental results to optimize the input process parameters for better performance of the dehumidifier-regenerator system.

- To study the performance of combined dehumidifier-regenerator system at the optimum conditions.

- To prepare and characterize desiccant doped novel sodium carboxymethyl cellulose films for potential air-dehumidification applications.

2.9. Closure

In this chapter, a comprehensive survey of literature on experimental studies related to desiccant system, thermal model for dehumidifier/regenerator system, recent advancement in desiccant materials, empirical models for desiccant system performance prediction and desiccant film based air dehumidification system for various applications are thoroughly reviewed. Furthermore, literature closure along with the objective of the present work are presented. The next chapter (Chapter 3) describes the investigation on various single desiccant solution systems numerically and selection of working fluid materials in detail.

CHAPTER 3

Investigation on various desiccant solution systems

3.1. Introduction

A numerical model based on energy, mass and species balance principles is solved using finite difference approach and validated against available experimental results. Consequently, the numerical model is employed to investigate the impact of hygroscopic desiccants on the outlet characteristic of a dehumidifier at various inlet conditions. The heat and mass transfer process of a dehumidifier is visualized by the distribution profile of thermodynamically influencing parameters. From thermodynamic point of view, the exergy is used as a tool that represents the available energy, which can be achievable from a particular form of energy by considering a dead state as the reference state. In dehumidification systems, desiccant solution and air mixture are the operational fluids where air is considered as an ideal mixture of water vapour and dry air. Therefore, the exergy destruction profile is also shown in this chapter in the perspective of latent and sensible heat transfer. On the other hand, in order to control the humidity level, air dry-bulb temperature needs to be brought down below its dew point temperature to condense out the moisture from the air. This eventually consumes a significant amount of total building energy in terms of electricity. Therefore, to minimize energy consumption, researchers are focusing towards an alternative latent heat load control system. In this regard, desiccant based sorption technologies are more effective compared to the conventional vapour compression system. Therefore, it is necessary to analyse the different desiccants' individual properties and their physical behaviour in material perspective. In this chapter, the thermo-kinetic properties of pure desiccants as well as their mixtures characterised using by X-ray diffraction (XRD), thermo-gravimetric (TG) and absorption rate, analyses through numerous control experiments are discussed.

3.2. Thermal Modelling

In the dehumidifier, the desiccant solution and the humid air streams are flowing in a cross-flow arrangement (Fig. 3.1). Air is flowing along the length (L) of the dehumidifier in the x-direction, whereas the desiccant solution is flowing along the height (H) in y-direction (Fig.

3.2). The following assumptions are made to study the heat and mass transfer phenomena inside the dehumidifier; (a) operating parameters of desiccant solution and humid air stream at the inlet and outlet are uniform, (b) adiabatic, leakage proof system and steady-state operation, (c) humid air and desiccant solutions are Newtonian fluid with constant thermophysical properties, (d) the local heat and mass transfer coefficients in the domain of study are constant and (e) effect of fouling is neglected.

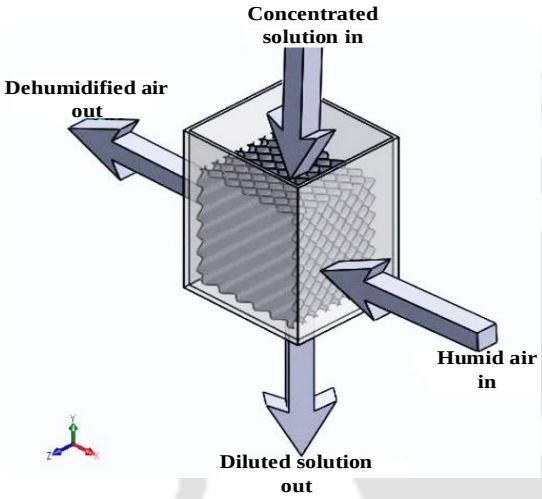

Fig. 3.1: Schematic diagram of a cross-flow packed bed adiabatic dehumidifier

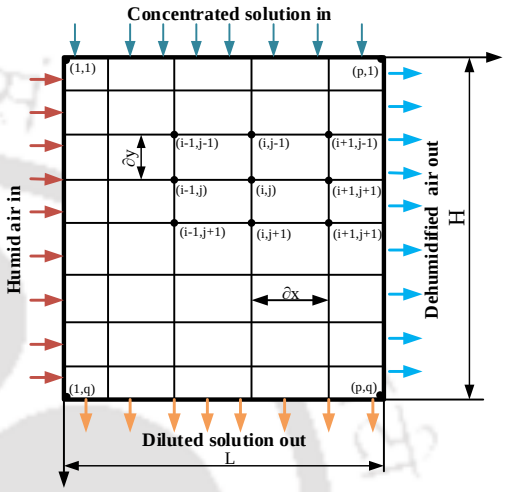

Fig. 3.2: Discretization of 2-D dehumidifier domain

The enthalpy balance for desiccant solution-humid air stream is given as follows (Das and Jain, 2015; Liu et al., 2007):

$$H\frac{\partial(h_d\,\dot{m}_d)}{\partial y}+\frac{\partial(h_a\,\dot{m}_a)}{\partial x}L=0 \tag{3.1}$$

The mass balance of water vapour between the humid air and liquid desiccant is given by Eq. (2)

$$L\frac{\partial(\omega_a\dot{m}_a)}{\partial x}+\frac{\partial\dot{m}_d}{\partial y}H=0 \tag{3.2}$$

The solute (liquid desiccant) mass balance is given as follows:

$$d\left(\dot{m}_d\xi_d\right)=0 \tag{3.3}$$

Overall enthalpy balance between humid air and desiccant using Eqs. (3.1-3.3) is given as (Das and Jain 2015; Liu et al., 2007):

$$\frac{\partial h_a}{\partial x} = \frac{NTU \bullet Le}{L}\left[(h_e - h_a) + L_H\left(\frac{1}{Le} - 1\right)(\omega_e - \omega_a)\right] \tag{3.4}$$

Where, Lewis number , $Le = \frac{U_h}{U_m C_{p,m}}$; where, U_h and U_m are heat transfer and mass transfer units between moist air and desiccant, respectively; $C_{p,m}$ (= C_{pda} + $\omega_a C_{pv}$) is specific heat of moist air; Le is assumed to be unity. Then, Eq. (3.4) becomes

$$\frac{\partial h_a}{\partial x} = \frac{NTU_e}{L}(h_e - h_a) \tag{3.5}$$

The overall mass balance between humid air and desiccant using Eqs. (3.2-3.4) is given as:

$$\frac{\partial \omega_a}{\partial x} = \frac{NTU}{L}(\omega_e - \omega_a) \tag{3.6}$$

The Number of Transfer Units (NTU) for latent heat exchange mentioned in Eqs. (3.5) and (3.6) can be represented as,

$$NTU = \left(U_m a_s V\right)/\dot{m}_a \tag{3.7}$$

Moreover, Eq. (3.7) can also be rewritten in terms of Sherwood number (Sh), which is a function of mass transfer coefficient (U_m) and diffusion coefficient (D_a), as shown in Eqs. 3.8 and 3.9.

$$NTU = Sh\frac{\rho_a D_a a_s V}{\dot{m}_a d_e} \tag{3.8}$$

$$Sh = \frac{U_m d_e}{\rho_a D_a} \tag{3.9}$$

The Sherwood number can be found out by adopting an empirical correlation. However, different researchers have developed different empirical correlations for Sherwood number for different desiccant configuration systems. Generally, Sherwood number can be represented as

a function of Schmidt number (Sc), Reynolds number (Re) and liquid to gas mass flux rates (L/G). The correlation of (Chung and Wu, 2000) is used in the present study where the constants are found out by newly fitted nonlinear regression analysis from the experimental data of (Liu et al., 2007). Then the expression for Sherwood number for LiBr becomes:

$$Sh = A \cdot Re_a{}^{B} \cdot Sc_a{}^{C} \cdot \left(\frac{F_d}{F_a}\right)^{D} \cdot \left(1-\frac{\xi}{100}\right)^{E} \quad ; \quad 1.58 < F_a\ (kg/m^2s) < 2.50 \ ; \ 2.04 < F_s\ (kg/m^2s) < 5.35. \tag{3.10}$$

where A, B, C, D and E are 0.011, 1.363, 0.333, 0.396 and 1.913, respectively. The air saturation enthalpy (h_e) is the air enthalpy that is in equilibrium with the desiccant solution at a particular solution temperature and concentration, as mentioned in Eq. (3.11).

$$h_e = C_{p,a}T_s + \omega_e\left(h_{fg} + C_{p,v}T_s\right) \tag{3.11}$$

Saturation humidity ratio at solution temperature can be determined from equilibrium status of humid air and is expressed in Eq. (3.12).

$$\omega_e = 0.62198\frac{p_v^e}{P - p_v^e} \tag{3.12}$$

where, P is the barometric pressure (kPa) and p_v^e is the equilibrium vapour pressure of desiccant solution (kPa), which is the function of desiccant temperature (T_s) and desiccant solution concentration (ξ). Equilibrium vapour pressure of single desiccant solution can be attributed using Antoine correlation (Patil et al., 1990) as given by Eq. (3.13).

$$\log_{10} p_v^e = X_1 + \frac{X_2}{T_s} + \frac{X_3}{T_s^2} \tag{3.13}$$

where constraints X_1, X_2 and X_3 are cubic functions of molality (m) of the desiccant solution given in Eqs. (3.14-3.16) (Patil et al., 1990) and constants are taken from Patil et al. (1990).

$$X_1(m) = X_1^{(0)} + X_1^{(1)}m + X_1^{(2)}m^2 + X_1^{(3)}m^3 \tag{3.14}$$

$$X_2(m) = X_2^{(0)} + X_2^{(1)}m + X_2^{(2)}m^2 + X_2^{(3)}m^3 \tag{3.15}$$

$$X_3(m) = X_3^{(0)} + X_3^{(1)}m + X_3^{(2)}m^2 + X_3^{(3)}m^3 \quad (3.16)$$

The specific heat capacity of desiccant solutions at constant pressure was estimated correlations used in literature (Conde, 2004; Bassuoni, 2014). The boundary conditions for x-y plane of the dehumidifier module are formulated in Eqs. (3.17-3.18)

$$\text{At}, x = 0, T_a = T_{a,in} \text{ and } \omega_a = \omega_{a,in} \quad (3.17)$$

$$\text{At}, y = 0, T_s = T_{s,in} \text{ and } \xi = \xi_{in} \quad (3.18)$$

In the direction of ensuring the exergy, a reference state, which is mechanically, chemically, and thermally equilibrium with the corresponding environment state needs to be defined. In HVAC applications, especially for dehumidification systems, humid air is considered to be an ideal mixture of dry air and water vapour. Therefore, the saturated condition (P_0, T_0, $\xi_{0,v}$) of ambient air is considered as ultimate dead state for humid air (Zhang et al., 2014; Zhang et al., 2019). More often ambient air is not in saturation condition. Hence, ambient temperature and pressure (T_0, P_0) is chosen as the restricted dead state in the current study. Moreover, the pressure in dehumidification systems is considered as standard atmospheric pressure for theoretical situations, which further implies negligible physical exergy. Chemical exergy is calculated by the reference chemical potential of the solute and solvent (Zhang et al., 2014). The total exergy (Ex_{tot}) is due to complete effect of thermomechanical exergy (commonly known as physical exergy) (Ex_{tph}) and chemical exergy (Ex_{che}) and is represented in Eq. (3.19) (Zhang et al., 2014; Zhang et al., 2019).

$$Ex_{tot}(T, \xi) = Ex_{tph}(T) + Ex_{che}(\xi) \quad (3.19)$$

The chemical exergy and physical exergy predominantly correspond to liquid desiccant concentration and temperature, respectively. More explicitly, the physical and chemical exergy of per unit mass for humid air and desiccant solution are expressed in Eqs. (3.20-3.23) (Zhang et al., 2014; Zhang et al., 2019).

Physical exergy of humid air: (3.20)

$$Ex_{tph,a}(T) = \left(C_{p,a} + \omega_a C_{p,v}\right) T_0 \left[\left(T_a/T_0\right) - 1 - \ln\left(T_a/T_0\right)\right]$$

Chemical exergy of humid air:

$$Ex_{che,a}(\xi) = R_a T_0 \left[\left(1+1.608\omega_a\right) \ln \frac{1+1.608\omega_{T_e}}{1+1.608\omega_a} + 1.608\omega_a \ln \frac{\omega_a}{\omega_{T_e}}\right] \quad (3.21)$$

Physical exergy of solution:

$$Ex_{tph,d}(T) = C_{p,d} T_0 \left[\left(T_s/T_0\right) - 1 - \ln\left(T_s/T_0\right)\right] \quad (3.22)$$

Chemical exergy of solution:

$$Ex_{che,d}(\xi) = \left(\mu_d^o + \mu_w^o\right) + \phi R_a T_s \ln\left(a_i m_i\right) + R_a T_s \left[\ln\left(a_w\right) + \ln\left(a_i \xi\right)\right] \quad (3.23)$$

where ϕ is the dissociation number, m_i is molality and a_i is the ionic activity coefficient (average) of the desiccant. Similarly, the exergy destruction represents the amount of irreversibility. For a steady, irreversible system with negligible exergy transfer, the irreversibility of the dehumidifier can be calculated by the difference between inlet and outlet exergy, as given in Eq. (3.24) (Zhang et al., 2019).

$$Ex_{des} = Ex_{in} - Ex_{out} \quad (3.24)$$

Total exergy destruction is the sum of physical and chemical exergy destruction. Particularly in dehumidifier, heat transfer corresponds to physical exergy destruction, whereas mass transfer corresponds to chemical exergy destruction. The final physical exergy destruction equation during infinitesimal sensible heat transfer process is written in Eq. (3.25) (Zhang et al., 2014; Zhang et al., 2019).

$$dEx_{ph,des} = T_0 \left[\left(1/T_a\right) - \left(1/T_s\right)\right] dQ_{ph} \quad (3.25)$$

where dQ_{ph} is the heat transfer rate between the humid air and the liquid desiccant in the liquid desiccant dehumidifier. The final chemical exergy destruction equation due to irreversible mass transfer during the dehumidification process is expressed in Eq. (3.26) (Zhang et al., 2014; Zhang et al., 2019).

$$dEx_{ch,des} = 1.608 \dot{m}_a R_a T_0 \left[\ln \frac{\omega_e}{1+1.608\omega_e} - \ln \frac{\omega_a}{1+1.608\omega_a}\right] d\omega \quad (3.26)$$

where dω is the mass (humidity) transfer rate between humid air and liquid desiccant in the liquid desiccant dehumidifier.

3.3. Simulation and Validation of the Model

The coupled governing equations (Eqs. 3.1-3.3 and Eqs. 3.5-3.6) for air and solution flows are solved using MATLAB® 2015b. In order to minimize the computational time and to get faster data acquisition, finite differences method (FDM) is adopted. The computational domain is discretized into p × q number of grids, as shown in Fig. 3.2. The packed bed dehumidifier height, 'H' is divided into small girds in y-direction, q, and p is number of girds in the x-direction along the length, 'L' of the dehumidifier (Fig. 3.2). Mass and energy balances are solved for each grid point, as shown in Fig. 3.2. In order to guarantee the accuracy of numerical results and low computational cost, simulations with different grid sizes were performed for testing the dependency of numerical results on the grid size. The numerical tests are carried out to decide the optimum grid size, and it is found that 50 × 50 grids are optimum for the current study. The result difference is less than 1 % compared with 60 × 100 grids. Therefore, in the present study, the dehumidifier model with 50 × 50 grids are chosen for performing the numerical simulations. Therefore, in the present study, the dehumidifier model with 50 × 50 grids elements are chosen for performing the numerical simulations. Eqs. (3.1-3.3) and (3.5-3.6) are rewritten in discretized form as Eqs. (3.27-3.31) (Liu et al., 2007).

$$\dot{m}_a\left(h_{a,i+1,j}-h_{a,i,j}\right)=\frac{q}{p}\left(\dot{m}_{d,i,j}h_{d,i,j}-\dot{m}_{d,i,j+1}h_{d,i,j+1}\right) \tag{3.27}$$

$$\dot{m}_a\left(\omega_{a,i,j}-\omega_{a,i+1,j}\right)=\frac{q}{p}\left(\dot{m}_{d,i,j+1}-\dot{m}_{d,i,j}\right) \tag{3.28}$$

$$\dot{m}_{d,i,j+1}\ \xi_{i,j+1}=\dot{m}_{d,i,j}\ \xi_{i,j} \tag{3.29}$$

$$h_{a,i+1,j}-h_{a,i,j}=\frac{NTU_{lat}}{p}\left(h_{T_d,sat,i,j}-h_{a,i,j}\right) \tag{3.30}$$

$$\omega_{a,i+1,j}-\omega_{a,i,j}=\frac{NTU_{lat}}{p}\left(\omega_{T_d,sat,i,j}-\omega_{a,i,j}\right) \tag{3.31}$$

The known value of inlet humid air and desiccant stream conditions are allowed to solve the Eqs. (3.27-3.31) in MATLAB endeavour to obtain the outlet parameters of air and desiccants profile inside the dehumidifier. The mesh (i, j) provides the condition of desiccant and air outlet of this mesh, which is eventually the inlet condition of mesh (i + 1, j) of air and mesh (i, j + 1) for desiccant solution. The following stages are followed to achieve the outlet parameters and to visualize the heat and mass transfer process of the dehumidifier module (Fig. 3.3).

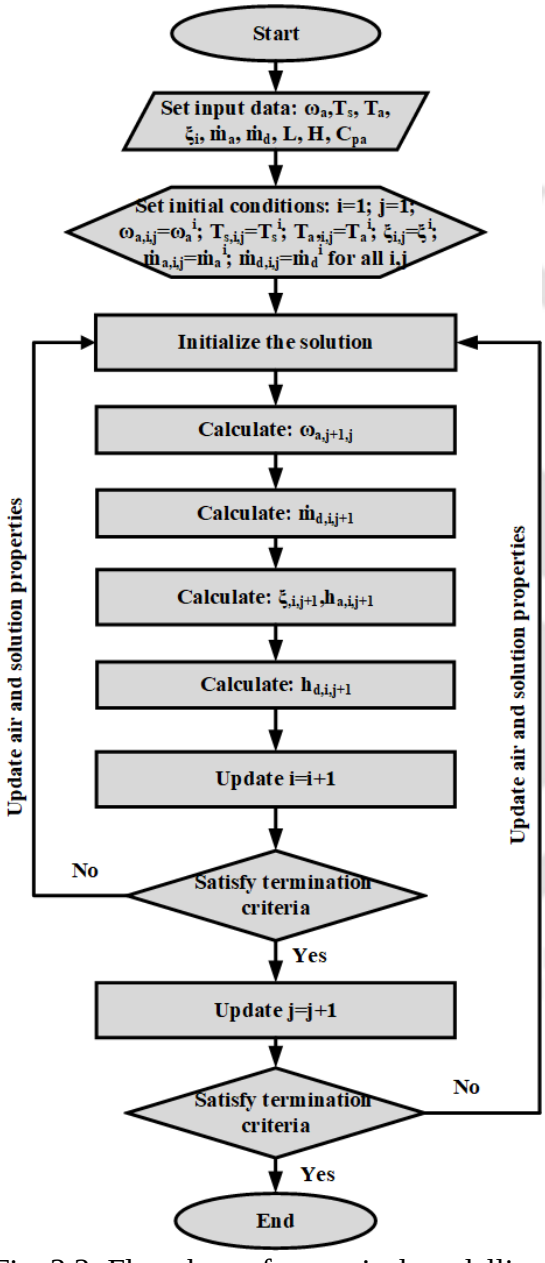

Fig. 3.3: Flowchart of numerical modelling

Step 1: Calculate the air outlet specific humidity $\omega_{a,\,i+1,\,j}$ using Eq. (3.31).

Step 2: Calculate the desiccant mass flow rate $\dot{m}_{d,\,i,\,j+1}$ using Eq. (3.28) for known air outlet specific humidity $\omega_{a,\,i+1,\,j}$.

Step 3: Calculate the desiccant concentration $\xi_{i, j+1}$ using Eq. (3.29) for known desiccant mass flow rate $\dot{m}_{d, i, j+1}$.

Step 4: Calculate air saturation enthalpy at solution temperature using Eq. (3.11) and this helps to calculate the air outlet enthalpy $h_{a, i+1, j}$ using Eq. (3.30).

Step 5: Calculate the enthalpy of desiccant at the outlet $h_{d,i,j+1}$ using Eq. (3.27) for known desiccant outlet mass flow rate and air outlet enthalpy.

Step 6: Calculate the air outlet temperature $T_{a, i+1, j}$ with the help of air physical properties and air outlet enthalpy.

Step 7: Calculate the outlet temperature of desiccant solution $T_{s, i, j+1}$ with the help of desiccant physical properties and desiccant outlet enthalpy.

Table 3.1: Model parameter values used in the current simulation study (Liu et al., 2007; Liu et al., 2011b)

Parameter	Unit	Value
Air mass flux rate	F_a, kg/m^2-s	1.97
Desiccant mass flux rate	F_d, kg/m^2-s	3.08
Specific heat of salt (LiBr)	C_p, kJ/kg.$^\circ$C	2.3
Molality	m_i	9.69
Diffusion coefficient	D_a, m^2/s	2.33×10^{-5}
Specific surface area of packing material	a_s, m^2/m^3	396
Volume of dehumidifier	V, mm^3	550 × 400 × 350
Equivalent diameter of the channel	d_e, mm	7.85

Table 3.2: Comparison of predicted process parameters between the present model and the literature for a dehumidifier

	F_a (kg/m^{2}s)	T_a (^{o}C)	ω_a (kg/kg$_{da}$)	F_d (kg/m^{2}s)	T_s (^{o}C)	ξ_d (%)
Liu et al. (2007)						
Inlet parameters	1.97	31.7	0.013	3.08	22.9	45.7
Outlet parameters predicted by experiment	-	26.9	0.0099	-	27.8	45.7

Outlet parameters predicted by modeling	-	27.6	0.010	-	27.5	45.6
Relative error (%)	-	-2.60	-1.01	-	1.08	0.22
Outlet parameters predicted by present model	-	27.5	0.0098	-	27.66	45.62
Relative error of the present model with respect to outlet parameters predicted by experiment (Liu et al., 2007) (%)	-	-2.23	1.01	-	0.50	0.18
Langroudi et al. (2014)						
Inlet parameters	4.93	27.7	0.021	22.1	21.8	40
Outlet parameters predicted by experiment	-	24.3	0.0146	-	29.1	39.77
Outlet parameters predicted by modeling	-	24.5	0.0144	-	29.3	39.78
Relative error (%)	-	-0.82	1.37	-	-0.69	-0.03
Outlet parameters predicted by present model	-	24.48	0.0144	-	29.28	39.78
Relative error of the present model with respect to outlet parameters predicted by experiment (Langroudi et al., 2014) (%)	-	-0.74	1.37	-	-0.62	-0.03

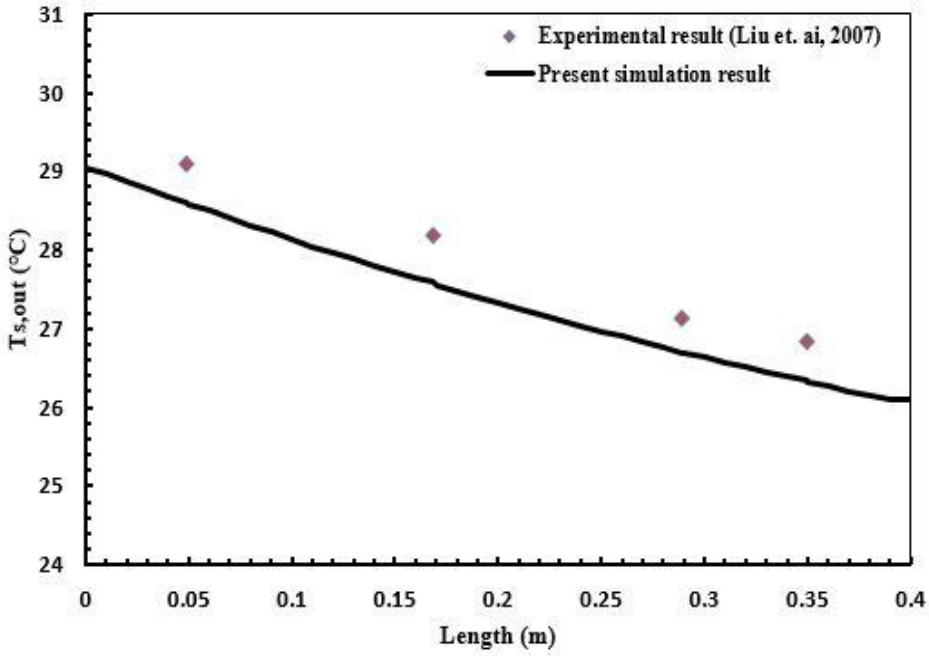

Fig. 3.4: Comparison of present simulation results with experimental outcomes for variation of desiccant outlet temperature in the transverse direction

The model parameters of the dehumidifier, which are used for describing the heat and mass transfer phenomena, are reported in Table 3.1. Figure 3.4 shows the comparison between current numerical study and the experimental results presented by Liu et al. (2007) for desiccant outlet temperature ($T_{s,out}$) variation along the length of the dehumidifier. A comparison of present simulation study with the literature results (Liu et al., 2007) is also shown in Table 3.2. As illustrated in Fig. 3.4 and Table 3.2, the present study is in good agreement with the experimental results reported in the literature (Liu et al., 2007). The maximum deviation of the predicted results by the present model with the literature experimental results is less than ± 3%.

3.4. Results and Discussion

3.4.1. Parametric study on dehumidifier outlet parameters

3.4.1.1. Effect of inlet solution concentration on outlet air specific humidity: For a given solution temperature, higher the inlet solution concentration, the lower is the vapour pressure of desiccant solution. Hence, increase the vapour pressure difference between the desiccant surface and the air, which makes the potentiality to increase more mass transfer. This causes in gradual change in outlet air specific humidity, as shown in Fig. 3.5a. Therefore, the higher the concentration, the more will be the moisture removed. However, in the case of LiCl at 40-45% concentration it almost shows same humidity value and after that, it is not absorbing that much

of moisture might be for crystallization problem. That means the risk of crystallization at normal desiccant temperature is higher at high concentration.

3.4.1.2. Effect of inlet solution concentration on air outlet temperature: In this present study, the air inlet temperature is considered 31.7^{o}C then there is a significant decrease in the air outlet temperature, with a lower inlet desiccant concentration, as shown in Fig. 3.5b. As in the lower concentration, the dehumidification capacity of air is less so the mass transfer between the air and desiccant solution also be the less that causes the less release of sorption heat and latent heat of vapourization. In other words, as in the lower concentration, the warm humid air has a tendency to release its temperature to desiccant solution during the mass transfer process and in higher concentration of desiccant solution having low vapour pressure that may make not to release air temperature in an effective way to desiccant solution.

3.4.1.3. Effect of inlet solution concentration on desiccant outlet temperature: Fig. 3.5c shows that there is a noticeable increment in the solution outlet temperature when the desiccant solution inlet concentration is increased. As the liquid desiccant concentration increases, there is an increase in the mass transfer potential. This high moisture transfer potentiality results in high desiccant temperature since the sorption heat and latent heat of vaporization is released during the mass transfer process.

3.4.1.4. Effect of inlet solution concentration on desiccant outlet concentration: The mass transfer occurred between the air streams to the desiccant solution due to the vapour pressure differences. And in this present study, the size of the dehumidifier is 550×400×350 mm is considered where the specific humidity variation found over the range of concentration and the maximum specific humidity change in that specified range is from 0.013 to 0.0081 that means the maximum absorption by the desiccant solution is less compared to the desiccant concentration value. Additionally, the predicted results for this dehumidifier has shown that the maximum outlet solution concentration varies by 0.52%. Therefore, Fig. 3.5d shows the almost same at inlet and outlet solution concentration.

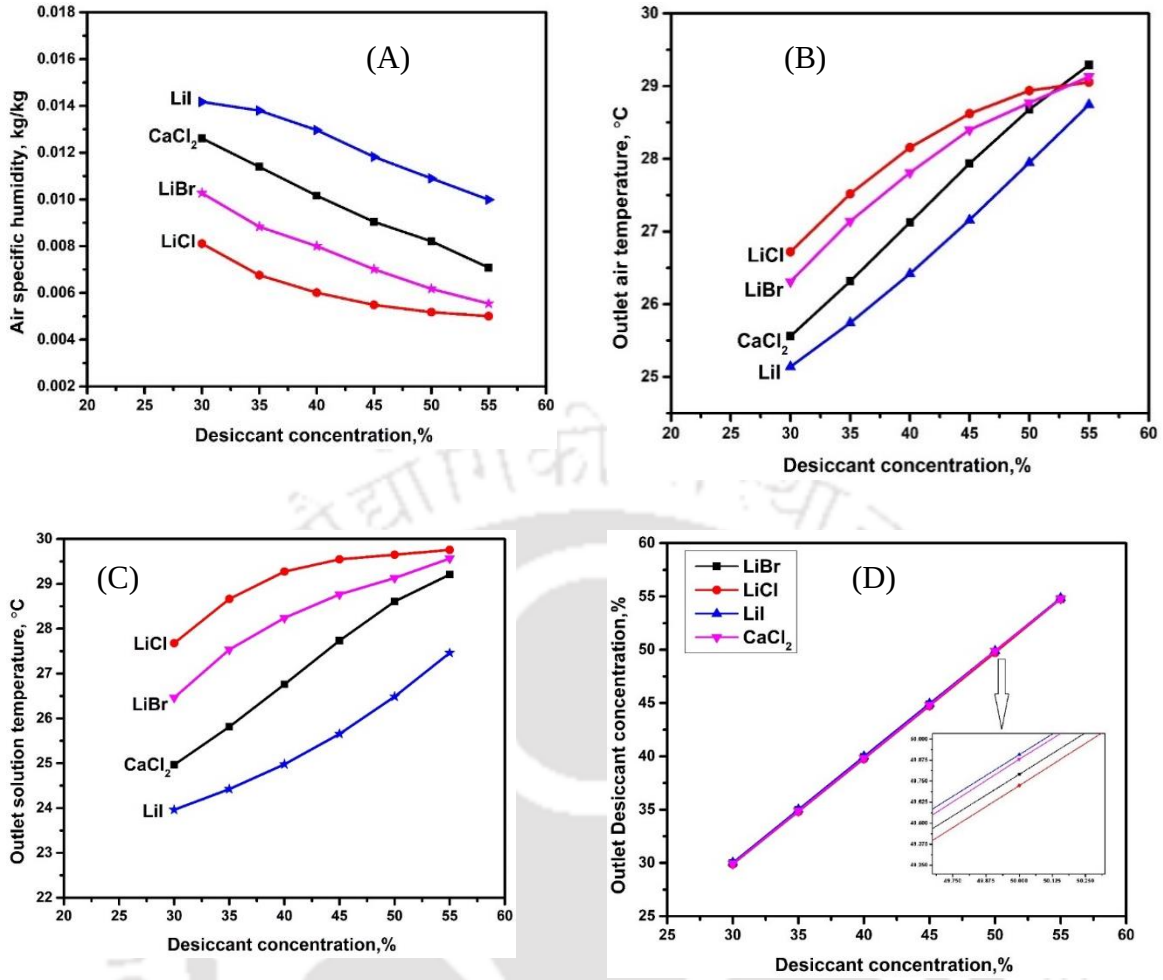

Fig. 3.5: Effect of inlet solution concentration on (A) outlet air specific humidity, (B) air outlet temperature, (C) desiccant outlet temperature and (D) desiccant outlet concentration

3.4.2. Distribution profile of thermodynamic properties

In order to visualize the desiccant-air interaction and heat and mass transfer phenomena inside an air-desiccant dehumidifier, variation of thermodynamics properties with respect to inlet condition is shown in Fig. 3.6. The warm moist air is cooled and dehumidified along the air flow direction, while the cool-strong desiccant becomes hot and diluted along its flow direction.

3.4.2.1. Air temperature variation: The air is flowing in the transverse direction whereas, the desiccant is flowing in longitudinal direction of the dehumidifier. As the air stream passes, it contacts the cold and concentrated desiccant solution that further reduces temperature of air in the transverse direction of the dehumidifier. At the air outlet, the top side air stream has the lowest temperature since it comes into contact with cold and concentrated desiccant.

3.4.2.2. Air specific humidity variation: As the inlet air specific humidity increases, the partial vapour pressure of air also increases (Das and Jain, 2015). Therefore, the vapour pressure difference between the air and the desiccant solution increases and that further increases the mass transfer potential, which causes the gradual change in specific humidity. The cold and concentrated desiccant solution has lower vapour pressure compared to the moist air due to their temperature and concentration differences. The moist air is flowing in the transverse direction and it interacts with the cold - concentrated desiccant solution. Due to vapour pressure difference between air and desiccant, the desiccant solution absorbs moisture from the air, and the air gets dehumidified.

3.4.2.3. Solution concentration variation: The desiccant solution is flowing in the longitudinal direction and absorbs moisture from the moist air due to vapour pressure difference between them. At solution outlet, the lowest desiccant concentration is observed on the left side (shown in Fig. 3.6c). This is because of high vapour pressure difference at inlet as more humid air interacts with the solution. Due to high mass transfer driving force, desiccant absorbs more moisture and the solution gets diluted. Therefore, the vapour pressure difference decreases considerably from left to right and a concentration gradient is observed at the solution outlet.

3.4.2.4. Solution temperature variation: As the desiccant flows, it absorbs moisture from air and becomes diluted due to vapour pressure difference. At the outlet, the highest desiccant solution temperature is found on the left side. The desiccant solution at this location interacts with high specific humidity air and thus having higher mass transfer potential from the air to the desiccant. This high moisture transfer potential results in higher desiccant temperature due to comparatively more amount of sorption heat release and higher latent heat of vaporization during the mass transfer process. The change in temperature at desiccant outlet is shown in Fig. 3.6(d).

3.4.2.5. Specific enthalpy variation (Solution/Air): Along the transverse direction (x = 0 to L and y=H), the difference in air specific enthalpy is about 8.88 kJ/kg (Fig. 3.6e). While in the longitudinal direction (y = 0 to H & x=L), the difference in desiccant specific enthalpy is 7.15 kJ/kg (Fig. 3.6f). The humid air in the dehumidifier is dehumidified and cooled as it flows towards the flow direction. However, the desiccant solution absorbs moisture and becomes diluted as it passes over the transverse direction, as shown in Fig. 3.6.

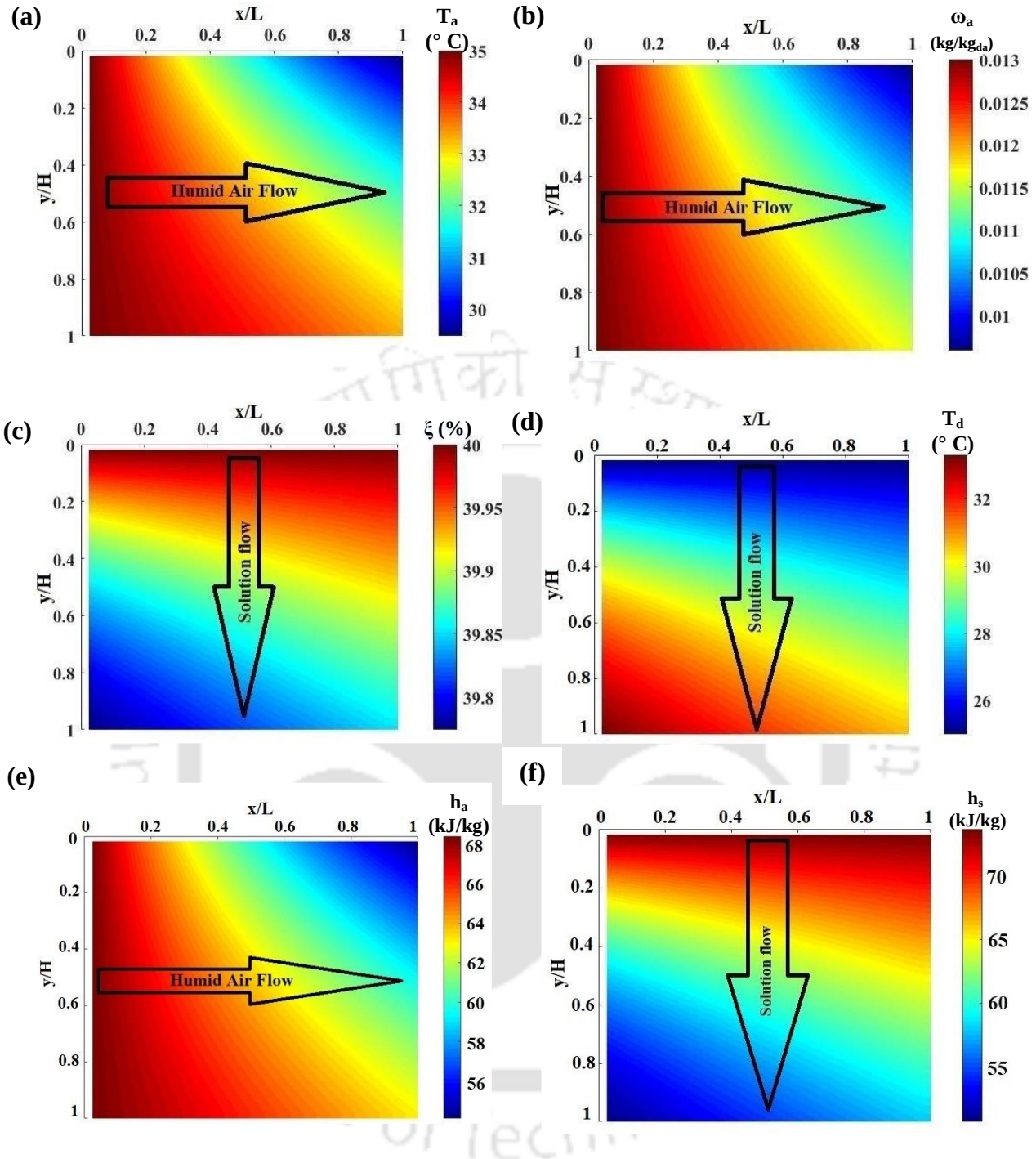

Fig. 3.6: Variation of (a) air temperature (T_a,°C), (b) air humidity(ω_a, kg/kg$_{da}$), (c) solution concentration (ξ, %), (d) solution temperature (T_d,°C), (e) air enthalpy (h_a, kJ/kg) and (f) solution enthalpy (h_d, kJ/kg) in dehumidifier

It can be noticed from Fig. 3.6f that the lowest desiccant specific enthalpy is observed at the left corner (y=H) of the desiccant outlet, since it contacts the hotter and humid air there. Similarly, at air outlet (x = L), the top side air specific enthalpy is less because air reacts with

colder and concentred desiccant solution for longer period at that region compared to the rest of the locations (Fig. 3.6e).

Similarly, the variation of solution temperature (T_d,°C), solution concentration (ξ, %), air humidity(ω_a, kg/kg$_{da}$) and air temperature (T_a,°C) inside the regenerator is depicted in Fig. 3.7.

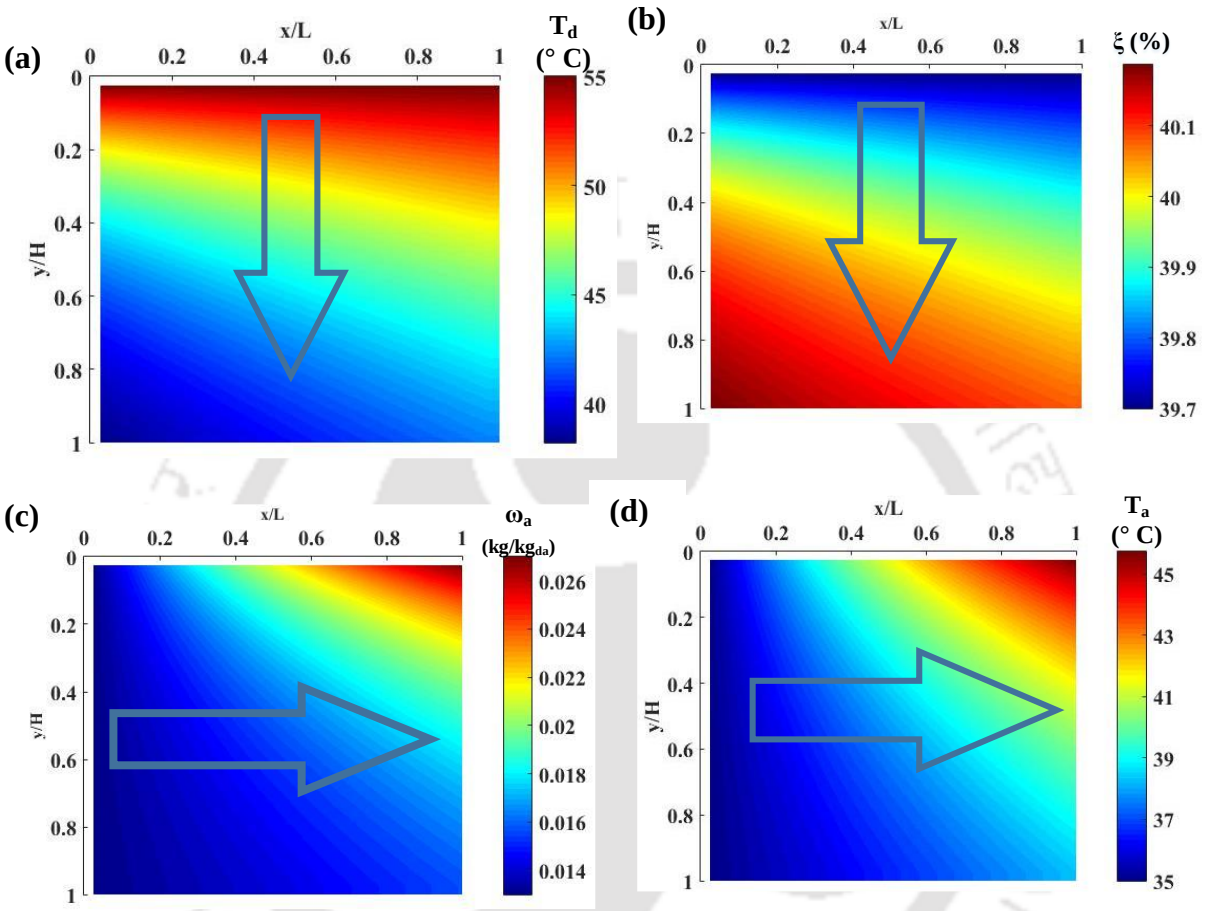

Fig. 3.7: Variation of (a) solution temperature (T_d,°C), (b) solution concentration (ξ, %), (c) air humidity(ω_a, kg/kg$_{da}$), (e) air temperature (T_a,°C) in regenerator

3.4.3. Exergy destruction in the heat and mass transfer operation

The physical and chemical exergy destruction profile is shown in Fig. 3.8a-b. The physical exergy destruction pattern for the optimal blend at T_a and T_d of 35°C and 25°C, respectively at L/G ratio of 2 is shown in Fig. 3.8a. Fig. 3.8a demonstrates the contour plots of the physical exergy destruction over the entire dehumidifier domain. It is noted that maximum physical exergy destruction occurs at the region between outlet of the air and desiccant solution inlet.

This is due to higher heat transfer at that stated location, as shown in Fig. 3.8a. Similarly, Fig. 3.8(b) demonstrates contour of the chemical exergy destruction over the entire dehumidifier domain. It can be observed that maximum chemical exergy destruction is in the top side of the solution inlet because more amount of humid air is interacting with the cooled desiccant solution at the stated location. However, the desiccant solution is not able to absorb the entire moisture from the air. The maximum physical exergy destruction value is 0.06 kW at T_a and T_d of 35°C and 25°C, respectively at L/G ratio of 2 (optimal blend condition), whereas the chemical exergy destruction value is approaching to 0.88 kW at the same condition. This clearly expressed that the latent exergy destruction is more compared to the physical exergy destruction, which is as expected because latent loads are always higher than sensible loads of any particular system except for desert climates (Harriman et al., 1997).

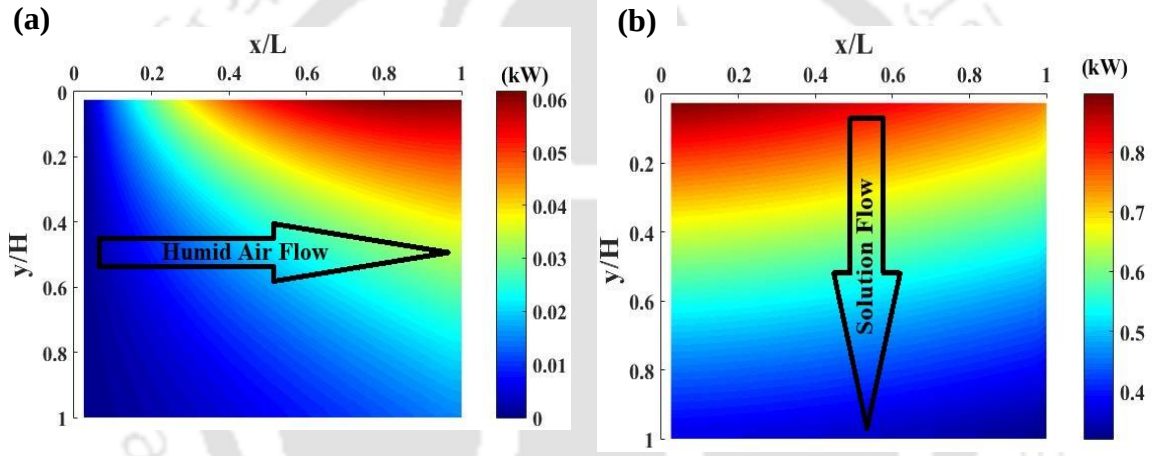

Fig. 3.8: (a) Physical exergy destruction and (b) chemical exergy destruction in the dehumidifier

3.4.4. Comparison of cross and counter-flow configuration for air dehumidification

For a particular inlet condition (specific humidity: 0.013 kg/kg air temperature: 31.7°C, solution temperature: 22.9°C, L/G ratio: 1 and desiccant concentration as 40%), it is observed that counter flow configuration can provide deep dehumidification. The comparison of cross and counter-flow configuration for dehumidification is mentioned in Table 3.3.

Table 3.3: Comparison of cross and counter-flow configuration's performance in dehumidification

Configuration	Crossflow		Counter-flow	
	ω_a(kg/kg$_{da}$)	T_s (°C)	ω_a (kg/kg$_{da}$)	T_a (°C)
LiBr	0.0089	27.8	0.00811	27.67
LiCl	0.0066	28.2	0.0062	28.2

3.4.5. Influences of the packing height on the dehumidifier performance

The influences of the packing height on the latent effectiveness are shown in Fig. 3.9. Fig. 3.9 revealed that the dehumidifier's latent effectiveness increases with the packing height. This is due to the fact that the increase of the mass transfer area at higher packing height. Further, it can be observed that the packing height is not sensitive beyond 0.75 m. Moreover, the increase of the packing height would increase the occupied space and the investment. Therefore, the column height is fixed as 0.75 m for the present study.

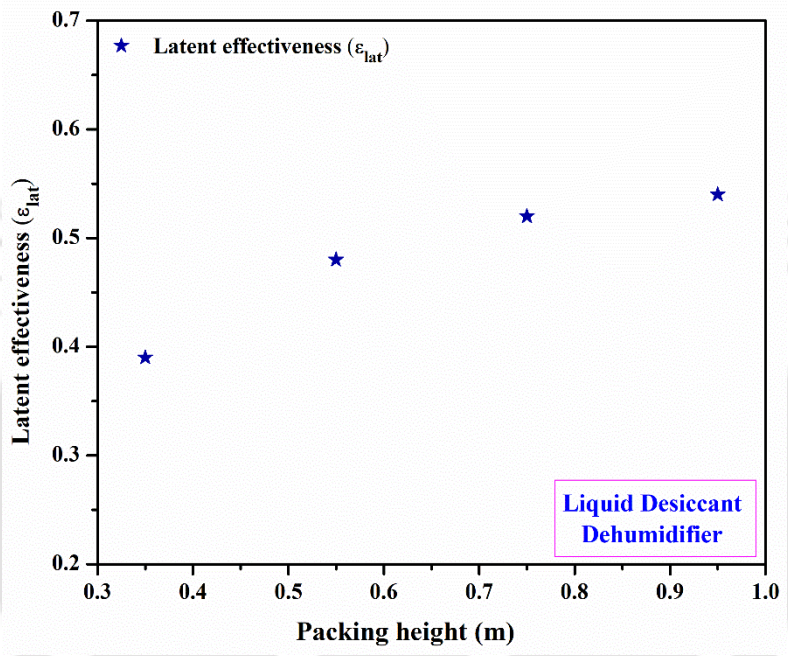

Fig. 3.9: Influence of packing height on the dehumidification performance

3.5. Selection of desiccant

The 'Antonie equation' is the most frequently used empirical correlation, which relates the vapour pressure of desiccant as a function of temperature and concentration. The vapour pressure correlation was derived from curve-fitted connections obtained from experimental datasets (described in section 3.2). In this section, the 'Antonie equation' is used to find the vapour pressure of the different desiccant solutions, as shown in Eq. (3.13). The vapour pressures of several common aqueous desiccant solutions are shown in Fig. 3.10. It can be noticed from Fig. 3.10 that the required concentrations (i.e., desiccant's mass fraction in the aqueous solution) for various desiccants to work under different operating conditions. A liquid desiccant with a higher concentration possesses a lower vapour pressure that allows more water vapour to be transported from the air to the liquid desiccant. The aqueous LiCl desiccant showed the minimum vapour pressure among the other commercial desiccants. However, LiCl desiccant is more corrosive,

expensive and not stable at ambient conditions (Fumo and Goswami, 2002). It is also observed that $MgCl_2$ may not be suitable for deep dehumidification because it crystallizes at a concentration beyond 35% (Chen et al., 2020). LiBr desiccant performs well at higher concentrations, whereas $CaCl_2$ desiccant performed well at lower concentrations (Fig. 3.10). Therefore, the binary mixture of LiBr and $CaCl_2$ would be the most prominent combination as a research interest.

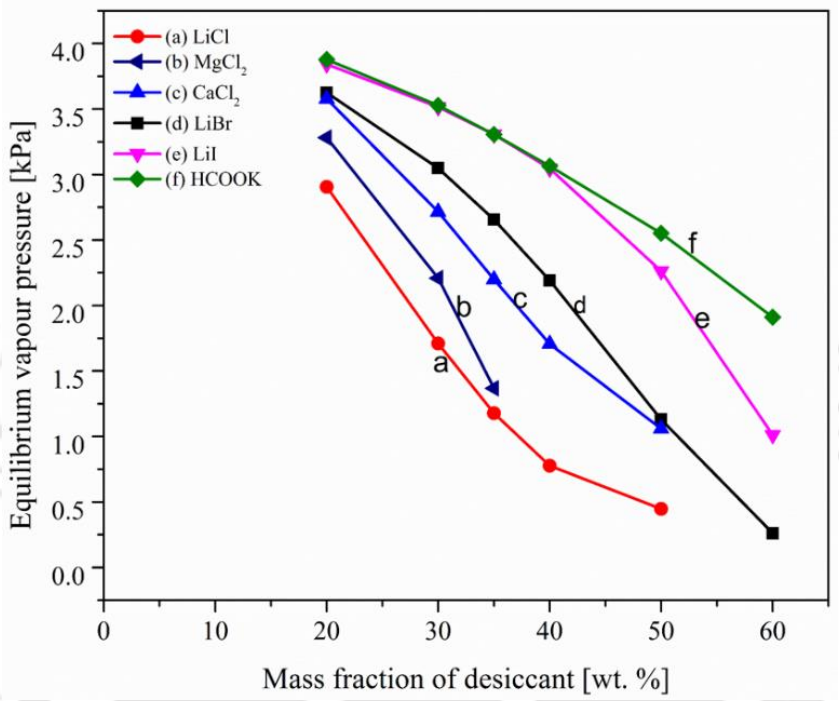

Fig. 3.10: Vapour pressures of different liquid desiccants at 25°C

3.5.1. Material preparation and measuring procedures

The solid form of LiBr and $CaCl_2$ desiccants were procured from Parad Chem Corporation (Gujrat, India). Generally, LiBr and $CaCl_2$ are in dry powder form and white in colour. LiBr and $CaCl_2$ are mixed, crushed and grinded with the help of mortar and pestle to convert into more fine particles /powder in a controlled environment and stored in an air-sealed container. Subsequently, different proportions of LiBr and $CaCl_2$, i.e., 90:10, 85:15, 80:20 and 75:25 are weighted with the help of electronic weight machine to get mixtures, as shown in Fig. 3.11. Fig. 3.11 shows the different samples for the experiments, where 'a' and 'b' for LiBr and $CaCl_2$. 'c', 'd', 'e', 'f' are the ratios of 90:10, 85:15, 80:20 and 75:25, respectively, where LiBr weight are in decreasing order of 100 to 75 while $CaCl_2$ weight is in increasing order of 0 to 25.

Two gram of desiccant/ desiccant mixtures was taken from each small airtight containers and put on glass slides for XRD analysis. In the present study, step-change was taken as 0.2°, and the 2θ range was 10-90°. For the absorption rate analysis, 1g of each powdered samples were taken in Petri-plates and the weight gain due to moisture absorption was measured using an electronic weight machine (accuracy: ± 0.001 g). The weight of each Petri-plate was noted in the time interval of 5 minutes. The temperature of desiccant was recorded by an infrared gun thermometer (accuracy: ± 0.5 °C). Throughout the experiments, dry-bulb and wet-bulb temperatures were 22 °C and 20 °C, respectively. In case of TG and DSC analysis, 8g of each sample was used in the crucible. The experimental temperature range was fixed up to 1000 °C and accordingly, experiments were performed. Samples were heated in the ratio of 10 °C/min in an inert condition. In the present study, argon was used as an inert gas. All tests were performed in Central Instruments Facility (CIF) laboratory of Indian Institute of Technology Guwahati (26.18 °N, 91.69 °E).

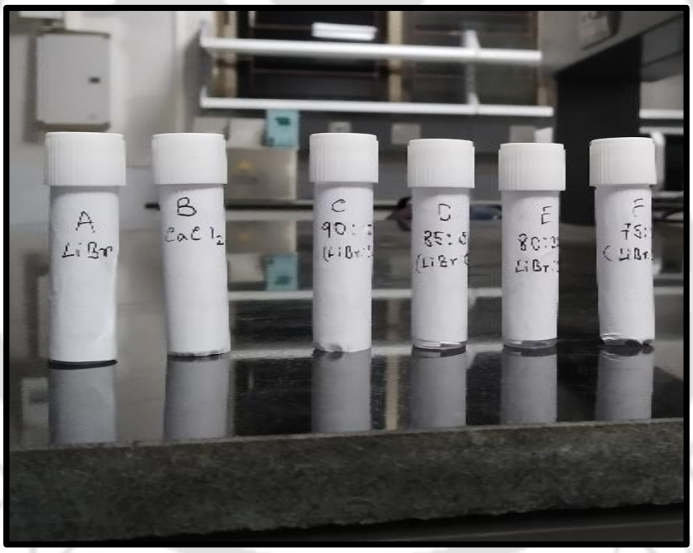

Fig. 3.11: Image of prepared samples (a: LiBr; b: $CaCl_2$; c-f: LiBr:$CaCl_2$ (c: 90:10; d: 85:15; e: 80:20 and f: 75:25))

3.5.2. Absorption rate analysis

Fig. 3.12 represents the absorption rate of pure LiBr, $CaCl_2$ and LiBr+$CaCl_2$ mixtures at different time-periods. In Fig. 3.12, left ordinate represents the weight of the desiccants and the corresponding temperature is represented in right ordinate. The instantaneous rate of absorption for LiBr and $CaCl_2$ can be calculated from Fig. 3.12. It is found that the absorption rate of LiBr and $CaCl_2$ are 0.143 g/hr and 0.142 g/hr, respectively. Similarly, the instantaneous rate of

absorption of 90:10, 85:15, 80:20, and 75:25 mixtures are 0.247 g/hr, 0.271 g/hr, 0.342 g/hr and 0.297 g/hr, respectively.

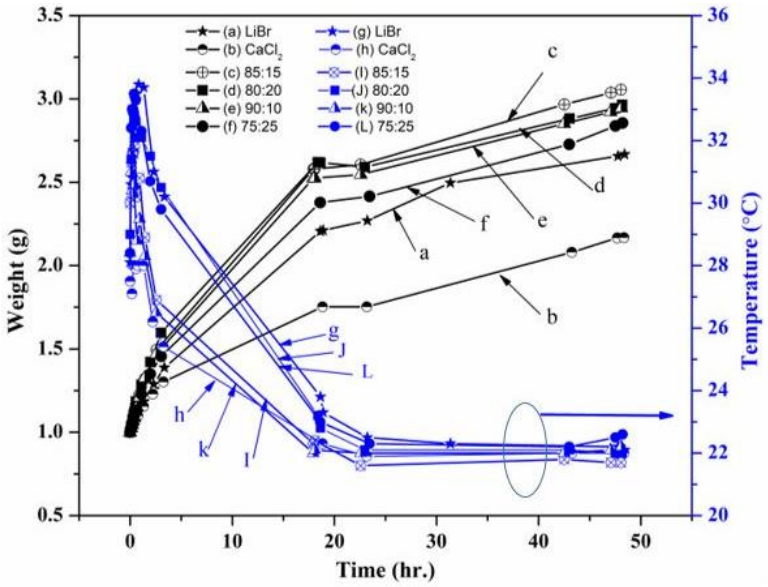

Fig. 3.12: Absorption rate of pure LiBr, $CaCl_2$ and LiBr+$CaCl_2$ mixtures at different time period

It is observed that the overall absorption rate of pure LiBr and $CaCl_2$ are 0.0342 g/hr and 0.0222 g/hr, respectively. Fig. 3.12 predicts overall absorption rate of 0.0404 g/hr, 0.0427 g/hr, 0.0408 g/hr and 0.0385 g/hr for 90:10, 85:15, 80:20 and 75:25 mixtures, respectively. The weight versus time data of pure as well as mixtures of desiccants indicates that instantaneous rate of absorption, as well as overall absorption rate of mixtures, are better than those for pure desiccants. It can also be noticed that during the absorption process, i.e., mass transfer operation the sorption heat is released, and as a result, the temperature of the desiccant sample is appreciably raised. Further, it is clearly observed that after 2 hr of operation, the temperature of all the samples drops and reaches towards room temperature. This suggests that during the mass transfer process (moisture is transferred from surrounding air to the desiccant), the temperature of the sample can be higher than room temperature, which means sorption heat is dominating the sensible heat. Moreover, it is found that the temperature of the pure $CaCl_2$ is lower than the other samples, due to its high thermal diffusivity compared to other samples (Conde, 2004). Further, the instantaneous absorption rate of 80:20 (LiBr: $CaCl_2$) is higher compared to other desiccants, whereas the overall absorption rate of 85:15 is greater than all other samples. Hence, it is favourable to use 80:20 for faster absorption process and 85:15 for

a prolonged absorption process. Therefore, 85:15 and 80:20 mixtures are chosen along with pure LiBr and $CaCl_2$ for further thermal characterization.

3.5.3. Corrosion analysis

A. Methods and Materials

A traditional triple-electrode system equipped with a potentiostat (PGSTAT 204, Switzerland) is utilized to perform electrochemical measurements. For the reference electrode, Ag/AgCl (3 M KCl) is used, and for the counter electrode, a Pt wire is employed. The working electrode used in the present study is a cylinder of stainless steel (304) having a diameter of 2.51 cm (Fig. 3.13) with an exposed surface area of 4.94 cm^2 to the electrolyte solution. The solution temperature was maintained at 25 ± 1°C. Throughout the experiments; the corrosion cell was housed inside a faraday cage to minimize the external noises. The surface of the sample electrode was grinded respectively with 220, 320, 600, and 1000 grade silicon carbide (SiC) paper and was lastly polished with 1.0 μm and 0.3 μm alumina powder. After that, the foreign particles from the surface of the sample electrode were rinsed off with distilled water, and any other remaining particles on the sample's surface were removed through an ultra-sonic process. At the last step, the electrode was washed with millipore water and dried gently using tissue paper. The test sample underwent such pre-treated protocols to ensure that the obtained findings could be repeatable and reproducible. In order to ensure the findings could have reproducibility and repeatability, all of the experiments were conducted a minimum of three times. Subsequently, the linear polarization test was conducted with the following parameters: a potential electrode ranges of ± 20 mV versus open-circuit potential (OCP) and a scan ratio of 0.166 mV/s. On the whole, all the experiments were carried out with different electrolyte solutions such as LiBr (45%), LiBr+$CaCl_2$ (45%) and $CaCl_2$ (45%). The corrosion rate is calculated by Eq. (3.32) (ASTM G102) [19]:

$$\text{Corrosion rate}\left(\text{mm/year}\right) = \frac{3.27\times10^{-3}\times I_{corr}\times EW}{\rho} \tag{3.32}$$

where I_{corr} is the corrosion current density (μA/cm^2), EW is the equivalent weight and ρ is density of the sample.

Fig. 3.13: Stainless steel 304 material samples

B. Results of corrosion characteristics

In the current investigation, different samples are tested to understand the effect of different solutions on corrosion characteristics on stainless steel. The potentiodynamic polarization behaviour of stainless steel of various desiccant solutions is illustrated in Fig. 3.14.

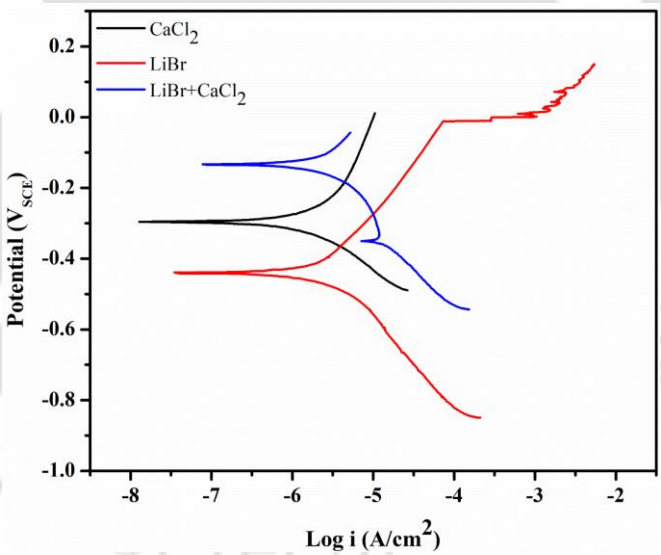

Fig. 3.14: Tafel plots for the stainless steels 304 in halide solution

The values of E_{corr} and I_{corr} obtained from the selected polarization curves are mentioned in Table 3.5. It is observed from the resulting polarization curves (Fig. 3.14) that the solution possesses a significant effect on stainless steel's electrochemical behaviour in the electrolyte system. One of the main observations from these polarization curves is that the I_{corr} value for LiBr, $CaCl_2$ and LiBr+$CaCl_2$ (85:15) is 3.6×10^{-6} A cm^{-2}, 1.7×10^{-6} A cm^{-2} and 1.9×10^{-6} A cm^{-2}, respectively. Subsequently, the corrosion rate for the LiBr, $CaCl_2$ and LiBr+$CaCl_2$ (85:15) is found to be 0.0303

mm/ year, 0.0144 mm/ year and 0.0161 mm/ year, respectively. Further, it is observed from Table 3.4 that the binary mixture of LiBr+$CaCl_2$ (85:15) has a lower corrosion rate compared to the pure LiBr desiccant solution.

Table 3.4: Values of open-circuit potential (OCP) and parameters obtained from the electrochemical polarization test

Solution (45 wt.%)	OCP (mV_{SCE})	I_{corr} ($\mu A/cm^2$)	E_{corr} (V_{SCE})	Corrosion rate (mm/year)
LiBr	-0.35048	3.6363	-0.4385	0.0303
$CaCl_2$	-0.39156	1.7265	-0.2965	0.0144
LiBr+$CaCl_2$ (85:15)	-0.37862	1.9292	-0.1357	0.0161

3.5.4. Structural and morphological characterization: XRD Analysis

In general, pure LiBr and $CaCl_2$ exist in its hydrated form. XRD works based on the principle of Bragg's law, $\lambda=2d' \sin\theta$ (where $d'=d/n$; where, λ is x-ray wavelength; d is inter-plane spacing; n is number of planes, θ is angle between transmitted beam and reflected beam). Diffraction happens in the subsurface atoms, whereas reflection is a surface phenomenon. Diffraction occurs at some specific angles, on the other hand, reflection can happen at any incident angle. Therefore, XRD analysis of a particular compound has to be a unique pattern. XRD analysis can also provide information about the material's inherent characteristics. Further, step size, 2θ range and step per time, sample alignment, filter and slit size has to be fixed before scanning. With this broad information, XRD plots of all samples are depicted in Fig. 3.15.

XRD peaks of LiBr (Fig. 3.15a) were found at 2θ = 28.77°, 33.22°, 47.29°, 55.89°, 58.62°, 68.68°, 75.73°, 78.11° and 87.13°. These results (peaks) are matched with cubic crystalline structure (ICSD PDF Card No.: 01-071-3745) and similar observation also reported by (Gordeeva et al., 2009). Similarly, Fig. 3.15b shows the crystalline phase of $CaCl_2$. Peaks were observed for $CaCl_2$ at 2θ = 32.23°, 46.01°, 56.98°, 66.67° and 75.64°. These peaks are also matched with the orthorhombic crystalline structure (ICSD PDF Card No.: 01-070-2740). Therefore, Fig. 3.15(a) and (b) proves that LiBr and $CaCl_2$ are in acceptable purity. Now, Fig. 15c shows crystalline peaks of mixture 90:10 (LiBr: $CaCl_2$) at 2θ = 28.33°, 31.62°, 32.73°, 46.84°, 55.57°, 58.24°, 75.44°, 77.73° and 86.77°. It also can be noticed from Fig. 3.15(c) that all the peaks were shifted to lower angle than pure LiBr peak angles. It is due to mixing of

orthorhombic $CaCl_2$ with cubic LiBr, which increases the lattice parameters than pure cubic LiBr.

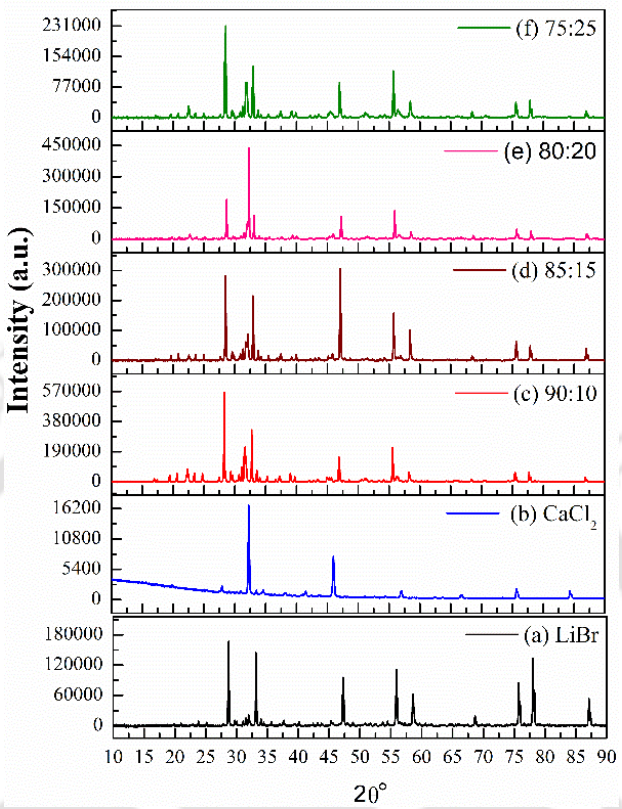

Fig. 3.15: XRD analysis of (a) LiBr, (b) $CaCl_2$, (c) 90:10 (LiBr:$CaCl_2$), (d) 85:15 (LiBr:$CaCl_2$), (e) 80:20 (LiBr:$CaCl_2$) and (f) 75:25 (LiBr:$CaCl_2$)

Fig. 3.15d shows crystalline peak of 85:15 (LiBr: $CaCl_2$) at 2θ = 28.51°, 32.11°, 32.93, 47.11°, 55.77°, 58.42°, 75.6°,77.93° and 86.93°. It can be noticed that peaks of 85:15 were at higher angle than 90:10, whereas lower angle than pure crystalline LiBr. It reveals that the crystalline system of 85:15 has lower lattice parameters compared to 90:10 while higher lattice parameters than pure LiBr. Similarly, Fig. 3.15e shows crystalline peaks of 80:20 (LiBr: $CaCl_2$) at 2θ = 28.67°, 32.26°, 33.11°, 47.22°, 55.91°, 58.57°, 68.62°, 75.71°, 78.02° and 87°. Peaks were at higher angle than 90:10 and 85:15, whereas lower angle than pure LiBr, suggested that lattice parameters of 80:20 are lower than 90:10 and 85:15, whereas higher than pure LiBr. Further, Fig. 3.15f also shows crystalline peaks of 75:25 (LiBr: $CaCl_2$) at 2θ = 28.53°, 31.91°, 32.97°, 46.97°, 46.86°, 55.71°, 58.46°, 68.46°, 75.57°, 77.89° and 86.91°. The lattice parameters of 75:25 were lower than 90:10 and 85:15, whereas higher than 80:20 and pure LiBr.

It can be concluded from the overall XRD study that as the concentration of $CaCl_2$ increases, peaks of $CaCl_2$ and LiBr were slightly shifted, thus change in mixture properties can be

expected. Moreover, some crystalline peaks of $CaCl_2$ and LiBr were disappeared for all mixtures, might be due to the interaction and miscibility of these two desiccants.

3.5.5. TG and DSC analysis

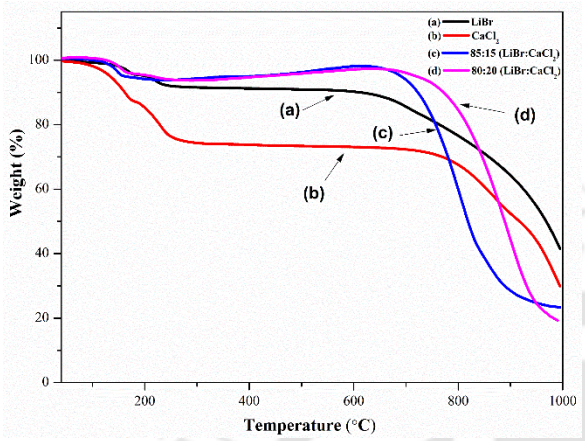

Fig. 3.16: TG curves of samples (a: LiBr; b: $CaCl_2$; d: 85:15 and e: 80:20)

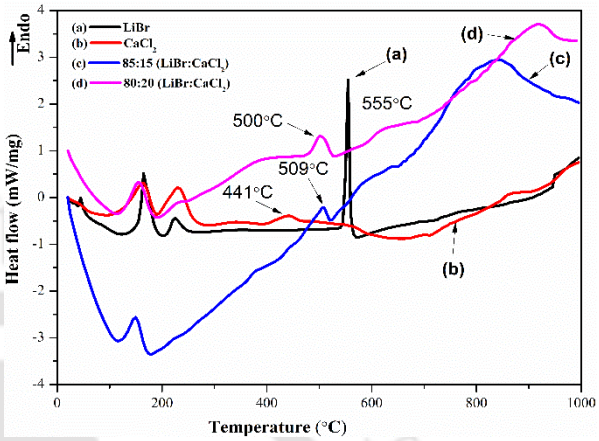

Fig. 3.17: DSC curves of samples (a: LiBr; b: $CaCl_2$; d: 85:15 and e: 80:20)

The thermal characteristic of any material can be analysed with TG and DSC. TG graph indicates the change in mass as a function of temperature. However, the peak in DSC curve reveals the amount of energy required to increase temperature; generally, at that points the phase transformation takes place. TG/DSC graph allows to estimate melting point, decomposition temperature along with latent heat of fusion and latent heat of evaporation of a material.

Fig. 3.16a shows TG graph of LiBr. It shows that the decomposition of LiBr occurs in a three-step. Fig. 3.17a represents the DSC curve of LiBr. The first two endothermic peaks were at 166°C and 225°C for LiBr (Fig. 3.17a) due to surface dehydration from LiBr. The heat required for the surface dehydration process was estimated to be 79.27 and 27.62 kJ/kg at 166 °C and 225 °C, respectively. The mass loss due to surface dehydration of LiBr was found to be 4.2% (Fig. 3.17a). The third peak of LiBr was observed at 555°C, which is corresponding to the melting point (Gordeeva et al., 2009) of LiBr (Fig. 3.17a). As shown in Fig. 3.16b, the decomposition of $CaCl_2$ takes place in a four-step. Due to the evaporation of physically and chemically bound water in $CaCl_2$, two endothermic peaks were observed from 160-230°C. It was calculated that the amount of heat required for evaporation of water was found to be 81.45 kJ/kg and 118.57 kJ/kg at 160°C and 230°C, respectively. The mass loss was 25.16% at 250°C due to the dehydration of $CaCl_2$. Furthermore, an endothermic peak was observed at 441°C in

DSC curve (Fig. 3.18b) while no mass change in TG curve (Fig. 3.16b) because of the melting point of $CaCl_2$.

A two-step decomposition (Fig. 3.16c) was exhibited for 85:15 (LiBr: $CaCl_2$) mixture. Two endothermic peaks were observed in DSC curve corresponding to the decomposition temperature of 85:15 (LiBr: $CaCl_2$). The first (148.6 °C) and second peak (509 °C) were attributed to evaporation of water and melting point of 85:15 mixture (Fig. 3.17c), respectively. Similarly, the mixture of 80:20 (LiBr: $CaCl_2$) was also found to have two-step decomposition in TG curve (Fig. 3.16d). However, as shown in Fig. 3.17d, the first peak was shifted to higher temperature (156.11°C) while the second peak was shifted to lower temperature (500°C). It was estimated that the amount of heat required for evaporation of water from 85:15 and 80:20 mixtures was found to be 59.36 kJ/kg and 78.99 kJ/kg, respectively. It can be deduced from the latent heat of evaporation values, the pure $CaCl_2$ (22.63 kJ/kg) requires high energy than the prepared mixtures for regeneration process. Likewise, the fusion enthalpy of pure $CaCl_2$ (22.63 kJ/kg) and LiBr (149.78 kJ/kg) was higher than the prepared mixtures due to their high crystallinity. Therefore, the application of these mixtures as desiccant might reduce the cost of regeneration.

The pure LiBr was blended with commercially available $CaCl_2$ in different proportions. The LiBr at high concentration serves as a vapour pressure suppression agent, whereas $CaCl_2$ performing well at lower concentrations. However, the initial phase of the desiccant is solid and miscible in water in almost all proportions. The blending of desiccants was done based on mass concentration (solute/solution). It was found that the overall moisture absorption rate of 85:15 (LiBr: $CaCl_2$) mixture was higher compared to other desiccants. Hence, 85:15 mixture is chosen for the present study. There is a problem with the miscibility of LiBr and $CaCl_2$ desiccant with water that further restricts the flexibility of maximum concentration limit. In order to know the behaviour of mixture desiccant, a laboratory-based test was performed, and the phase separation was observed above 55% of total desiccant concentration, whereas, solution was not absorbing water vapour effectively below 30%. Subsequently, the phase separation was observed beyond 55% of total desiccant concentration (particularly due to the formation of various tetrahydrates, where some of these are metastable (Yao, 2014)) and the water vapour was not effectively absorbed below 30% of total desiccant concentration. Conversely, the properties of liquid desiccant such as vapour pressure, density of the mixture and specific heat of solution are required for evaluating the dehumidifier performance.

In the case of vapour pressure estimation, the kinetic gas theory-based equation is used. The vapour pressure of desiccant solution is calculated by Langmuir equation (Langmuir, 1913), as shown in Eq. (3.33).

$$(dm/dt) = \alpha\sqrt{\frac{M}{2\pi R_u T}}p_v \tag{3.33}$$

where (dm/dt) is the mass change rate, i.e., evaporation rate (calculated from the thermo-gravimetric analysis), M is the molecular mass of the evaporating substance, R_u is the universal gas constant, T is the temperature, p_v is the vapour pressure of the desiccant and α is the evaporation coefficient. The evaporation coefficient, α, depends on the experimental conditions such as pressure, temperature, nature of the crucible gas, and geometry structure of the crucible, but not on the substance. In the present study, the evaporation coefficient, α, was determined based on the experimental results for a reference substance (i.e., pure water) with the known vapour pressure. During the test, the sample was placed in a sealed crucible with a 0.35 mm diameter hole on the lid of the thermo-gravimetric analyzer. The crucible was then placed on the holder of the balance inside the thermogravimetric analyzer. The sample was purged by a pure nitrogen gas flow in order to maintain the water content outside the crucible close to zero. Subsequently, it is found that the presented method can estimate the vapour pressure with an error bar of ± 0.02 kPa. Price (2001) and Ren et al. (2019) have also considered the same methodology for estimating different solution's vapour pressure.

Fig. 3.18 shows the spider diagram, presented the vapour pressure of mixed (LiBr: $CaCl_2$) and pure (LiBr) desiccants solution at different concentrations and temperatures. It represents different indicators where the colour lines represent the different temperature values of the desiccant solution. The higher the value in the spider diagram, the higher the value of the vapour pressure (kPa). The scale of the vertical/horizontal axes is 0 to 7 kPa. It can be observed from Fig. 3.18 that the value of vapour pressure is 3.78 kPa at 45°C for 45 wt.% mixed desiccants, whereas at the same concertation and temperature, the vapour pressure of pure desiccant is 3.69 kPa. Similarly, at 30 wt.% of pure desiccant and mixed desiccant in 20°C, the vapour pressure becomes 1.67 kPa and 1.64 kPa, respectively. From the results, it can be concluded that the vapour pressure of pure (LiBr) and mixed desiccant (LiBr: $CaCal_2$) has the same vapour pressure at different concentrations and temperatures.

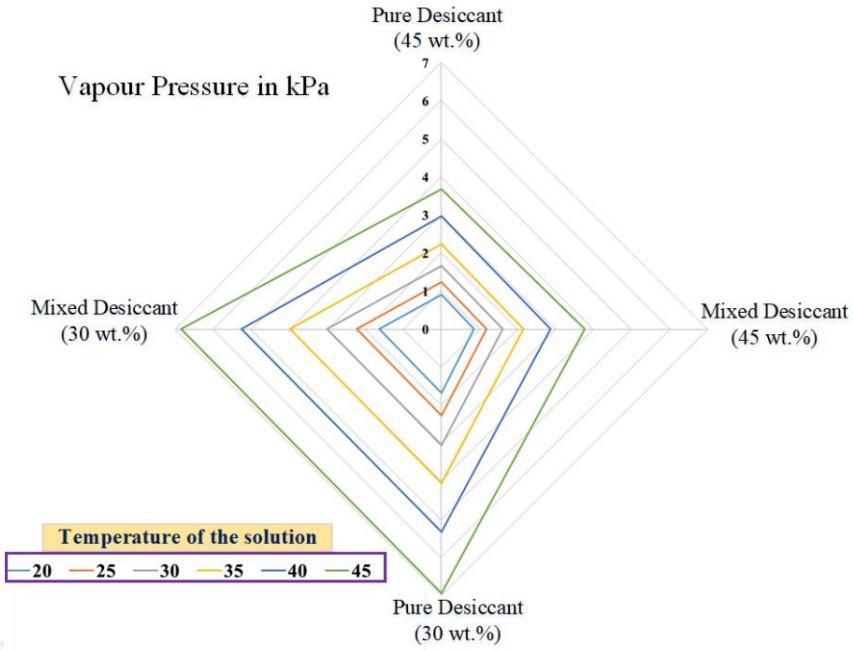

Fig. 3.18: Comparison of the vapour pressure of mixed (LiBr: $CaCl_2$) and pure (LiBr) desiccants at different concentrations and temperatures

3.5.6. Density/concentration analysis

The change of desiccant concentration is difficult to measure experimentally, as the desiccant concentration does not show any significant change in concentration. In this present thesis work, concentration is derived from the desiccant density at the corresponding temperature. During the experimental runs, the desiccant concentration was estimated based on the temperature and density measurements (Eq. 3.34). In order to ensure a correlation of desiccant concentration as a function of density and temperature of the desiccant solution, a total of 8 samples of LiBr+$CaCl_2$ solutions were prepared with different concentrations varied from 20% (wt./wt.) to 55% (wt./wt.) with 5% (wt./wt.) increments. Anton-Paar 4500M vibrating tube density meter (accuracy: ± 0.00005 g/cm^3) was used for density measurement of each sample in a temperature range of 20 – 80°C with a 5.0°C increment, where the temperature of the desiccant solution was measured by the thermostat with temperature stability of ± 0.01°C.

The maximum temperature of 80°C was selected because it is expected that the maximum temperature can be reached with a relatively high temperature up to 80°C in the dehumidification/regeneration system. The gravimetric method is used to determine the desiccant concentrations of the prepared samples. The measured density is presented in terms of concentration and temperature, as shown in Fig. 3.19.

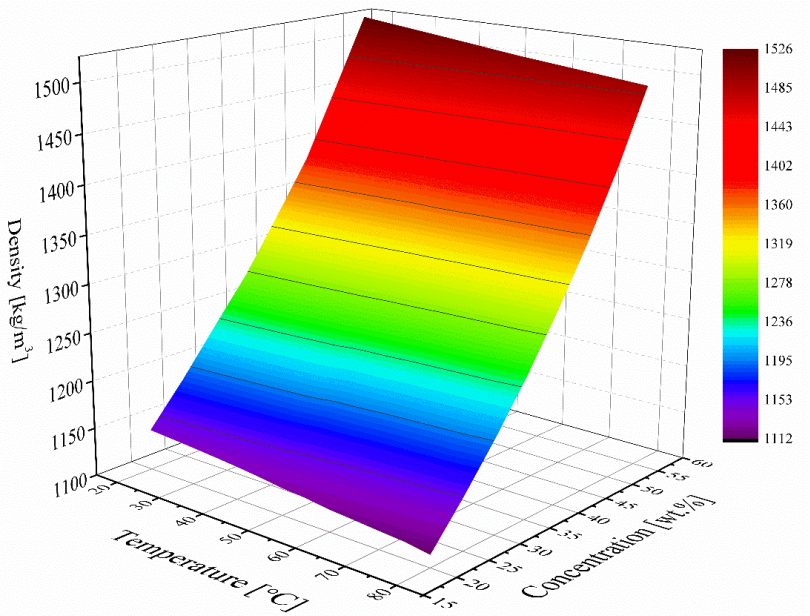

Fig. 3.19: Density variation of $LiBr+CaCl_2$ Solution

A total of 72 number data are collected and based on these measured data, an empirical equation is developed, as expressed in Eq. 3.34, where ξ, T_s and ρ are the desiccant concentration (wt.%), temperature (K) and density (kg/m^3) of the $LiBr + CaCl_2$ solution, respectively, and $C_1 – C_4$ are the coefficients with the values 1144,6.655,0.000914, and -0.481, respectively. The comparison of predicted density with experimental density is shown in Fig. 3.20.

$$\rho = f\ (\xi, T_s) \tag{3.34}$$

$$\rho\ [kg/m^3] = C_1+C_2\xi+C_3\xi^3+C_4T_s \tag{3.34a}$$

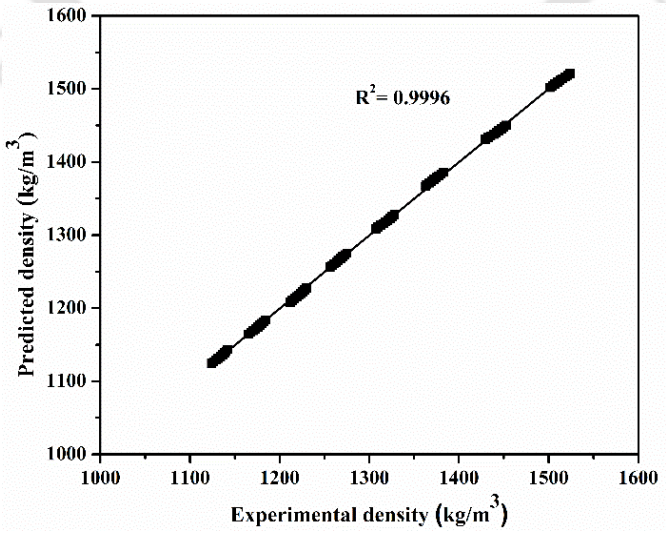

Fig. 3.20: Comparison of predicted density with experimental density

3.5.7. Other thermal-physical properties of desiccant

Differential Scanning Calorimetry (DSC) (Make: Netzsch, Model: STA449F3A00) was used in the case of specific heat capacity measurement. The uncertainty present in the measurement was ± 2%. In case of viscosity measurement, 'Brookfield Viscometer' was used. The uncertainty present in the viscosity measurement was ± 1%. In case of surface tension measurement**,** 'automatic surface tensiometer DY 300' was used. The uncertainty present in the measurement was ± 0.2 mN/m. The vapour pressure is estimated based on the kinetic gas theory-based equation. The mass loss of the sample is measured using a thermogravimetric analyzer (i.e. TGA 5500), and the result is then used to determine the vapour pressure of the solution by the Langmuir equation for free vaporization. Subsequently, the estimated values of vapour pressure, density, specific heat capacity, viscosity and surface tension are 1.18 kPa, 1383.4 kg/m^3, 2.8 kJ/(kg°C), 2.9 mPa-s and 0.053 N/m, respectively, at 25°C and mass concentrations of 45% LiBr + $CaCl_2$ solution.

3.5.8. Contact angle inscription

After obtaining the optimum blend combination, a preliminary analysis was accomplished to confirm the optimum combination feasibility and that was ensured by explaining the mechanism of wettability improvement in terms of static contact angle inscription. The contact angle on a plane glass for both solutions (pure LiBr and optimum desiccant mixture) was measured by a goniometer (Make: Rame-hart instrument Co. with an accuracy of 0.1°). The contact angle of LiBr and optimum LiBr + $CaCl_2$ solution is shown in Fig. 3.21.

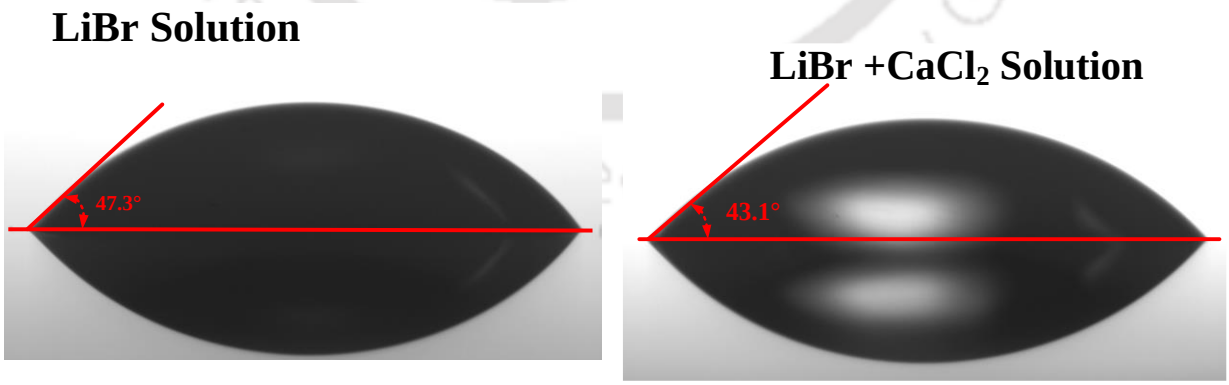

Fig. 3.21: Contact angle of LiBr and LiBr + $CaCl_2$ (optimum) solution

The equilibrium contact angle was measured, but in practice, it would be an apparent contact angle because no surface is completely smooth at the molecular level. According to the Wenzel

state model for an acute equilibrium contact angle, the apparent contact angle becomes lesser than the equilibrium's angle for a pinned droplet. Additionally, since the surface roughness would reduce the contact angle, it could be even lesser than the equilibrium contact angle. It was observed from Fig. 3.21 that the contact angle decreased from 47.3° for LiBr solution to 43.1° for the blend solution. The smaller contact angle corresponded to better wettability and improvement in moisture removal. The slight reduction in the contact angle resulted in the modest improvement of the wetting area. Thus, the slight improvement in wettability provided a more significant contact area between the liquid desiccant and the processed air. Therefore, LiBr + $CaCl_2$ may have a higher moisture removal rate compared to the LiBr solution.

3.5. Closure

The FDM based model empowers a more realistic mapping of the domain of an adiabatic dehumidifier as the predicted results are closer to experimental data. It seems that the differences between the FDM approach and the experiments are an effect of the simplification concerning the numerical model geometry. Moreover, the simulation results showed that the inlet concentration differences impact dehumidification. The primary objective of the present investigation is to analyse the potential of single halide salt solution as desiccant and to predict the performance of a dehumidifier. Further, the mixture desiccant properties are measured using different sophisticated instruments. The following conclusions can be made from this chapter:

- Irreversibility in heat and mass transfer operation is investigated in terms of physical and chemical exergy destruction. It is found that the maximum chemical and physical exergy destruction is 0.88 kW and 0.06 kW, respectively.
- The aqueous LiCl desiccant showed the minimum vapour pressure among the other commercial desiccants. However, LiCl desiccant is more corrosive and not stable at ambient conditions.
- LiBr desiccant is performing well at higher concentrations, whereas, $CaCl_2$ desiccant performed best at lower concentrations. Therefore, LiBr and $CaCl_2$ would be the most prominent combination as a research interest.
- XRD pattern of LiBr, $CaCl_2$ and their mixtures demonstrated that lattice parameters for mixtures were different compared to pure individual desiccants. The lattice parameters were decreased as the proportion of $CaCl_2$ in the mixture is increased till 80:20 (LiBr: $CaCl_2$).

- Adsorption rate analysis showed that LiBr and $CaCl_2$ mixtures had a better rate of absorption than pure LiBr and $CaCl_2$.
- The overall absorption rate of 85:15 was higher than other prepared samples. Hence, it is favourable to use 85:15 for the prolonged absorption process.
- Pure $CaCl_2$ is not a viable option for low-cost regeneration compared to other prepared samples.

CHAPTER 4

Experimental studies on solar evacuated tube collectors

4.1. Introduction

Solar collectors are efficient in utilising solar thermal energy for heating applications as their efficiency is quite high even in the medium temperature range, which motivated to design a high efficient collector system. In this chapter, an experimental investigation is carried out by developing an evacuated tube solar collector system with U-tube configuration using water as a working fluid. The manifolds are connected in series and each manifold is connected with ten solar U – tube evacuated collectors in parallel. The performance of the collector system is continuously measured throughout the day. Further, a trade-off study is carried out considering all the performance parameters. On the basis of experimental datasets, a multilayer perceptron (MLP) architecture is developed to predict thermal efficiency, useful heat gain and water outlet temperature of the evacuated tube collector as a function of solar irradiation, mass flow rate of water and water inlet temperature.

4.2. Experimental setup and methodology

The test rig consists of three central components: 3-manifolds (M1, M2, and M3), storage tank, and pump. Each manifold contains ten ETCs and ETCs are concentric, evacuated glass tubes (Fig. 4.1a). The ETCs include copper U-tubes, which are connected to headers for cold and hot water. However, between ETC and U-tubes, an aluminium fin is mechanically fitted, as shown in Fig. 4.1(b) and 4.1(c). The solar collector system is installed at Indian Institute of Technology Guwahati, India (latitude 26.1879° N, longitude 91.6916° E). Each manifold is fabricated with dimensions of 1200 mm × 1900 mm, and comprises of ten borosilicate ETCs with 58 :47: 1800 mm of outer diameter: inner diameter: length, respectively, with a spacing of 120 mm between the tubes. A steel frame holds the ETCs to ensure tilt angle flexibility. Typically, the tilt angle is equal to the local latitude angle and the ETCs are fixed at south-facing as shown in Fig. 4.1. There are two sizes of copper tubes namely, U-tube with wall thickness of 0.58 mm and header tube with wall thickness of 1.2 mm. U-tubes, which are in contact with an aluminium fin (1700 mm in length), are inserted in the ETCs. Aluminium fins are in contact with the inner surface of the glass tube, as shown in Fig 4.1(b). The header tubes are on the same horizontal level. The purpose of header tubes is to carry the cold and hot water;

two limbs of the U-tube are attached to two header tubes. The header tubes are properly insulated with two layers of glass wool of thickness 20 mm.

The manifolds are fixed in such a way that one manifold outlet connects with the adjacent manifold inlet, as shown in Fig. 4.1. Heat trapped by the ETCs is absorbed by the U-tubes and then it is transmitted to the water which is pumped towards the hot header tube of the manifolds and finally reaches the storage tank. The hot header tube of manifold M1 is connected to cold header tube of the second manifold, etc. and thus the water temperature increases significantly. Finally, the tank water gets heated up as the outlet water of the ETCs exchanges its heat with the water in the storage tank.

ETCs have vacuum insulation of 5×10^{-8} bar with a typical absorptivity of 0.90 to 0.93. Details of technical specifications are shown in Table 4.1. The cylindrical storage tank (620 mm inner diameter, 3 mm thickness, 900 mm length) is insulated by two layers of nitrile foam rubber (each of 30 mm thick) to reduce heat losses. A 0.5 HP capacity pump is used to pump the cold water from the storage tank into the manifolds. Two stainless-steel ball valves are attached to the pump to regulate the flow rates and accordingly, analysis is done for three different mass flow rates of 0.037 kg/s, 0.05 kg/s and 0.08 kg/s. The connection between storage tank to pump, pump to manifold M1 and manifold M3 to storage tank is made with 19.05 mm diameter hose pipes having 50 bar pressure bearing capability.

The evacuated tube comprises of an inner and an outer concentric tube; the clearance is evacuated, then the tubes are sealed at the end. Hazami et al. (2013) and Nkwetta et al. (2013) have shown that the evacuated space between the tubes is excellent thermal insulation and minimizes the convection loss, thus improving the thermal efficiency. The incident solar radiation reaches the selective coating surface on the inside of the inner glass tube through two transparent glass tubes, where it is absorbed. The absorbed solar radiation is converted into heat and then transferred to the water flowing inside the U-tube. Circular aluminium fins, which are attached to the U-tubes, accumulate heat from the absorber tube and dissipate to U-tubes.

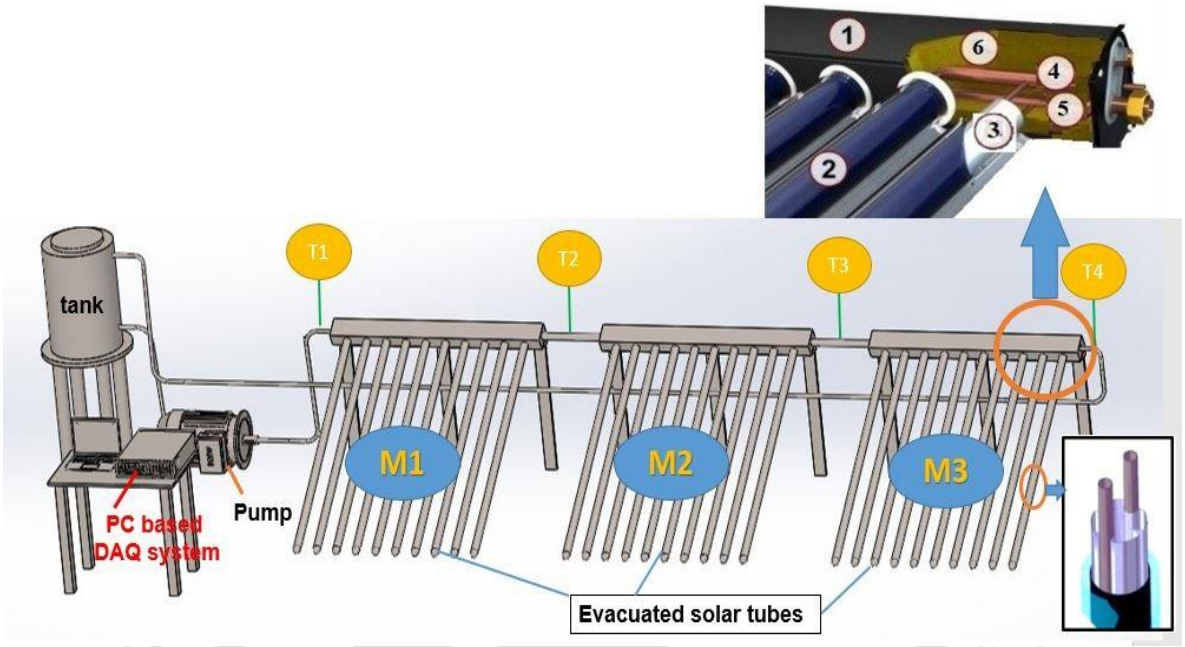

Fig. 4.1 (a): Schematic diagram of the experimental setup (1: Header casing, 2: ETC, 3: Aluminum fin, 4&5: Header tube, 6: Glass wool) (M1,M2,M3: Manifolds; T_1,T_2,T_3,T_4: water temperature)

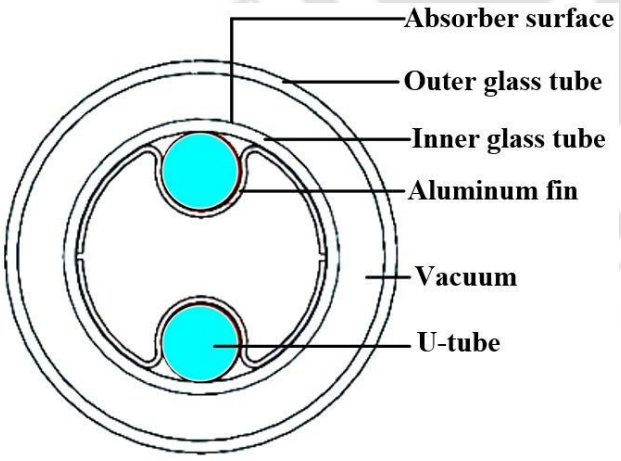

Fig. 4.1 (b): Cross-sectional view of ETC with inserted U- tube and fin

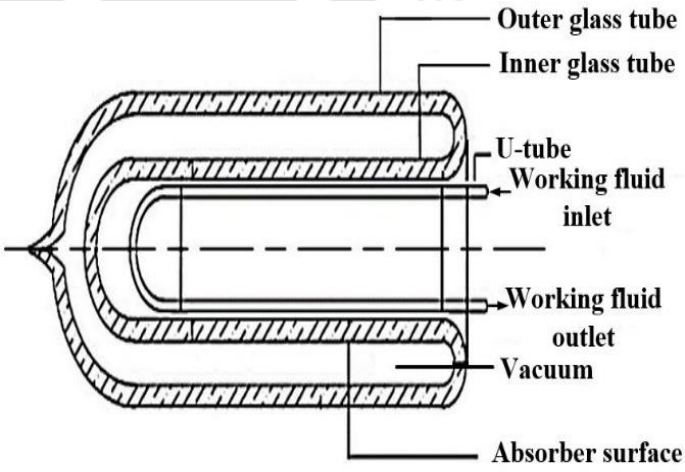

Fig. 4.1 (c): Longitudinal view of ETC with inserted U-tube and fin

Table 4.1: Technical specifications of solar U-tube ETC system

Specifications		**Description**
Model		"3- target" vacuum tube*
Material (glass)		3.3 Borosilicate glass
Tube length		1800 ± 0.1 mm
Inner and outer diameter		47 ± 0.1 mm and 58 ± 0.1 mm
Absorptive coating	Sediment method	Three target magnetron sputtering plating
	Material (coating)	Cu/SS-ALN/ALN (Solar selective coating)
	Emissivity	≤ 6.5% (80 ± 5°C)
	Absorptivity(α)	≥ 0.93 (AM 1.5)
Vacuum degree		≤ 5.0×10^{-3} Pa
Outer diameter of U-tube		9.53 mm
Thickness and length of U-tube		0.58 mm and 1700 mm
Tilt angle and facing of ETCs		26° and south
Transmitivity of glass tube (τ)		≥ 0.89 (AM 1.5)

*3- target: three-layer- bonding agent cum absorption layer (Aluminum nitride – stainless steel), absorption layer (Aluminum nitride), and anti-reflection layer (copper).

The solar irradiation is measured using pyranometer. The inlet and outlet temperatures of each manifold are measured using T-type thermocouples, which are denoted by T1, T2, T3, and T4 in Fig. 4.1. The outlet temperature (T2) of M1 is the inlet temperature of M2. Similarly, T3 is outlet temperature for M2 and inlet temperature of M3. The test was conducted from 8:00 A.M to 4:00 P.M (IST) in the month of August 2018. Air velocity and air temperature are measured by anemometer and T-type thermocouples, respectively. All the sensors are interfaced to a computer through an Agilent DAQ, which records the data every 10 s; the data are eventually synchronized by a GUI assisted Agilent DAQ post-processing software.

4.3. Measured data uncertainty analysis

An uncertainty analysis is made for all the measured and estimated quantities. The significance of such analysis is in support of the determination of associated uncertainty analysis concerning the repeatability and preciseness of the experimentation. Experimental uncertainty analysis is performed in two parts for the current experimental studies.

4.3.1. Sensitivity of the instrumentation

The inaccuracy and operating ranges of various instruments and sensors fitted in the setup are listed in Table 4.2.

Table 4.2: Technical specifications of measuring devices

Parameter	Device	Type	Inaccuracy	Operating Range
Air temperature	Thermocouple	T-type thermocouple	± 0.2 °C	28 to 38 °C
Water flow rate	Dasmash water meter	CM/L-0151526; IS:779/94; CLASS-A;	± 2% l/h	60 to 1500 l/h
Water temperature	Thermocouple	T-type thermocouple	± 0.2 °C	26 to 80 °C
Solar irradiation	Pyranometer	Apogee: Model SP – 110	± 3 W/m^2	0 to 1000 W/m^2
Air velocity	Hotwire anemometer	Testo 490	± 0.1 m/ s	0 to 25 m/s

4.3.2. Uncertainty of computed factors

The uncertainties of the performance parameters are calculated through analytical method given by Kline and McClintock (1953). This method prescribes the total uncertainty ΔU as a function of independent variables V_1, V_2, …., Vn (i.e., $\Delta U = f\ [V_1, V_2, \ldots, Vn]$) having individual errors ΔV_1, ΔV_2,…..,ΔV_n, as given by Eq. (4.1). According to this principle, the estimated uncertainties is recorded in Table 4.3.

$$\Delta U = \sqrt{\left(\frac{\partial U}{\partial v_1}\Delta V_1\right)^2 + \left(\frac{\partial U}{\partial v_2}\Delta V_2\right)^2 + \cdots + \left(\frac{\partial U}{\partial v_n}\Delta V_n\right)^2} \quad (4.1)$$

Table 4.3: Uncertainty of the computed performance parameters

Performance parameters	Independent variables	Instrument (s)	Uncertainty % of measuring devices	Uncertainty % of computed parameters
Thermal efficiency (η)	Flow rate of water, Temperature, Solar irradiation	Water flow meter, Thermocouple, Pyranometer	± 2% l/h ± 0.2 °C ± 2 W/m^2	± 2.2
Useful heat gain (Q_u)	Flow rate of water, Temperature	Water flow meter, Thermocouple	± 2% ± 0.2 °C	± 2.1

4.4. Experimental results and discussion

A solar ETC system having thirty U-tube ETCs connected in series is tested in a humid sub-tropical region. Fig. 4.2 (a, b and c) shows the variation in solar irradiation and thermal efficiency with time throughout a typical sunny day during summer having a peak solar irradiation of 755 W/m^2 with a time-averaged ambient temperature of 31°C during 08:00 to 16:00 h (IST). The solar collector system was exposed to sunlight at 08:00 h with fresh water having at 28.6-29.1°C. Subsequently, the water temperature is increased significantly. The outlet water temperature from the ETCs increased from 28.6°C to 86°C in a closed-loop operation.

Fig. 4.2 (a, b and c) shows the variation in solar irradiation, useful heat gain and thermal efficiency throughout the day for mass flow rates of 0.03 kg/s, 0.05 kg/s and 0.08 kg/s, respectively, for a typical humid subtropical region. It is observed that the intensity of radiation progressively increases and becomes maximum around 12 noon and then decreases (Fig. 4.2 (a, b and c)); the sudden depressions in solar irradiation indicate the presence of clouds. Fig. 4.3 (a, b and c) represents the temperature profile of each manifold, i.e., T_1, T_2, T_3, and T_4. The net temperature difference across each manifold is indicated for different inlet water temperatures for manifolds 1, 2, and 3. The total temperature rise across the whole collector is expressed as ΔT. The maximum ΔT for water flow rates of 0.03, 0.05 and 0.08 kg/s are 22.7 ºC, 14.9 ºC and 9.9 ºC, respectively. This analysis also shows the effect of mass flow rate and inlet temperature of working fluid on ΔT; it is found that a negative effect on ΔT exists for

increasing mass flow rate at same solar irradiation. The observed maximum outlet temperature was 86.8 ºC, 76.5 ºC and 69.01 ºC for mass flow rates of 0.03, 0.05 and 0.08 kg/s, respectively (Fig. 4.3 (a, b and c)).

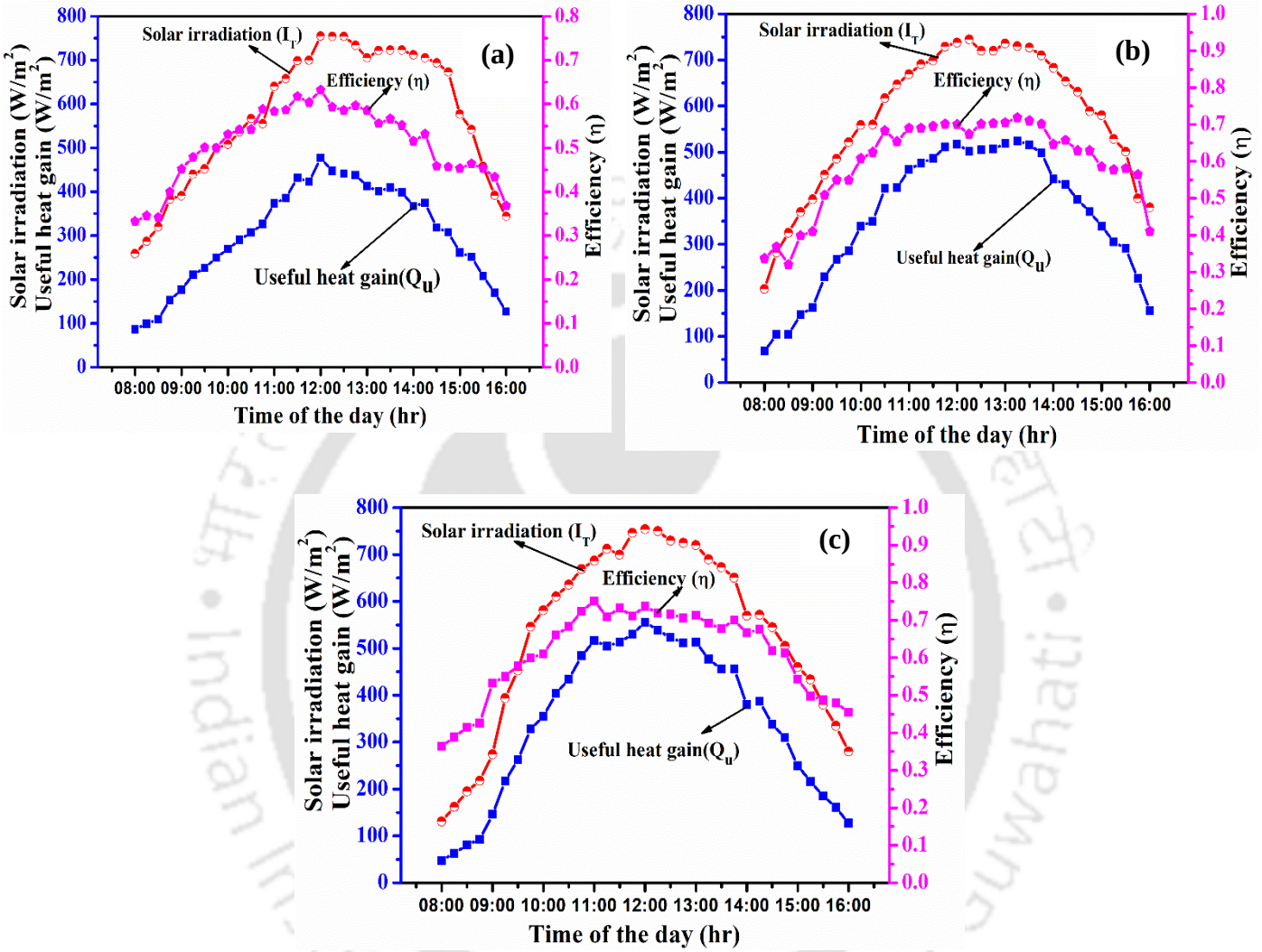

Fig. 4.2: Performance of U-tube ETCs under different mass flow rates (a) 0.03 kg/s, (b) 0.05 kg/s and (c) 0.08 kg/s

The maximum temperature obtained from the collector decreases with increase in mass flow rate. As the mass flow rate increases, the fluid has less time to be in contact with the collector. The thermal efficiency is maximum for each case at the mid-time of the day at which solar irradiation is maximum. The thermal efficiency of the collector is a function of mass flow rate, temperature difference, and intensity of solar radiation as expressed in Eq. (4.3). The maximum thermal efficiency of the entire system was found as 0.63, 0.718 and 0.75 for mass flow rates of 0.03, 0.05 and 0.08 kg/s, respectively. The maximum thermal efficiency increases with

decrease in mass flow rate because more amount of fluid comes in contact with the evacuated tube collector and more amount of heat is exchanged.

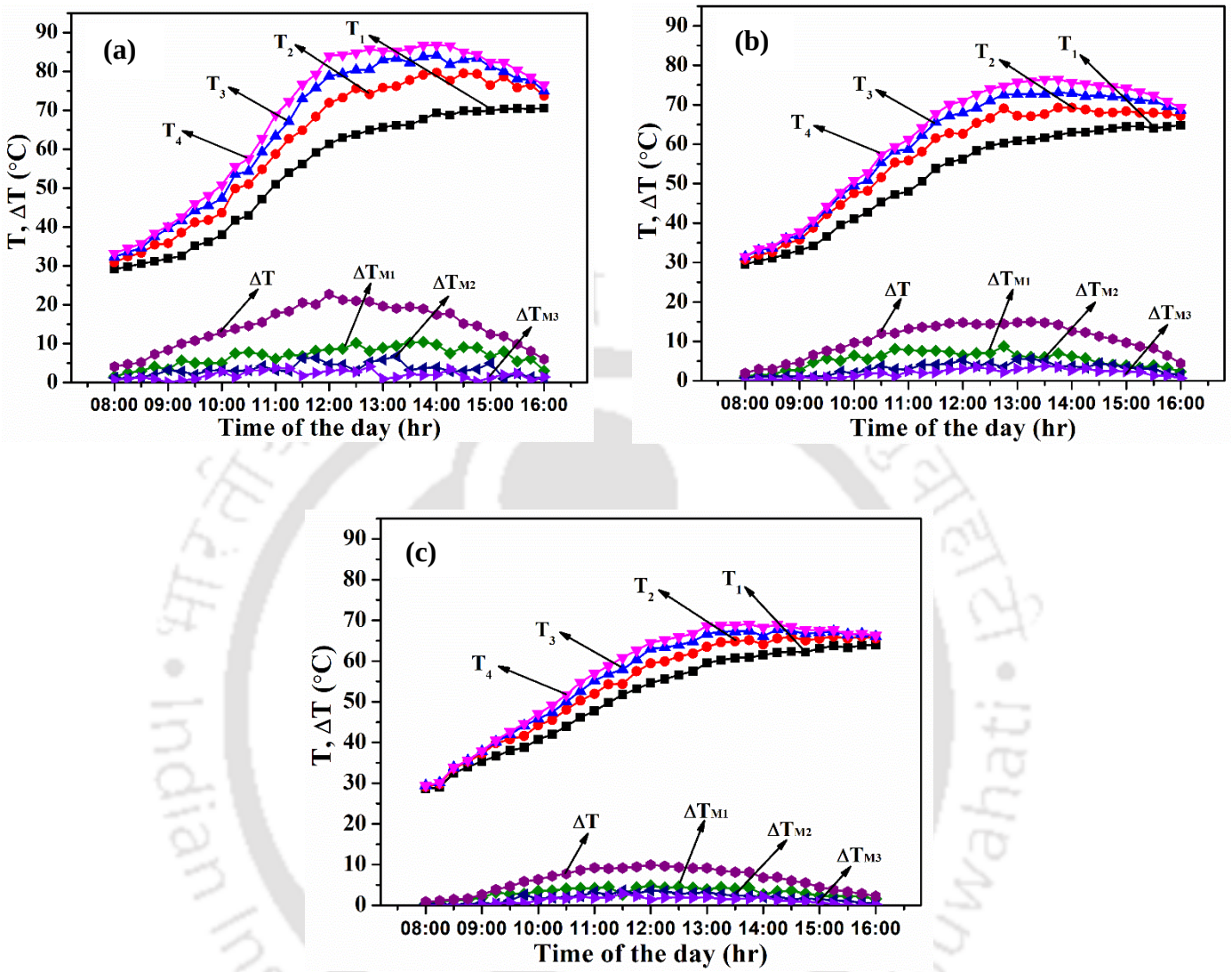

Fig. 4.3: Temperature of U-tube ETCs under different mass flow rates (a) 0.03 kg/s, (b) 0.05 kg/s and (c) 0.08 kg/s ($\Delta T = T_4-T_1$; $\Delta T_{M1} = T_2-T_1$; $\Delta T_{M2} = T_3-T_2$; $\Delta T_{M3} = T_4-T_3$)

It should be noted that there is always a heat loss from solar collector to ambient when the fluid inlet temperature is higher than the ambient temperature. In this respect, the thermal efficiency of the collector is presented against the thermal loss factor called reduced temperature difference, T_{red} as mentioned in Eq. (4.2). According to ASHRAE Standard, a linear curve is fitted between thermal efficiency and the reduced temperature difference (Fig. 4.4). As working fluid inlet temperature is low, the reduced temperature is negative at the initial time period of the experiment. The reduced temperature difference can particularly become negative in regions where the ambient temperature is low (Nie et al., 2017). Since, the present experimental study has been conducted in humid subtropical climate, due to which the reduced temperature

difference is negative only for few minutes of the initial time-period. Hence, only positive values of reduced temperature difference are considered for plotting the graph between thermal efficiency and reduced temperature difference. The maximum thermal efficiency was obtained at lower reduced temperature differences and at higher mass flow rates, as shown in Fig. 4.4 (a, b and c).

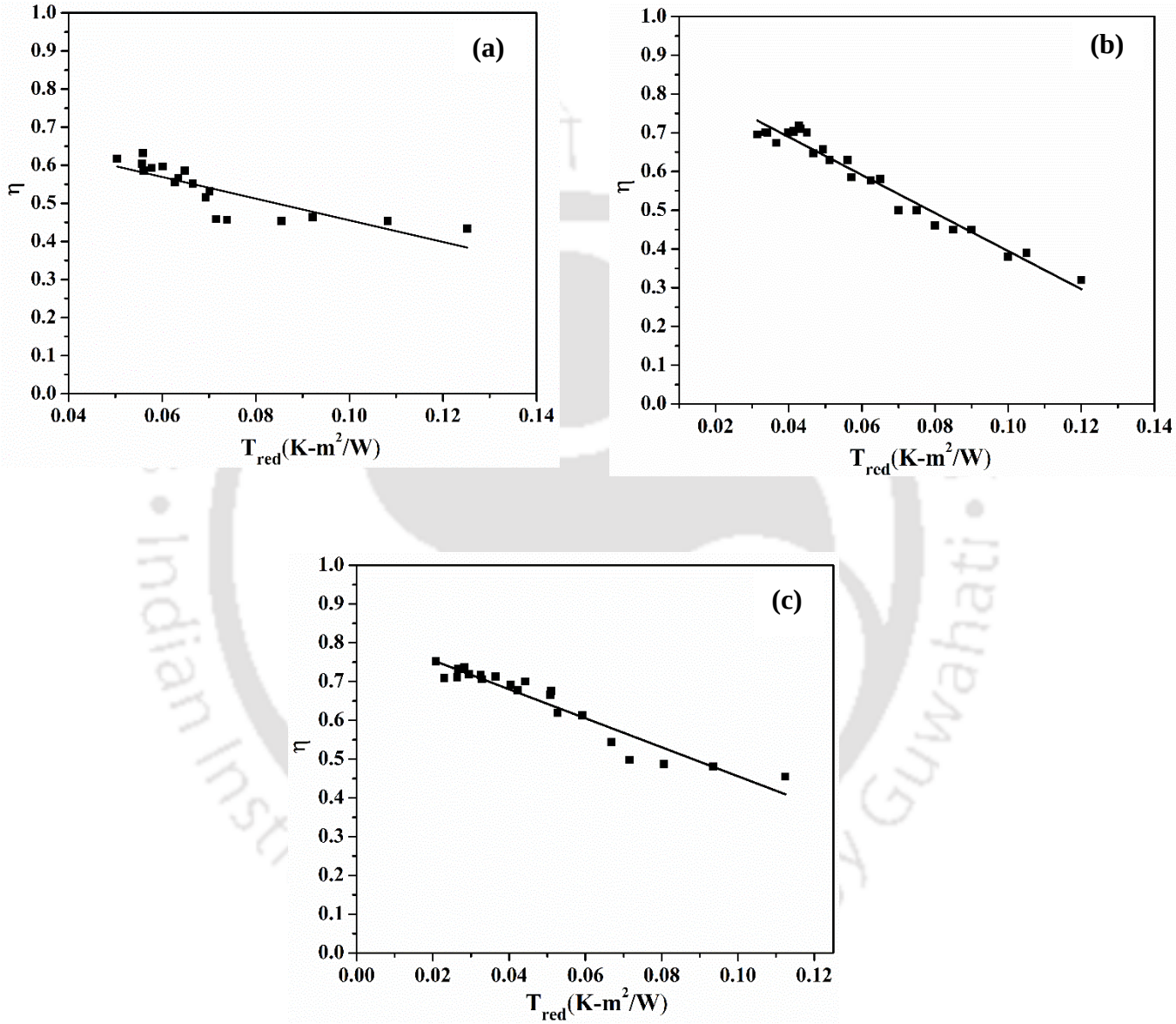

Fig. 4.4: Efficiency variation of U-tube ETCs with reduced temperature difference for different mass flow rates (a) 0.03 kg/s, (b) 0.05 kg/s and (c) 0.08 kg/s

Thus, the reduced temperature difference decreases slightly with increase in mass flow rate of working fluid. Zambolin and Col (2010) showed that the performance of the FPC is lower than that of the ETC for small reduced temperature difference values. It is found that the ETC performance is better than the FPC performance at T_{red} > 0.037 m^{2}K/W. The reduced

temperature difference varied from 0.05 to 0.1251 m^2K/W for 0.03 kg/s, 0.0208 to 0.12 m^2K/W for 0.05 kg/s, and 0.0207 to 0.112 m^2K/W for 0.08 kg/s, respectively. The heat gain (Eq. (4.5)) from the tested system was around 2.9 kW with the average system efficiency of 53%. Besides, one such unit of ETCs can annually generate heat on an average of 2.1 MWh.

$$\text{Reduced temperature difference : } T_{red}\left[m^2-K/W\right]=\left(T_f-T_a/I_T\right) \tag{4.2}$$

$$\text{Mean fluid temperature : } T_f[K]=\frac{T_i+T_o}{2} \tag{4.2a}$$

$$\text{Thermal efficiency : } \eta\,[-]=\frac{Q}{A_c I_T} \tag{4.3}$$

$$\text{Useful heat flux: } Q_u\left[W/m^2\right]=Q/A_c \tag{4.4}$$

$$\text{Heat gain: } Q\left[W\right]=\dot{m}_w C_p \Delta T \tag{4.5}$$

4.5. Overview and Development of MLP model

Artificial neural network is an effective data modelling tool, which is capable capturing and representing complex relationship between input and output variables. The most popular ANN model is the Multi-Layer Perceptron (MLP) model, which is the feed-forward network model (Cigizoglu, 2004; Eberhart, 2014; Roy et al., 2014c; Rajeev et al., 2015). MLP is a deep learning method and is capable of patterning simple and as well as complex functional behaviour. MLP consists of minimum three layers of nodes, such as an input layer, one or more hidden layers and a set of output layers. Every layer is associated with multiple nodes known as neurons. One layer of neurons is connected directly to the adjacent layer through weights. Every weight related to corresponding input becomes continuously stronger or weaker during each iteration. In each network, the input data or information are conveyed to the neurons of the hidden layer(s), where transfer functions pattern the behaviour of the information and allocate it to the neurons of the output layer by means of connecting weights (Eberhart, 2014). In order to ensure the relationship between input (inlet water temperature, solar irradiation, and mass flow rate of water) and output (outlet water temperature, useful heat gain, and thermal efficiency) variables, Pearson product moment correlation coefficient is used. The correlation between chosen input variables and desired outputs is evaluated based on the Pearson product

moment correlation coefficient value, which varies between [−1, 1]. For example, a zero correlation coefficient between 'x' and 'y' input-output pair signifies that the variation in the output 'y' is independent of any variations in the input 'x'. A positive correlation coefficient indicates direct-proportionality between 'x' and 'y'. However, a negative correlation coefficient indicates inverse-proportionality between 'x' and 'y'. The correlation values based on experimental data for the current study are presented in Table 4.4 and Fig 4.5.

Table 4.4: Pearson product-moment correlation coefficient for each desired output with chosen input variables

Output variables / *Input variables*	Q_u (useful heat flux)	η (Thermal efficiency)	T_o (Outlet water temperature)
$\dot{m}_w$ (mass flow rate)	0.1091	0.3417	-0.2825
T_1 (inlet water temperature)	0.4741	0.3714	0.9583
I_T (solar irradiation)	0.9560	0.8195	0.7101

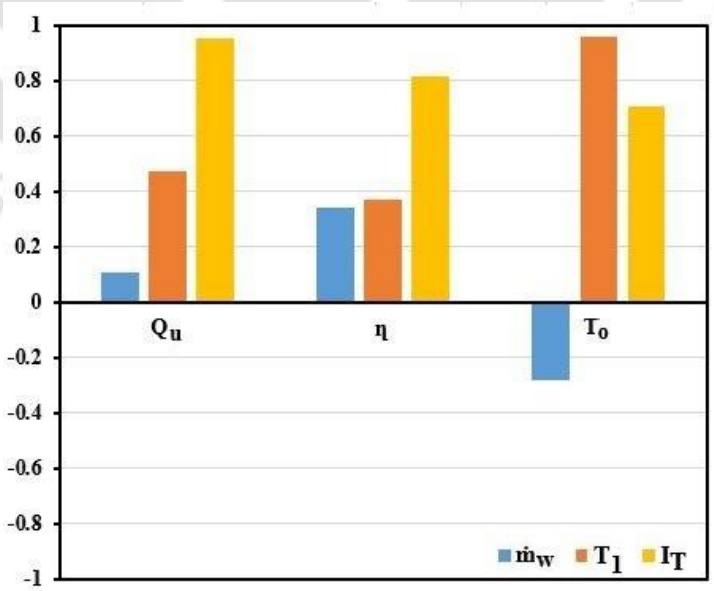

Fig. 4.5: Effect of chosen input variables on desired output variables based on their Pearson product-moment correlation coefficient

The solar irradiation, mass flow rate of working fluid (water) and inlet water temperature are selected as inputs of the network to forecast the solar collector outputs, such as useful heat gain, thermal efficiency and outlet temperature of working fluid. The MLP model is developed using the collected in-house experimental datasets. There are 99 nos. of non-repeated datasets (each dataset contains 6 data), which are used to pattern the relationship between input and output variables.

In order to avoid the saturation regions and gradient vanishing problem, the datasets are normalized to a corresponding range of 0.1–0.9, using Eq. (4.6) (Kakati et al., 2019; Menon, 1994; Yassin et al., 2016).

$$N_{\phi} = 0.1 + 0.8 \times \left(\frac{\phi - \phi_{min}}{\phi_{max} - \phi_{min}} \right) \tag{4.6}$$

where ϕ_{min} and ϕ_{max} are minimum and maximum values in the respective parameter datasets, respectively and N_{ϕ} is the normalized value of ϕ. After normalization, the datasets are divided into three kinds of samples with different proportions for training, validation, and testing, where 70% of the total datasets are randomly chosen for training so that the network is adjusted according to its error, and from the remaining, 15% datasets are assigned for cross-validation, which stands to train the network before network gets over-fitted (Roy et al., 2014a); the last 15% are chosen as a completely independent datasets to test the network. The MLP architecture is developed and the operation is done with MATLAB® 2015b.

Dikmen et al. (2014) optimized architecture for ETC with one hidden layer consisting of 12 numbers of neurons and reached up to R^2 value of 0.81. In the current study, an effort has been made to build a model for higher accuracy. However, the logistic sigmoid (logsig) activation function is used as an activation function in the output layer because it is easily differentiable, continuous and nonlinear function (Bhowmik et al., 2018; Negnevitsky, 2005b) whereas the hidden layer activation function is varied.

An increase in number of training data increases the generalization accuracy upto certain level only. However, an alternative approach is to improve the performance using regularization. In regularization, an extra term ($\frac{\lambda}{2m}\sum_{j=1}^{m} w_j^2$), which is used to minimize over-training issue (penalize the model for choosing higher values of weights (w_j)), is added to cost function (Mean Square Error (MSE)). Where m is number of training dataset. The parameter lambda (λ) is

called as regularization parameter, which is a hyperparameter that denotes the degree of regularization. Setting lambda to 0 results in no regularization, while large values of lambda correspond to higher regularization. Shi et al. (2010) investigated the impact of λ on regularization and observed that the value of $\lambda \geq 0.01$ would have less overfitting issue. Therefore, λ of 0.01 is chosen in the present investigation.

In addition, the Levenberg-Marquardt (TRAINLM) algorithm is chosen because of its better convergence (Bhowmik et al., 2017; Negnevitsky, 2005a; Rajeev, 2015; Timmerman, 2003), especially for regression finding (Hassoun, 1995; Timmerman, 2003). Further, to start the algorithm, the bias and weight values are initialized randomly before the training phase and then the training function (TRAINLM) updates bias and weight values in each iteration based on gradient descent rule (Hinton and Salakhutdinov, 2006; Ghobadian et al., 2009; Kakati et al., 2019; Mohandes et al., 1998; Paul et al., 2018). During every MLP model training, the minimum gradient of 10^{-7} and 10,000 epochs are used as stopping criteria. The predicted MLP outputs are then de-normalized by Eq. (4.7) to change the normalized results in their corresponding actual scale, which allows to make a comparative analysis of MLP prediction results with the respective experimental output.

$$D_{\phi} = \frac{(y-0.1)\times(\phi_{max}-\phi_{min})}{0.8} + \phi_{min} \tag{4.7}$$

where D_ϕ is the de-normalized data in actual scale, y is the normalized value corresponding to ϕ, ϕ_{max} and ϕ_{min} are the maximum and minimum values of ϕ. Fig. 4.6 depicts the steps involved in developing a trained MLP model for prediction of performance parameters of evacuated U-tube collectors.

4.6. Results and Validation of MLP model

Table 4.5 shows different configurations of MLP model with MSE value. The regression coefficient (R) for testing, training and validation and the MSE value are calculated at the end of each configuration run. It can be observed that the configuration with logarithmic sigmoid (layer-1) and hyperbolic tangent sigmoid (layer-2) transfer function with ten neurons in each hidden layer exhibits minimum MSE value as compared to all other algorithms. Accordingly, (3-10-10-3) topology is chosen as the best forecasting architecture to pattern the relationship

between input-output variables. The optimum configuration and optimal settings of MLP model are depicted in Fig. 4.7 and Table 4.6.

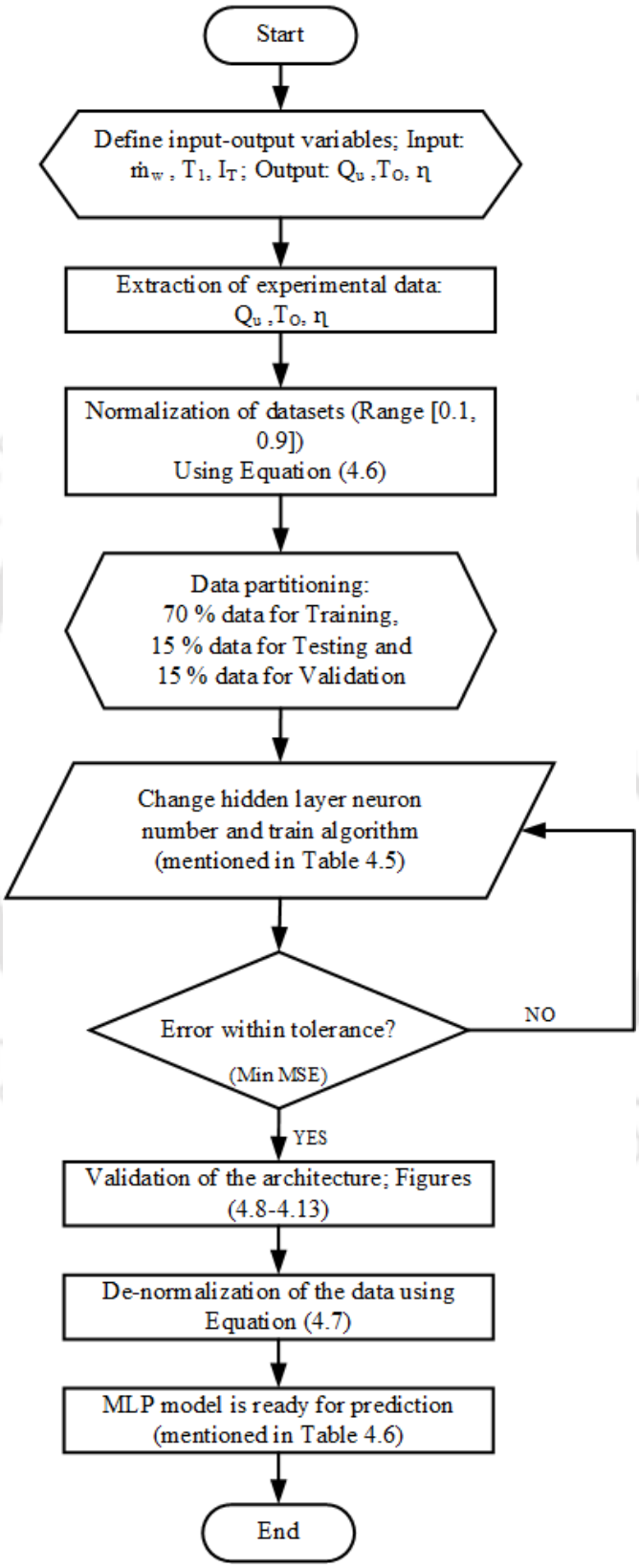

Fig. 4.6: Flowchart of the proposed MLP algorithm

The overall R-value of the minimum MSE - MLP network is depicted in Fig. 4.8. Subsequently, the selected model outcomes are validated with experimental results.

Table 4.5: Results for various numbers of neurons in two hidden layers

Trial no	Number of neurons	Transfer function (layer1-layer 2)	Regression co-efficient (R)				MSE
			Training	Validation	Testing	Overall	
1	5	logsig-logsig	0.91672	0.96900	0.95342	0.91681	0.015876
2	5	logsig-tansig	0.97289	0.98343	0.95540	0.97128	0.003789
3	5	logsig-purelin	0.99112	0.98275	0.98568	0.98960	0.001996
4	5	purelin-tansig	0.97191	0.96491	0.97460	0.97460	0.003943
5	5	purelin-logsig	0.89581	0.87420	0.89525	0.88895	0.016322
6	5	purelin-purelin	0.97864	0.97016	0.92497	0.97340	0.004058
7	5	tansig-tansig	0.98988	0.99345	0.95103	0.98861	0.001700
8	5	tansig-logsig	0.91888	0.89343	0.81993	0.90091	0.016214
9	5	tansig-purelin	0.98939	0.94323	0.99021	0.98444	0.001052
10	10	logsig-logsig	0.92970	0.87389	0.92479	0.91668	0.016000
11	**10**	**logsig-tansig**	**0.99594**	**0.99281**	**0.99249**	**0.99480**	**0.000926**
12	10	logsig-purelin	0.99308	0.99176	0.98777	0.99206	0.001457
13	10	purelin-tansig	0.97288	0.96905	0.96933	0.97100	0.004026
14	10	purelin-logsig	0.88972	0.90615	0.85668	0.88706	0.016333
15	10	purelin-purelin	0.97764	0.96185	0.95253	0.97315	0.004080
16	10	tansig-tansig	0.99448	0.99294	0.98557	0.99225	0.001397
17	10	tansig-logsig	0.90548	0.91612	0.90730	0.90485	0.016088
18	10	tansig-purelin	0.99317	0.98804	0.98851	0.99214	0.001399
19	10	logsig-tansig	0.99656	0.99105	0.94764	0.99063	0.001167
20	15	logsig-purelin	0.99268	0.99054	0.97998	0.98994	0.001150
21	15	logsig-logsig	0.91429	0.92253	0.92746	0.91531	0.016106
22	15	purelin-tansig	0.97432	0.94843	0.97631	0.97074	0.004191
23	15	purelin-logsig	0.89313	0.83869	0.90299	0.88771	0.011769
24	15	purelin-purelin	0.97619	0.94714	0.97057	0.97299	0.004135
25	15	tansig-tansig	0.99651	0.98720	0.99527	0.99509	0.001749
26	15	tansig- logsig	0.91426	0.93414	0.92972	0.91972	0.015879
27	15	tansig- purelin	0.99635	0.98368	0.96188	0.99147	0.001473

Bold indicates the optimal value

Figs. 4.9–4.11 show the comparison between MLP predicted outputs and actual collector experiment datasets for the outlet temperature of the working fluid, useful heat gain, and thermal efficiency. The reliability and robustness of the developed MLP model are calculated using MAPE (Mean Absolute Percentage Error), R, MSE, KGE (Kling-Gupta Efficiency),

MSRE (Mean Square Relative Error), NSE (Nash-Sutcliffee coefficient of Efficiency), and Theil U2 (Theil Uncertainty). A detailed description of the performance parameters of the MLP model is presented in Appendix A.

Table 4.6: Details of the network parameters developed in the present study

Network parameters	**Value**
Architecture	3-inputs, 3-outputs, and 2-hidden layers
Data partition	Training subset: 70% randomly selected experimental datasets
	Validation subset: 15% randomly selected experimental datasets
	Test subset: 15% randomly selected experimental datasets
Training algorithm	Levenberg–Marquardt
Stopping criteria	Stop the network training when the validation error starts increasing (minimum gradient: 10^{-7} and 10,000 epochs)

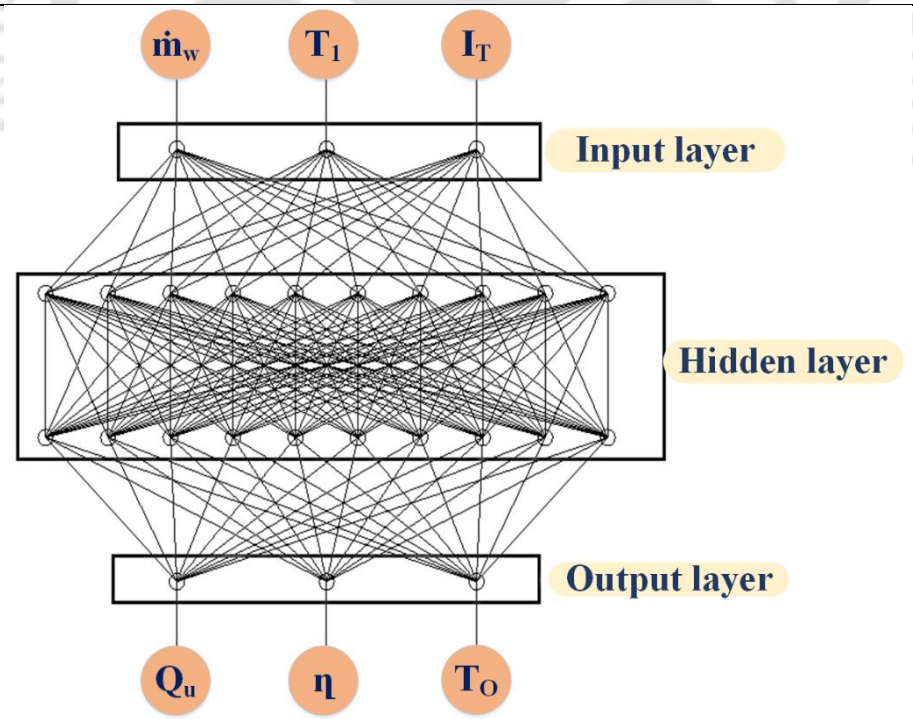

Fig. 4.7: Schematic of (3-10-10-3) MLP architecture: Two hidden layers with ten neurons each

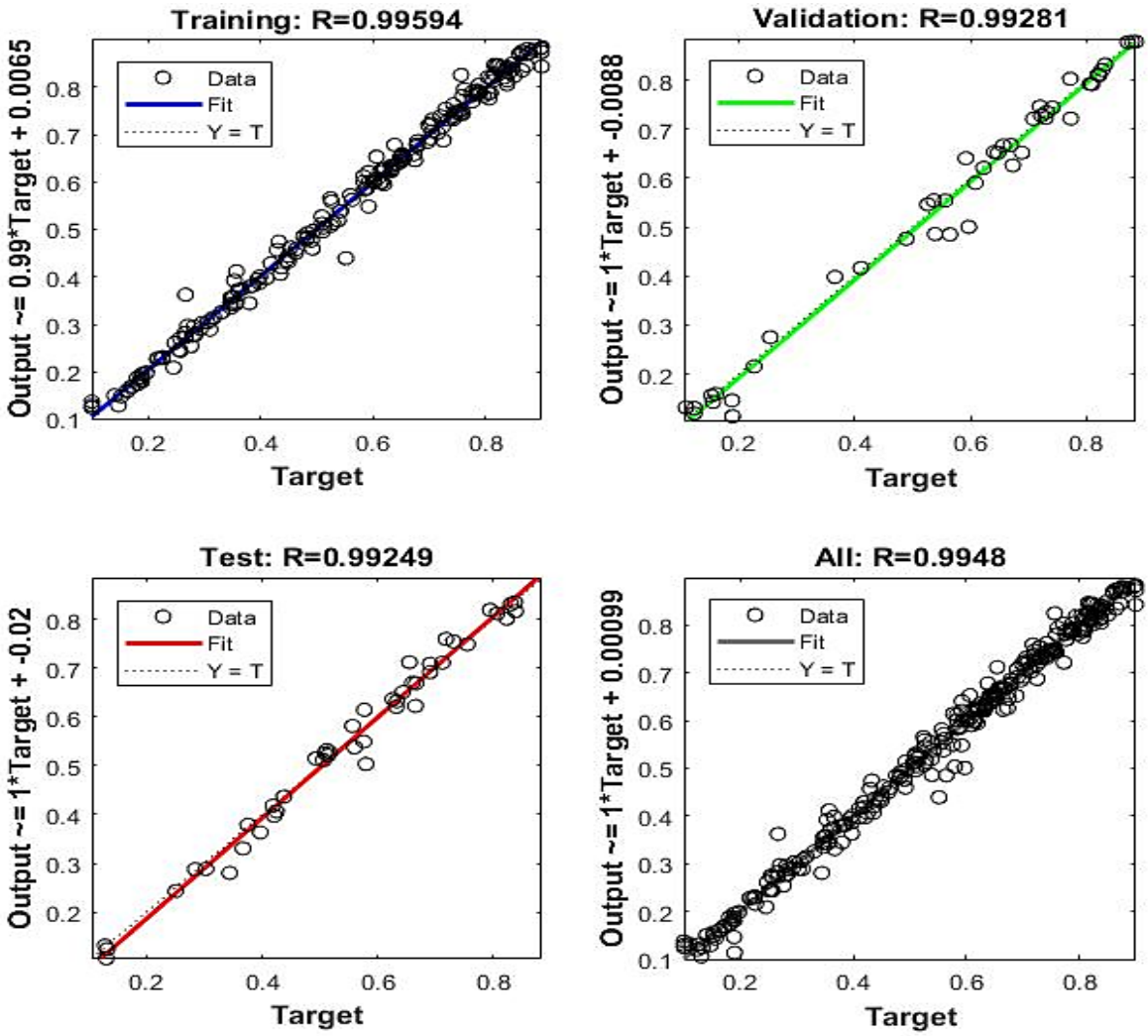

Fig. 4.8: Overall regression coefficient of developed model architecture

Fig. 4.9a-4.9b shows the variation of actual experimental useful heat gain (Q_u) against MLP predicted Q_u; MLP predicted Q_u closely agrees with the experimental one. The close agreement can be observed more explicitly from the correlation metrics value (Fig. 4.10) between MLP predicted and experimental results, such as 0.9966 for R, 0.9933 for R^2, 0.9877 for KGE and 0.9934 for NSE; these values lie within an acceptable range. As shown in Fig. 4.11, MLP model gives a very low MSRE of 0.00082, low MSE of 0.000926, MAPE of 3.4% (0.034), and Theil U2 of 0.03106 for predicting Q_u (Table 4.7).

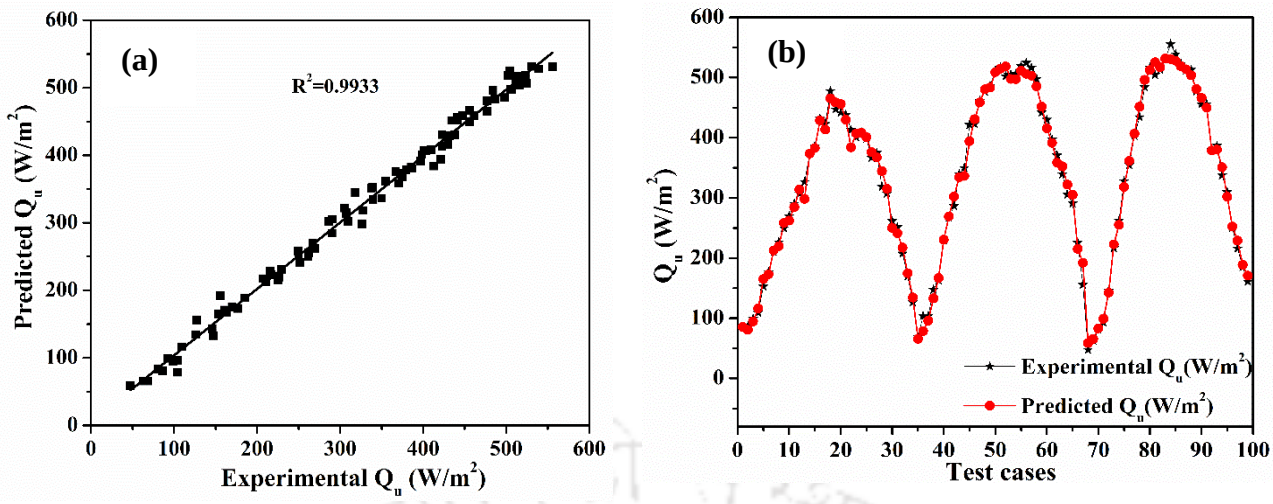

Fig. 4.9: Comparison of MLP model predicted Q_u (W/m^2) with measured Q_u (W/m^2)

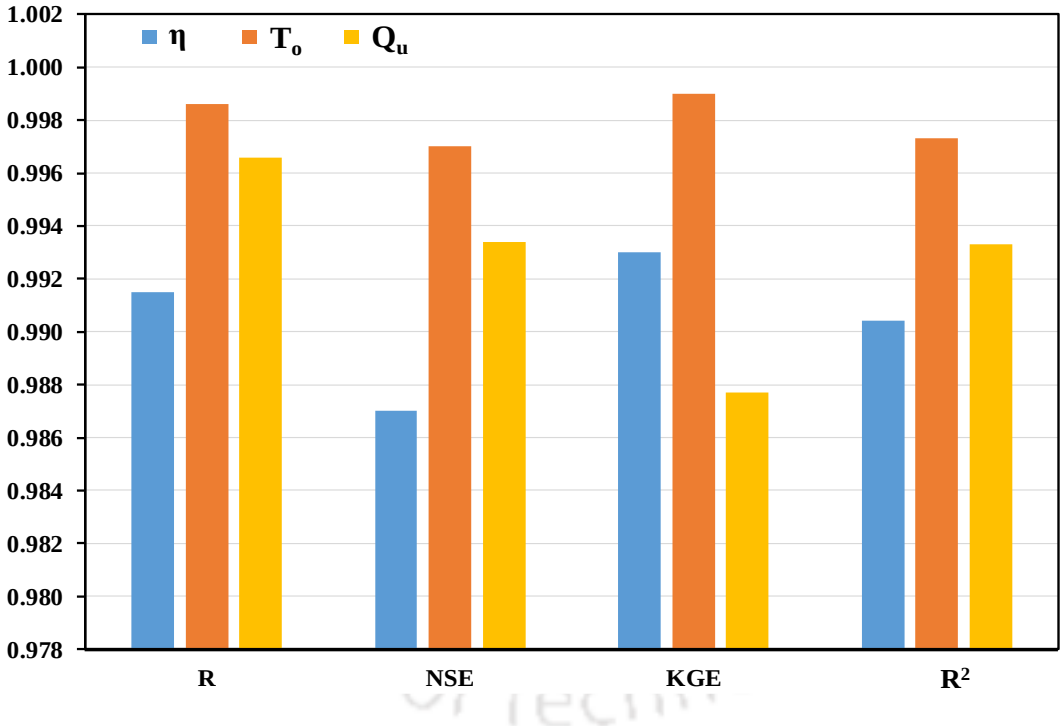

Fig. 4.10: Comparison between model correlation coefficient metrics

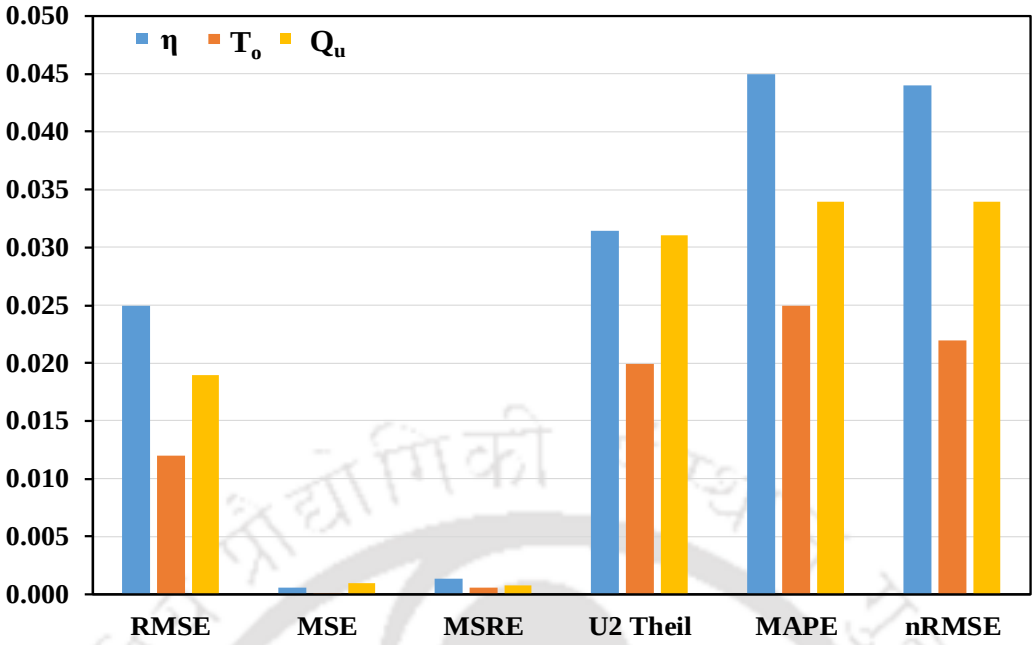

Fig. 4.11: Comparison between model error metrics

Table 4.7: Comparison between model error metrics

	Thermal Efficiency (η)	**Outlet water temperature (T_o)**	**Useful heat gain (Q_u)**
RMSE	0.025000	0.012000	0.030400
MSE	0.000611	0.000147	0.000926
MSRE	0.001373	0.000625	0.000820
U2 Theil	0.031390	0.019916	0.031068
MAPE	0.045000	0.025000	0.034000
nRMSE	0.044000	0.022000	0.034000

The difference between MLP model predicted thermal efficiency (η) and measured η are shown in Fig. 4.12a and 4.12b, respectively. As illustrated in Fig. 4.12, a good agreement between the predicted and experimental η is observed. A very high degree of correlation metrics value exists between MLP model and experimentally predicted η. The calculated values of KGE, R,

R^2, and NSE are 0.9931, 0.9915, 0.9904 and 0.9871, respectively, which converse the best conceivable stage of forecast capability of MLP model for η under collector paradigms (Fig. 4.10). In error metrics comparison, the MSE, MAPE, MSRE, and Theil U2 values do not exceed the upper tolerance limit of 5%. It is noted from Fig. 4.11 that the MAPE value for η is slightly higher than other parameters. This may indicate that the correlation achieved for η is inferior to other parameters; whereas the difference is lower than 5%, i.e., within the acceptable range (Table 4.8).

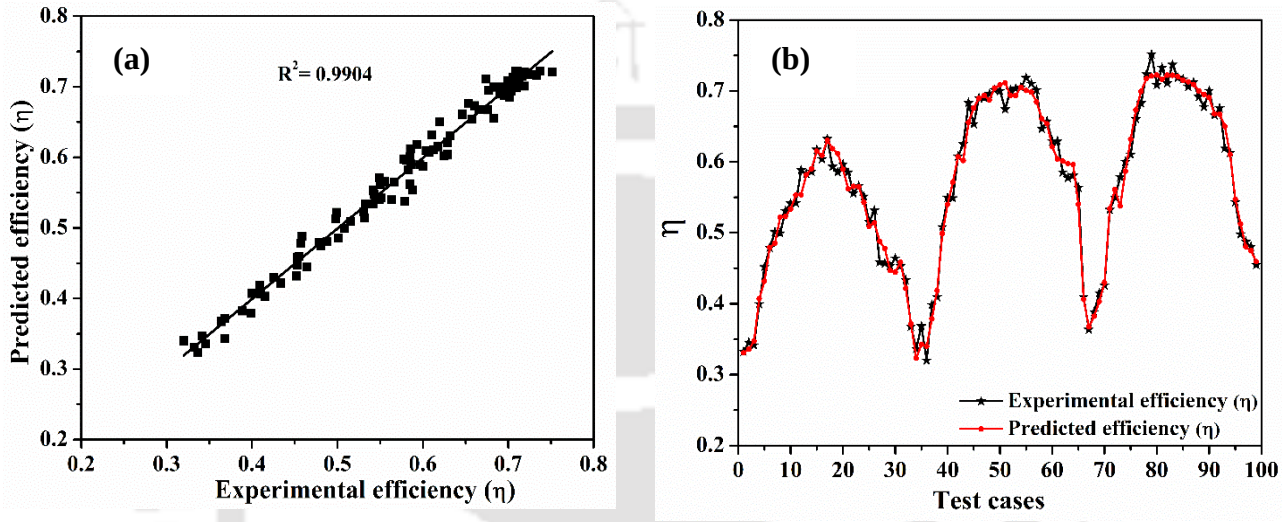

Fig. 4.12: Comparison of MLP model predicted efficiency (η) with measured efficiency (η)

Fig. 4.13a-4.13b demonstrates the comparative assessments between experimental T_O (°C) and MLP model predicted T_O (°C). Likewise, Fig. 4 shows the correlation metrics of 0.9991 for KGE, 0.9986 for R, 0.9973 for R^2 and 0.9972 for NSE; this indicates that the proposed MLP model has a robust predicting capability for real-time collector operation. Further, the different error dimensions such as Theil U2 (0.01991), MSE (0.0.00147), and MSRE (0.00062) are also within acceptable ranges for T_O (°C) (Fig. 4.11).

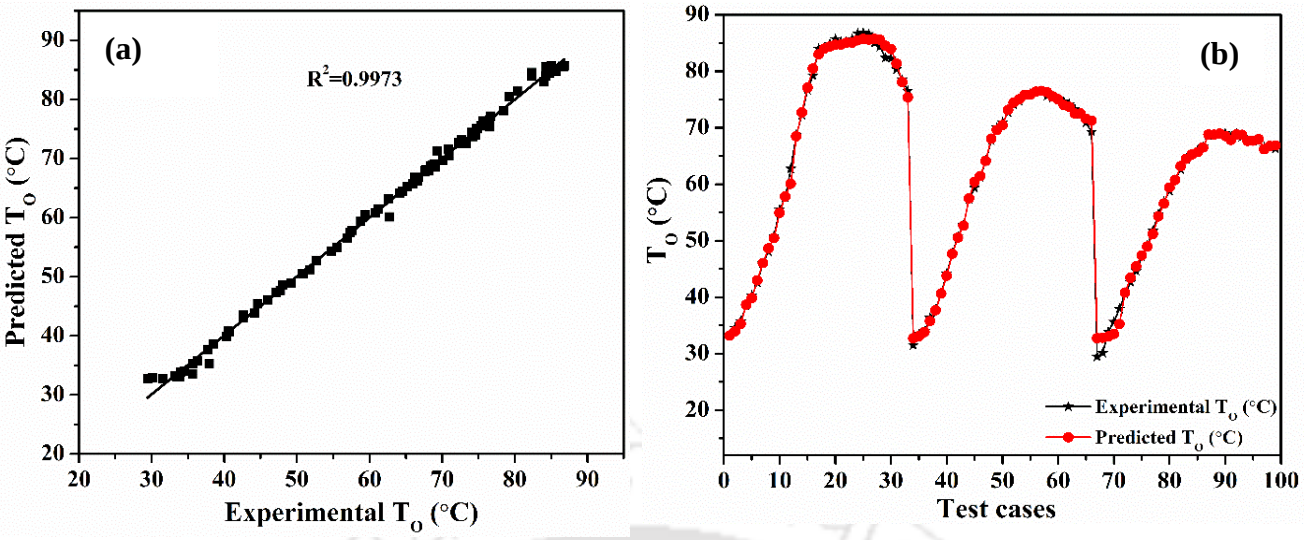

Fig. 4.13: Comparison of MLP model predicted T_O (°C) with measured T_O (°C)

4.7. Comparison of MLP with classical regression models

In order to estimate ETC performance parameters such as η, T_o and Q_u, in terms of $\dot{m}_w$, I_T, and T_1, the classical regression models are also generated. Model-I (Eqs. 4.8-4.10) and Model-II (Eqs. 4.11-4.13) are linear and non-linear regression model, respectively with the persistence of all input variables. Performance of all models (Model-1, Model-II and MLP) are compared based on three criteria nRMSE (Normalized Root Mean Square Error), R and R^2 for the same datasets. It is found that the non-linear relationship between input and output variables are more suitable compared to linear relationship between input and output variables and non-linear relationship can predict the output parameters more closely to the experimental one (Table 4.8). Comparison of the results shows that Model-I is the worst among all studied models. However, Model-II can predict the results more closely compared to Model-I, whereas in comparison with MLP, Model-II is not conducive. Table 4.8 also demonstrates that the best model to estimate all ETC performance parameters is the MLP model. Further, compared to classical regression models, R and R^2 values are higher and nRMSE value is lower for MLP model. Therefore, compared to Model-I and Model-II, MLP neural network is more suitable to estimate ETC performance parameters.

Linear Model (Model-I):

$$\eta = 0.1295 - 0.000964\ T_1 + 0.000648\ I_T + 1.438\ \dot{m}_w \quad (4.8)$$

$$Q_u = 78.8 - 0.001923\ T_1 + 0.04808\ I_T + 279\ \dot{m}_w \quad (4.9)$$

$$T_o = 19.124 + 1.00094\ T_1 + 0.020326\ I_T - 590.22\ \dot{m}_w \quad (4.10)$$

Non-linear Model (Model-II):

$$\eta = 0.145 + 1.4\dot{m}_w + 0.0056 I_T + 0.00108 I_T \dot{m}_w - 0.018 \sin\left(T_1\right)^2 - 0.025 \cos\left(T_1 \dot{m}_w\right) \quad (4.11)$$

$$Q_u = 6.64 I_T \dot{m}_w - 115 + \frac{0.0149 I_T}{\dot{m}_w} - 0.75715 \cos\left(T_1 \dot{m}_w\right) \quad (4.12)$$

$$T_o = 1.19 + 1.11 \cdot T_1 + \frac{-0.00158}{T_1 \cdot I_T \dot{m}_w} - 452.3\dot{m}_w - 163\dot{m}_w^2 \quad (4.13)$$

Table 4.8: Comparison between classical regression models with MLP

Parameters	Model (s)	Corr. Coff (R)	R^2	nRMSE
Efficiency (η)	Model-I	0.915	0.837	0.386
	Model-II	0.937	0.878	0.089
	MLP	0.991	0.990	0.044
Useful heat gain (Q_u)	Model-I	0.883	0.780	0.722
	Model-II	0.934	0.873	0.251
	MLP	0.966	0.993	0.034
Outlet water temperature (T_o)	Model-I	0.896	0.804	0.209
	Model-II	0.914	0.836	0.119
	MLP	0.998	0.997	0.022

In order to evaluate MLP model, k-fold cross-validation methodology is used. It may be noted that there is no general standard for choosing the number of fold, k (Wong et al., 2013). Kohavi (Kohavi, 1995) tested different number of folds (e.g., 2, 5, 10 and 20) and proved that this number may be selected randomly. Accordingly, five-fold cross-validation is employed in the present study. Any four out of five groups were then used to train the model, while the remaining one group was used to test the datasets. This process is repeated for five times, with

each group being used exactly once as the test datasets. In each of the five folds, the model MSE is calculated and the averaged MSE is found to be less than 0.00097. Hence, the MLP model can perform well and closely predict the ETC performance parameters.

4.8. Trade-off study between experimental and MLP model results

The real experimentally perceived T_O- η-Q_u trade-off domain is shown in Fig 4.14 and compared with T_O- η-Q_u trade-off domain obtained from MLP model (Fig. 4.14) for validating the robustness of developed MLP model. The experimental T_O-η-Q_u trade-off for the whole domain of collector operation under different mass flow rates is categorized as X-Y-Z regions (Fig. 4.14). In Fig. 4.14, Z region specifies the highest trade-off area for high useful heat gain. It is also seen from Fig. 4.14 that the higher useful heat gain appreciably enhances the efficiency for all operating conditions.

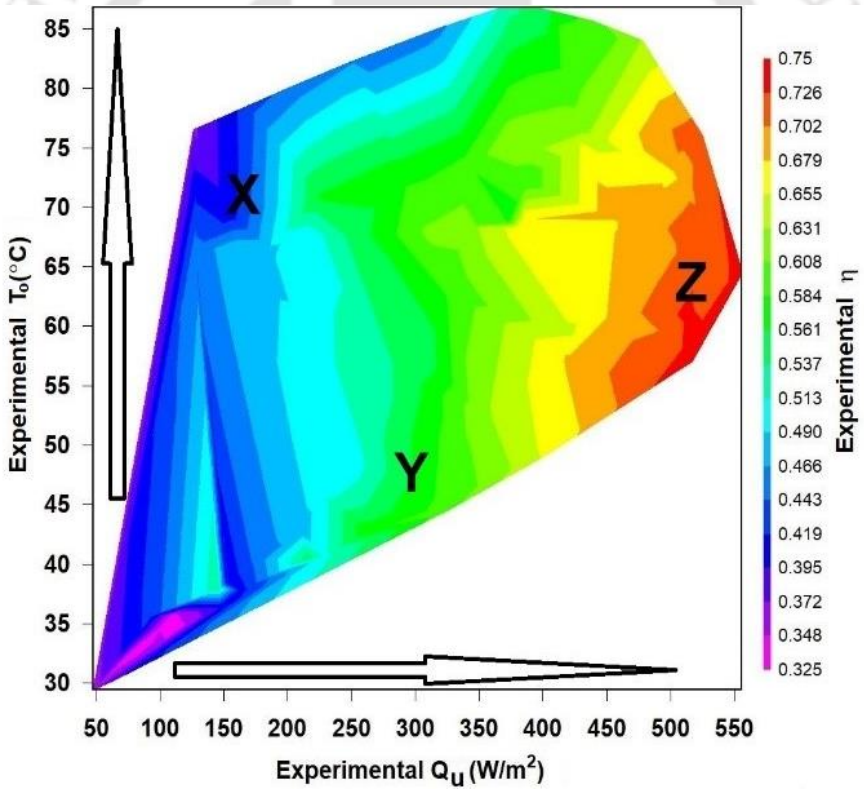

Fig. 4.14: Experimental Q_u-T_O-η trade-off

Further, it can be noticed that the outlet working fluid temperature also becomes higher at high useful heat gain. Fig. 4.14 also demonstrates the influence of useful heat gain on η and T_O for all mass flow rates of the working fluid over the entire range of experimental data. Fig. 4.15 indicates the effectiveness of proposed MLP model as a precise and inherent-robust model. It is noted that T_O- η-Q_u trade-off analysis based on developed AI-based MLP model can semi-

quantitively reproduce the experimental T_O-η-Q_u regions X, Y and Z (Fig. 4.15). This clearly shows that the developed MLP model is an effective and robust model to predict the real-time collector operation.

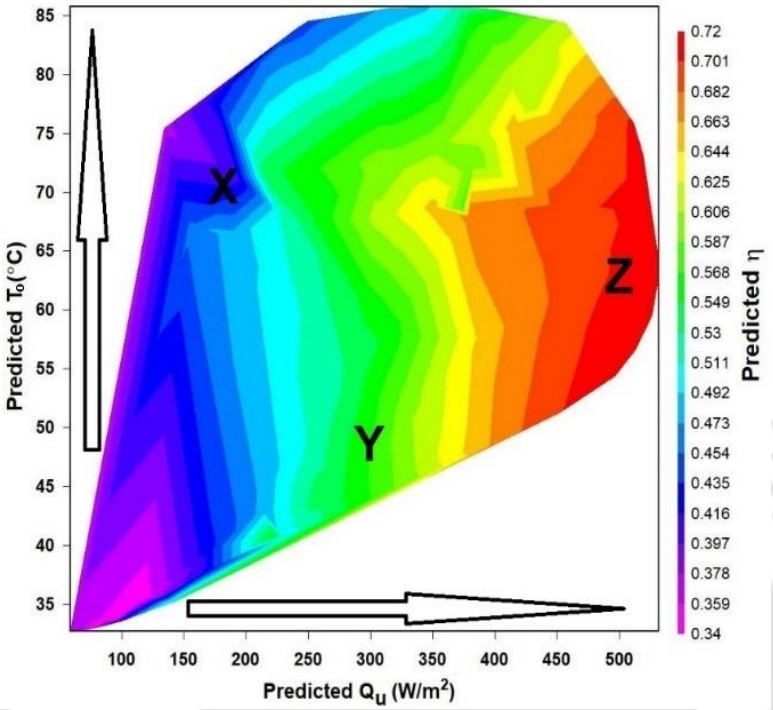

Fig. 4.15: MLP predicted Q_u-T_O-η trade-off

4.9. Closure

The utilisation of solar thermal energy for various medium-temperature heating applications can save a significant amount of electricity. Therefore, solar ETCs should be designed for higher efficiency over a yearly operation period. Respective experimental investigations have been carried out in an aluminium finned U-tube ETC using water as a working fluid. An AI-based MLP model has been developed and trained with the experimental datasets for predicting the performance of U-tube ETC. Important results obtained from experimental and AI-based investigations are summarized below:

- The peak thermal efficiency (around 70%) of the U- tube evacuated solar collector system during a sunny day was observed between 11: 00 AM – 1: 00 PM, whereas low energy efficiency (about 30%) was observed around 8:00 AM and 4: 00 PM.

- The maximum outlet temperature obtained from the collector was 86.7 ºC, 76.5 ºC, and 69.0 ºC for mass flow rates of 0.03, 0.05 and 0.08 kg/s, respectively.

- The maximum thermal efficiency of the entire system was found to be 63%, 72% and 75% for mass flow rates of 0.03, 0.05 and 0.08 kg/s, respectively.
- The maximum thermal efficiency was obtained at lower reduced temperature differences with higher mass flow rates. It was found that the reduced temperature was greater than 0.03 Km^2/W for all mass flow rates.
- The average daily useful heat gain from the system was around 2.9 kW with average efficiency of 53%. Besides, one such unit of ETCs can annually generate heat on an average of 2.1 MWh.
- MLP architecture with three neurons in input layer, two hidden layers with ten neurons in each layer and three neurons in the output layer (3-10-10-3) is found to be optimal architecture for mapping the performance-outlet temperature characteristics under different mass flow rates.
- The correlation metrics on the basis of R, NSE, KGE and R^2 shows that the MLP model predicted outputs well accurately with the experimental outputs.
- The error metrics on the basis of RMSE, MSE, MSRE, Theil U2, and MAPE confirms the effectiveness and robustness of MLP predictions.
- The MLP investigation is further supported by exploring the effectiveness of the models using T_O-η-Q_u trade-off characteristics in contrast to the actual observed trade-off zones, and that proves the efficiency of the developed neural network model to predict the real-time collector operations.

The developed MLP approach relates the input parameters (mass flow rate of water, solar irradiation, inlet water temperature effectively with output parameters (useful heat gain, outlet water temperature, thermal efficiency), which characterise the thermal performance of evacuated solar collectors. The MLP approach reliably replicates measured outputs/performance parameters for ETC.

CHAPTER 5

Experimental and numerical studies on liquid desiccant dehumidifier-regenerator system

5.1. Introduction

Liquid desiccant dehumidification is a promising energy-extensive process for air dehumidification, which can easily be driven by any waste or renewable heat sources. In the current chapter, a hybrid method is proposed by combining the solar evacuated tube collectors as a regeneration source to drive liquid desiccant system in a close-loop. Subsequently, an experimental setup has been fabricated to assess the performance of the overall system using a novel desiccant mixture. The overall energy balance between the ambient air and the liquid desiccant was also studied. Effects of independent parameters such as solution to airflow rate, solution concentration and temperature on the dehumidifier-regenerator performance parameters such as latent heat ratio, condensation rate, desiccant mass fraction index, evaporation rate and latent and enthalpy effectiveness were analysed. The airside pressure drop in the dehumidifier/regenerator was also estimated at different flow rates of desiccant. Further, the distribution profile of thermodynamically influencing parameters are visualized.

5.2. Experimental protocol

5.2.1. System description

The dehumidifier and regenerator are the major two components of desiccant dehumidification system, in which the heat and mass transfer phenomena occur between the moist air and the liquid desiccant solution. The geometry of dehumidifier and regenerator are completely identical, and they are insulated using two layers of nitrile foam (Make: A-Flex) rubber (each layer thickness of 6 mm). Dehumidifier and regenerator chambers (where the air and the liquid desiccant interact through the equivalent diameter of packing channel) are filled with acrylonitrile butadiene styrene (ABS) sheets (600 mm × 300 mm × 150 mm), having corrugation angle of 45° and specific surface area of 256 m^2/m^3. The equivalent diameter of flow channels is 10 ± 0.5 mm and made in a well-structured packing to confirm good contact between the desiccant solution and the air. A detailed representation of the entire system is depicted in Figs. 5.1-5.3. The specifications of experimental test rig are presented in Table. 5.1.

The chambers are made of stainless-steel material (having thickness of 3 mm) and painted with an anti-corrosive coating to prolong the lifetime of the chambers by preventing corrosion. The simplified view of the liquid desiccant system is shown in Fig. 5.2. The design guidelines given in (Elsarrag et al., 2005) are followed to determine the packing chamber dimensions. In the current study, the experiments are carried out to dehumidify the air for a cooling capacity of 1 TR. Accordingly, the mass flow rate of air is estimated as 400 CFM. Based on that, the spectrum of solution and airflow rates are estimated.

Table 5.1: Technical specifications of the dehumidifier

Parameter	**Specifications**
Dehumidifier material	Stainless steel (304 grade)
Dehumidifier dimensions (m)	0.6×0.6×0.75
Packing material	ABS (Acrylonitrile Butadiene Styrene)
Packing dimensions (m)	0.6×0.3×0.15 (10 nos.)
Dehumidifier connection pipes	1-inch diameter
Flute height (m)	0.01
Flow pattern	Counter-flow
Specific surface area of the packing (m^2/m^3)	256
Centrifugal Blower	2 Nos. (0.375 kW)
Solution Pump	2 Nos. (0.375 kW)
Water pump	2 Nos. (0.375 kW)

5.2.2. Methodology

Three different fluids (desiccant solution, moist air and process water) are used in the liquid desiccant system. The desiccant solution is pumped by an anti-corrosive pump to shower the liquid desiccant over structured packing. Three equally spaced half-inch pipes with 4 mm pore size are used to spry the desiccant solution evenly. The air blower forces the air into the chambers from the bottom (upwards) through the inlet duct (25 cm × 30 cm) and desiccant flows in the downward direction. The counter-flow configuration is chosen because of its better dehumidification performance compared to the cross-flow type (Cho et al., 2019). Fig. 5.1

elaborates the elementary transport processes of air and desiccant when flowing through the dehumidifier and the regenerator.

When the moist air is passing over the desiccant, desiccant absorbs the moisture from the surrounding air. As a result, the concentration of desiccant gets decreased (i.e., process 1–2 in Fig. 5.1). The pictorial view of liquid desiccant dehumidification/regeneration system is shown in Fig. 5.3a. Due to absorption of moisture from the air, the temperature of air might increase/decrease, based on the condition of desiccant, whereas the air specific humidity decreases (i.e., process a1–a2), which results in the dehumidification of air. Subsequently, the diluted solution from the dehumidifier is pumped to a heat exchanger I (HX I) to raise its temperature (i.e., process 2–3). The temperature of desiccant is increased sufficiently with the purpose of releasing the absorbed moisture into the flowing air in the regenerator (i.e., process 3–4). The pictorial view of packed bed chamber is shown in Fig. 5.3b. In this proposed system, a solar collector system, which consists of three-manifolds of evacuated tube collectors (ETCs), a thermal storage tank and an auxiliary electric heater (AEH), is used to offer the required heat for thermal regeneration. The AEH is used only when solar irradiance is not sufficient to provide enough heat. Heat exchanger I (HX I) is used to avoid the direct fluid interaction between the diluted solution and the working fluid (water) in the collector and that, however, rises the diluted solution temperature before sending to the regeneration process. With the help of flow control valves, the flow rate is regulated, and water is pumped to the heat exchanger I (HX I) followed by the solar evacuated tube collector (process 6-9).

The solar part consists of U-tube based ETCs. Three major components: 3-manifolds (M1, M2, and M3), pump and water tank are associated with the solar evacuated tube collector system. Each manifold is fabricated with dimensions of 1200 mm × 1900 mm and comprises of ten borosilicate ETCs with a spacing of 120 mm between the tubes. ETCs are concentric, and vacuum is created by pumping out the air from the annular space between the concentric dual tubes, and then the two tubes are fused on top. An aluminum fin is mechanically fitted between the ETC and the U-tube, as shown in Fig. 5.1. The embedded copper U-tubes are connected to header (cold/hot) tubes. The purpose of header is to carry the cold and hot water; two limbs of the U-tube are connected to two header tubes. The hot header tube of M1 is connected to cold header tube of the second manifold and so on. The pictorial view of solar evacuated tube collector system is shown in Fig. 5.3c. The header tubes are appropriately insulated with two layers of glass wool having a thickness of 20 mm. The heat trapped by ETCs is absorbed U-tubes and then, it is transmitted to the working fluid, which is pumped towards the hot header

tube of the manifolds, eventually reaches the water tank. Finally, the tank water gets heated up as the outlet water of the ETCs exchanges its heat with the water in the water tank. Details of technical specifications are shown in Table 4.1.

Owing to the desorption process, the air humidity ratio and air temperature might increase (i.e., process a3–a4), leading to humidified air. Subsequently, the solution becomes strong and the strong solution from the regenerator then passes to a water-cooling coil (circular copper coil of 5 turns and of 1-inch mean diameter) to cool the desiccant solution (i.e., process 4–5). The shell and tube heat exchanger II (HX II) is further used to cool the strong desiccant solution temperature through water as a cooling medium (i.e., process 5–1). Further to maintain the desired desiccant temperature independently and steady, the heat exchanger (HX II) is introduced. Besides, the desired mass fraction of desiccant solution was prepared and stored in the dehumidifier/regenerator of the liquid desiccant system.

5.2.3. Instrumentation

Once the conditions of airstream and desiccant solution met the desired status level and got stabilized, the DAQ system is switched on. Every run of the experiment could last for 15 min with stable inlet conditions. In the present experiments, the readings were scanned and recorded in every 5 s. The desiccant properties were measured and recorded while the outlet desiccant solution was collected to test its temperature and density, which were later used for estimating the concentrations of the solution (detailed in section 3.5.1.6). The experiments were conducted in humid climate conditions at the Indian Institute of Technology Guwahati, India (latitude 26.18 °N, longitude 91.69 °E). The inlet and outlet humidity ratio and air temperature were measured with a humidity sensor (± 2% RH) and calibrated T-type thermocouple (± 0.1°C), respectively. The air velocity was measured using a Testo 425 hot-wire anemometer (± 0.1 m/s). The liquid flow rate was measured with a water meter and chronograph. All the sensors were interfaced to a computer using DAQ Factory® based Agilent® (Agilent 13970A) empowered with 50 Hz sampling frequency data acquisition platform synchronized onto a GUI based Data Analysis® post-processing software. Further, the technical specifications of measuring instruments are mentioned in Table 5.2.

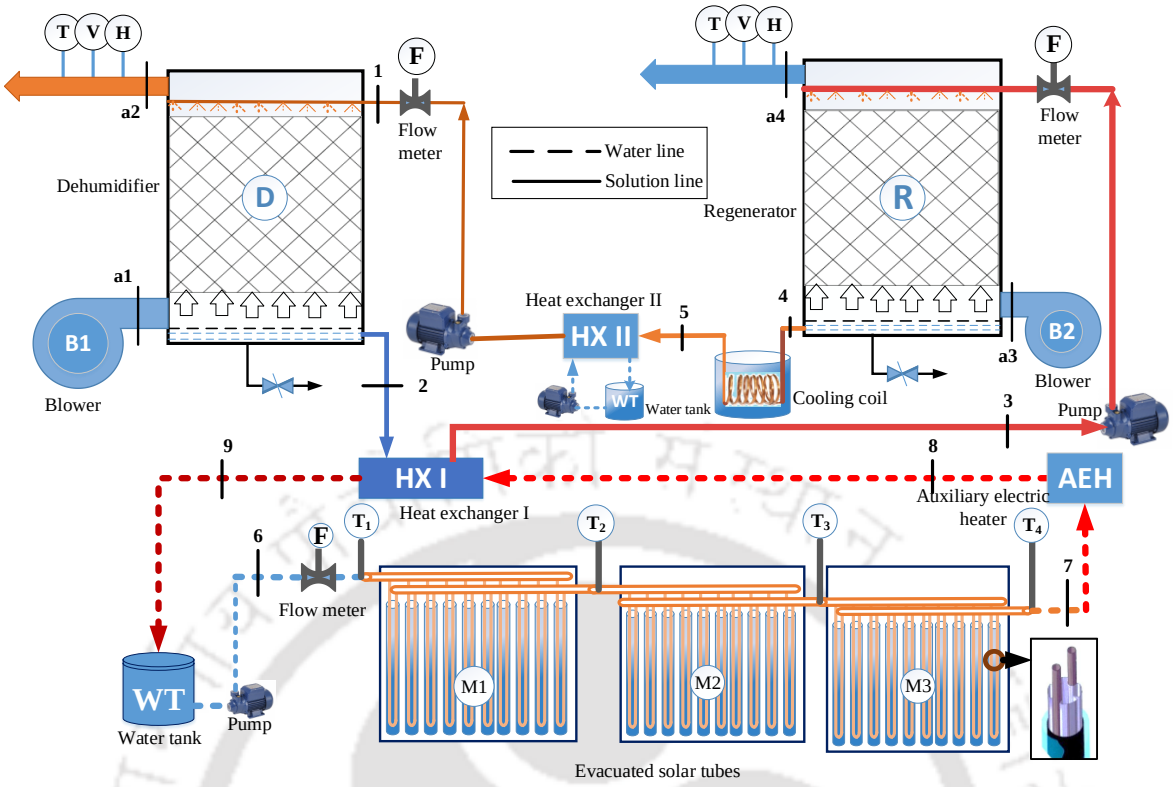

Fig. 5.1: Schematic view of solar-assisted liquid desiccant dehumidification system (T: Temperature sensor; V: Velocity sensor; H: Humidity sensor; F: Flowmeter; HX: Heat exchanger; D: Dehumidifier; B1 and B2: Blower; M1, M2 and M3: Manifolds; R: Regenerator; WT: Water tank; AEH: Axillary electric heater)

Table 5.2: Technical specifications of measuring instruments

Parameter	**Device**	**Type**	**Accuracy**	**Range**
Air flow rate	Anemometer	Testo 490	± 0.1 m/s	0 to 25 m/ s
Air/Solution temperature	Temperature sensor	T-type thermocouple	± 0.1°C	20 to 100°C
Air humidity ratio	Humidity sensor	EQ310CTH	± 2% RH	0 to 100 % RH
Solution flow rate	Flow meter	CM/L-0151526	± 2% l/h	50 l/h to 1500 l/h
Density	Hydrometer	Anton-paar 4500M	± 0.005 kg/m^3	0 g/cm^3 to 3 g/cm^3 (Temperature: 0°C to 100°C)

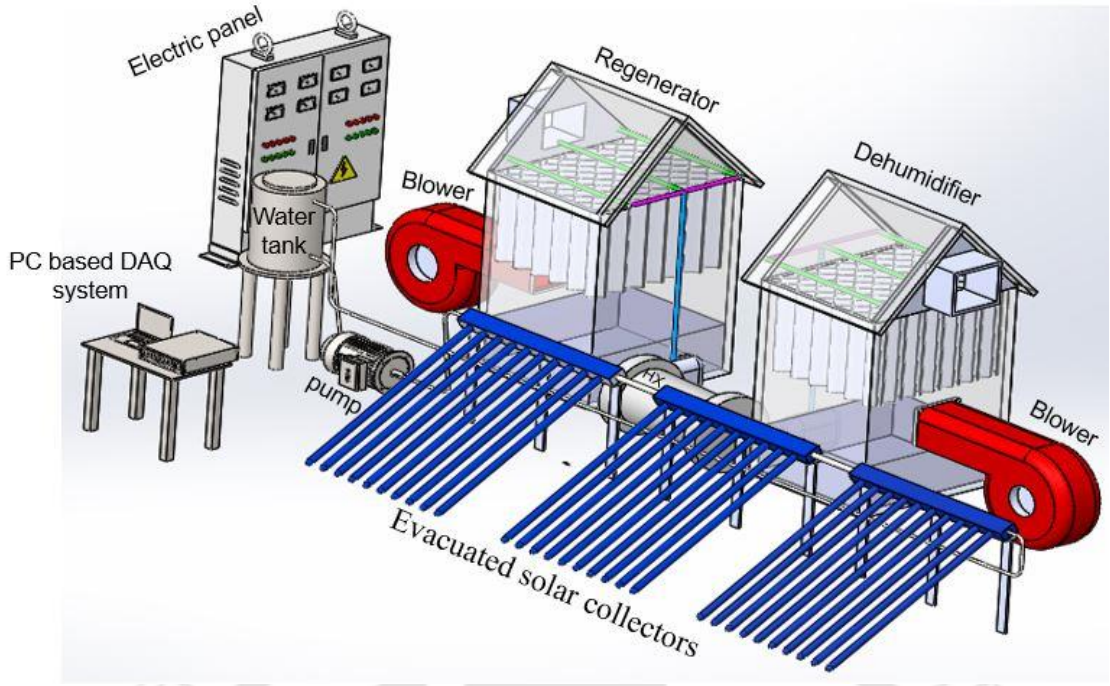

Fig. 5.2: Schematic of simplified 3D view of experimental setup

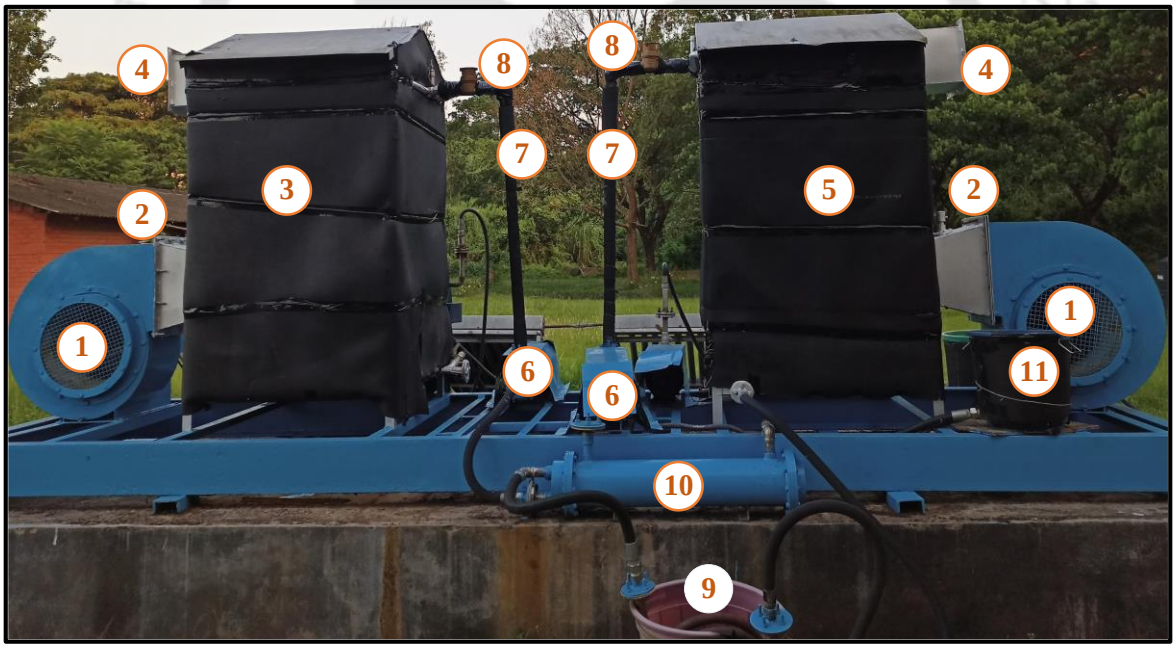

Fig. 5.3 (a): Pictorial view of liquid desiccant dehumidification/regeneration system, (1)-blower, (2)- airflow regulating valve, (3)-dehumidifier, (4)- air outlet, (5)- regenerator, (6)-solution pump, (7)- solution flow regulating valve, (8)- flow meter, (9) -cooling coil, (10) -shell and tube heat exchanger, (11) - water tank

Fig. 5.3 (b): Pictorial view of packed bed chamber

Fig. 5.3 (c): Pictorial view of solar evacuated tube collectors

5.3. Performance indices

The effectiveness of liquid desiccant dehumidifier/ regenerator system can be evaluated for solution or airside based on the desired process of the systems. In the case of dehumidifier, the attention is on the airside (dehumidification of air), and accordingly, the dehumidification effectiveness value is computed using air properties. Because, the dehumidifier is rated based on the air dehumidification capacity. However, in the case of regenerator, the attention is on the solution-side, i.e., outlet solution concentration. So, the effectiveness of regenerator is

estimated based on solution properties. Therefore, the airside and solution-side effectiveness along with the overall system-effectiveness, are mentioned in this section.

5.3.1. Effectiveness at airside

5.3.1.1. Condensation Rate (CR)

CR expresses the mass of water vapour condensed from air in to desiccant solution per unit time and area during air dehumidification process, as mentioned in Eq. (5.1).

$$CR\ [g/m^2s] = F_a\,(\omega_{a,i} - \omega_{a,o}) \tag{5.1}$$

Where, ω is the humidity ratio (g_{wv}/kg_{da}) and F_a is the mass flux rate (kg/m^2-s). Moreover, the condensation rate does not solely represent system performance. The high velocity of air eventually has high CR, so it does not exactly confirm the high-water vapour condensation rate. Therefore, the performance can be low even at high CR.

5.3.1.2. Latent Effectiveness (ε_{lat})

Latent effectiveness (ε_{lat}) is the ratio of actual change in air humidity ratio across the dehumidifier to the maximum possible change in air humidity ratio, as shown in Eq. (5.2).

$$\varepsilon_{lat} = \frac{Q_{lat}}{Q_{lat,max}} \tag{5.2}$$

$$\varepsilon_{lat} = \frac{\omega_{a,i} - \omega_{a,o}}{\omega_{a,i} - \omega_e} \tag{5.2a}$$

In the case of an adiabatic dehumidifier, the maximum possible difference in air humidity ratio can be achieved when the specific humidity of air and inlet desiccant solution is in equilibrium, i.e., when the air specific humidity is equal to the air specific humidity at the surface of the inlet desiccant solution. This is called equilibrium specific humidity (ω_e). The ω_e of air at desiccant surface can be represented as a function of inlet desiccant concentration (ξ) and temperature (T_s).

$$\omega_e = 0.622\left(\frac{P_V(\xi, T_s)}{P_{atm} - P_v(\xi, T_s)}\right) \tag{5.2b}$$

5.3.1.3. Enthalpy Effectiveness (ε_h)

It is the ratio of the actual air enthalpy change across the dehumidifier to the maximum possible change in air enthalpy, as mentioned in Eq. (5.3).

$$\varepsilon_h = \frac{h_{a,i} - h_{a,o}}{h_{a,i} - h_e} \tag{5.3}$$

$$h_e = C_{pa} T_{s,i} + \omega_e \left(h_{fg} + C_{pv} T_{s,i} \right) \tag{5.3a}$$

where, latent heat of condensation of water vapour is represented by h_{fg} in kJ/kg.

5.3.1.4. Latent Heat Ratio (LHR)

LHR is defined as the ratio between latent heat to the total heat of sensible heat and latent heat during the dehumidification process, as shown in Eq. (5.4).

$$LHR = \frac{Q_{lat}}{Q_{lat} + Q_{sen}} = \frac{1}{1 + \frac{1}{\varepsilon_{lat}} \cdot L^*} \tag{5.4}$$

$$L^* = \frac{\Delta T_{sa}}{\Delta \omega_{sa}} \cdot \frac{C_{pa}}{h_{fg}} \tag{5.4a}$$

Where, $\Delta T_{sa} = T_{a,i} - T_{s,i}$; $\Delta \omega_{sa} = \omega_{a,i} - \omega_{s,i}$; $\omega_s = \omega_e$

5.3.2. Effectiveness at solution-side

5.3.2.1. Evaporation Rate (ER)

ER indicates the amount of water vapour removed from the diluted desiccant solution per unit time and area. More specifically, the rate of water vapour evaporation from the diluted desiccant solution to the air is expressed by ER and can be represented in Eq. (5.5).

$$ER\ [g/m^2 s] = F_a\ (\omega_{a,o} - \omega_{a,i}) \tag{5.5}$$

The desiccant regeneration process is accomplished to concentrate the diluted desiccant solution to maintain the closed-loop operation of desiccant cycle. Therefore, it is essential to estimate the change of solution mass fraction across the regenerator during the regeneration process.

5.3.2.2. Desiccant Mass Fraction Increase (DMFI)

DMFI expresses the change in solution concentration during the regeneration process. Generally, it is expressed as

$$\text{DMFI}\ (\%) = \xi_o - \xi_i \tag{5.6}$$

where, ξ_i and ξ_o are desiccant solution concentrations at the inlet and outlet of regenerator during regeneration process.

5.3.2.3. Sensible and Latent Effectiveness

Solution-side sensible effectiveness is the ratio of the rate of heat transfer from/to the solution to the maximum possible rate of heat transfer in the regenerator. The rate of heat transfer is equal to the rate of total energy transfer from/to the solution, which is estimated from the change in solution enthalpy, i.e., subtracted by the rate of latent energy transfer from/to the solution, which is estimated from the phase change energy of water vapour in the solution side. The solution-side sensible effectiveness can be estimated as:

$$\varepsilon_{s,sen} = \frac{\left(\dot{m}C_p\right)_s \left(T_{s,o} - T_{s,i}\right) - \dot{m}_{salt} h_{fg} \left(\xi_{s,o} - \xi_{s,i}\right)}{\left(\dot{m}C_p\right)_{min} \left(T_{a,i} - T_{s,i}\right)} \tag{5.7}$$

$$\dot{m}_{salt} = \frac{\dot{m}_s}{1+\xi_s} \tag{5.7a}$$

$$\xi_s = \frac{1-C_s}{C_s} \tag{5.7b}$$

where h_{fg} and ξ are the enthalpy of vaporization of water and concentration, respectively. In case of salt solution, specific heat capacity is assumed to be constant, as shown in Eq. (5.7). In addition to that, the solution absorption energy is neglected in Eq. (5.7) since the change in the solution concentration in the liquid desiccant regenerators is quite small as compared to the original concentration and this energy is very small as compared to the energy transfer due to phase change of water to/from the salt solution in the liquid desiccant regenerators (Ghadiri Moghaddam et al., 2014).

The liquid desiccant solution-side latent effectiveness is the rate of latent energy transfer to/from the desiccant solution to the maximum possible rate of latent energy transfer in the desiccant solution side and is calculated by Eq. (5.8).

$$\varepsilon_{lat} = \frac{\dot{m}_{salt} h_{fg} \left(\xi_{s,o} - \xi_{s,i} \right)}{\dot{m}_{min} h_{fg} \left(\omega_{a,i} - \omega_{e} \right)} \tag{5.8}$$

5.3.3. Overall system performance

The overall performance of the system can be estimated by the coefficient of performance (COP), which is the ratio of desired output to the energy required to drive the system. In the present investigation, the energy consumption by the system mainly consists of two parts. One is the heat energy required for the desiccant regeneration (electric heater) and the power requirement for the blowers and pumps. It is well established that heat and power have different grades of energy. Therefore, the electric coefficient of performance (ECOP), thermal coefficient of performance (TCOP) and system coefficient of performance (COP_{sys}) are chosen to assess the performance of proposed hybrid system.

ECOP is the ratio between total dehumidification output (Q_d) of the process air to the electric energy (Q_E) consumed for the regenerating system, as shown in Eq. (5.9).

$$ECOP = \frac{Q_d}{Q_E} \tag{5.9}$$

TCOP is the total dehumidification output of the process air to the thermal regenerating (Q_T) heat (power by the electric heat and solar energy), as shown in Eq. (5.10).

$$TCOP = \frac{Q_d}{Q_T} = \frac{Q_d}{Q_S + Q_E} \tag{5.10}$$

Solar energy is abundant and free in nature. Therefore, the heat source that comes from the sun is cost-free ($Q_s = 0$). Further, the capital cost, operational and maintenance (O&M) costs of the solar panel are not considered. Then, Eq. (5.10) yields as

$$TCOP = \frac{Q_d}{Q_E} = ECOP \tag{5.10a}$$

The COP_{sys} is the ratio between the total dehumidification output of the process air to the total power consumed by the system, which is the combination of the power taken by blowers (Q_B) and pumps (Q_P) and the axillary electric heater (Q_E), as shown in Eq. (5.11).

$$COP_{sys} = \frac{Q_d}{Q_E + Q_P + Q_B} \tag{5.11}$$

$$COP_{sys} = \frac{ECOP}{1 + \frac{1}{Q_E}(Q_P + Q_B)} \tag{5.11a}$$

where, $Q_d = \dot{m}_{deh} h_{fg} \pm \dot{m}_a C_{pa} |T_{a2} - T_{a1}|$ and $Q_E = \dot{m}_w C_{pw} (T_{w,i} - T_{w,o})$; T_{a1} and T_{a2} are the inlet and outlet dry-bulb temperatures of process air in the dehumidifier, respectively in °C, $\dot{m}_w$ is the water mass flow rate across the heater in kg/s and $T_{w,i}$ and $T_{w,o}$ are the water temperatures at the inlet and outlet temperature of heater, respectively in °C. The ± sign represents either air is heated (-) or cooled (+) depending on the inlet desiccant solution temperature in the dehumidifier.

5.4. Experimental uncertainty analysis

The uncertainty arises mainly due to the inaccuracies of different instruments used in the experimental studies and calibration in a particular condition. The uncertainties associated in the experimental results are estimated using an analytical method proposed by Kline and McClintock (1953). The Kline and McClintock method is based on a specific uncertainty of the individual experimental instruments. Let Δy be the uncertainty in the results and Δx_1, Δx_2, Δx_3, …, Δx_n are the uncertainties in the independent variables. Then, the uncertainty in the results can be estimated by Eq. (5.12).

$$\Delta y = \left[\left(\frac{\partial f_1}{\partial x_1} \right)^2 (\Delta x_1)^2 + \left(\frac{\partial f_2}{\partial x_2} \right)^2 (\Delta x_2)^2 + ... + \left(\frac{\partial f_n}{\partial x_n} \right)^2 (\Delta x_n)^2 \right]^{\frac{1}{2}} \tag{5.12}$$

$$\frac{\Delta y}{y} = \left[\left(\frac{\partial f_1}{\partial x_1} \right)^2 \left(\frac{\Delta x_1}{y} \right)^2 + \left(\frac{\partial f_2}{\partial x_2} \right)^2 \left(\frac{\Delta x_2}{y} \right)^2 + ... + \left(\frac{\partial f_n}{\partial x_n} \right)^2 \left(\frac{\Delta x_n}{y} \right)^2 \right]^{\frac{1}{2}} \tag{5.12a}$$

where *f* is a function of independent variables, x_1, x_2, ..., x_n. Δx_i (i = 1, 2, ...) represents the absolute uncertainty related with the variables and $\Delta y/y$ is the relative uncertainty. Based on these relations, a detailed uncertainty analysis is performed. It is found that the overall uncertainties are less than ± 2.7% for all dehumidifier and regenerator performance parameters.

5.5. Results and discussion

5.5.1. Energy balance between air and desiccant solution

The energy balance analysis between the air and the desiccant solution is performed to ensure the adiabatic condition of the experiments. The overall energy exchange between the air and the desiccant solution for the dehumidifier/ regenerator with counter-flow configuration can be estimated as

$$Q_e = \dot{m}_a dh_a = d\left(\dot{m}_s h_s\right) \tag{5.13}$$

Air enthalpy:

$$h_a = C_{p,m} T_a + h_{fg} \omega_a \tag{5.14}$$

Change in solution enthalpy:

$$dh_s = C_{p,s} dT_s \tag{5.15}$$

$$d\dot{m}_s = \dot{m}_a d\omega_a \tag{5.16}$$

where h_s and h_a are enthalpies of solution and air, respectively; ω_a is air humidity ratio; $\dot{m}_a$ and $\dot{m}_s$ are mass flow rates of air and solution, respectively. Fig. 5.4a-b shows the experiment results of the air and the desiccant solution energy balance of dehumidifier and regenerator, respectively. The assumed adiabatic conditions during experimental runs are confirmed by Fig. 5.4a-b, which expresses the energy balance on the airside /on solution side for dehumidifier/regenerator chambers. The results showed that enthalpy deviation between the air and the solution are within ±15%, which specifies that the experimental adiabatic condition was adequately maintained. Dehumidifier deals with lower temperatures compared to the regenerator, so the enthalpy associated with regenerator is always more (Fig. 5.4a-b). More specifically, in dehumidifier, the variation of energy lies in 6 kW, whereas in the regenerator it varies within 17 kW.

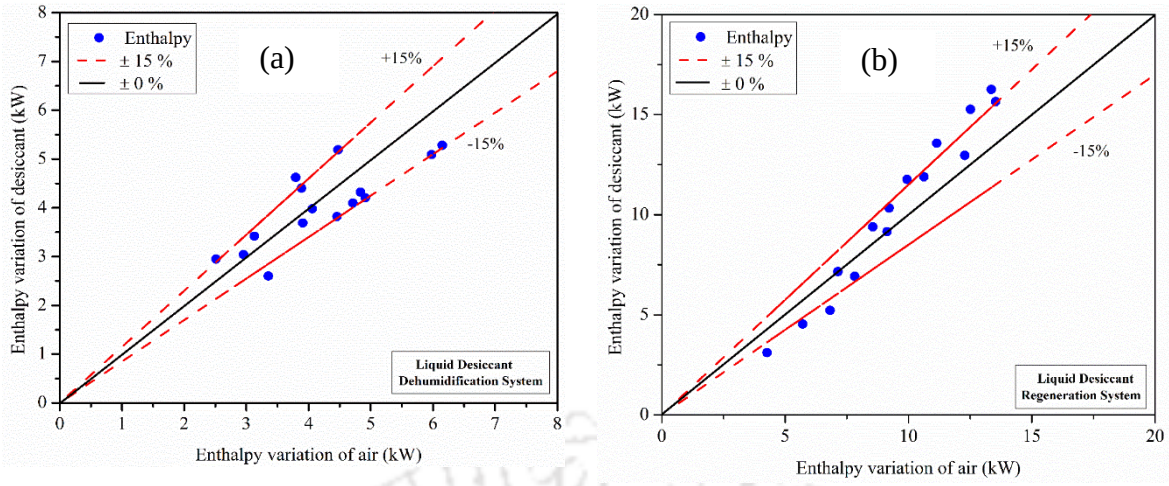

Fig. 5.4: Energy balance analysis between air and desiccant solution for (a) dehumidifier and (b) regenerator

5.5.2. Performance estimation under various operating conditions

In order to analyze the dehumidifier/regenerator performance, the experimental investigation has been done under different dehumidification operating conditions listed in Table 5.3.

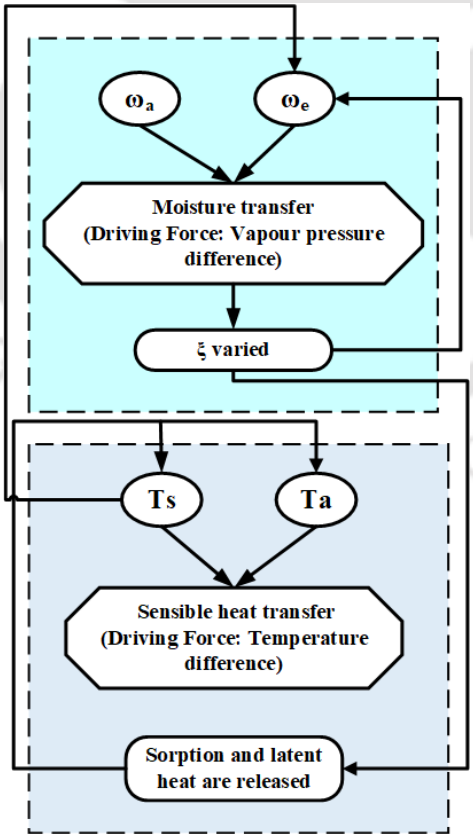

Fig. 5.5: Fundamental heat and mass transfer processes in liquid desiccant system

The solution to air mass flow rate (L/G), solution concentration (ξ) and solution temperature (T_s) were varied to study the corresponding dehumidification /regeneration performance. The performance of the system is discussed in terms of CR, LHR, ε_{lat} and ε_h for dehumidifier and ER, DMFI, ε_{lat} and ε_{sen} for regenerator.

Table 5.3: Operating parameters and their ranges with reference values for liquid desiccant system

Parameters	Dehumidifier		Regenerator	
	Range	Reference value	Range	Reference value
Air humidity ratio (g_{wv}/kg_{da})	21.6-27.2	27.2	21.6-27.2	27.2
Air flow rate (kg/m^2- s)	-	0.55	0.138-1.106	1.106
Air temperature (°C)	31.3-34.2	31.3	31.3-34.2	31.3
Solution flow rate (kg/m^2- s)	0.554-2.77	1.383	-	0.553
Solution temperature (°C)	25-33	29.1	52.3-70.1	69.5
Solution concentration (wt.%)	30-50	50	30-50	50
L/G ratio	1-5	2.5	0.5-4	0.5

The air specific humidity (ω_a) and equilibrium specific humidity (ω_e) difference are the driving force of the mass (moisture) transfer. Owing to this process, desiccant concentration (ξ) was varied. Similarly, solution temperature (T_s) and air temperature (T_a) difference is the driving force of heat transfer. Due to this process, the sorption and latent heat are released, and that greatly influence T_a and ω_e. The fundamental heat and mass transfer processes in liquid desiccant packed bed dehumidification system is shown in Fig. 5.5.

5.5.3. Effect on dehumidifier

5.5.3.1. Effect of solution to air (L/G) ratio variation

Fig. 5.6a-b demonstrates the experimental results of dehumidifier performance parameters for the solution to airflow rate ratio range of 1 to 5. During the dehumidifier experiments, the air mass flow rate was fixed as constant (described in section 2.2), where the increase in L/G ratio specifies the higher solution flow rate. The CR shows an apparent increasing trend with L/G (Fig. 5.6a-b). This is happening due to the fact that, with increase in the desiccant flow rate, the interaction time between the air and the desiccant decreases; therefore, the variation of desiccant temperature and concentration in dehumidifier decreases. Thus, the variation in the average surface vapour pressure of desiccant in the dehumidifier remains close to desiccant inlet vapour pressure. However, at high L/G, air would interact with the fresher desiccant solution. Hence, the difference between the average water vapour pressure of the air and the

desiccant in the dehumidifier remains high. This signifies a higher CR and a lower air outlet humidity ratio. Similarly, LHR and ε_h are found to increase with a similar rate (Fig. 5.6a-b) at high L/G due to lower outlet air humidity ratio and less variation of outlet solution temperature. It can also be observed in Fig. 5.6b that CR increases more rapidly at lower L/G than at higher ratios. This is because, the increase in L/G increases the wetting of packing material and hence increases the mass transfer area between the two fluids. However, at higher L/G, the wettability effect is not prominent. Indeed, the higher solution flow rate may pose resistance to the airflow through the control volume (pore of the packing material). In the same way, ε_{lat} is increased at a similar rate because of the lower outlet air humidity ratio at higher L/G. The higher L/G increases the mass transfer coefficient between the air and the desiccant in the dehumidifier, ensuring further increase in ε_{lat}.

5.5.3.2. Effect of desiccant temperature (T_s) variation

Fig. 5.6c-d demonstrates the influence of inlet T_s on CR, LHR, $\varepsilon_{h,}$ and ε_{lat}. The experimental results showed that ε_{lat} of the dehumidifier increases when the inlet T_s decreases from 37°C to 25°C (Fig. 5.6c). However, at high inlet T_s, CR behaves positively (increasing trends). This is due to increase in T_s increases the desiccant surface vapour pressure. Hence, the difference between the average vapour pressure of desiccant and the air decreases in the dehumidifier. As a result, mass transfer potential between the moisture in the air and the desiccant solution reduces. This signifies a higher air outlet humidity ratio and therefore, CR value decreases at higher inlet T_s. It also noticed that after 31°C, ε_{lat} increases slightly. This may be due to the reduction in surface tension of the desiccant solution at a higher desiccant solution temperature. Low desiccant surface tension enhances the wettability and the wet area of the packing material. As the inlet conditions of air are constant, increasing the desiccant T_s also leads to reduction in mass transfer potential (due to the low vapour pressure difference). In the same way, with increase in desiccant inlet T_s decreases ε_h and LHR (Fig. 5.6c-d). However, higher inlet desiccant T_s leads to higher LHR (Fig. 5.6d) as the denominator of Eq. (5.4) become lower.

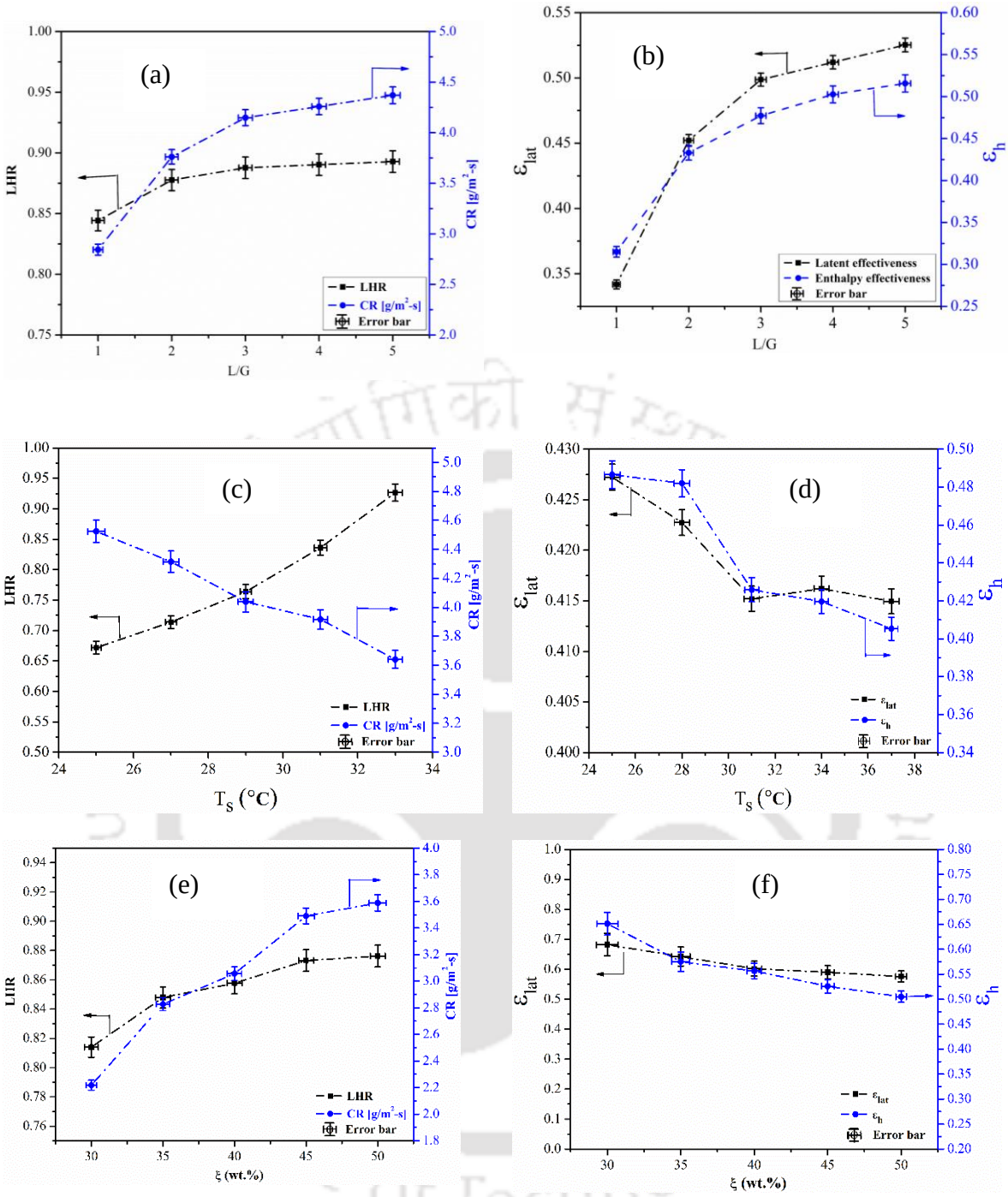

Fig. 5.6: Influences of solution to airflow rate, solution concentration and solution temperature on condensation rate, latent heat ratio, latent and enthalpy effectiveness

5.5.3.3. Effect of desiccant concentration (ξ) variation

The effect of inlet ξ (from 30% to 50 %) on CR, LHR, ε_h and ε_{lat} is shown in Fig. 5.6e-f. It is observed that higher inlet ξ increases both CR and LHR. As per the kinetic theory of the liquid, an increase in ξ decreases the vapour pressure of the desiccant surface and as a result, higher

driving force is generated for mass transfer from air to the desiccant solution. Due to the higher vapour pressure difference between the air and the desiccant surface, the outlet air humidity ratio becomes lower and, hence, higher CR and LHR. The vapour pressure of the desiccant surface depends on ξ as well as the desiccant solution temperature. A high concentrated desiccant solution may increase the absorption heat release and as a result, solution temperature is increased. Subsequently, the difference between average water vapour pressure of desiccant and air is decreased. However, higher inlet ξ increases the solution surface tension; as a result, the wettability of the packing material is reduced. Conversely, the interaction time rises with viscosity. The former affects the performance more than the latter. Owing to this, ε_{lat} and ε_{h} reduce slightly with increase in inlet ξ (Fig. 5.6e). These results also get support from the observations reported by (Zurigat et al., 2004a). However, the solution density increases with solution concentration. Further, the temperature of the desiccant solution increases with ξ, since the specific heat decreases with increasing ξ.

5.5.4. Effect on regenerator

In this section, the performance of the regenerator is tested under different test conditions.

5.5.4.1. Effect of L/G variation

Fig. 5.7a-b presents the experimental results of regenerator performance with different L/G ratios (varied from 0.5 to 4). The airflow rate was varied over a range to regenerate a constant mass flow rate of desiccant solution. Especially, increase in L/G ratio specifies the lower rate of airflow. Fig. 5.7a-b demonstrates the influence of L/G on ER, DMFI, ε_{lat} and ε_{sen}. The ER was decreased from 18.4 to 13.9 g/m^2-s, when L/G was increased from 0.5 to 4. A similar trend is also observed for DMFI (Fig. 5.7b). This may be because of less amount of air contact with the wet zone area of packing surface at lower airflow rate and hence, packing surface area is utilized ineffectively. Therefore, the less solution will not interact with the fresh air, as a result, solution concentration is not varied much at higher L/G. Although the change in air humidity is high at higher L/G, the mass flow rate of air is low, that eventually brought the ER lower at higher L/G. Residence time for the air in the dehumidifier is decreased at higher L/G, as a result, the mass transfer coefficient is decreased. Therefore, the outlet air humidity ratio is higher at higher L/G and thus, a lower value of ε_{lat} is observed. Very high air flow rates may pose resistance to the flow of the desiccant solution through the control volume (pore of the packing material) and increase the tendency of desiccant carryover with the process air.

Further, it is also noticed that ε_{lat} got enhanced at higher L/G. This is due to the ineffective utilization of contact area and wet zone area of the packing material. According to the definition of ε_{sen} and ε_{lat}, the denominator of Eqs. 5.7-5.8 is less at higher L/G and lower airflow rate. Therefore, values of ε_{sen} and ε_{lat} show an increasing trend at higher L/G.

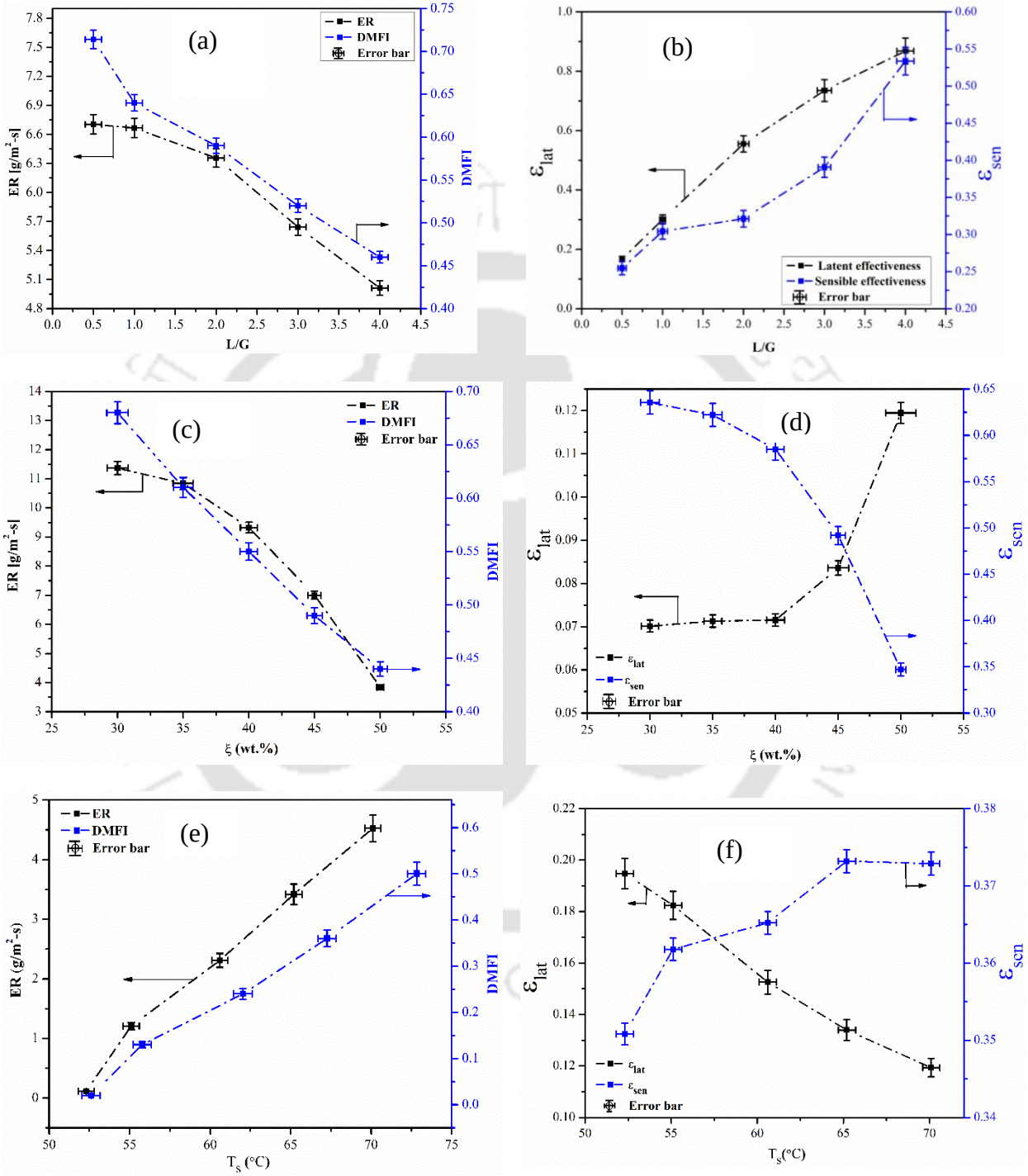

Fig. 5.7: Influences of solution to airflow rate, solution concentration and solution temperature on evaporation rate, desiccant mass fraction rate, sensible and latent effectiveness

5.5.4.2. Effect of desiccant concentration (ξ) variation

The effect of inlet ξ (from 30% to 50%) on regeneration performances are plotted in Fig. 5.7c-d. In the present study, ER is decreased from 11.4 to 3.9 g/m^2-s. Besides, with an increase of inlet ξ, the DMFI was found to decrease significantly. The reason for drop in ER and DMFI maybe because of the lower desiccant solution surface vapour pressure at higher ξ. Therefore, the difference between the average vapour pressure of air and the desiccant solution becomes lower, as a result, the moisture transfer driving force is reduced. Thus, ER and DMFI are found to decrease with increase in inlet ξ. However, it can be noted that ε_{lat} has an increasing trend with ξ. Because, the difference between the air inlet specific humidity and the equilibrium specific humidity at solution surface decreases with increase in ξ. In the meantime, the outlet desiccant solution temperature is higher at a lower ξ. Thus, these combined effects resulted in a decreasing trend of ε_{sen} from 63% to 34% during regeneration.

5.5.4.3. Effect of desiccant temperature (T_s) variation

Fig. 5.7e-f demonstrates the influence of desiccant temperature (T_s) on ER, DMFI, ε_{lat} and ε_{sen}. Better regeneration performance has been observed at higher T_s. In the current study, ER and temperature were increased from 0.1 g/m^2-s to 4 g/m^2-s and from 52 to 72.8°C, respectively. Meanwhile, DMFI was also enhanced. Further, through experimentation, it is observed that the desiccant solution started to regenerate after the solution temperature of 52°C. The rise in T_s could have improved the regeneration performance during the regeneration process, whereas increase in solution temperature may affect the dehumidification process. The high inlet T_s increases the vapor pressure of desiccant compared to air, so ER and DMFI are found to increase. At higher inlet T_s, the difference between the air specific humidity at solution surface and the ambient air specific humidity increases and therefore, ε_{lat} is also found to decrease. Similarly, as the inlet T_s increases, the difference between the inlet T_s and the temperature of the air increases, resulting in lower ε_{sen}.

5.5.5. Pressure drop analysis

The pressure drop on the airside in a packed column was measured experimentally at different desiccant flow rates. The effect of air stream flow rate on the pressure drop of counter-flow packed liquid desiccant dehumidifier under the different solution flow rate is demonstrated in Fig. 5.8, where F_a and F_s are air and solution mass flux rate, respectively. Pressure drop is directly proportional to airflow rate. The outcomes of present study verify the advantage of the

structured packed bed dehumidifier due to their low-pressure drop. At lower values of F_a, the pressure drop is affected mostly by F_s because the gas, due to its low density, needs more cross-sectional area between packing sections for the airflow. At higher F_s values, however, pressure drop increases rapidly due to choking of packing flute heights by the liquid. The pressure drop of structural packed bed dehumidifier is higher with increase in airflow rate due to the frictional loss between air and packing material. With increase in air flow rate, the amount of air itself resists to go through the packing sections, which results in a rapid rise in pressure drop.

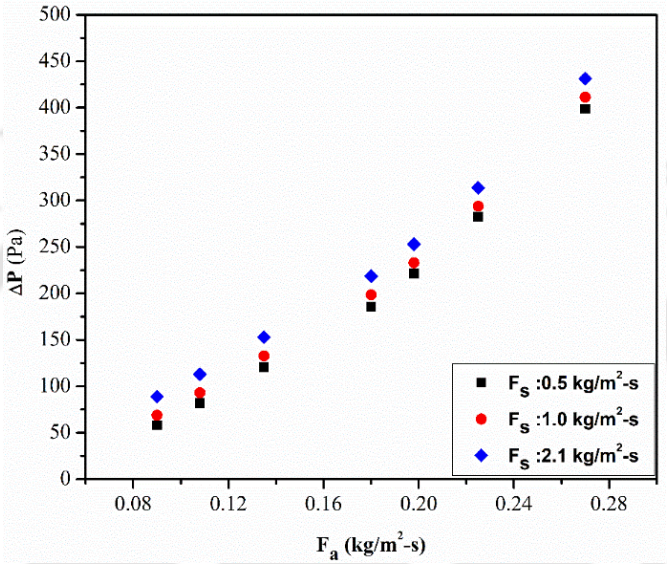

Fig. 5.8: Influence of air mass flow rate on pressure drop for the packed bed system

5.5.6. Psychrometric representation of dehumidification process

In the dehumidification process, as depicted in Fig. 5.9, the minimum achievable outlet air humidity ratio is the inlet equivalent humidity ratio of air at the desiccant surface (solution inlet point: in psychrometric chart). The air is dehumidified due to the desiccant solution and is checked under different operating conditions. The air gets heated and dehumidified during the dehumidification process, and thus the direction of heat transfer is opposite to the mass transfer direction in the dehumidifier. For instance, the measured inlet and outlet conditions of desiccant solution and air at the dehumidifier at $\dot{m}_a$ = 0.553 kg/m^2-s and $\dot{m}_s$ = 0.165 kg/m^2-s are shown on the psychrometric chart to visualize the heat and mass transfer phenomena of the air and desiccant solution process. It can be noticed from Fig. 5.9 that the air enters to the dehumidifier at humidity ratio of 23 g_{wv}/kg_{da} with a temperature of 30.5°C, and the air got dehumidified to 16 g_{wv}/kg_{da} and the temperature increased subsequently to 32.5°C.

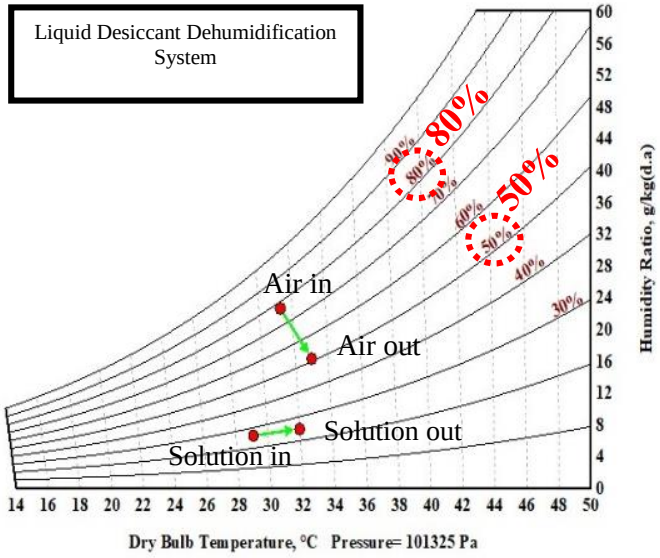

Fig. 5.9: A typical experimental air inlet - outlet and desiccant inlet-outlet condition in a liquid desiccant dehumidifier system

5.6. Performance trends comparison over different operating conditions

The effects of independent parameters on the performance parameters of dehumidifier/regenerator for the present study and other literature studies are summarized in Table 5.4. Figs. 5.7-5.8 illustrate the performance tends of the current experiment study. The arrows in Table 5.4 represent the effect of each independent parameter on the respective performance parameter. The earlier researchers mainly focused on ε_{lat} and CR in the case of the dehumidifier.

Table 5.4: Performance trends of present study with existing dehumidifiers/ regenerator's results under different operating conditions

			Dehumidifier			**Regenerator**		
Author (s)	System type	**Parameter**	**$T_{s,i}$**	**ξ**	**L/G**	**$T_{s,i}$**	**ξ**	**L/G**
		Unit	(°C)	(wt.%)	-	(°C)	(wt.%)	-
Wang et al. (2016)	Structural packing dehumidified (LiCl)	Range	16.4-35.4	31.7-40.1				
		ε_{lat}	↓	↓				
Moon et al. (2009)	Structural packing dehumidif	Range		33-42				
		ε_{lat}		↓				

	ied ($CaCl_2$)							
Martin and Goswami (2000)	TEG	Range	23-36	94-96	3.5-15.4			
		ε_h	⬇	↔	⬆			
Bassuoni (2011)	Structur6al packing dehumidified / Regenerators ($CaCl_2$)	Range	14-30	34-50	0.1-0.4	52-83	34-50	0.1-0.4
		ε_{lat}	-	-	⬆	⬇	⬆	⬆
		CR	⬇	⬆	⬆	-	-	-
Yang et al. (2019)	Internally heated Regenerators (LiCl)	Range	-	-	-	36-65	24-32	.38-.65
		RR	-	-	-	⬆	⬇	⬇
		DMFI				⬆	⬇	⬇
Present study	dehumidified / Regenerators	Range	25-33	30-50	1-5	52.3-70.1	30-50	0.5-4
		CR/ER	⬇	⬆	⬆	⬆	⬇	⬇
		ε_{lat}	⬇	⬇	⬆	⬇	⬆	⬆
		ε_h/ ε_{sen}	⬇	⬇	⬆	⬆	⬇	⬆
		LHR /DMFI	⬆	⬆	⬆	⬆	⬇	⬇

⬆with increasing independent variable, the performance parameter increases; ⬇performance parameter decreases with increasing independent variable; ↔ less significant effect on the performance parameter with increasing the independent variable

However, in the present study, the effects of LHR and ε_{lat} for the dehumidification and DMFI, ER, ε_h and ε_{sen} for regenerator are also analyzed. Therefore, the L/G, ξ and T_s are chosen as independent parameter whereas, CR/ER, ε_{lat}, $\varepsilon_h/\varepsilon_{sen}$ and LHR/DMFI as performance indices for the convenience of comparing with literature. Compared to the earlier studies, the desiccant to airflow rate ratio (L/G) used in this study is significantly higher (Gao et al., 2012; Liu et al., 2006; Longo and Gasparella, 2005; Zurigat et al., 2004). Accordingly, it represents the possibility of operating the desiccant system at low flow rates of desiccant with structured packing. The range of solution inlet temperatures is wider than literature (Fumo and Goswami, 2002; Gommed et al., 2004; Liu et al., 2015). Similarly, the inlet desiccant concentration is also wider than literature (Fumo and Goswami, 2002; Moon et al., 2009). It can be noticed

from Table. 5.3 that the performance trends offered by the different other literature were mostly consistent with the present study. For instance, CR is found to increase with L/G and ξ, but drops with T_s. The ER increases with the T_s whereas, descending with ξ and L/G in every system. In the meantime, the performance seems to be more sensitive in the membrane than that of the adiabatic packed bed system. For example, ξ displayed a significant effect on the ER in the regenerator, while its effect was almost insignificant in Yin and Zhang (2010) in membrane-type dehumidification. This could be attributed to the significantly expanded mass and heat transfer area in the packed bed chamber where the heat transfer was stimulated considerably, and thus more responsive to the temperature changes of the air stream.

Furthermore, some different trends are also being observed by Martin and Goswami (2000). The influence of the inlet ξ on the ε_h is found to be decreasing trend in the current study, while the influence is not significant with Martin and Goswami (2000) study. The reason may be TEG was used as liquid desiccant and higher range of inlet ξ was investigated (i.e., from 94 to 96). Another reason could be the higher ξ clogs the packing pores and deteriorates the dehumidification performance.

5.7. Correlations of Sherwood number for dehumidifier and regenerator

Coupled heat and mass transfer phenomena occurring inside the dehumidifier/ regenerator are difficult to be decoupled by mathematical or analytical methods without using decoupled heat and mass transfer results from experimental data. Various parameters, including the air and solution flow rates, the air and solution thermo-physical properties and the packed bed structure affect the heat and mass transfer inside the packed bed. These parameters can be grouped into properly selected dimensionless numbers and can be correlated to the heat and mass transfer coefficients as described in the following subsections. The mass transfer coefficient can be related to Sh. Sh can be correlated to the Re and mass flow rate of the air and solution as shown on the right-hand side of Eq. (5.17) and Eq. (5.18).

For dehumidifier

$$Sh = 19.15\,Re_a^{-1.19}\,\omega_a^{-1.075}\left(\frac{F_s}{F_a}\right)^{0.1833}\left(1-\frac{\xi}{100}\right)^{1.719} \tag{5.17}$$

For regenerator

$$Sh = 0.0182\omega_a^{-1.06}\left(\frac{F_s}{F_a}\right)^{0.0962}\left(1-\frac{\xi}{100}\right)^{-1.39} \quad (5.18)$$

The comparison of the predicted humidity ratio difference from the developed thermal model with the experimental datasets, which was obtained from the field analysis of liquid desiccant dehumidification and regeneration system is presented in Fig. 5.10. It is found that for a given range of operating conditions, the developed thermal model is well matched with the experimental data within an error of ± 10%. Therefore, it can be concluded that the thermal model is well agreed with the experimental results.

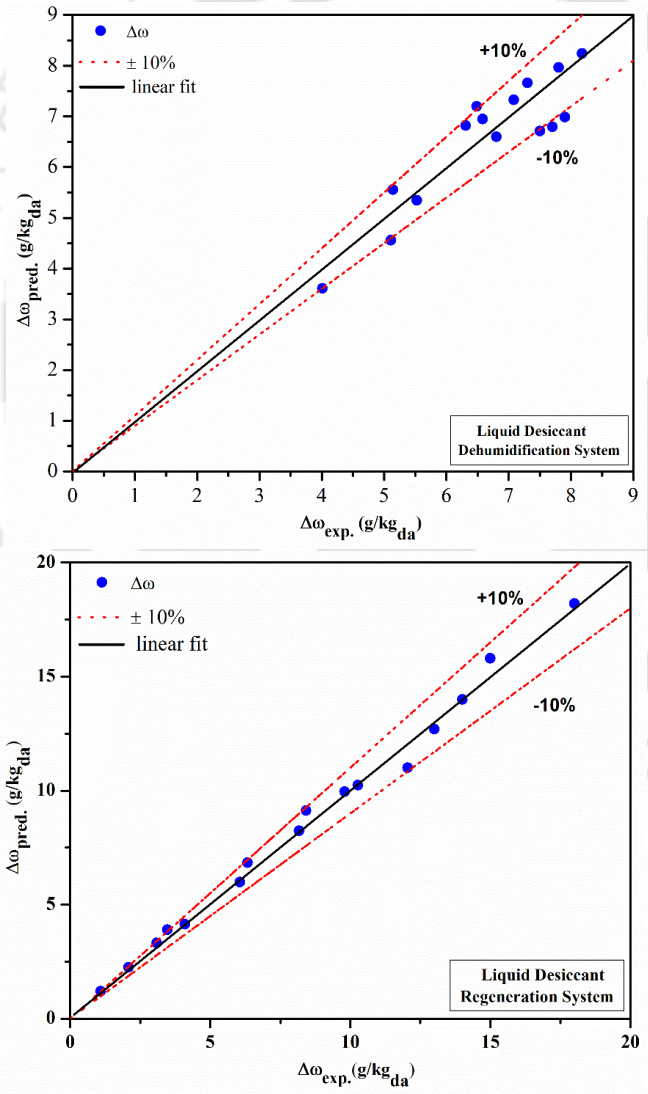

Fig. 5.10: Comparison between present experimental results with model predicted outcomes of humidity ratio difference

5.8. Counter plots of thermodynamics properties

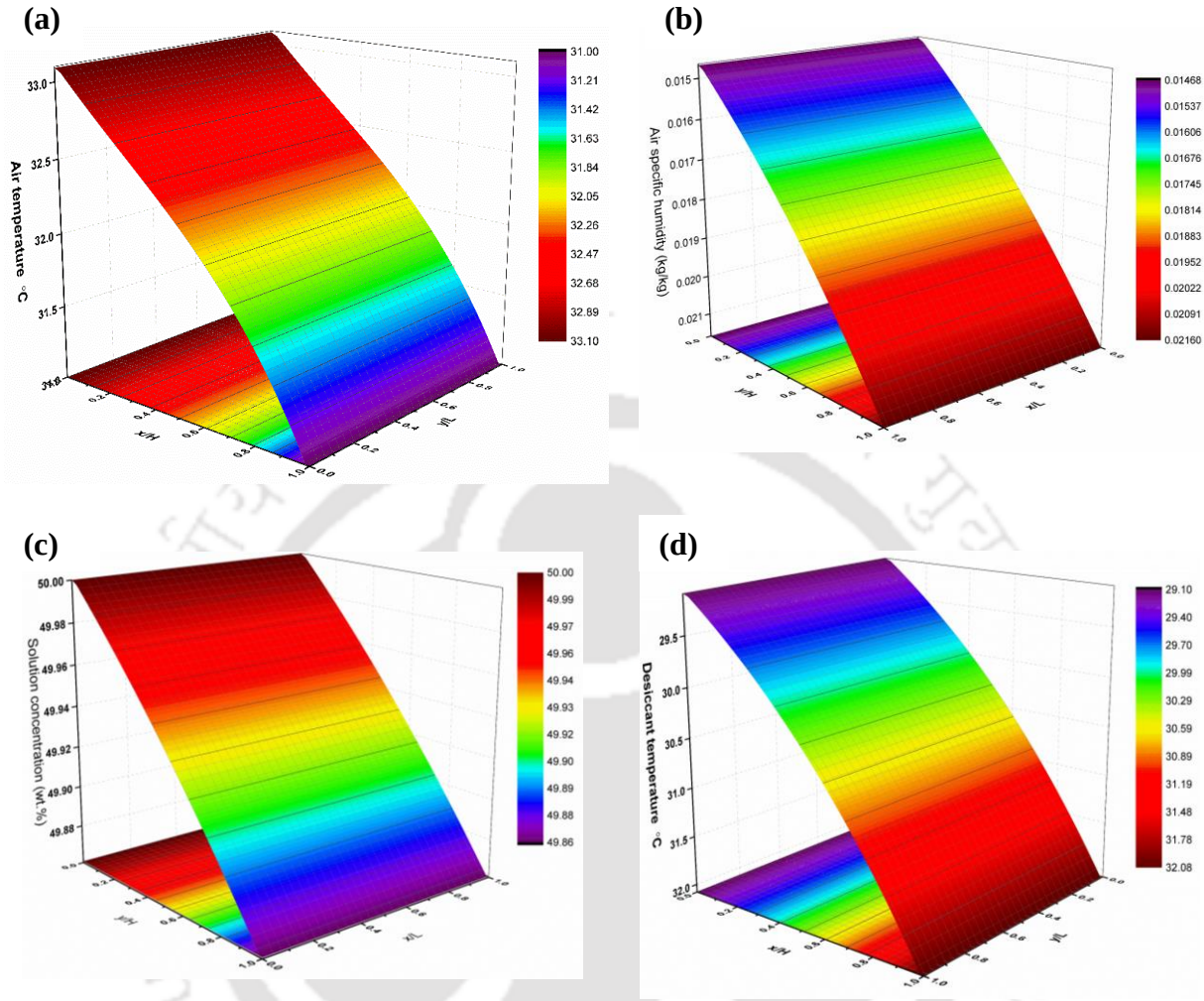

Fig. 5.11: Variation of (a) air temperature (T_a,°C), (b) air humidity(ω_a, kg/kg), (c) solution concentration (ξ, %) & (d) solution temperature (T_s,°C) in dehumidifier

5.8.1. Air temperature variation: The air is flowing bottom to top and the desiccant is flowing along the height of the dehumidifier (top to bottom). As the air stream passes, it contacts the cool and strong desiccant solution that reduces temperature of air as length increases. At the air outlet, the top side air stream has the lowest temperature since it comes into contact with cold and stronger desiccant.

5.8.2. Air specific humidity variation: As the inlet air specific humidity increases the partial vapour pressure of air also increases (Das and Jain, 2015). Therefore, the vapour pressure difference is increased between the air and the desiccant solution and that further increases the

mass transfer potential, which causes the gradual change in specific humidity. The cold - strong desiccant solution has lower vapour pressure compared to the moist air due to their temperature and concentration differences. The moist air is flowing along the height and when it passes over the height, it interacts with cold and strong desiccant solution. Due to the vapour pressure difference, desiccant solution absorbs the moisture from air and air gets dehumidified.

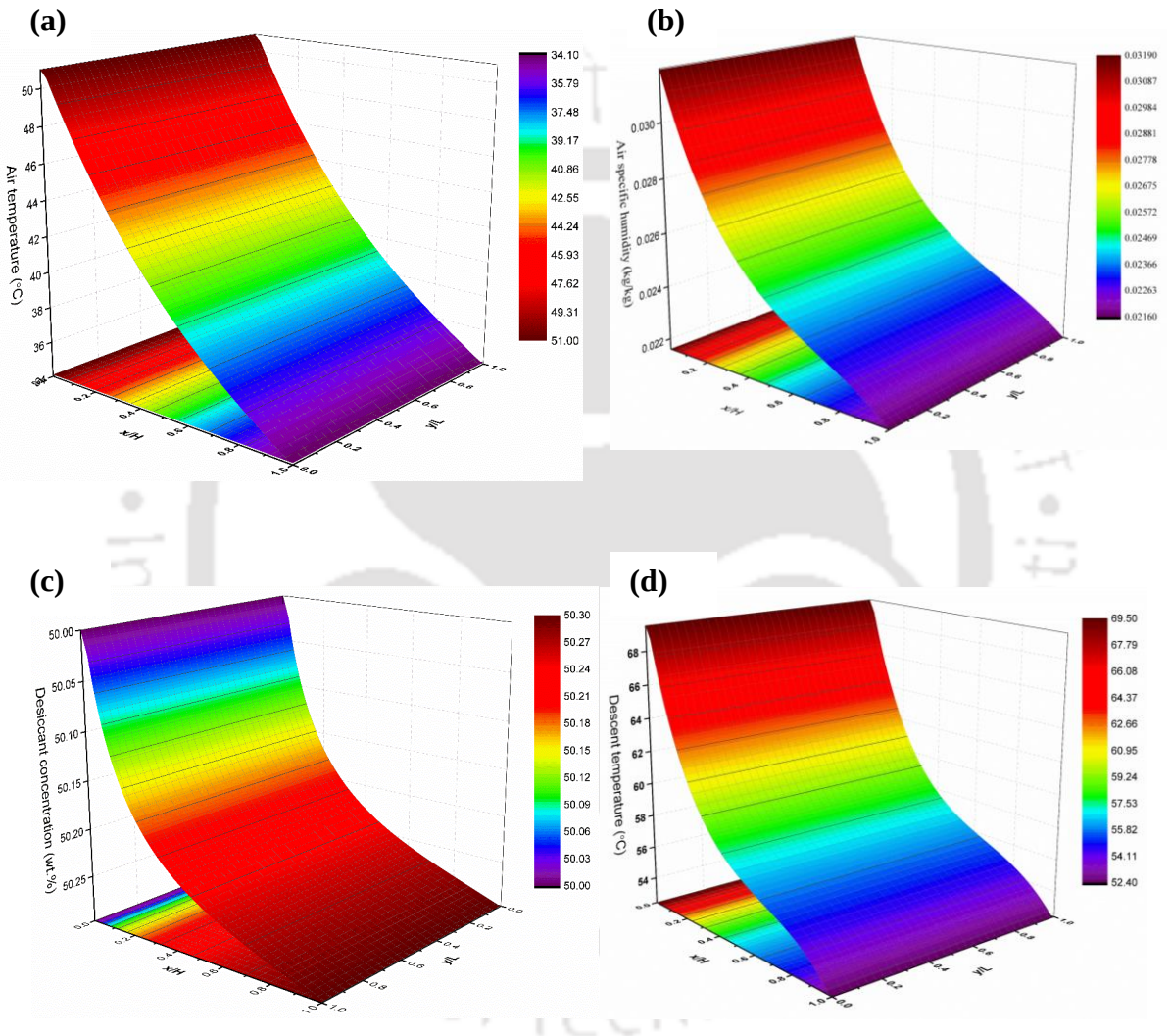

Fig. 5.12: Variation of (a) air temperature (T_a,°C), (b) air humidity(ω_a, kg/kg), (c) solution concentration (ξ, %) & (d) solution temperature (T_s,°C) in regenerator

5.8.3. Solution concentration variation: The desiccant is flowing along the height and the solution absorbs moisture from the moist air due to the vapour pressure difference between them. Due to the high mass transfer driving force, desiccant absorbs more moisture and solution

gets diluted. Therefore, the vapour pressure difference decreases considerably from top to bottom and a concentration gradient has been observed at the solution outlet.

5.8.4. Solution temperature variation: As the desiccant flows, it absorbs moisture from air and becomes diluted due to vapour pressure difference. As the desiccant solution at bottom interacts with high specific humidity air and thus having higher mass transfer potential from the air to the desiccant. This high moisture transfers potential results in high desiccant temperature (since the sorption heat and latent heat of vaporization are released at the mass transfer operation). The change in temperature at desiccant outlet is shown in Fig. 5.11.

Similarly, the variation of air temperature (Ta, °C), air humidity (ω_a, kg/kg), solution concentration (ξ, %) and solution temperature (T_d, °C) in regenerator are explained in Fig. 5.12.

5.9. Closure

The experimental setup of the solar-driven liquid desiccant system has been fabricated and the coupled heat and mass transfer characteristics of liquid desiccant system during dehumidification and regeneration in different control settings are experimentally analyzed. The advantage of the present study is the usage of solar thermal energy instead of complete electrical power input for the regeneration of dilute desiccant. In the current work, an additional comprehensive studies on the influence of operating parameters on the performance of liquid desiccant dehumidifier/ regenerator are presented. CR, ε_{lat}, LHR and ε_h for dehumidifier and ER, ε_{sen}, ε_{lat} and DMFI for regenerator are considered as the performance indicators. Based on the presented experimental and developed model results, the following major generic and overall conclusions are arrived.

- The experimental results showed that the airside (dehumidifier) and solution-side (regenerator) latent effectiveness increase with solution to air mass flow rate. However, the solution-side latent effectiveness is higher than the airside effectiveness.
- For tested liquid desiccant dehumidifier, condensation rate and latent effectiveness lies in the range of 2.2 to 4.6 g/m^2-s and 36 to 68%, respectively. Whereas, the evaporation rate, sensible and the latent effectiveness of the regenerator lies in the range of 0.1–11.2 g/m^2-s, 25.9–63% and 10-92% depending on the operating conditions.

- CR increases as L/G increase, which indicates that an increase in L/G significantly improve the heat and mass transfer coefficient. Hence, this factor increases the driving factor of the dehumidifier/ regenerator.
- It is found that pressure drop is directly proportional to the airflow rate. For the given operating conditions, the pressure drop of the structured packed bed counter-flow dehumidifier was found in the range of 50 to 400 Pa.

It is demonstrated that solar-based desiccant regeneration systems have a potential for reactivation of diluted desiccant, especially in hot and humid climates. Further research will be needed to improve overall system performance.

CHAPTER 6

Study of Combined Dehumidifier-Regenerator System and Correlation Development

6.1. Introduction

The substantial potential of thermally driven desiccant systems have been explored for dehumidifying air in HVAC systems. These systems offer an optimal trade-off footprint regarding desiccant temperature - solution flow rate- solution concentration compared to the conventional air conditioning systems. Generally, liquid desiccant dehumidifier is influenced by different operating parameters, hence accurate prediction of its resulting characteristics is imperative for a better overall understanding of systems. This motivated to accomplish a comprehensive study on dehumidifier performance for precise prediction and optimization of process parameters to achieve better dehumidification performance. In this chapter, the application of contemporary LiBr+$CaCl_2$ desiccant is considered for air dehumidification in an adiabatic, counter-flow liquid desiccant dehumidifier. Further, developed the relationships between the performance parameters and control variables through the application of various well-known artificial intelligence-based methods such as artificial neural network (ANN), adaptive neuro-fuzzy inference system (ANFIS), and gene expression program (GEP). The sensitivity analysis of independent variables on performance parameters is also carried out using cosine amplitude method. The results demonstrate that the inlet air temperature and air specific humidity are having a higher influence on the dehumidifier effectiveness and sensible heat ratio, respectively. Finally, an algorithm involving the combination of multi-objective optimization with the regression models is also proposed for the optimization of the input process parameters to achieve better dehumidification performance.

6.2. Regression models

6.2.1. Classical regression models

The classical regression model is developed for estimating dehumidifier/regenerator performance parameters such as LHR, ε_{lat} and CR for dehumidifier, and ε_{sen}, ε_{lat} and ER for regenerator with the persistence of all independent variables (T_s, T_a, ω_a, L/G and ξ). The classical non-linear regression (NLR) model is explained in Eqs. 6.1-6.6. The outputs of the model are validated against the experimentally obtained datasets for all cases of dehumidifier/regenerator experimentation and the deterministic error present in the model

output for adjudging the model integrity is also estimated. Performance of models are verified based on the statistical parameters of coefficient of determination (R^2), Root Mean Square Error (RMSE), correlation coefficient (R), absolute error metric of Mean Absolute Percentage Error (MAPE) and normalized Mean Absolute Percentage Error (nMAPE) for the same datasets (Betiku et al., 2016). Statistical equations are mentioned in Appendix A (Eqs. A1-A5).

Non-Linear Regression (NLR) Models

For dehumidifier:

$$\varepsilon_{lat} = 0.321 + 0.2599(L/G) + 0.00591T_a + 0.0052(L/G)^3 - 0.6161\xi\omega_a - 0.0616(L/G)^2 + 0.01T_s \quad (6.1)$$

$$CR = 3.256 + 0.0321T_a(L/G) + 0.0007795\xi^2 - 0.1099T_s - 0.1058(L/G)^2 + 0.001\omega_a \quad (6.2)$$

$$LHR = 1.0905 + 0.01012(L/G) + 0.002664\xi + 0.000505T_s^2 - 0.03167T_a + 0.1\omega_a \quad (6.3)$$

For regenerator:

$$ER = 5.381 + 0.0008624T_s^2 - 0.004735T_a\xi + 0.001\omega_a + 0.01(L/G) \quad (6.4)$$

$$\varepsilon_{lat} = 0.0012 + 0.0071927\xi(L/G) - 0.0015581T_s - 0.0394286(L/G)^2 + 0.0001\omega_a + 0.01T_a \quad (6.5)$$

$$\varepsilon_{sen} = -0.4632 + 28.416\omega_a + 5.487\times10^{-3}(L/G) + 8.7237\times10^{-4}(L/G)^4 + 5.5284\times10^{-5}\xi^2 + 0.001T_s + 0.012T_a \quad (6.6)$$

Table 6.1: Statistical values of the performance parameters

	Dehumidifier			Regenerator		
	ε_{lat}	LHR	CR	ER	ε_{sen}	ε_{lat}
NLR model:						
R	0.953	0.989	0.987	0.978	0.932	0.990
R^2	**0.909**	**0.980**	**0.974**	**0.957**	**0.868**	**0.981**
RMSE	0.029	0.188	0.110	0.250	0.469	0.233
MAPE (%)	4.900	22.50	2.400	14.70	13.50	15.40
nRMSE	0.064	0.224	0.030	0.122	1.276	0.859

It is found from Table 6.1 that classical regression models are not predicting the performance parameters precisely. Therefore, it is essential to build an AI model to represent the performance parameters precisely as a function of independent variables.

6.2.2. Methodology of intelligent models

6.2.2.1. Artificial Neural Network (ANN) model

ANN is a typical artificial intelligence method, which is developed in analogy to the human brain information-processing system. It is also a profound computational mathematical tool when complicated non-linear relationships exist between the dependent and independent variables. The most well-known type of ANNs in regression is known as Multi-Layer Perceptron (MLP), which includes one (or more) hidden layers, an input layer, and an output layer. These specific layers each include numerous nodes, most commonly known as neurons. The MLP network is a deep learning method that is capable of pattern the simple and as well as complex functional behaviour. This process can be better illustrated by the schematic of the ANN neuron, as shown in Fig. 6.1. Detailed information about MLP is available in the Appendix B.

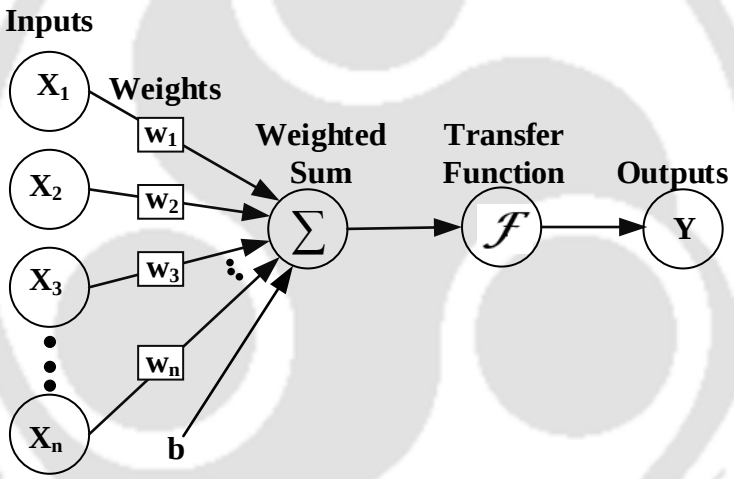

Fig. 6.1: General structure of ANN model

6.2.2.2. Adaptive Neuro-Fuzzy Inference System (ANFIS) model

Jang (1993) developed and presented ANFIS centred on the incorporation of both a fuzzy inference approach and ANN. Fig. 6.2 illustrates the general structure of ANFIS model. The five levels that frame a typical ANFIS architecture are multiplication, fuzzification, multiplication, normalization, de-fuzzification, and summation. ANFIS approach is a rule-based fuzzy logic algorithm and these rules are formed during the training process of the architecture. Detailed information about ANFIS is available in the Appendix C.

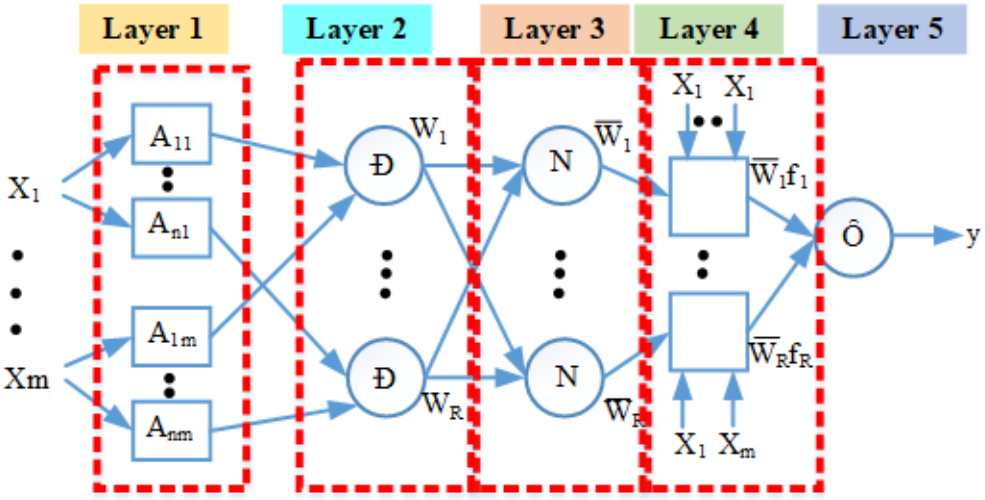

Fig. 6.2: General structure of ANFIS model

6.2.2.3. Gene expression program (GEP) model

Genetic algorithm (GA) and Genetic programming (GP) methods use genetic operators, which are sometimes difficult to apply to real-time problems.

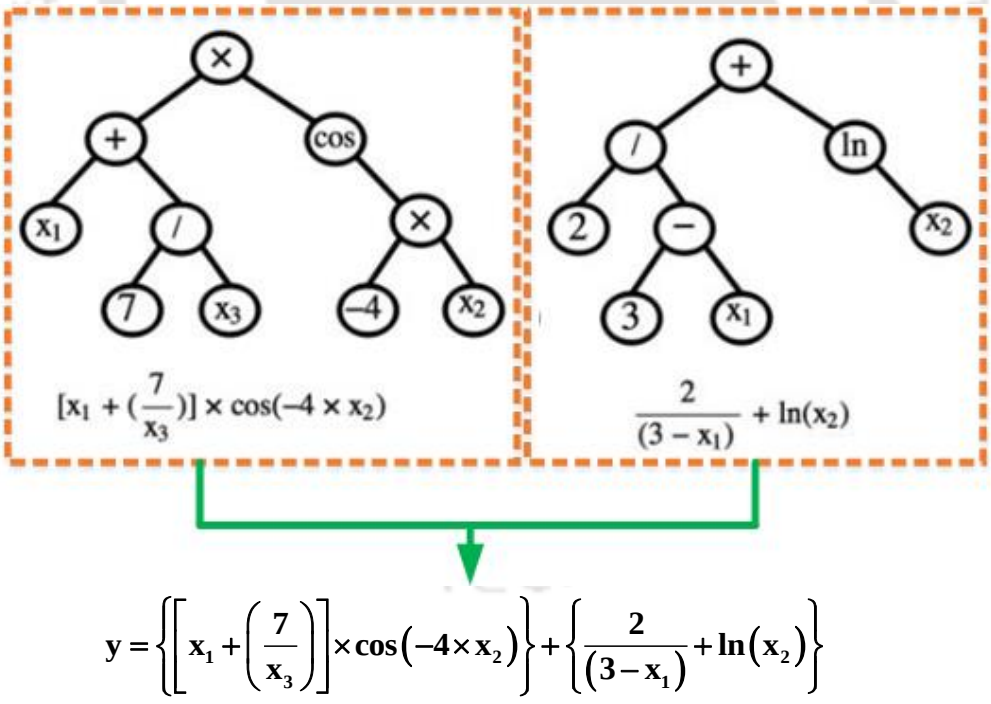

Fig. 6.3: A typical formulation of GEP model with three predictor inputs (linking function: addition)

In these methods, algorithm progresses with higher complexity and may result in infeasible solutions. In order to minimize these problems, Ferreira (2001) gave an effort to introduce the

GEP. GEP is a genotype-phenotype system that mathematically represents the gene and its evolution (Ferreira, 2001). It is the developed version of GA and GP. These models are evolved to find out the solution to the problem based on Darwin's theory of reproduction, crossover, and mutation (Roy et al., 2015). The completed model contains a linear sequence of each gene connected using the linking function (+), as shown in Fig. 6.3. Detailed information about GEP is available in the Appendix C.

6.3. Multi-Objective Optimisation

In general, optimisation technique is used to find the most effective result in terms of highest or lowest achievable performance under certain constraints. Multi-objective optimisation always deals with two or more objective functions where all or even one of the objective must be conflicting or competing to a certain extent, i.e., one objective increases, then other decreases and vice versa. The primary objective of this chapter is to find the optimal process input parameters at which the dehumidifier can provide maximum performance running with LiBr+$CaCl_2$ mixture desiccant solution.

6.3.1. Objective Function for the optimisation

In the present work, three performance parameters are studied for which the optimum independent parameters are to be found out. In order to ensure this, an objective function needs to be defined corresponding to the aim of the problem, explicitly designated as maximising function or minimising function (Li et al., 2019). Another significant part of objective function is definition of constrains for any specific objective function. The range of each independent parameter can be defined based on two most extreme values within the respective parameter dataset. Therefore, the objective function and its constrains can be expressed as functions, $f(\mathrm{X})=\{f_1(\mathrm{X}),f_2(\mathrm{X}),.....,f_n(\mathrm{X})\}$ over the feasible design space. The problem is modelled as follows:

$$\text{Objective Function}: \begin{cases} \text{Maximize}: f(\mathrm{X})=\{f_1(\mathrm{X}),f_2(\mathrm{X}),.....,f_n(\mathrm{X})\}, \\ \text{Or,} \\ \text{Minimize } f(\mathrm{X})=\{1/f_1(\mathrm{X}),1/f_2(\mathrm{X}),.....1/f_n(\mathrm{X})\} \end{cases} \quad (6.7)$$

And, Subjected to $X_k^u \le X_k \le X_k^l$, k= 1,2,.....K.

where $f_1(X), f_2(X), ..., f_n(X)$ are the individual objective functions. X_k^u and X_k^l are the lower and upper bounds of X_k, respectively.

6.3.2. Fuzzy logic based inference system using genetic algorithm

In an actual scale, LHR value (0.692 to 0.825) is small enough to compare with other parameters, due to which it may get neglected during the simulation process. Therefore, parameters are normalised in order to minimise the influence of any particular parameter with others using Eq. (6.8).

$$N_i = \left(\frac{\Psi_i - \Psi_{min}}{\Psi_{max} - \Psi_{min}} \right) \quad (6.8)$$

where $\psi_i = \psi_1, \psi_2..., \psi_n$ and N_i are the i^{th} normalised data. Then, all values come under the range of [0,1]. Fuzzy logic optimisation is based on the fuzzy set theory, which consists of fuzzy sets instead of classical crisp sets (Kang et al., 2015; Wedding, 2002). For instance, a fuzzy set F in universe of discourse Y, which is characterised by a membership function $\mu_F(y)$: Y [0, 1], and the grade of $\mu_F(y) \in [0, 1]$ that convey the value of y in fuzzy set F. Then the fuzzy set F is represented mathematically as

$$F = [(y, \mu_F(y)] \quad (6.9)$$

or

$$F = [\mu_F(y_1), \mu_F(y_2), \mu_F(y_3), ..., \mu_F(y_m)] \quad (6.9a)$$

where $y \in Y$ and m are number of fuzzy variables. Fuzzy logic mapping comprises predominantly three processes, namely: fuzzification, fuzzy inference (fuzzy implication and fuzzy aggregation) and defuzzification. Fuzzification is the process through that different linguistic variables; linguistic values are fuzzified by assigning different types of fuzzifiers (membership functions) and by assigning different fuzzy set operations. The main aim of this process is to convert the linguistic variables into fuzzy variables. Subsequently, the rule-base fuzzy set is designed. The rule-base of fuzzy controller comprises of a set of rules, called "If

and Then" rules. Generally, IF conditions are called the antecedents (inputs) and the THEN condition is consequents (outputs). In the present study, the three antecedents y_1 (CR), y_2 (ε_m) and y_3 (LHR), and one consequents z (MPCI) is considered, as

Rule 1: If y_1 is F_1 AND y_2 is G_1 AND y_3 is H_1 THEN z is I_1

Rule 2: If y_1 is F_2 AND y_2 is G_2 AND y_3 is H_2 THEN z is I_2

Rule 3: If y_1 is F_3 AND y_2 is G_3 AND y_3 is H_3 THEN z is I_3

. . . .

. . . .

. . . .

Rule m: If y_1 is F_m AND y_2 is G_m AND y_3 is H_m THEN z is I_m

Each row of the fuzzy rules, F_i, G_i, H_i and I_i are the fuzzy subsets (F, G and H are CR, Ɛm and LHR, respectively, and I is fuzzy set of MPCI) defined by respective membership functions $\mu_{F(i)}$, $\mu_{G(i)}$, $\mu_{H(i)}$, and $\mu_{I(i)}$, where, y_1, y_2, y_3 and z are the fuzzy grades of fuzzy sets F, G, H and I, respectively. In order to evaluate each rule, Mamdani fuzzy implication process is used, where, the triangular memberships for different fuzzy sets are considered because it covers more range and easy to implement for the current problem. Then the rules can be mathematically expressed as follows (Wedding, 2002):

$$\mu_{FG}(y,z)= \min [\mu_F(y), \mu_G(z)] \quad (6.10)$$

Subsequently, the results of all rules are analysed by fuzzy aggregation process. In this process, disjunctive aggregation of fuzzy rules is used and aggregated the outputs using fuzzy union of all individual rules, which can be mathematically expressed as (Wedding, 2002)

$$\mu_F(y)= \mu_F(y_1)+ \mu_F(y_2)+ \mu_F(y_3)+\ldots\ldots\ldots\ldots+\mu_F(y_m) \quad (6.11)$$

After the fuzzy inference process, the output result is obtained as fuzzy variables. Hence, defuzzification is required to convert the fuzzy variables into its absolute value. In defuzzification process, the centre of area (centroid) method is used to accomplish the defuzzification for obtaining non-fuzzy (crisp) value z_0 (Pombeiro et al., 2017; Wedding, 2002)

$$z_0 = \frac{\sum y^* \left[\mu_F(y)\right]}{\sum \left[\mu_F(y)\right]} \tag{6.12}$$

where $y^*$is centroid of each of the membership function. The obtained defuzzified output (z_0) is known as MPCI, which is used for obtaining the optimum process parameter value. Subsequently, different process parameters are calculated corresponding to the respective constraints for particular MPCI with the help of genetic algorithm.

6.4. Results and Discussion

6.4.1. Artificial neural network architecture

In this present study, sixteen experimental datasets are utilized for modelling. The six parameters, i.e., T_a, F_a, F_s, ω_a, T_s, and ξ are used as network inputs. In order to provide a precise and robust model, CR, ε, and LHR were approximated explicitly using a multi-layer perceptron neural network system. In order to train the model, the present work applied a conventional feed-forward neural network equipped with a back prop learning algorithm. From the complete datasets, 70% is randomly designated as the training group, and 30% of the left over datasets are used for testing and validation. A variety of training functions are used to train the ANN algorithm in order to achieve a satisfactory accuracy during prediction.

Finally, it is noticed that TrainLM training function is more suitable for the present study. Both the output and hidden layers employed a tangent sigmoid transfer function. Subsequently, to prevent over-fitting while the networks were trained, 15% of the data samples are assigned to validation testing and the outstanding 15% of the data samples are reserved for testing the trained networks. However, due to the complexity of the current problem, the networks with only one hidden layer were unsuccessful because of a significant residual present between the corresponding experimental and the predicted datasets despite of the others set parameters. Therefore, networks composed of more than one hidden layer is chosen for testing and evaluation to achieve the necessary precision. After applying ANNs with two hidden layers, a change in the quantity of neurons in the layers was noted (between 1-12). Subsequently, the optimal network topology is 5-10-10-3 (i.e., 5 input neurons in layer 1, 10 neurons in hidden layer 1, 10 neurons in hidden layer 2, and 3 output neurons) for the ε, CR, and LHR, as shown in Fig. 6.4.

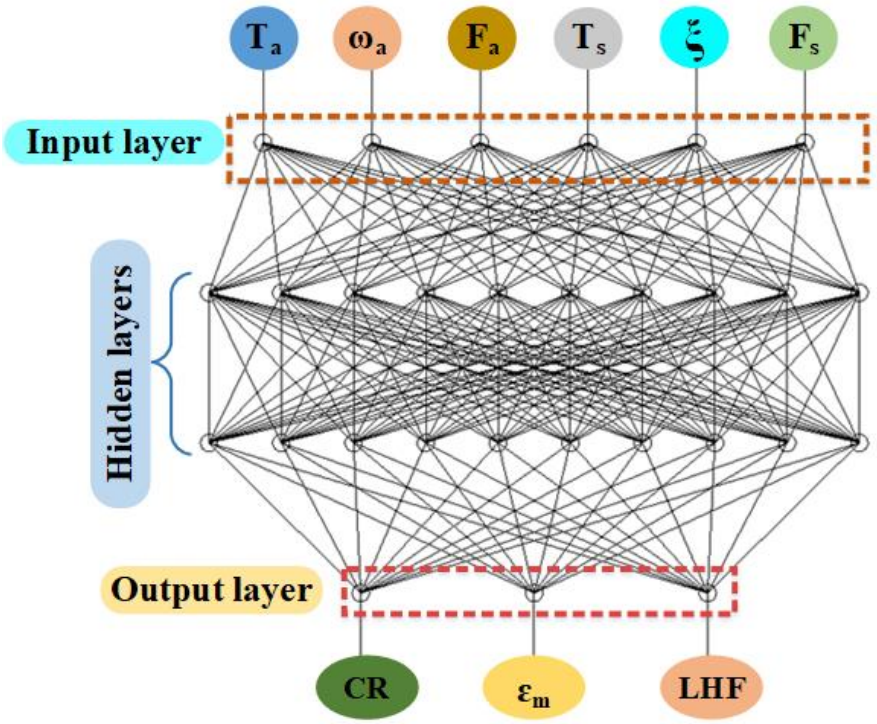

Fig. 6.4: Architecture of proposed ANN model (6-10-10-3: Two hidden layers with ten neurons each)

6.4.2. Adaptive neuro-fuzzy inference system architecture

Adaptive neuro-fuzzy inference system (ANFIS) is an artificial intelligent algorithm that integrates the fuzzy logic (FL) theory and adaptive neural network (ANN) rules inside the adaptive network frameworks. The ANFIS is used in the present study to predict the performance of the dehumidifier/regenerator. ANFIS is drawing a relation between the input and output datasets. In the present study, T_s, T_a, ω_a, F_a, F_s and ξ are chosen as input parameters to the ANFIS whereas, ε_{lat}, LHR and CR (for dehumidifier) and ε_{sen}, ε_{lat} and ER (for regenerator) are considered as the prediction parameters (output). The ANFIS structure designed with five different layers, these are input layer (input), input membership function layer (inputmf), rule layer (rule), output membership function layer (outputmf) and the final output layer (output). In the current study, different network has been built and tested to get the optimum configuration and to search for the best possible combination of input parameters that produce the target result with greater accuracy. The configuration parameters which required to be modified to improve the proficiency of the ANFIS model are the types of input MFs, number of membership functions (MFs), optimization methods (hybrid or back-propagation), type of output MFs (linear or constant) and the number of epochs (Betiku et al., 2016). Five

different common shapes of membership functions (i.e., triangular, trapezoidal, Gaussian, sigmoid and bell-shaped) and different number of input membership functions are altered. The comparison of five different membership functions designates that Gaussian type membership function accomplishes slightly superior predicting accuracy than others. For every input variable, nine membership functions have been considered. Consequently, nine numbers of fuzzy rules and logical AND operator are found to be suitable to express the dehumidifier/regenerator output parameters.

In the present ANFIS model, fuzzy logic membership functions are adjusted using a hybrid learning algorithm that is a back-propagation gradient descent method combined with least-square method for adapting to the required environments. Such a hybrid learning system makes ANFIS a well-organized mode for learning non-linear functions and, subsequently, becomes a robust and efficient predictor. In a conventional fuzzy system, IF-THEN based relationship between the output and input is crafted manually. Conversely, ANFIS is adaptive and can automatically adjust the fuzzy membership rules as per the need of the system and makes the model robust. Simultaneously, the outcomes are patterned by the factors in the layout of the Sugeno category IF-THEN rules. The final ANFIS architecture for the present study is depicted in Fig. 6.5. The membership function specifies how every attribute in the input domain is patterned to a membership value. The ANFIS operation is performed in MATLAB® 2015b. Detailed information about ANFIS is available in the literature (Betiku et al., 2016; Boyacioglu and Avci, 2010; J. S. R. Jang, 1993).

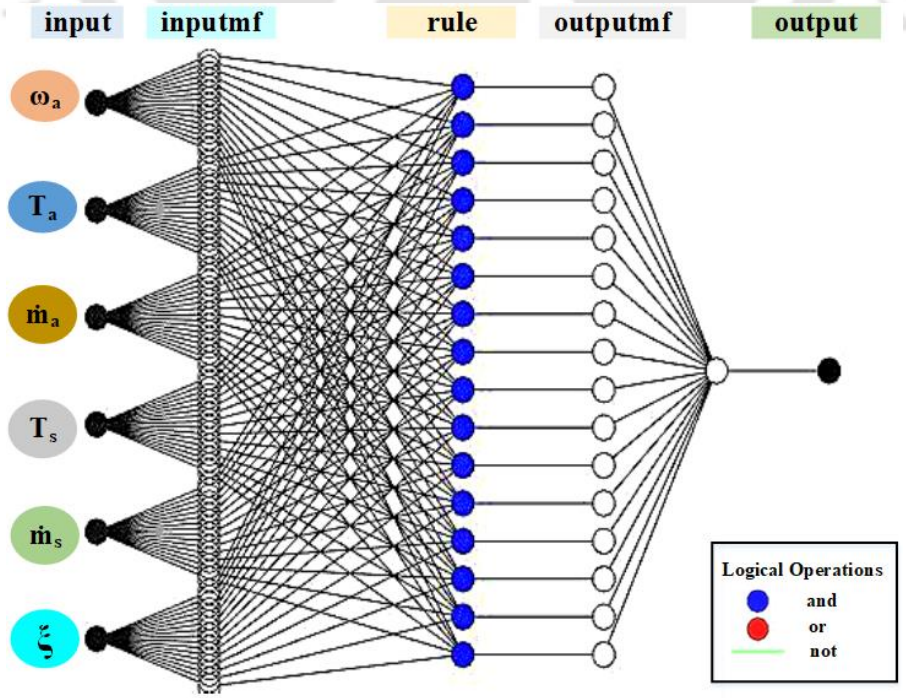

Fig. 6.5: Network architecture for ANFIS

6.4.3. Gene expression programing model architecture

The optimum parameter for number of genes, head size and number of chromosomes are presented in Table 6.2. The mathematical equations can be derived by reading the circles from top to bottom and left to right from the expression trees, which are represented in Appendix C and mathematical equations are represented in Eqs. (6.13–6.15). The mathematical functions and operators used for the prediction and development of the mathematical model are Addition (+), Cosecant (Csc), Cosine (Cos), Cotangent (Cot), Division (/), Natural logarithm (Ln) Inverse (Inv), Multiplication (*), Secant (Sec), Sine (Sin), Subtraction (-), Tangent (Tan), x to the power of 2 (X2), x to the power of 3(X3) and x to the power of 4 (X4).

Table 6.2: Optimum values for GEP parameters

Parameter type	**Parameters**	**Value**
General settings	Generation size	600,000
Chromosomal architecture	Number of chromosomes	30
	Number of genes	3 (for CR model)
		3 (for ε_{lat} model)
		5 (for LHR model)
	Head size	8
	Linking function	Multiplication (for CR model)
		Addition (for ε_{lat} model)
		Addition (for LHR model)
Genetic operators	Mutation rate	0.044
	Gene transposition rate	0.1
	One-point recombination	0.3
	Two-point recombination	0.3
	IS Transposition	0.005
	RIS Transposition	0.005
	Inversion rate	0.1
	Gene recombination rate	0.1

$$\begin{aligned}\mathrm{CR}\left[\mathrm{g/m^2-s}\right] = &\left(\left(\left(\cot\left(T_s\right)+\zeta\right)+\left(3.746\ F_s\right)\right)-\left(F_s\times\cos\left(\zeta\right)\right)\right)\\ &\times\left(F_a\ln\left(\left(\left(\ln\left(\left(F_a-0.50958\right)\right)+\left(0.4538-T_s\right)\right)^2\right)\right)\right)\\ &\times\left(\left(F_a+\left(\ln\left(\left(T_s\times F_s\right)\right)/\left(-8.5004+T_a\right)\right)\right)\times\omega_a\right)\end{aligned} \tag{6.13}$$

$$\begin{aligned}\varepsilon_{lat}\left[\%\right] = &\cot\left(\left(\left(\csc\left(\left(1/6.9316\right)\right)\right)/\sec\left(6.86635\right)\right)\times\zeta\right)\\ &+\left(\left(\cos\left(\left(\left(1.69729^4\right)\times\left(F_a-T_s\right)\right)\right)/F_s\right)+T_a\right)\\ &+\left(\left(\left(\sec\left(F_a\right)/\csc\left(F_s\right)\right)/\omega_a\right)/\cot\left(\left(F_a{}^4\right)\right)\right)\end{aligned} \tag{6.14}$$

$$\begin{aligned}\mathrm{LHR}\left[-\right] = &\left(\omega_a/\left(\left(\cos\left(4.0954\right)+\left(\csc\left(\cos\left(T_a\right)\right)^3\right)\right)+\csc\left(\left(F_s{}^4\right)\right)\right)\right)\\ &+\cot\left(-1.45359\right)\\ &+\left(\left(\cos\left(\sin\left(F_s\right)\right)+\cot\left(-2.92641\right)\right)/\left(\cot\left(\sin\left(F_s\right)\right)+\left(\left(\omega_a-\zeta\right)-\left(F_s{}^3\right)\right)\right)\right)\\ &+\left(\left(\left(\sin\left(\left(\cos\left(\left(-3.283+F_s\right)\right)\times\left(\sin\left(-6.59046\ F_a\right)\right)\right)^3\right)\times\cos\left(T_a\right)\right)+\omega_a\right)\right)\\ &+\cos\left(\left(\cot\left(\left(\cos\left(\sec\left(T_s\right)\right)-\left(\zeta^4\right)\right)\right)\times\left(\left(\omega_a\times\sec\left(T_a\right)\right)\times F_a\right)\right)\right)\end{aligned} \tag{6.15}$$

Similarly, the GEP meta-models of ER, ε_{lat} and ε_{sen} are represented in Eqs. (6.16 - 6.18) for the regenerator.

$$\begin{aligned}\mathrm{ER} = &529.91+0.237T_s-0.107/\dot{m}_a+36.865\omega_a\xi+0.001\dot{m}_s+147357.61{\omega_a}^2\\ &-19.31T_a-0.0173\xi^2\end{aligned} \tag{6.16}$$

$$\begin{aligned}\varepsilon_{lat} = &1.61+0.001\omega_a+42.052\dot{m}_a^2-0.00397T_s-9.355\dot{m}_a+0.001\xi-0.0694\dot{m}_aT_a\\ &-51.51\dot{m}_a^3+0.001\dot{m}_s\end{aligned} \tag{6.17}$$

$$\varepsilon_{sen} = 64.81 + 0.001\dot{m}_s + 0.149\xi + \left(44.66/\xi\right) + \left(0.000676/\dot{m}_a^2\right) + 0.001\omega_a - \left(360.822/(0.0568 + 0.3145T_a)\right) - 0.00167\xi^2 + 0.001T_s - 1.031T_a \quad (6.18)$$

6.4.4. Performance evaluation and validation

The purpose of AI methods to map the system performance parameters, and it was noted that the established AI models had been tested on a statistical platform. The coefficient of determination, R has measured the prediction accuracy, and the best-generated models are those with R ⩾ 0.8. Later, Armstrong and Fildes (1995) suggested that there is no single statistical parameter that would measure the model accurately in the sense of capturing the necessary complexity of experimental data. Therefore, it is imperative to simultaneously consider multiple criteria and evaluate model applicability based on various respective criteria.

Table 6.3: Statistical parameters of the developed AI models for the external validation

Parameters	**CR**	**ε_{lat}**	**LHR**
R	ANN-0.981 ANFIS-0.994 **GEP-0.997**	ANN-0.96 ANFIS-0.983 **GEP-0.9997**	ANN-0.971 ANFIS-0.994 **GEP-0.996**
R^2	ANN-0.962 ANFIS-0.988 **GEP-0.995**	ANN-0.921 ANFIS-0.966 **GEP-0.999**	ANN-0.943 ANFIS-0.988 **GEP-0.993**
KGE	ANN-0.967 ANFIS-0.988 **GEP-0.99**	ANN-0.933 ANFIS-0.963 **GEP-0.996**	ANN-0.955 ANFIS-0.988 **GEP-0.994**
NSE	ANN-0.96 ANFIS-0.986 **GEP-0.994**	ANN-0.908 ANFIS-0.966 **GEP-0.997**	ANN-0.943 ANFIS-0.987 **GEP-0.993**
MAE	ANN-0.005 ANFIS-0.003 **GEP-0.002**	ANN-0.005 ANFIS-0.003 **GEP-0.001**	ANN-0.009 ANFIS-0.004 **GEP-0.003**
MAPE	ANN-2.8% ANFIS-1.7% **GEP-0.9%**	ANN-0.7% ANFIS-0.4% **GEP-0.2%**	ANN-5.3% ANFIS-2.4% **GEP-1.5%**
RMSE	ANN-0.007 ANFIS-0.004 **GEP-0.003**	ANN-0.007 ANFIS-0.004 **GEP-0.001**	ANN-0.013 ANFIS-0.006 **GEP-0.005**
nRMSE	ANN-0.041 ANFIS-0.024 **GEP-0.015**	ANN-0.01 ANFIS-0.006 **GEP-0.002**	ANN-0.071 ANFIS-0.034 **GEP-0.025**

A significant quantity of goodness-of-fit indices in each estimation process is presented to determine the model robustness with the empirical data (Schermelleh-Engel and Müller, 2003). Therefore, in the present study, several statistical parameters are calculated founded on both

the model and experimental outcomes for evaluating the developed models' performance (Chen and Yang, 2004; Roy et al., 2014a). Deb et al. (2016) used some set of criteria for their proposed models when testing the external verification of models. Their proposition suggested that the KGE between the predicted (t_i) and actual data (h_i) should be near 1, and the error indices like MAPE and RMSE should be less than 0.1. Roy et al. (2014a) also used one performance parameter called NSE for external predictability assessment of m1dels. It was shown that the model validation criterion is NSE ~ 1. The external validation value for different statistical parameters for the developed models are shown in Table 6.3.

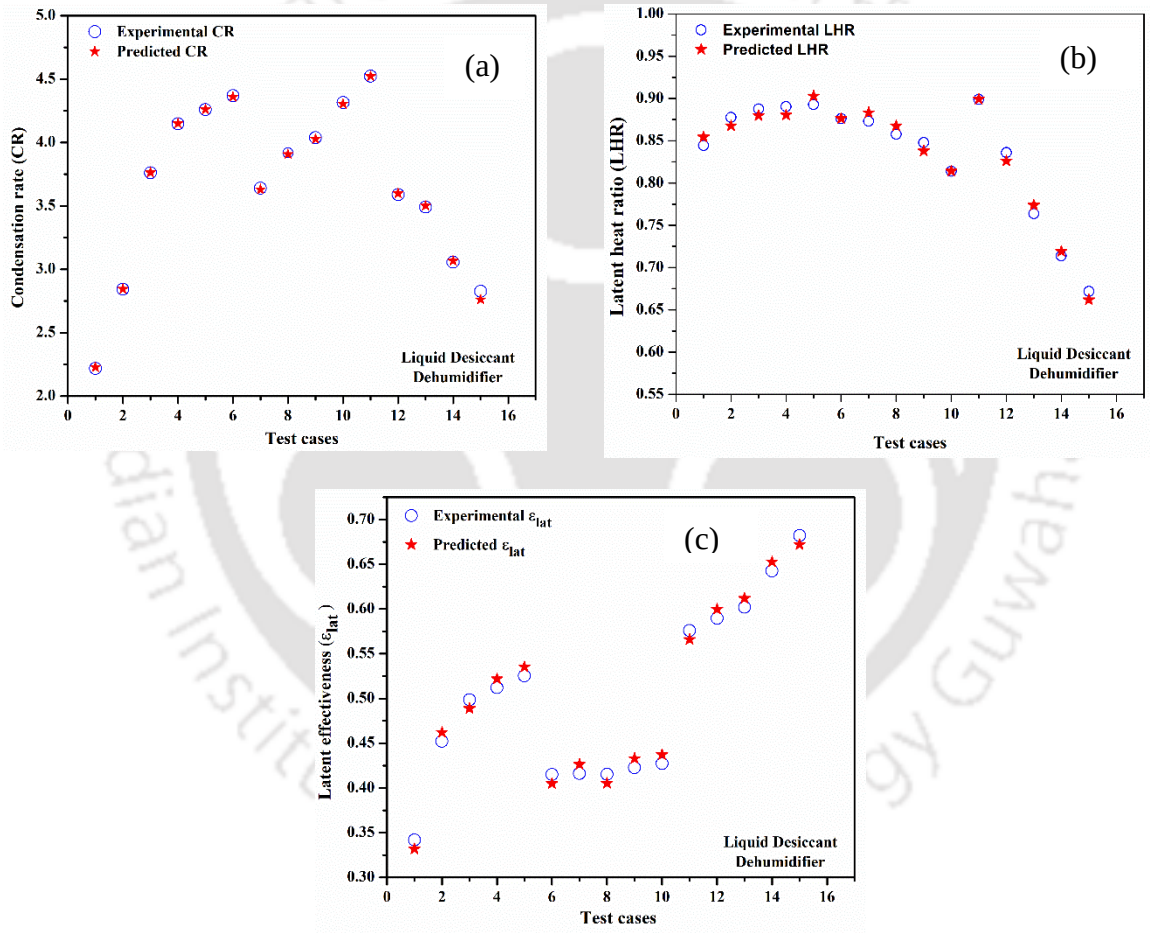

Fig. 6.6: Comparison of GEP predicted results with the experimentally measured results of the dehumidifier (a) CR, (b) LHR and (c) ε_{lat}

Finally, ANFIS, GEP and ANN results are validated against the acquired experimental datasets for all cases, as shown in Figs. 6.6-6.7. Figs. 6.6-6.7 depict the CR, ε_{lat} and LHR of predicted values obtained from ANN, GEP, ANFIS models with the experimental results, respectively.

The assessment patterns of the three AI models are similar to the experimental pattern for all dehumidifier performance parameters. After an in-depth study of Figs. 6.6-6.7, the consistent concurrency of the values predicted by the GEP model is able to predict with higher accuracy with actual investigational results. The attained findings indicated that GEP outcomes show superior performance than the ANN, ANFIS models in predicting the response variables. It was observed that the GEP-model prediction of the output of the dehumidifier parameters provided remarkable correlation statistics in comparison to ANN and ANFIS models (Table 6.3). The maximum deviation between the GEP and the experimental value of the CR, ε_{lat} and LHR is ± 1.5%, ± 0.28% and ± 1.8%, respectively. It is noted that Theil U2 value for CR, ε_{lat} and LHR for GEP models is 0.0144073, 0.001856 and 0.021942, respectively. Similarly, a comparison of GEP predicted results with the experimental results of the regenerator showed a maximum deviation of 1.5%.

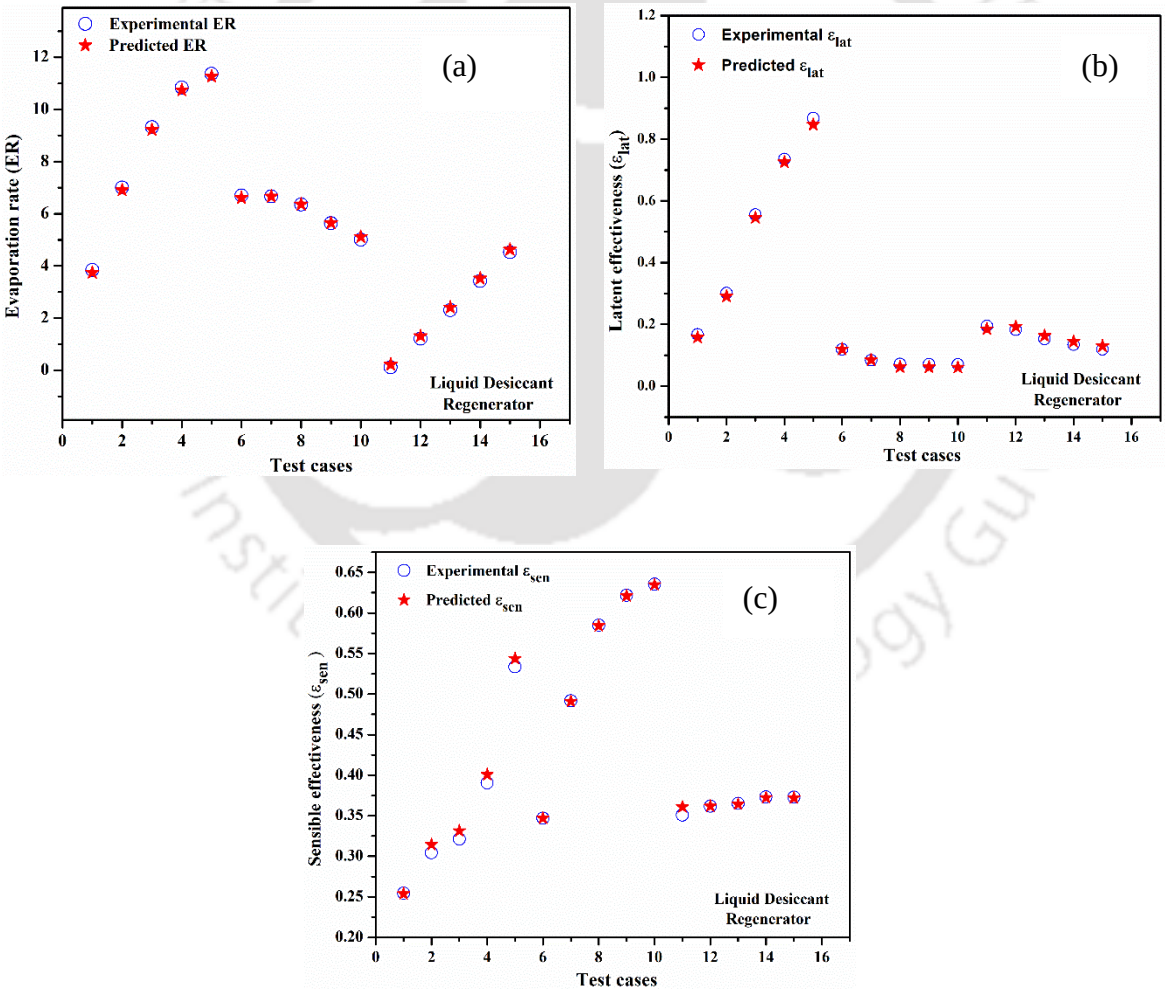

Fig. 6.7: Comparison of GEP predicted results with the experimentally measured results of the regenerator (a) ER, (b) ε_{lat} and (c) ε_{sen}

6.4.5. Optimization of dehumidifier/regenerator inlet parameters

6.4.5.1. Effects on CR, ε_{lat} and LHR

The experimental tests were carried out using different concentrations of LiBr+$CaCl_2$ mixture in a dehumidifier with different control settings and the performance characteristics, namely CR, ε_m and LHR, were calculated after each operation. The pure LiBr desiccant operation measured CR, ε_m, and LHR as 1.65 g/m^2-s, 36.28% and 0.693, respectively (when 0.5532 kg/m^2-s of F_a; 30.1°C of T_a; 0.0219 kg_{wv}/kg_{da} of ω_a; 0.5532 kg/m^2-s of F_s; 24.5°C of T_s and 30.4 %wt. of ζ). However, when 0.5242 kg/m^2-s of F_a, 32.1°C of T_a, 0.026 kg_{wv}/kg_{da} of ω_a, 0.786 kg/m^2-s of F_s, 26.6°C of T_s and 30.4 %wt. of ζ, the estimated values CR, ε_{lat}, and LHR were 1.822 g/m^2-s, 37.27% and 0.739, respectively. Number of experiments were preliminarily performed to test the performance parameters under different mixed desiccant operations. It was observed that mixed LiBr and $CaCl_2$ desiccant considerably increased the condensation rate, whereas the moisture effectiveness and latent heat factor were comparable with pure LiBr. The mixture desiccant operation results are shown in Table 6.4.

Table 6.4: Experimental results of mixed desiccant system

Case no	Independent variables (d)						Performance parameters (R)		
	F_a [kg/m^2-s]	T_a [°C]	ω_a [kg_{wv}/kg_{da}]	F_s [kg/m^2-s]	T_s [°C]	ζ [wt.%]	CR [g/m^2-s]	ε_{lat} [%]	LHR
1	0.553	29.8	0.0225	0.553	24.64	30.4	1.711	34.55	0.696
2	0.544	29.6	0.0228	0.544	24.5	40.1	2.395	32.89	0.762
3	0.534	28.4	0.0216	0.534	23.4	40.2	2.213	32.22	0.757
4	0.795	29.1	0.0208	0.397	23.8	47.8	4.681	38.68	0.772
5	0.524	32.1	0.0264	0.262	26.7	48.1	2.704	26.10	0.780
6	0.524	31.4	0.0257	0.786	26.3	30.4	2.015	36.04	0.741
7	0.620	31.3	0.0234	1.240	26.4	40.1	3.357	42.10	0.783
8	0.524	32.1	0.0262	0.786	26.5	40.2	2.838	34.77	0.779
9	0.710	31.3	0.0241	0.533	26.0	47.8	4.729	37.82	0.796
10	0.713	30.9	0.0240	1.248	25.74	48.1	5.522	43.61	0.816
11	0.754	28.9	0.0213	1.130	23.8	30.4	3.119	48.84	0.722
12	0.524	28.8	0.0217	1.048	23.3	40.1	2.456	35.98	0.758
13	0.778	29.1	0.0215	1.945	23.94	40.2	5.074	52.16	0.789
14	0.524	28.9	0.0215	1.442	23.9	47.8	2.879	34.56	0.793
15	0.539	28.8	0.0215	1.618	23.4	48.1	2.749	31.49	0.779
16	0.524	28.7	0.0215	1.310	23.54	55.1	2.982	30.46	0.828

However, such high condensation rate may be due to higher thermal diffusivity of $CaCl_2$ compared to pure LiBr. Accordingly, the temperature of solution changes appreciably during

the mass transfer operation and hence the equilibrium vapour pressure difference remains high between the desiccant and air. Moreover, CR values increase with concentration and decrease with higher solution temperature, which makes a higher tendency of water vapours present in air to condense into the liquid phase desiccant solution. As per the kinetic theory of gas, fewer molecules can escape from the liquid surface into the gas phase at higher concentration and lower temperature of solution. Hence, the vapour pressure of the solution is decreased. The F_a, T_a, ω_a, F_s and T_s value almost kept the same for case 1 and 2, whereas, the solution concentration (ζ) was increased from 30.4% to 40.1% for case 2. The higher value of desiccant concentration in the dehumidifier signifies the higher vapour pressure difference between the air and desiccant surface. Therefore, the desiccant would have a higher tendency to condense the water vapours present in air into the liquid phase desiccant solution. Hence, the CR value was increased for case 2 as compared to case 1. Conversely, ε_{lat} is the ratio of actual change in specific humidity across the dehumidifier to the maximum possible change in air specific humidity at the same operating condition. For case 2, the maximum possible change in air specific humidity is increased due to higher desiccant concentration as compared to case 1. So that, the ε_{lat} value was decreased for case 2 as compared to case 1. However, due to the higher vapour pressure difference between the air and desiccant surface, the outlet air humidity ratio becomes lower for case 2 than case 1. Besides, higher concentrated desiccant solution may release higher absorption heat and as a result, outlet air temperature value was increased. Hence, higher LHR for case 2 as compared to case 1. $CaCl_2$ based mixed desiccant experiments revealed that mixed desiccant could overcome the inherent paradox of simultaneously increasing condensation rate and comparable moisture effectiveness and LHR in dehumidifier operation for all cases of mixture operation compared with pure LiBr operation (Table 6.4).

Table 6.4 depicts the parametric design space provided by test cases examined during experimentation. Fig. 6.8 exhibits the sampling design space produced for particular input parameters mentioned in Table 6.4. In Fig. 6.8, the abscissa and ordinate shows the number of runs and ranges of CR, respectively. The ε_{lat} and LHR can be visualised by the colour code and bubble diameter (where large diameter represents the large value, 0.82), respectively. Further, Fig. 6.8 expresses that all performance parameters are not maximum for any given set of data. In other words, performance parameters are maximum at the different composition / operating conditions of the process. In order to overcome from this complexity, a trade-off analysis among the performance parameters (ε_m-CR-LHR) is also investigated to rationalise the effectiveness of the liquid desiccant dehumidifier. This is because the coupled heat and mass

transfer process is complicated in nature where the output air/ desiccant solution temperature is varying for different composition/operating conditions due to different rate of sorption and sensible heat release. In some operation/composition, the sorption heat is dominated over sensible heat and in some cases, sensible heat between the air and desiccant is dominated. Therefore, there is a strong need for multi-objective optimisation to get the maximum performance for a particular inlet setting.

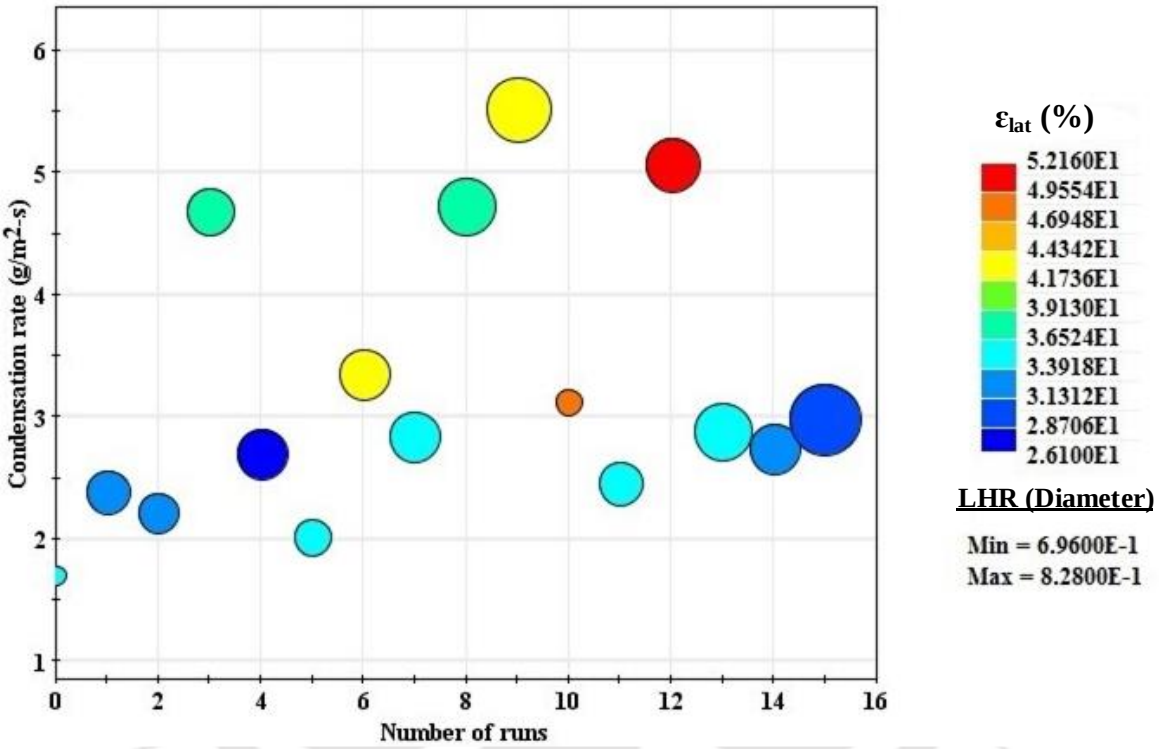

Fig. 6.8: Parametric design space produced by test cases examined during experimentation

6.4.5.2.Sensitivity Analysis

Sensitivity analysis is a method to identify the relative influence of each independent parameter on the respective performance parameter. As the coupled heat and mass transfer phenomena is complicated in nature, and so all six independent parameters are considered for the present study. The input parameters are air temperature, air specific humidity, mass flux rate of air, solution temperature, solution mass flux rate, solution concentration, and the output parameters are condensation rate, moisture effectiveness and latent heat factor. In order to accomplish the sensitivity analysis, the cosine amplitude method (Zendehboudi et al., 2017) is adopted for the

present study. Each pattern (i.e., input-output pair) can be written in common X-space. The data pairs used to construct a data array X are defined as:

$$X = \left\{ x_1, x_2, x_3, ..., x_i, ..., x_n \right\} \tag{6.19}$$

The elements x_i in the array X is a vector of lengths of m:

$$x_i = \left\{ x_{i1}, x_{i2}, x_{i3}, ..., x_{im} \right\} \tag{6.20}$$

The expression of this method is denoted as:

$$R_{ij} = \frac{\sum_{k=1}^{n} \left(\chi_{ik} \times \chi_{jk} \right)}{\sqrt{\sum_{k=1}^{n} \chi_{ik}^2 \sum_{k=1}^{n} \chi_{jk}^2}} \tag{6.21}$$

In this expression, *n* symbolises the number of data points, χ_i represents the input variables, and χ_j stands for output variables. The resulting value from this method ranges from 0 to 1. Commonly, a value closer to 1 indicates that the input has a higher impact on the corresponding output. The effect of each independent parameter on the performance parameters (i.e., input-output pair) is shown in Fig. 6.9. It is observed from Fig. 6.9 that the air mass flux rate, solution concentration as well as specific humidity have a significant impact on the CR. Similarly, it is observed that the air mass flux rate and solution temperature have the most significant effect on ε_m. Further, it is also found that air temperature and solution temperature are the most effective parameters, whereas solution mass flux rate is the least effective parameters for LHR. (Fig. 6.9).

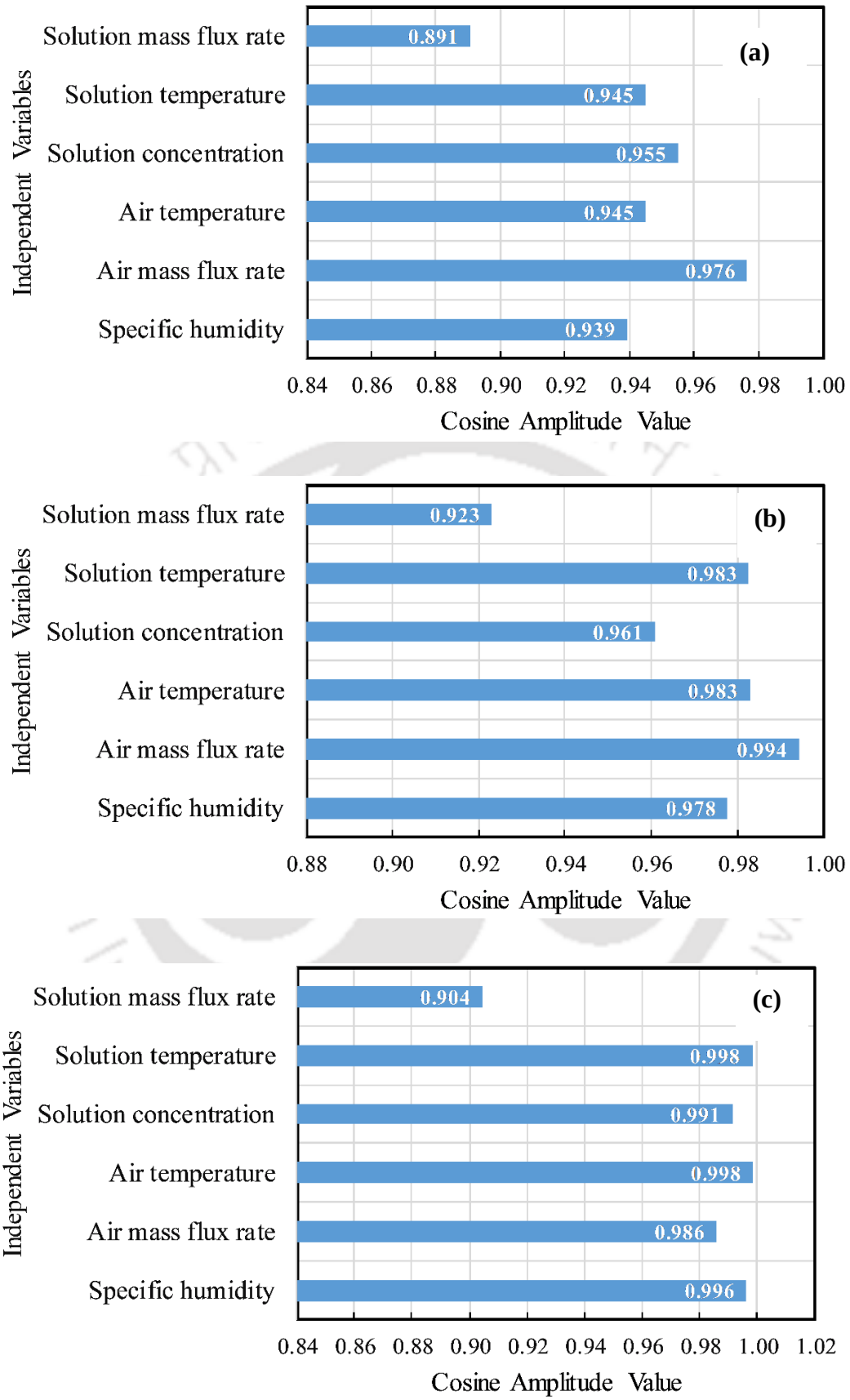

Fig. 6.9: Sensitivity analysis of independent parameters on dehumidifier performance parameters (a) CR (b) ε_m (c) LHR

6.4.5.3. Optimisation Results and Validation

The simulation is performed in MATLAB environment, where three models of CR, ε_m and LHR obtained from GEP are coded in MATLAB® 2015b (computer configuration: RAM: 8GB, HD:500 GB, Intel(R) HD Graphics 4600) and fuzzy rules are also coded and fitted in the form of fuzzy inference system (FIS). In the present study, the developed GEP equations (Eqs. 6.13-6.15) are considered as objective functions. Subsequently, a new model is developed by combining three GEP models and one fuzzy rule-sets model and run in genetic algorithm with a random generation size. The final optimal control settings and genetic parameters for the present LDCs are mentioned in Table 6.5.

Table 6.5: Details of model parameters developed on MATLAB

Parameter type	**Values**
Topology	4 Input (3 GEP Model and 1 Fuzzy Model)
Active function	Optimtool
Elite count	0.05×Population size
Population type	Double vector
Crossover function	Constraint dependent
Mutation function	Constraint dependent
Migration fraction	0.2
Migration direction	Forward
Stopping criteria	200 (Generation)
Function tolerance	1.00e-06
Penalty factor	100

Fig. 6.10 shows the fitness value against the number of generation during optimisation algorithm, where points (red) at the bottom denote the best fitness values, while points above them (blue) denote the averages of the fitness values in each generation. The proposed GEP-Fuzzy-GA algorithm performs better in terms of convergence, as the fitness value reaches convergence before 200 generations with less than 5 min of computation time. The computation time of GEP-Fuzzy logic is competitive with the one used by original GA algorithm. Moreover, from Fig. 6.10, it can be noticed that the objective function gradually decreases to 55 generations and then becomes stable. Finally, fitness value is obtained as 1.17 within the generation size of 200. However, this has confirmed the tendency of optimality for dehumidifier performance spectrum with F_a = 0.766 kg/m^2-s, T_a = 30.745 °C, ω_a = 0.023 kg_{wv}/kg_{da}, F_s = 1.812 kg/m^2-s, T_s = 24.01°C and ζ = 48.1%, for which calculated CR, ε_m and

LHR are 5.875 g/m^2-s, 48.65% and 0.82, respectively. Subsequently, the experiments were conducted in a dehumidifier by maintaining the optimum process parameters (when, 0.765 kg/m^2-s of F_a, T_a = 30.1°C, ω_a = 0.024 kg_{wv}/kg_{da}, F_s = 1.8 kg/m^2-s, T_s = 24°C and ζ = 48%) to ensure the robustness and accuracy of such optimisation approach for real-time implementation. The experimental results showed optimum CR of 5.584 g/m^2-s, ε_m of 42% and LHR of 0.83, which endorses good agreement between model and experimental results (with an error < 8%).

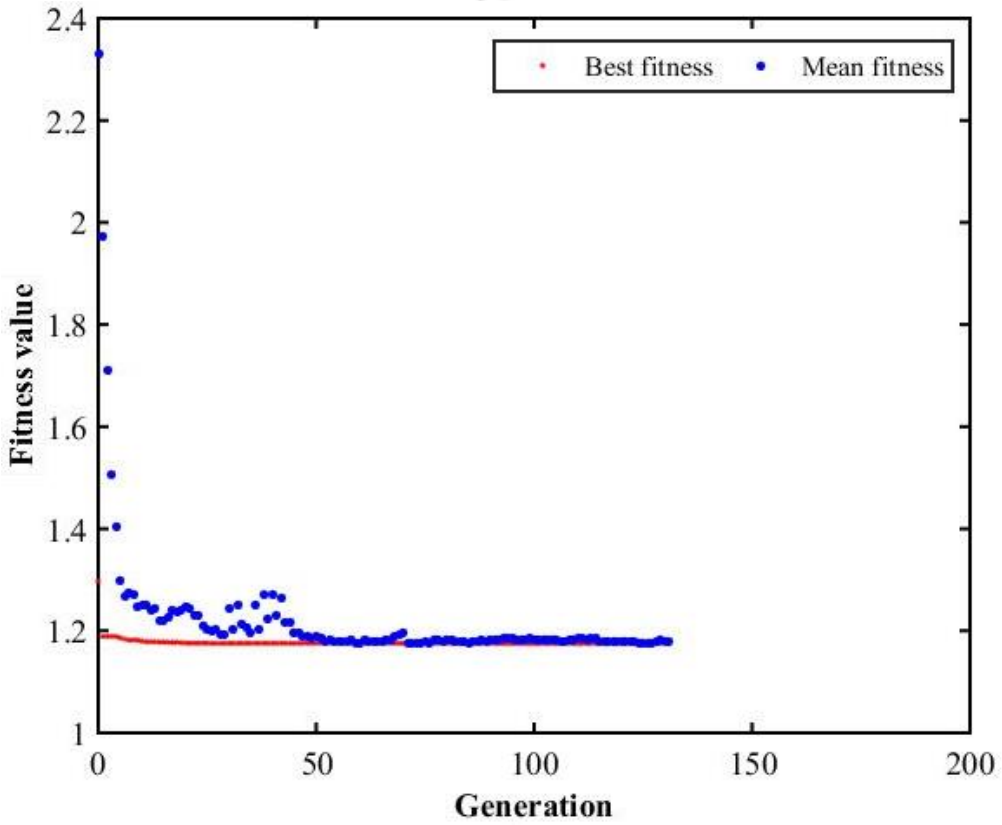

Fig. 6.10: Fitness value points (best and mean) with each generation

Similarly, for regenerator, the computation time of GEP-Fuzzy logic is competitive with the one used by original GA algorithm. It can be noticed that the objective function gradually decreases to 55 generations and then becomes stable. Finally, fitness value is obtained as 1.17 within the generation size of 200. However, this has confirmed the tendency of optimality for dehumidifier performance spectrum with F_a = 0.766 kg/m^2-s, T_a = 30.745°C, ω_a = 0.023 kg_{wv}/kg_{da}, F_s = 1.812 kg/m^2-s, T_s = 24.01°C and ζ = 48.1%, for which calculated CR, ε_m and LHR are 5.875 g/m^2-s, 48.65% and 0.82, respectively. Subsequently, the experiments were conducted in a dehumidifier by maintaining the optimum process parameters (when, 0.765

kg/m^2-s of F_a, T_a = 30.1 °C, ω_a = 0.024 kg_{wv}/kg_{da}, F_s = 1.8 kg/m^2-s, T_s = 24 °C and ζ = 48%) to ensure the robustness and accuracy of such optimisation approach for real-time implementation. The experimental results showed optimum CR of 5.584 g/m^2-s, ε_m of 42% and LHR of 0.83, which endorses good agreement between model and experimental results (with an error < 8%).

6.5. Combined dehumidifier-regenerator experiments and COP of the system

The desiccant solution concentration cannot be randomly changed for a particular application. However, Fig. 6.11 is provided for comparative purposes, demonstrating the impact of desiccant solution concentration on desiccant system performance, when F_a = 0.199 kg/m^2-s, T_a = 34.1°C, ω_a = 0.0272 kg_{wv}/kg_{da}, F_s = 0.497 kg/m^2-s and T_s = 32°C for dehumidifier, while for regenerator, F_a = 0.996 kg/m^2-s, T_a = 34.1°C, ω_a = 0.0272 kg_{wv}/kg_{da} and F_s = 0.497 kg/m^2-s. For a given thermal/total input, desiccant system performance can be represented as the dehumidification output. Moreover, for the solar thermal output, the experiment was carried out during the month of August 2019. The experiment was performed every day for 3 h from 11:00 h to 13:00 h. The maximum solar radiation intensity recorded was in the range of 767–843 W/m^2, during which the efficiencies of U- tube-based evacuated collectors was around 72%. The maximum outlet water temperature of the S-ETC panel was 86°C during the experiment at a flow rate of 0.1 kg/s. Extra 7°C heat was supplied to heat the water by an auxiliary electric heater and finally, water temperature reached 93°C. Fig. 6.11 demonstrates that COP and TCOP increase with desiccant solution concentration. This is due to the fact that for a given thermal/total input, dehumidification output is more for LiBr+$CaCl_2$ desiccant solution. As the operating solution concentration increases, the required regeneration solution temperature was changed from 55°C at a 30% solution concentration to 74°C at a 50% solution concentration. At the same time, the obtained dehumidification output was 1.3 kJ/m^2-s at solution concentration between 30% and 50%. Increasing the solution concentration would increase the affinity of the desiccant solution to absorb more moisture. As the moisture absorbed from process air increases, the dehumidification load removed from the air also increases. This leads to increase in COP_{sys} and TCOP. As higher COP is desirable, lower solution concentration may not necessarily be used. With a thermal input of around 70°C, a solution concentration between 30% and 50% can be selected. When the system concentration was increased from 30 to 50 wt.%, the TCOP value was increased to 1.1, which is 79.3% higher than the TCOP at 30 wt.% solution concentration. The obtained higher COP_{sys} was 0.63, which is 82.2% higher than COP_{sys} at 30 wt.% solution concentration. It can be concluded that a LiBr

+$CaCl_2$ solution is a good choice of working fluid in the liquid desiccant air conditioning system due to its low-temperature regeneration requirement. With the inlet solution concentration of 30 – 50 wt.% and heat source Q_s, the thermal coefficient of performance (TCOP) and system coefficient of performance (COP_{sys}) were found between 0.28 – 0.46 and 0.16 – 0.27, respectively. Therefore, it is in good thermal agreement with the outlet water temperature of the solar evacuated tube collector system.

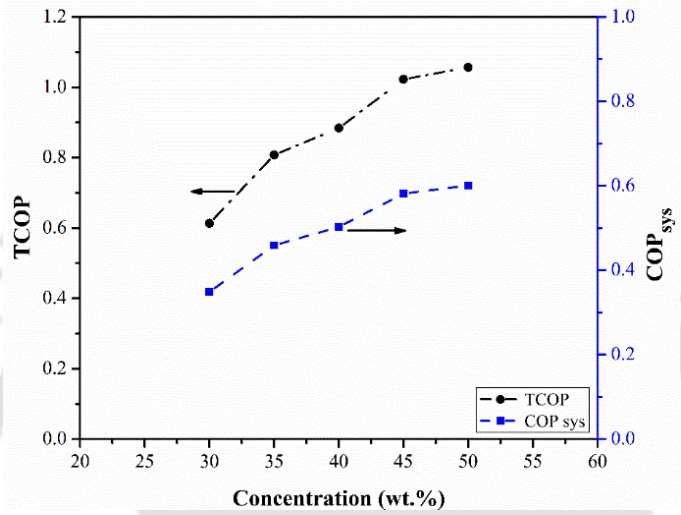

Fig. 6.11: Effect of concentration on thermal COP and system COP

6.6. Closure

The present work deals with the evaluation of performance of a LiCl+$CaCl_2$ liquid desiccant in a counter-flow, packed bed dehumidifier at different operating/working conditions. Based on the dehumidifier experimental performance datasets, AI affiliated models are developed to pattern input-output relationship between the process and performance parameters for different operational strategies. The present study introduces an innovative and specific approach to estimate potentiality of air dehumidification through the application of artificial intelligence (AI) assisted Gene Expression Programming (GEP), Artificial Neural Network (ANN), as well as Neuro-Fuzzy Inference System (ANFIS) models. Experimental results have also been applied and compared with the AI model predictions. Good agreement is observed between the output from AI models and the corresponding experimental datasets with higher precision for the liquid desiccant dehumidifier parameters. Further, the multi-objective optimization for dehumidifier system is developed to explicitly solve the independent parameters of the objective function through evolution within the domain and find the optimum input variables value to formulate the optimal model structure. Meanwhile, the sensitivity analysis is

performed. In this chapter, an experimental study on mixed desiccant system tested with optimised dehumidifier inlet parameters to obtain the maximum performance characteristics is presented. The GEP meta-model is established based on the experimental results. The GEP meta-model is found to possess higher prediction capability as experimental results. The fuzzy logic is made to get the intermediate results within certain constraints which successfully emulated using genetic algorithm. A novel approach is obtained to perform the multi-responsive optimisation by integrating GEP meta-models with fuzzy logic combined GA. The following are the major generic and specific conclusions drawn from the current study.

- The proposed AI models could potentially function as a reliable predictive tool to predict the experimental results. AI models showed a specific, non-linear interpretation of the dehumidifier performance that would provide a relationship to the predictor input data with the response data.
- It is found that the dehumidifier performance parameters can be predicted by ANN (5-10-10-3), ANFIS (5-16-1) and GEP (3-5 genes). Subsequently, it is observed that the AI-based GEP model has the best prediction capability compared to the other developed AI models.
- It is observed that air mass flux rate, solution concentration and specific humidity have a significant impact on CR, whereas, air mass flux rate and solution temperature are the most effective parameters for ε_m and LHR, respectively.
- Using GEP model, an empirical correlation between process (F_a, T_a, ω_a, F_s, T_s, and ζ) and response (CR, ε_m and LHR) parameters in the form of expression trees as well as mathematical expressions are obtained. The correlation metrics and error metrics statistically confirm the effectiveness and robustness of the GEP predictions.
- The optimum inlet process parameters are found to be F_a = 0.766 kg/m^2-s, T_a = 30.745°C, ω_a = 0.023 kg_{wv}/kg_{da}, F_s = 1.812 kg/m^2-s, T_s = 24.01°C and ζ = 48.1%. The predicted values of CR, ε_m and LHR from GEP meta-model are 5.875 g/m^2-s, 48.65% and 0.82, respectively at this optimum inlet conditions.
- At near optimum point (F_a = 0.76 kg/m^2-s, T_a = 30.1°C, ω_a = 0.024 kg_{wv}/kg_{da}, F_s = 1.8 kg/m^2-s, T_s = 24°C, and ζ = 48%), the experimental results CR of 5.584 g/m^2-s, ε_m of 42% and LHR of 0.83, respectively were obtained. The experimental and predicted results for the optimum dehumidifier performance parameters (CR, ε_m, LHR) showed a very good agreement to each other (>8%) and that endorses the great reproducibility of the experimental inferences.

- TCOP and COP of the proposed system were estimated as 1.1 and 0.62, respectively. The enthalpy of the dehumidifier and regenerator system lies between 2.2 - 6.1 kW, and 0.1 - 7.1 kW, respectively.

This study will be more helpful for the design engineers and researchers for precise modelling and prediction of real-time dehumidifier operational value in view of minimising the building energy consumption with enhanced dehumidification performance. However, the methodology of the current optimisation can be used to optimise the input process parameters of a dehumidifier for various other desiccant mixture to achieve enhanced performance.

CHAPTER 7

Study of liquid desiccant doped hydrogel films for air dehumidification applications

7.1. Introduction

The safety of liquid desiccant systems is still a considerable concern due to the carryover of desiccant solutions by the process air (Fu et al., 2017). The general desiccant solution consists of chemicals like LiBr, LiCl, and $CaCl_2$, which include a large number of halogen ions (i.e., Br^-, Cl^-). These ions carryover can also cause corrosion of air ducts or other indoor devices. Higher mass flow rates of desiccant solution and air in random packing materials or counter-flow type dehumidifiers can increase the potential risk of carryover (Chen et al., 2020). It has the potential to pollute indoor air quality and affects human health. Skin contact with lithium halides can result in skin dehydration (Fu et al., 2017). Besides, sometimes liquid desiccant is emitted out to the environment during regeneration. Conversely, amongst many polymers, cellulose is a non-toxic, natural, abundant, renewable and biodegradable polymer. In addition, amongst various celluloses, sodium carboxymethyl cellulose (NaCMC) is a water-soluble hetero polysaccharide, which is highly hydrophilic due to the presence of abundant carboxyl (—COOH) and hydroxyl (—OH) groups (Dharmalingam et al., 2020). Further, it has excellent film-forming properties. These stimuli-responsive hydrogel films can undergo a drastic change in volume with respect to ambient conditions by absorbing moisture from the air. It can be found that the NaCMC films undergo a drastic change in its hydrophilic property with respect to temperature. These unique properties make the hydrogel films as energy-efficient materials for air dehumidifying applications. Additionally, the incorporation of desiccant solution while the preparation of those stimuli-responsive hydrogel films would be a potential research interest for air dehumidification applications. In this chapter, an effort has been made to develop LiBr and $CaCl_2$ desiccant mixture doped hydrogel films using a sustainable substance of citric acid (CA) as a crosslinker. To the best of authors' knowledge, no study was reported concerning cellulose-based desiccant doped hydrogel films for potential air dehumidification applications. Therefore, objectives of the present chapter are: (i) to develop citric acid crosslinked hydrogel films containing various amounts of desiccant (5-20%), (ii) to investigate the homogeneity, mechanical properties and WVP of desiccant doped hydrogel films, (iii) to analyze the performance of the developed films at different relative humidity conditions by

sorption rate, and (iv) to examine the films regeneration capability by thermo-gravimetric analysis (TGA).

7.2. Materials and methods

7.2.1. Materials

Sodium carboxymethyl cellulose (NaCMC, 400–800 cps at 2% water, 25°C) and citric acid were procured from HiMedia Laboratories Pvt. Ltd. (Mumbai, India). The solid form of $CaCl_2$ and LiBr desiccants were purchased from Balaji traders (Guwahati, India) and Parad Chem Corporation (Gujrat, India), respectively.

7.2.2. Preparation of desiccant doped hydrogel films

The chronological steps for the preparation of desiccant doped hydrogel films are schematically represented in Fig. 7.1. Initially, a desiccant solution containing LiBr and $CaCl_2$ was prepared by mixing in the ratio of 85:15 (wt.%) in 100 ml of water. It was assured that all desiccants were completely dissolved in the solution for further procedure. Subsequently, 5%, 10% and 20% desiccant solutions were prepared. Then, 2 g of NaCMC was gradually added into another 100 ml of water at room temperature under vigorous magnetic stirring at 1200 rpm. The solution was left for 2 h to dissolve NaCMC wholly without any precipitation until a homogeneous solution was formed. An amount of 0.4 g citric acid was added into NaCMC solution. The stirring was continued with the help of a magnetic stirrer for 30 minutes to ensure the complete dissolution of citric acid. A volume of 1 ml from the desiccant solution was taken (equivalent to 5 wt.% with respect to NaCMC) and added into the above solution. In order to obtain a homogeneous solution, the final solution was stirred for twelve hours at room temperature. The beaker (having film-forming solution) was kept in a vacuum desiccator for 10 h to remove all submerged air bubbles from the solution. Subsequently, the solution was poured into a clean Petri-dish and kept at 80°C for 5 h. The films were peeled off and kept in a vacuum desiccator. Similarly, by adding 10 wt.% and 20 wt.% of the desiccant solution into NaCMC solution, the respective desiccant concentration films were prepared. For control (without desiccant) films, the desiccant solution was not added into the NaCMC solution; other

than that, all steps have remained the same. The photographic view of the desiccant doped hydrogel films can be found in Appendix D.

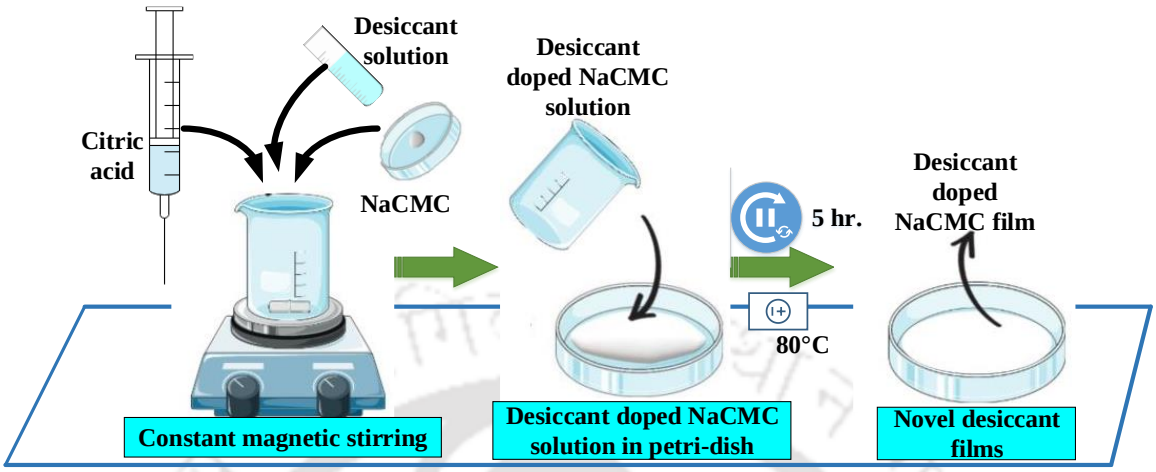

Fig. 7.1: Schematic representation of novel desiccant doped hydrogel films prepared by solvent evaporation method

7.3.Characterization

7.3.1. Fourier transform infrared spectroscopy (FTIR)

ATR- FTIR (Make: Shimadzu, model: IRAffinity-1, Japan) method was used to analyze the presence of crosslinking agent in the film samples using absorbance mode from 4000–400 cm^{-1} with 30 scans and 4 cm^{-1} resolutions.

7.3.2. Moisture absorption of films

The hydrogel films (with or without desiccants) were cut into the sizes of 5 cm × 5 cm, as shown in Fig. 7.2. The moisture absorption of the films can be expressed by the amount of moisture absorbed with respect to time. The amount of moisture absorption is calculated using Eq. (7.1).

Moisture absorption [g_{H_2O} / g_{film}] = (mass of H_2O)/(mass of dried film) (7.1)

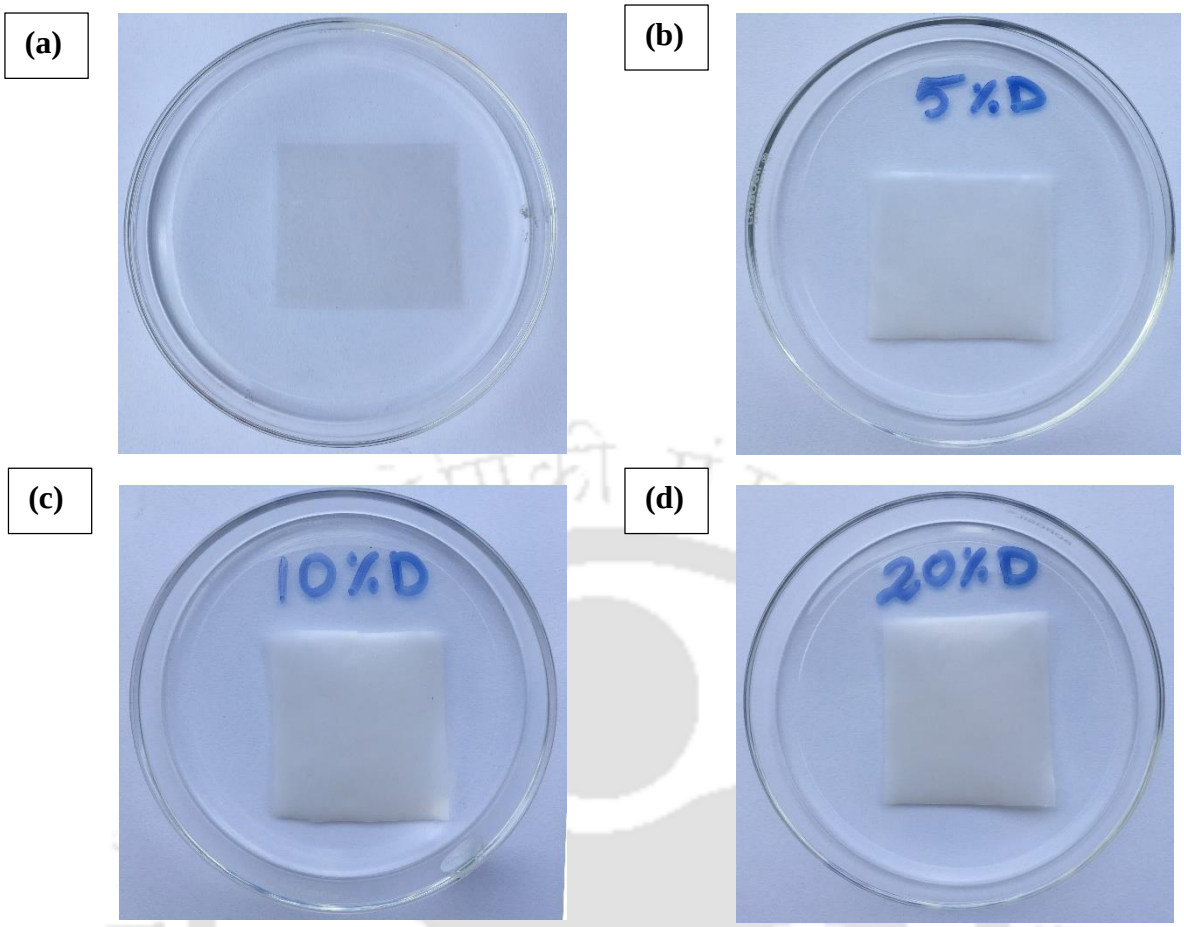

Fig. 7.2: Photographic view of (a) control (without desiccant) film; (b) 5% desiccant doped hydrogel film; (c) 10% desiccant doped hydrogel film and (d) 20% desiccant doped hydrogel film

7.3.3. X-ray diffractometer (XRD)

All the samples were analyzed for their crystalline phase using X-ray powder diffractometer (XRD) (Make: Rigaku; model: SmartLab; USA). The Nickel mono-chromator filtered CuKα radiation (λ = 0.15418 nm) was used to record the XRD pattern in the range of 5–70° (2θ) at a high voltage and current of 45 kV, 112 mA, respectively. The step size was 0.01° (2θ) and a scan rate of 20°/min. The samples were mounted on a zero background silicon wafer embedded in a generic sample holder.

7.3.4. Swelling degree (SD) of films

Completely dried and square-shaped NaCMC based control and desiccant doped hydrogel films of 25 cm^2 were weighed. Then the films were immersed in excess swelling medium (water) at 25°C. Subsequently, the swollen films were taken out from the water at different

time intervals and weighed after blotting out excess surface water using filter paper. Finally, the SD results were calculated according to Eq. (7.2).

$$SD(\%) = \frac{M_s - M_d}{M_d} \times 100 \tag{7.2}$$

where M_s and M_d correspond to mass of hydrogel films in the swollen state and initial dried state, respectively. The datasets of the swelling experiments were the mean results of triplicate measurements.

7.3.5. Thermo-gravimetric analysis (TGA)

The thermal stability of control and desiccant doped films were studied by TGA (Make: NETZCH, model: TG 209 F1 Libra, Germany) using an alumina crucible. The chosen temperature range was from 20°C to 200°C under nitrogen gas flow (purge: 40 ml/ min, protective: 20 ml/min) at a heating rate of 10°C/min.

7.3.6. Thickness of films

Unbroken, smooth and relatively uniform thickness films were chosen for thickness measurement. The film samples were cut into strips (80 mm × 80 mm). The thickness of each strip was measured at five different points using a digital micrometre (Mitutoyo, Japan) having an accuracy of ± 0.001 mm and the mean values were reported.

7.3.7. Mechanical properties of films

A smooth and undamaged film sample was selected and cut into rectangular strips (80 mm × 15 mm). All the films were preconditioned at 25°C and 65 ± 5% relative humidity for 24 h. Then, the mechanical properties of films such as tensile strength and elongation (%) were measured (Make: Globe Tex; model: GTI-TS110, India) according to ASTM D882-12 standard. The set parameters for measuring mechanical properties are as follows: gauge length of 80 mm, crosshead speed of 5 mm/min, and load cell of 100 N. The tensile strength of hydrogel films is calculated using Eq. (7.3).

$$\sigma_t = \left(F \times 10^{-6}\right) / A_c \tag{7.3}$$

where σ_t is the tensile strength (MPa), F is the maximum tensile force when the sample fractures (N), and A_c is the cross-sectional area of the sample (m^2).

The elongation (%) of hydrogel films is calculated using Eq. (7.4).

$$E\ (\%) = L/L_0 \times 100 \tag{7.4}$$

where, E is the elongation (%), L is the displacement corresponding to the maximum tensile force when the film fractures (mm), and L_0 is the initial length of films (mm).

7.3.8. Water Vapor Permeability (WVP)

Water vapor transmission rate (WVTR) measurements were performed using a PERMATRAN-W® Model 1/50 (Mocon, USA) ensuing ASTM standard E398-03. A smooth and undamaged film sample was selected and cut into circles using a round sampler (50 cm^2), and the thickness of each circular film sample was measured. The samples were conditioned in diffusion cell by purging with nitrogen gas (~99.999% purity) for a minimum of 24 h under equilibrium humidity. The relative humidity (RH) was set to 100% in the wet chamber and 5% in the dry chamber, yielding a driving force of 95% RH. The circular film was tested in the chamber at atmospheric pressure and at a temperature of 37.8 ± 0.1°C. Tests were carried out three times and the average value was reported. The water vapor permeability (WVP) values were calculated in terms of WVTR using Eq. (7.5).

$$\text{WVP}\ \left(\text{g}/\text{m}-\text{day Pa}\right) = \frac{\text{WVTR}}{\Delta \text{P}} \times l \tag{7.5}$$

where *l* is the average thickness of the film (m) and Δp is the difference in partial pressure (Pa) of the water vapor across the film in the test chamber.

7.4. Results and discussion

The influence of desiccant mixtures (LiBr and $CaCl_2$) on physical and thermal properties of NaCMC hydrogel films are presented in this section. Furthermore, the weight ratio of LiBr and $CaCl_2$ desiccants, NaCMC and CA concentration were chosen based on our previous studies (Dharmalingam et al., 2020).

7.4.1. FTIR analysis

In order to investigate the crosslinking of citric acid (CA) with NaCMC, FTIR analysis was carried out for neat NaCMC based films and 20% CA incorporated NaCMC films (Fig. 7.3). Absorbance peaks of neat NaCMC films at 3340 cm^{-1}, 2920 cm^{-1}, 1586 cm^{-1}, 1416 cm^{-1}, 1327 cm^{-1} are due to –OH stretching, -CH stretching, -COOH stretching, $-CH_2$ scissoring and –OH bending vibrations, respectively. The sugar ring vibrations are observed from 1200 cm^{-1} to 1000 cm^{-1}. A small peak around 895 cm^{-1} is due to C-O-C stretching vibrations (Fig. 7.3a) (Dharmalingam et al., 2019). It can be clearly observed from Fig. 7.3b that the addition of CA into neat NaCMC films did not shift the vibrations of NaCMC, whereas a new peak at 1727 cm^{-1} is appeared in the spectra due to ester bond formation (Dharmalingam et al., 2019). It is noteworthy to mention that this ester bond is emerged due to crosslinking of –OH groups of NaCMC with –COOH groups of CA. Therefore, it can be concluded that the presence of crosslinking was confirmed by FTIR analysis in NaCMC/20% CA hydrogel films.

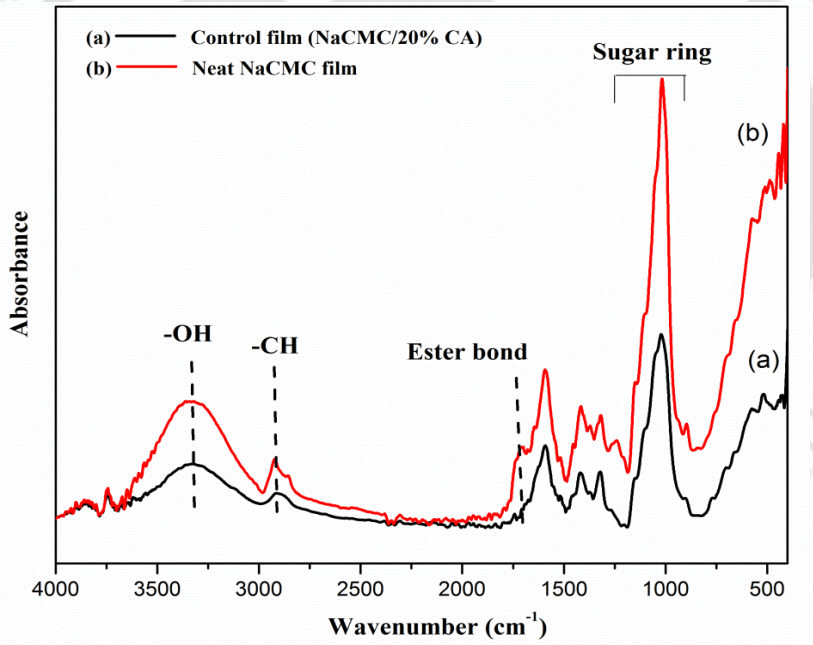

Fig. 7.3: FTIR spectra of (a) Neat NaCMC hydrogel films (b) NaCMC/20% CA crosslinked films

7.4.2. XRD analysis

XRD pattern of control, 5%, 10%, and 20% desiccant doped hydrogel films is shown in Fig. 7.4. It can be noted that mixed desiccant of LiBr: $CaCl_2$ (85:15) showed crystalline peaks at 2θ = 28.5°, 33.09°, 47.07°, 55.74°, and 58.27° (Fig. 7.4a). A broad amorphous peak around 2θ of 22° was observed in control films. It is due to the presence of NaCMC in films (Fig. 7.4b). It

is clear that characteristics peaks of LiBr and $CaCl_2$ were disappeared in all desiccant doped NaCMC films due to homogeneous dispersion of desiccants with NaCMC film-forming solution (Fig. 7.4c-e). Since amorphous films can hold a large amount of moisture than the crystalline, absence of crystalline peaks of LiBr: $CaCl_2$ in NaCMC films is an added advantage for air dehumidification applications. However, there were no other new characteristics peaks found as the concentration of desiccants increased in NaCMC films. NaCMC peak was slightly shifted towards the right (Fig. 7.4c-e) with increasing concentration of desiccants. It might be attributed to miscibility and interaction of desiccants with CA crosslinked NaCMC films.

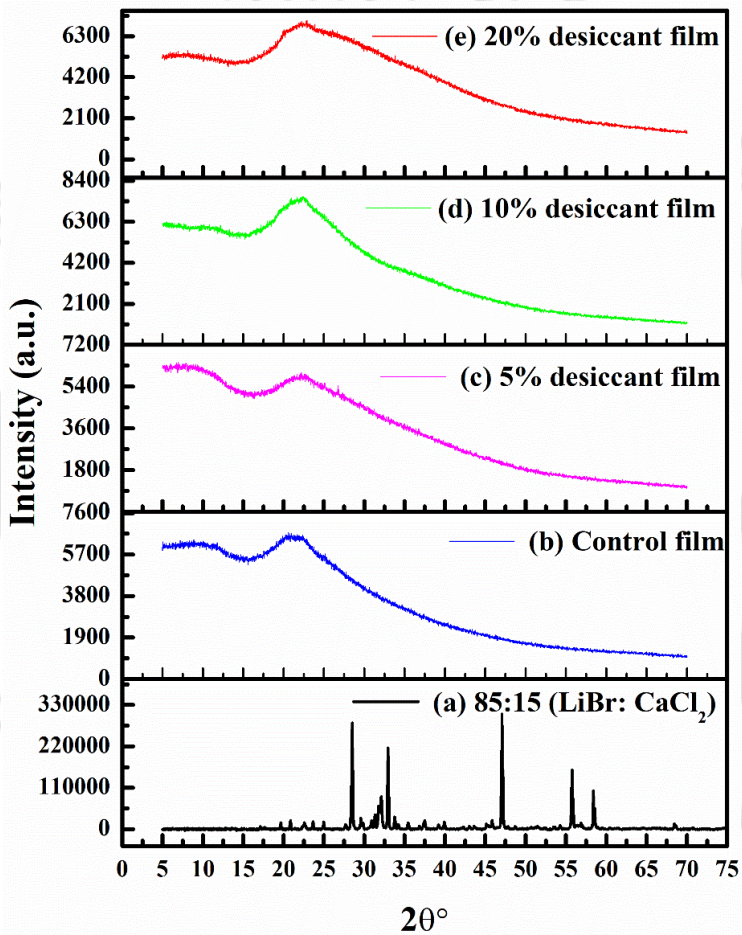

Fig. 7.4: XRD pattern of (a) LiBr: $CaCl_2$ (85:15 wt.%) desiccant mixture, (b) control films and various amounts of desiccant doped hydrogel films of (c) 5%; (d) 10% and (e) 20%

7.4.3. TG analysis

The thermal stability of the developed hydrogel films containing desiccants is important to interpret the rate of water desorption and regeneration temperature for hydrogel films. The TG and derivative thermo-gravimetric (DTG) curve of control films and LiBr with $CaCl_2$ doped

NaCMC films of various concentrations are shown in Figs. 7.5 and 7.6, respectively. It can be seen from Fig. 7.5 that the desorption of water starts from 20°C for all the developed films. Further, it can be observed that the control films showed the minimum weight loss rate at 24.3°C. Hence, control films can be used for dehumidification purposes when the temperature is less than or equal to 24.3°C. The maximum desorption temperature was observed at 86.1°C (Fig. 7.6a) for control films. This temperature indicated that the control films were required to be heated at a temperature of 86.1°C for the maximum moisture desorption rate (i.e., regeneration of the films).

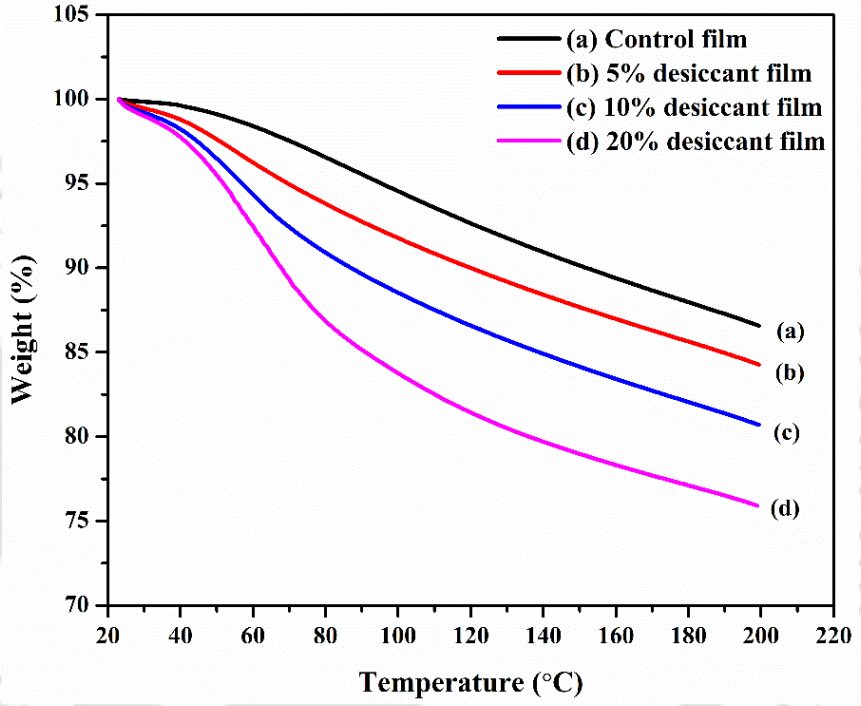

Fig. 7.5: TG curve of (a) control films and various amounts of desiccant doped hydrogel films of (b) 5%; (c) 10% and (d) 20%

Addition of desiccant materials enhanced the rate of decomposition in the hydrogel films. It was observed that the weight loss of 20% desiccant doped hydrogel films was higher than the control films, 5% and 10% desiccant doped hydrogel films at higher temperatures. This is due to higher plasticizing effect of desiccants in the hydrogel films (Fig. 7.5). It was observed that the minimum desorption rate is observed at 23.3°C (Figs. 7.5b and 7.6b). Therefore, these films required a temperature which is less than or equal to 23.3°C for absorption of moisture from the air. Absorption of moisture may be maximum at a temperature of 23.3°C for 5% desiccant films. The maximum desorption temperature was found to be 57.8°C for 5% desiccant films (Fig. 7.6b). Therefore, it can be concluded that the maximum regeneration temperature for 5%

desiccant films is 57.8°C. The minimum desorption of moisture was observed at 23°C and 24°C for 10% and 20% desiccant doped hydrogel films, respectively (Figs. 7.5c-d and 7.6c-d). The maximum desorption temperature was found to be lower for 10% desiccant doped films (55.3°C) than 20% desiccant films (60.2°C). It can be concluded that the minimum moisture desorption temperature is decreased from 24.3°C to 23°C as the concentration of desiccant increased from 0% to 10%, whereas it is increased from 23°C to 24°C as the concentration of desiccant increased from 10% to 20%. The regeneration temperature was also decreased from 86.1°C to 55.3°C, when increasing desiccant concentrations from 0% to 10% and then it was increased to 60.2°C for 20% desiccant films. The maximum regeneration rate of control films, 5%, 10% and 20% desiccant films were found to be 1.01 %/min, 1.32 %/min, 2.01 %/min, and 2.8 %/min, respectively. A higher regeneration temperature was observed for 20% desiccant films when compared with 10% desiccant films due to drastic increase in desiccant concentration in the hydrogel films. Furthermore, higher regeneration temperature might be due to higher moisture absorbing capacity of 20% desiccant films.

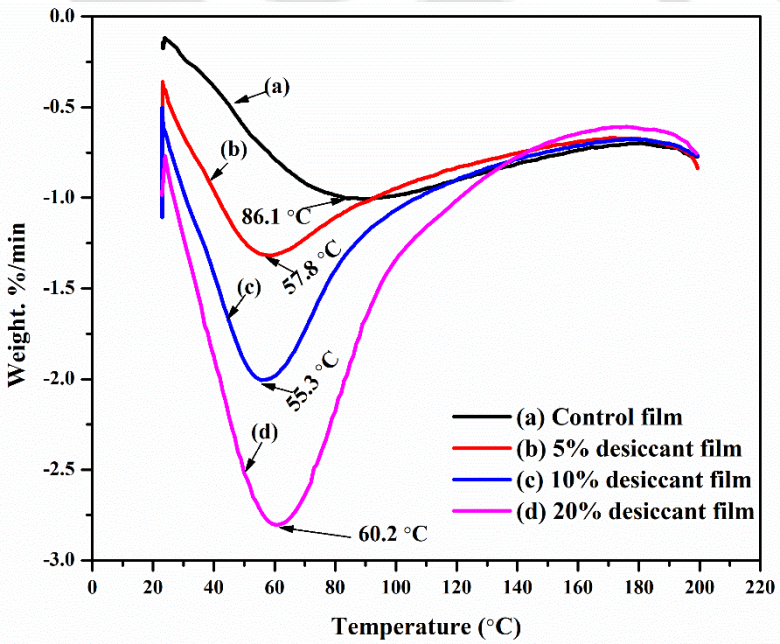

Fig. 7.6: DTG curve of (a) control films and various amounts of desiccant doped hydrogel films of (b) 5%; (c) 10% and (d) 20%

7.4.4. Swelling behaviour of hydrogel films

The swelling behaviour of NaCMC based control films and desiccant doped hydrogel films are depicted in Fig. 7.7. The results of swelling degree analysis (Fig. 7.7) revealed the presence of crosslinking agent (citric acid), which held the polymer from disintegration. The SD was around 140.2% for control films and increased substantially to 220.5% for the desiccant doped

(20%) films. The addition of desiccants might have contributed to a higher swelling degree in the order of increasing desiccant concentration. As the desiccant concentration in the films increased from 5% to 20%, the polymer swelled faster, and the equilibrium swelling ratio was enhanced accordingly. It was noted that there is no significant difference in swelling degree when desiccant concentration is increased from 10% to 20% due to unbound desiccant dissolution in the water.

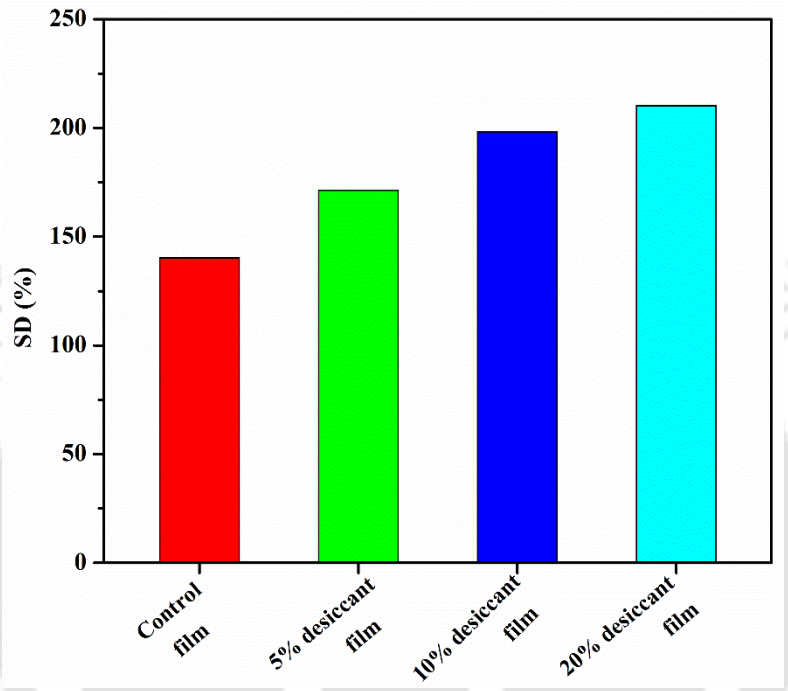

Fig. 7.7: Swelling behavior of (a) control films and hydrogel films with various amounts of desiccant dopes of (b) 5%; (c) 10% and (d) 20%

7.4.5. Water Vapor Permeability (WVP) Test

Determination of WVP of desiccant doped hydrogel films is important to decipher their water vapour transmission capability across films. WVP of desiccant doped hydrogel films depends on film structure, porosity, additives, temperature, pressure and relative humidity. Fig. 7.8 shows WVP of various amounts of desiccants doped hydrogel films. It was found that WVP decreased with desiccant amount. The presence of intermolecular space, which provides a path for water vapour, is essential in the films and determines the water vapour permeability. According to moisture absorption analysis, increase in amount of desiccants improves the moisture absorption capability. Therefore, the high amount of desiccant doped hydrogel films

reduced the molecular space due to interaction between polymers and desiccants resulting in low WVP.

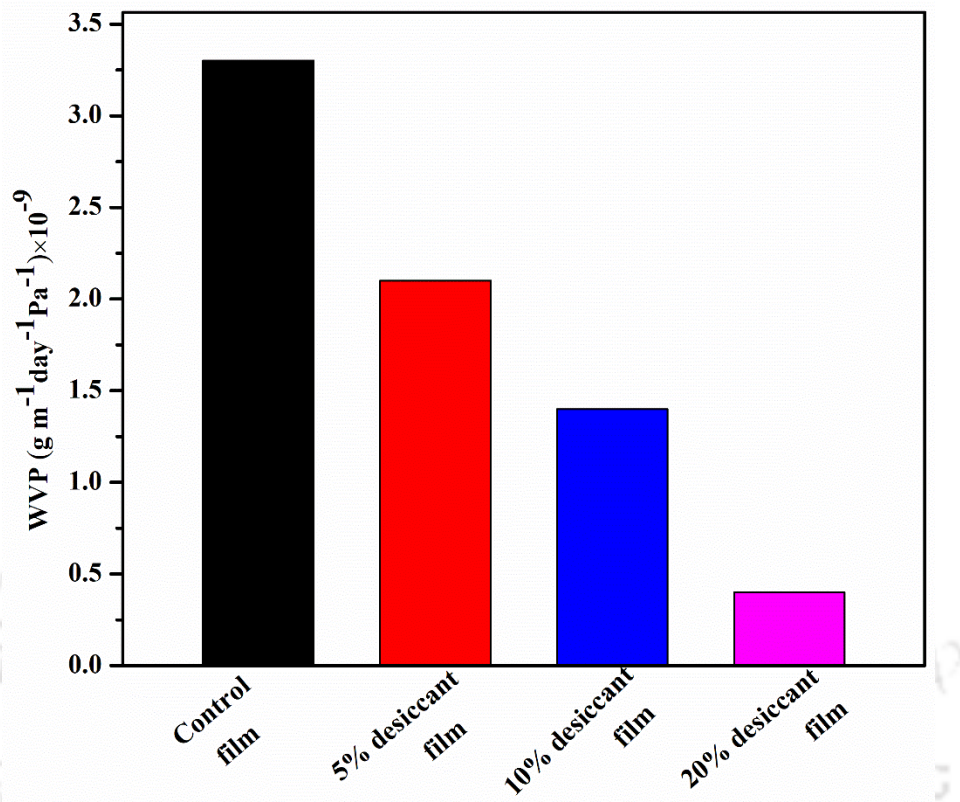

Fig. 7.8: Water vapor permeability of (a) control films and various amounts of desiccant doped hydrogel films of (b) 5%; (c) 10% and (d) 20%

7.4.6. Mechanical properties

The mechanical properties of desiccant doped hydrogel films are shown in Fig. 7.9. The prepared films are required to exhibit a balance between stress-resistant and flexibility for withstanding the air flow pressure as well as for handling. Generally, doped desiccants act as plasticizing agent in the hydrogel films. Therefore, increasing amounts of desiccants lowered the tensile strength value while increasing the elongation (%) of films. It was found that control films showed a maximum tensile strength of 17 MPa and elongation (%) of 10%. An increasing amount of desiccant from 5% to 10% decreased the tensile strength value considerably. On the other hand, it was observed that the elongation (%) was increased for 5-10% of desiccant amounts. However, a very high amount of desiccant (20%) doped films significantly lowered both tensile strength and elongation (%). It is due to the high plasticizing effect of desiccant materials. Stress-strain curves are provided to understand the mechanical properties of

hydrogel films. Fig. 7.10 represents the mechanical load vs displacement of developed hydrogel films. The term stiffness can be defined as the extent to which an object resists deformation in response to an applied force. In other words, the stiffness of the hydrogel films can be defined as the force required to produce unit displacement and can be calculated from stress-strain curves. It is found that the stiffness of the hydrogel films was 5.349 N/mm, 3.015 N/mm, 1.641 N/mm and 0.997 N/mm for control films, 5%, 10% and 20% desiccant doped films, respectively.

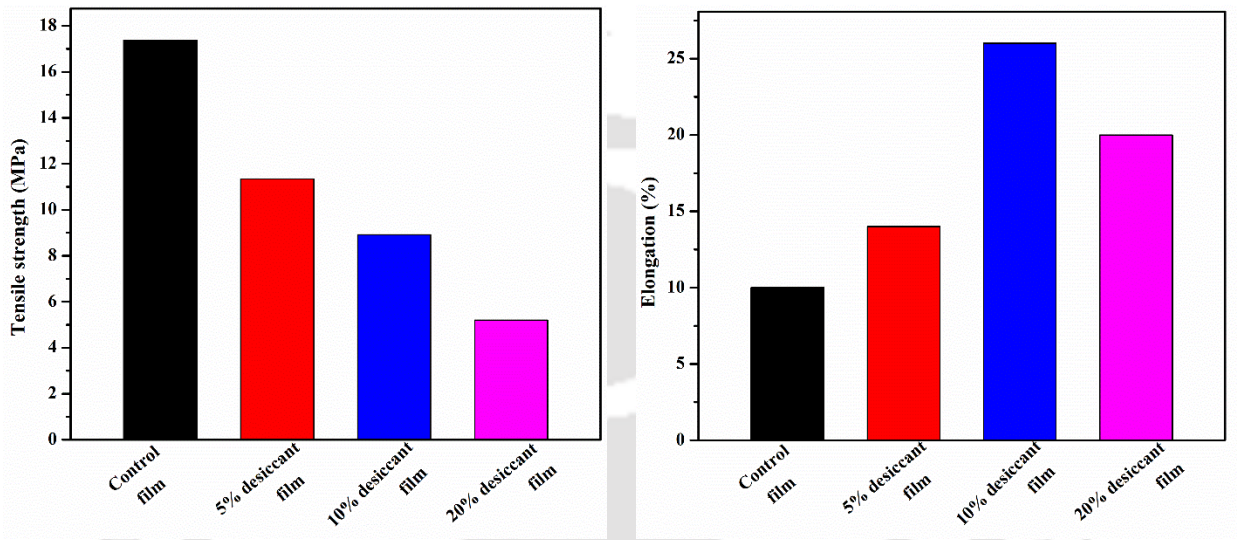

Fig. 7.9: Mechanical properties of different hydrogel films

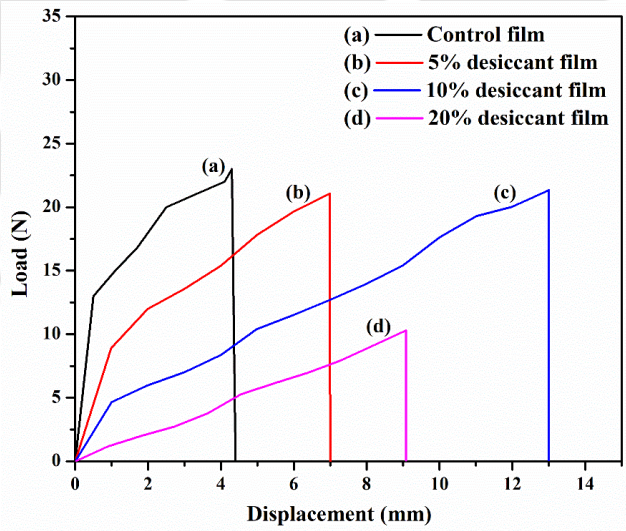

Fig. 7.10: Load vs displacement of (a) control films and various amounts of desiccant doped hydrogel films of (b) 5%; (c) 10% and (d) 20%

7.4.7. Moisture absorption analysis

Figs. 7.11 and 7.12 represent the moisture absorption capability of control films (without desiccant), 5%, 10%, and 20% desiccant doped NaCMC films at different time periods with different relative humidity settings. The instantaneous absorption capacity (i.e., for first 5 min) of control, 5%, 10%, and 20% films was found to be 0.00354 g/g, 0.01351 g/g, 0.02439 g/g and 0.02441 g/g, respectively (Fig. 7.11a-d). It was observed that the instantaneous absorption rate was maximum for 20% desiccant films and minimum for control films. The overall moisture absorption capacity (i.e., up to 40 min.) of 5%, 10% and 20% desiccant films was found to be 0.1091 g/g, 0.15241 g/g, 0.17851 g/g and 0.2 g/g, respectively. It was perceived that instantaneous as well as the overall rate of absorption of the films were increased with desiccant concentrations (Fig. 7.11b-d).

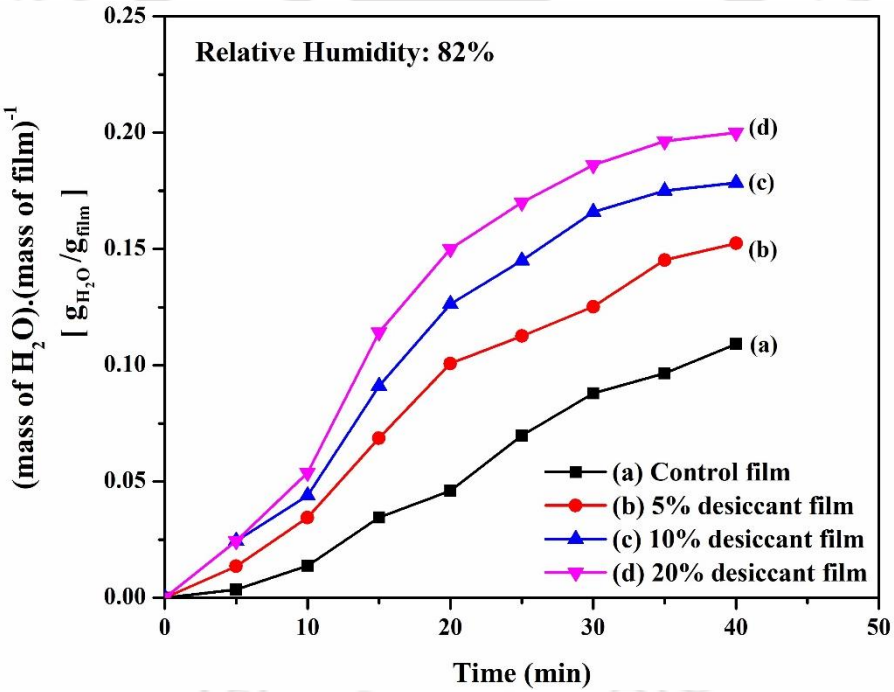

Fig. 7.11: Moisture absorption rate of (a) control films and various amounts of desiccant doped hydrogel films of (b) 5%; (c) 10% and (d) 20% at different time periods (Relative Humidity: 82%)

Similarly, the second set of experiments for moisture absorption analysis was performed at a relative humidity of 91% (Fig. 7.12a-d). Instantaneous moisture absorption capacity (i.e., for 5 min) of control, 5%, 10% and 20% desiccant films was found to be 0.0069 g/g, 0.01724 g/g, 0.03794 g/g and 0.03802 g/g, respectively. It is revealed that the instantaneous moisture absorption capacity of 20% desiccant films was higher among all films (Fig. 7.12). The overall

moisture absorption capacity (i.e., up to 40 min) of control, 5%, 10% and 20% desiccant films was found to be 0.17783 g/g, 0.19946 g/g, 0.22 g/g and 0.23 g/g, respectively. It can be deduced that the moisture absorption rate was higher for 20% films due to the high concentration of desiccant molecules in NaCMC films.

It was noticed from the experimental datasets that the amount of moisture absorbed by the hydrogel films at 45 min was 1% less than the amount of moisture absorbed at 40 min for both the humidity conditions (i.e., 82% RH and 91% RH). Therefore, in the present study, the moisture absorption rate of different developed hydrogel films is shown upto 40 min.

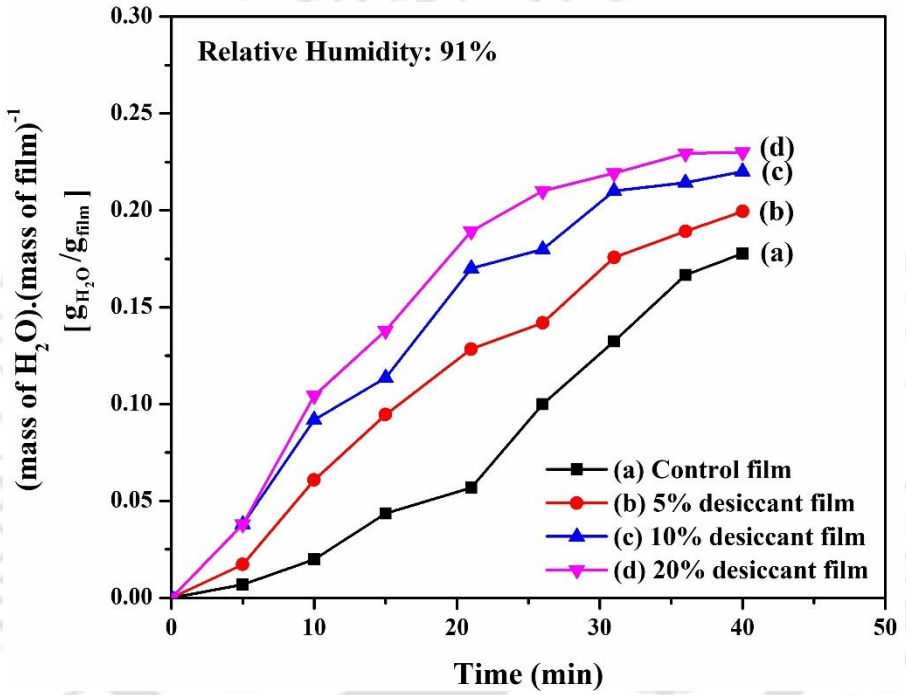

Fig. 7.12: Moisture absorption rate of (a) control films and various amounts of desiccant doped hydrogel films of (b) 5%; (c) 10% and (d) 20% at different time periods (Relative Humidity: 91%)

Figs. 7.11-7.12 depict that the overall moisture absorption rate is higher for 20% films in both cases (i.e., relative humidity of 82% and 91%). It was observed from the experimental observations that the absorption rate of the moisture is higher at higher relative humidity. Further, Figs. 7.11-7.12 show that the instantaneous absorption rate of 20% desiccant films at a relative humidity of 91% is 0.03802 g, whereas, at the same condition for the 10% desiccant films is 0.03794 g/g. It elucidated that the absorption rate is only increased by 0.21% with the increment of desiccant concentration from 10% to 20%. However, the films regeneration temperature of 20% desiccant films is 8.86% higher than the 10% desiccant films (Fig. 7.6).

Therefore, 10% desiccant films are a suitable option compared to the other developed films for continuous air dehumidification operation.

7.5. Performance behaviour of novel hydrogel films over other available film materials

Sängerlaub, (2019) developed a low-density polyethylene (PE-LD) monolayer films with a nominal silica gel concentration of 0.2, 0.4, and 0.6 g dispersed silica gel per 1 g film (PE-LD). It was found that the moisture absorbed up to 0.15 g/g of the dried film. In contrast, the overall moisture absorption capacity of developed hydrogel films (i.e., 5%, 10% and 20% desiccant films were 0.19946 g/g, 0.22 g/g 0.23 g/g, respectively. Further, the regeneration temperature of silica gel dispersed PE-LD monolayer films has not been studied yet (Sängerlaub, 2019). However, the authors found the suitable regeneration temperature for 5%, 10% and 20% desiccant films as 57.8°C, 55.3°C and 60.2°C, respectively. Further, the present study revealed that the developed 10% desiccant doped hydrogel films are more suitable for air dehumidification systems as the moisture absorption rate of 10% films is 0.22 g/g and required only a lower regeneration temperature of 55.3°C compared to other developed hydrogel films.

7.6. Closure

Citric acid crosslinked NaCMC films containing desiccants were developed and investigated for their physical and thermal properties. Subsequently, the moisture absorption capability was compared between the control (without desiccant) films and desiccant doped films. Based on the above experimental investigations, the following key observations can be enumerated:

- X-ray diffraction (XRD) results of control films and 5%, 10%, 20% desiccant doped films exhibited that the films were homogeneous and there were no crystalline phases of desiccants in the developed films.
- It was found that 10% films required a minimum regeneration temperature of 55.3°C. Furthermore, the regeneration rate was higher for 10% films compared to the control films, 5%, and 20% desiccant films.
- It was found that 10% films exhibited a higher elongation (%) and tensile strength compared to 20% films.
- WVP analysis showed that the rate of water transmission was reduced in the range of 3.3×10^{-9} to 0.4×10^{-9} g m^{-1} day^{-1} pa^{-1} from 0% to 20% desiccants.

- The result of moisture absorption analysis showed that 20% desiccant films have higher instantaneous and overall moisture absorption rate among all the developed films at different relative humidity settings.
- The lower regeneration rate and comparable instantaneous absorption rate was found for 10% desiccant films.

Therefore, it is recommended from the above findings that 10% desiccant doped NaCMC films are more suitable for air dehumidification applications.

CHAPTER 8

Conclusions and Future Scope

This chapter outlines the major conclusions drawn from the numerical, experimental and optimization studies of the solar-assisted liquid desiccant dehumidification/regeneration system. Further, the key observations made from the liquid desiccant film based air dehumidification are also summarized.

8.1. Numerical studies on liquid desiccant dehumidification/regeneration system

The thermal model is developed for liquid desiccant dehumidifier/regenerator to analyse the heat and mass transfer phenomena between the air-desiccant surface. A finite-difference model (FDM) based algorithm is used for solving the developed thermal models of the liquid desiccant dehumidifier/regenerator, respectively. The FDM-based model empowers a more realistic mapping of an adiabatic dehumidifier/ regenerator domain as the predicted results, which are closer to experimental data. The distribution contours are plotted for analysing the heat and mass transfer characteristics along with the height of the liquid desiccant dehumidifier/regenerator and observed that condensation/evaporation rate decreases along the ambient air flow direction. Further, the effect of inlet parameters on the performance of the liquid desiccant dehumidifier/regenerator is analysed. The key observations from the numerical studies are as follows:

- The aqueous LiCl desiccant showed the minimum vapour pressure among the other commercial desiccants. However, LiCl desiccant is more corrosive and not stable at ambient conditions.
- LiBr desiccant is performing well at higher concentrations, whereas, $CaCl_2$ desiccant performed best at lower concentrations.
- Irreversibility in heat and mass transfer operation is investigated in terms of physical and chemical exergy destruction. The maximum chemical and physical exergy destruction is found to be 0.88 kW and 0.06 kW, respectively.
- The distribution profiles of the desiccant/air outlet properties inside the dehumidifier/regenerator chamber are visualized. The maximum specific humidity variation is found in the top of the dehumidifier as the moist air interacts with the more cold - concentrated desiccant solution at that stated location.

- Based on the analysis of air and desiccant temperature and concentration fields, the desiccant concentration difference in the transverse direction of the desiccant flow can be reasonably neglected. In contrast, the differences of air temperature, air humidity ratio and desiccant temperature in their flow transverse directions cannot be neglected.
- It is found that a higher non-linearity exists in the regenerator's distribution profiles compare to the dehumidifier's distribution profile due to the higher temperature difference that exists in the regenerator between the air and desiccant.

8.2. Experimental studies on liquid desiccant dehumidification/regeneration system

The experimental setup of the solar-driven liquid desiccant system has been fabricated. The coupled heat and mass transfer characteristics of the liquid desiccant system during dehumidification and regeneration in different control settings are experimentally analysed. The advantage of the present study is the usage of solar thermal energy instead of complete electrical power input for the regeneration of dilute desiccant. In the current work, an additional comprehensive studies on the influence of operating parameters on the performance of liquid desiccant dehumidifier/ regenerator are presented. Based on the presented experimental and developed model results, the following major generic and overall conclusions are arrived.

- XRD pattern of LiBr, $CaCl_2$ and their mixtures demonstrated that lattice parameters for mixtures were different compared to pure individual desiccants. The lattice parameters were decreased as the proportion of $CaCl_2$ in the mixture is increased till 80:20 (LiBr: $CaCl_2$).
- Adsorption rate analysis showed that LiBr and $CaCl_2$ mixtures had a better rate of absorption than pure LiBr and $CaCl_2$.
- The overall moisture absorption rate of 85:15 (LiBr: $CaCl_2$) was higher than other prepared samples.
- It can be concluded that mixed desiccants (LiBr and $CaCl_2$) can help in achieving the target of increasing CR without compromising ε_m and LHR when compared to pure desiccants in dehumidifier operations.
- The performance of aqueous desiccant blends was experimentally investigated at different concentrations (from 30 to 55 wt.%). Within the operating range, the result showed that

the mixture desiccant could increase the condensation rate where the moisture effectiveness and latent heat factor were comparable with the pure LiBr.

- The experimental results showed that the airside (dehumidifier) and solution-side (regenerator) latent effectiveness increase with solution to air mass flow rate. However, the solution-side latent effectiveness is higher than the airside effectiveness.
- For tested liquid desiccant dehumidifier, condensation rate and latent effectiveness lies in the range of 2.2 to 4.6 g/m^2-s and 36 to 68%, respectively. Whereas, the evaporation rate, sensible and the latent effectiveness of the regenerator lies in the range of 0.1–11.2 g/m^2-s, 25.9–63% and 10-92% depending on the operating conditions.
- CR increases as L/G increase, which indicates that an increase in L/G significantly improve the heat and mass transfer coefficient. Hence, these two factors increase the driving factor of the dehumidifier/ regenerator.
- It is found that pressure drop is directly proportional to the airflow rate. For the given operating conditions, the pressure drop of the structured packed bed counter-flow dehumidifier was found in the range of 50 to 400 Pa.
- TCOP and COP of the proposed system were estimated as 0.62 and 1.1, respectively. The enthalpy of the dehumidifier and regenerator system lies between 2.2 - 6.1 kW, and 0.1 - 7.1 kW, respectively.

8.2.1. Evacuated U – tube solar collector system

The utilisation of solar thermal energy for various medium-temperature heating applications can save a significant amount of electricity. Therefore, solar ETCs should be designed for higher efficiency over a yearly operation period. Respective experimental investigations have been carried out in an aluminium finned U-tube ETC using water as a working fluid. An AI-based MLP model has been developed and trained with the experimental datasets for predicting the performance of U-tube ETC. Important results obtained from experimental and AI-based investigations are summarized below:

- The peak thermal efficiency (around 70%) of the U- tube evacuated solar collector system during a sunny day was observed between 11: 00 AM – 1: 00 PM, whereas low energy efficiency (about 30%) was observed around 8:00 AM and 4: 00 PM.

- The maximum outlet temperature obtained from the collector was 86.7 ºC, 76.5 ºC, and 69.0 ºC for mass flow rates of 0.03, 0.05 and 0.08 kg/s, respectively.
- The maximum thermal efficiency of the entire system was found to be 63%, 72% and 75% for mass flow rates of 0.03, 0.05 and 0.08 kg/s, respectively.
- The maximum thermal efficiency was obtained at lower reduced temperature differences with higher mass flow rates. It was found that the reduced temperature was greater than 0.03 Km^2/W for all mass flow rates.
- The average daily useful heat gain from the system was around 2.9 kW with an average efficiency of 53%. Besides, one such unit of ETCs can annually generate heat on an average of 2.1 MWh.
- MLP architecture with three neurons in the input layer, two hidden layers with ten neurons in each layer and three neurons in the output layer (3-10-10-3) is found to be optimal architecture for mapping the performance-outlet temperature characteristics under different mass flow rates.
- The correlation metrics on the basis of R, NSE, KGE and R^2 shows that the MLP model predicted outputs well accurately with the experimental outputs.
- The error metrics on the basis of RMSE, MSE, MSRE, Theil U2, and MAPE confirms the effectiveness and robustness of MLP predictions.
- The MLP investigation is further supported by exploring the effectiveness of the models using T_O-η-Q_u trade-off characteristics in contrast to the actual observed trade-off zones, and that proves the efficiency of the developed neural network model to predict the real-time collector operations.

8.3. Artificial intelligence-based modelling and optimization studies

The present work deals with the evaluation of performance of a LiCl+$CaCl_2$ liquid desiccant in a counter-flow, packed bed dehumidifier at different operating/working conditions. Based on the dehumidifier experimental performance datasets, AI affiliated models are developed to pattern input-output relationship between the process and performance parameters for different operational strategies. The present study introduces an innovative and specific approach to estimate potentiality of air dehumidification through the application of artificial intelligence (AI) assisted Gene Expression Programming (GEP), Artificial Neural Network (ANN), as well as Neuro-Fuzzy Inference System (ANFIS) models. Experimental results have also been

applied and compared with the AI model predictions. Good agreement is observed between the output from AI models and the corresponding experimental datasets with higher precision for the liquid desiccant dehumidifier parameters. Further, the multi-objective optimization for dehumidifier system is developed to explicitly solve the independent parameters of the objective function through evolution within the domain and find the optimum input variables value to formulate the optimal model structure. Meanwhile, the sensitivity analysis is performed. The GEP meta-model is established based on the experimental results. The GEP meta-model is found to possess higher prediction capability as experimental results. The fuzzy logic is made to get the intermediate results within certain constraints which successfully emulated using a genetic algorithm. A novel approach is obtained to perform the multi-responsive optimisation by integrating GEP meta-models with fuzzy logic combined GA. The following are the major generic and specific conclusions drawn from the current study.

- The proposed AI models could potentially function as a reliable predictive tool to predict the experimental results. AI models showed a specific, non-linear interpretation of the dehumidifier performance that would provide a relationship to the predictor input data with the response data.
- It is found that the dehumidifier performance parameters can be predicted by ANN (5-10-10-3), ANFIS (5-16-1) and GEP (3-5 genes). Subsequently, it is observed that the AI-based GEP model has the best prediction capability compared to the other developed AI models.
- It is observed that air mass flux rate, solution concentration and specific humidity have a significant impact on CR, whereas air mass flux rate and solution temperature are the most effective parameters for ε_m and LHR, respectively.
- Using GEP model, an empirical correlation between process (F_a, T_a, ω_a, F_s, T_s, and ζ) and response (CR, ε_m and LHR) parameters in the form of expression trees as well as mathematical expressions are obtained. The correlation metrics and error metrics statistically confirm the effectiveness and robustness of the GEP predictions.
- The optimum inlet process parameters are found to be F_a = 0.766 kg/m^2-s, T_a = 30.745°C, ω_a = 0.023 kg_{wv}/kg_{da}, F_s = 1.812 kg/m^2-s, T_s = 24.01°C and ζ = 48.1%. The predicted values of CR, ε_m and LHR from GEP meta-model are 5.875 g/m^2-s, 48.65% and 0.82, respectively at this optimum inlet conditions.
- At near optimum point (F_a = 0.76 kg/m^2-s, T_a = 30.1°C, ω_a = 0.024 kg_{wv}/kg_{da}, F_s = 1.8 kg/m^2-s, T_s = 24°C, and ζ = 48%), the experimental results CR of 5.584 g/m^2-s, ε_m of 42%

and LHR of 0.83, respectively were obtained. The experimental and predicted results for the optimum dehumidifier performance parameters (CR, ε_m, LHR) showed a very good agreement to each other (>8%) and that endorses the great reproducibility of the experimental inferences.

8.4. Desiccant film based air dehumidification results

Citric acid cross-linked NaCMC films containing desiccants were developed and investigated for their physical and thermal properties. Subsequently, the moisture absorption capability was compared between the control (without desiccant) films and desiccant doped films. Based on the above experimental investigations, the following key observations can be enumerated:

- X-ray diffraction (XRD) results of control films and 5%, 10% and 20% desiccant doped films exhibited that the films were homogeneous and there were no crystalline phases of desiccants in the developed films.
- It was found that 10% films required minimum regeneration temperature of 55.3°C. Furthermore, the regeneration rate was higher for 10% films compared to the control films, 5%, and 20% desiccant films.
- It was found that 10% films exhibited a higher elongation (%) and tensile strength compared to 20% films.
- WVP analysis showed that the rate of water transmission was reduced in the range of 3.3×10^{-9} to 0.4×10^{-9} g m^{-1} day^{-1} pa^{-1} from 0% to 20% desiccants.
- The result of moisture absorption analysis showed that 20% desiccant films have higher instantaneous and overall moisture absorption rate among all the developed films at different relative humidity settings.
- The lower regeneration rate and comparable instantaneous absorption rate was found for 10% desiccant films.

8.5. Significance of findings

The significant findings of current thesis work are listed, as follows:

- The overall moisture absorption rate of 85:15 (LiBr: $CaCl_2$) was higher than other prepared desiccant samples.
- The maximum outlet temperature obtained from the solar evacuated tube collector was 86.7ºC, 76.5ºC, and 69.0ºC for mass flow rates of 0.03, 0.05 and 0.08 kg/s, respectively.

- The maximum thermal efficiency of the solar evacuated tube collector system was found to be 63%, 72% and 75% for mass flow rates of 0.03, 0.05 and 0.08 kg/s, respectively.
- The average daily useful heat gain from the developed solar evacuated tube collector system was around 2.9 kW with average efficiency of 53%. Besides, one such unit of ETCs can annually generate heat on an average of 2.1 MWh.
- MLP architecture with three neurons in input layer, two hidden layers with ten neurons in each layer and three neurons in the output layer (3-10-10-3) is found to be optimal architecture for mapping the performance-outlet temperature characteristics of solar evacuated tube collector system under different mass flow rates.
- The performance of aqueous desiccant blends of LiBr+$CaCl_2$ was experimentally investigated at different concentrations (from 30 to 55 wt.%). Within the operating range, the result showed that the mixture desiccant could increase the condensation rate where the moisture effectiveness and latent heat factor were comparable with the pure LiBr.
- For tested liquid desiccant dehumidifier, condensation rate and latent effectiveness lies in the range of 2.2 to 5.6 g/m^2-s and 36 to 68%, respectively. Whereas the evaporation rate, sensible and the latent effectiveness of the regenerator lies in the range of 0.1–11.2 g/m^2-s, 25.9–63% and 10-92% depending on the operating conditions.
- The experimental results showed that the airside (dehumidifier) and solution-side (regenerator) latent effectiveness increase with solution to air mass flow rate. However, the solution-side latent effectiveness is higher than the airside effectiveness.
- CR increases as L/G increase, which indicates that an increase in L/G significantly improve the heat and mass transfer coefficient. Hence, this factor increases the driving factor of the dehumidifier/ regenerator.
- It is found that the air side pressure drop in the dehumidifier/regenerator is directly proportional to the airflow rate. TCOP and COP of the proposed dehumidifier-regenerator system were estimated as 1.1 and 0.62, respectively.
- It is found that the dehumidifier performance parameters can be predicted by ANN (5-10-10-3), ANFIS (5-16-1) and GEP (3-5 genes). Subsequently, it is observed that the AI-based GEP model has the best prediction capability compared to the other developed AI models.
- The optimum inlet process parameters are found to be F_a = 0.766 kg/m^2-s, T_a = 30.745°C, ω_a = 0.023 kg_{wv}/kg_{da}, F_s = 1.812 kg/m^2-s, T_s = 24.01°C and ζ = 48.1%. GEP meta-model

predicted that the CR, ε_m and LHR values are 5.875 g/m^2-s, 48.65% and 0.82, respectively at this optimum inlet conditions.

- At near optimum point (F_a = 0.76 kg/m^2-s, T_a = 30.1°C, ω_a = 0.024 kg_{wv}/kg_{da}, F_s = 1.8 kg/m^2-s, T_s = 24°C, and ζ = 48%), the experimental results CR of 5.584 g/m^2-s, ε_m of 42% and LHR of 0.83, respectively were obtained. The experimental and predicted results for the optimum dehumidifier performance parameters (CR, ε_m, LHR) showed a very good agreement to each other (>8%) and that endorses the great reproducibility of the experimental inferences.
- X-ray diffraction (XRD) results of control films and 5%, 10%, 20% desiccant doped films exhibited that the films were homogeneous and there were no crystalline phases of desiccants in the developed films.
- It was found that 10% desiccant doped films required minimum regeneration temperature of 55.3°C. Furthermore, the regeneration rate was higher for 10% desiccant doped films compared to the control films, 5%, and 20% desiccant films.
- The lower regeneration rate and comparable instantaneous absorption rate was found for 10% desiccant films.

8.6. Scope for future work

In this present work, laboratory-scale experiments were done. Though the number of publications on liquid desiccant has been enormous, the liquid desiccant air dehumidification's practical uses in real buildings are still limited. Therefore, publications related to the system's engineering case studies and practical operations should be encouraged. The liquid desiccant system's few relevant areas have been identified, and further investigation is needed on them. Listed below are the recommended topics for research in the near future:

- Liquid desiccant dehumidification system performance can be investigated to enhance the performance of regeneration/dehumidification rate with other different desiccant blends. The optimization of those blends ratio is in high demand.
- A comprehensive overall economic analysis of the system needs to be carried out and determine its practical feasibility, sustainability in contrast with the stand-alone conventional system.

- The capability of liquid desiccant system to deactivate or kill viruses, bacteria, capture air's particulate matter, and extract volatile organic compounds (VOC) to ensure better indoor air quality still needs to be studied.
- In the outlet air, the percentage of Li^+, Cl^- and Br^- ions are needed to be studied constructively.
- The benefit of integrating the latent heat recovery at the outlet of regenerator needs to be studied.
- Desiccant performance over the cyclic operations in the dehumidifier and regenerator are in high interest of research.
- Different U- tube geometry can be designed and experimentally studied to extract more energy density from the solar collectors.
- Different packing material density effects on dehumidification/regeneration performance, and optimization of the packing materials' flute heights can be studied
- The potentiality of desiccant doped hydrogel films can be investigated as packing materials for air dehumidification applications.

References

Abdullah M.Z., Yusup S., Mohd Bukhari N.A., 2014, Synthesis and dehumidification performance of calcium chloride derived from the waste shells of Anadara granosa Appl. Mech. Mater., 625, pp. 924-927, https://doi.org/10.4028/www.scientific.net/amm.625.924

Ameel T.A., Gee K.G., Wood B.D., 1995, Performance predictions of alternative, low cost absorbents for open-cycle absorption solar cooling Sol. Energy, 54, pp. 65-73, 10.1016/0038-092X(94)00103-K

Anantharaj, R., & Banerjee, T., 2011. Quantum chemical studies on the simultaneous interaction of thiophene and pyridine with ionic liquid. AIChE Journal, 57(3), 749-764.

Anand, K., Sharma, R. P., & Mehta, P. S., 2011. Experimental investigations on combustion, performance and emissions characteristics of neat karanji biodiesel and its methanol blend in a diesel engine. Biomass and bioenergy, 35(1), 533-541.

Ahmed S.Y., Gandhidasan P., Al-Farayedhi A.A., 1998, Thermodynamic analysis of liquid desiccants Sol. Energy, 62, pp. 11-18, https://doi.org/10.1016/S0038-092X(97)00087-X

Afonso, C.F.A., 2006. Recent advances in building air conditioning systems. Applied Thermal Engineering 26, 1961–1971.

Arica MY. 2007, Immobilization of polyphenol oxidase on carboxymethylcellulose hydrogel beads: Preparation and characterization. Polymer International 2000;49:775–81. doi:10.1002/1097-0126()49:7<775::AID-PI454>3.0.CO;2-O.

Agrawal, A., Goyal, V., Mishra, P., 2019. Adaptive Control of a Nonlinear Surge Tank-Level System Using Neural Network-Based PID Controller, in: Malik, H., Srivastava, S., Sood, Y.R., Ahmad, A. (Eds.), Applications of Artificial Intelligence Techniques in Engineering. Springer Singapore, Singapore, pp. 491–500. https://doi.org/10.1007/978-981-13-1819-1_46

Ahmed, C.S.K., Gandhidasan, P., Al-Farayedhi, A.A., 1997. Simulation of a hybrid liquid desiccant based air-conditioning system. Applied Thermal Engineering 17, 125–134.

Ali, A., Vafai, K., 2004. An investigation of heat and mass transfer between air and desiccant film in an inclined parallel and counter flow channels. International Journal of Heat and Mass Transfer 47, 1745–1760. https://doi.org/10.1016/j.ijheatmasstransfer.2003.10.008

Ali, A., Vafai, K., Khaled, A.-R., 2004. Analysis of heat and mass transfer between air and falling film in a cross flow configuration. International Journal of Heat and Mass Transfer 47, 743–755. https://doi.org/10.1016/j.ijheatmasstransfer.2003.07.017

Ali, A., Vafai, K., Khaled, A.A., 2003. Comparative study between parallel and counter flow configurations between air and falling film desiccant in the presence of nanoparticle suspensions. International Journal of Energy Research 745, 725–745. https://doi.org/10.1002/er.908

Alizadeh, S., 2008. Performance of a solar liquid desiccant air conditioner–An experimental and theoretical approach. Solar Energy 82, 563–572. https://doi.org/10.1016/j.solener.2007.10.009

Alosaimy, A.S., Hamed, A.M., 2011. Theoretical and experimental investigation on the application of solar water heater coupled with air humidifier for regeneration of liquid desiccant. Energy 36, 3992–4001. https://doi.org/10.1016/j.energy.2011.05.002

Armstrong, J.S., Fildes, R., 1995. On the Selection of Error Measures for Comparisons Among Forecasting Methods. Journal of Forecasting 14, 67—71.

ASHRAE, 2016. HVAC&R Industry. A weekly eNewsletter from ASHRAE. ASHRAE 15, 3.

Atalay, S.D., Calis, G., Kus, G., Kuru, M., 2019. Performance analyses of statistical approaches for modeling electricity consumption of a commercial building in France. Energy and Buildings 195, 82–92. https://doi.org/10.1016/j.enbuild.2019.04.035

Ayata, T., Erdemir, D., Ozkan, O.T., 2017. An investigation for predicting the effect of green roof utilization on temperature decreasing over the roof surface with Gene Expression Programming. Energy and Buildings 139, 254–262. https://doi.org/10.1016/j.enbuild.2017.01.014

Babakhani, D., Soleymani, M., 2010. Simplified analysis of heat and mass transfer model in liquid desiccant regeneration process. Journal of the Taiwan Institute of Chemical Engineers 41, 259–267. https://doi.org/10.1016/j.jtice.2009.10.006

Babakhani, D., Soleymani, M., 2009. An analytical solution for air dehumidification by liquid desiccant in a packed column. International Communications in Heat and Mass Transfer 36, 969–977.

Barkenbus, J.N., 2006. Putting energy efficiency in a sustainability context: The cold facts about refrigerators. Environment 48, 10–20. https://doi.org/10.3200/ENVT.48.8.10-20

Barrios, S., Bertinelli, L., Strobl, E., 2006. Climatic change and rural–urban migration: The case of sub-Saharan Africa. Journal of Urban Economics 60, 357–371.

Basavaraja, K.T., Kiran, T., Sushanth, T., Reddy, T.S., 2019. Heat Load Calculation with Duct Design of a Multi Storeyed Residential Building. International Journal of Trend in Scientific Research and Development Volume-3, 1150–1156. https://doi.org/10.31142/ijtsrd23301

Bassuoni, M.M., 2011. An experimental study of structured packing dehumidifier/regenerator operating with liquid desiccant. Energy 36, 2628–2638. https://doi.org/10.1016/j.energy.2011.02.004

Betiku, E., Odude, V.O., Ishola, N.B., Bamimore, A., Osunleke, A.S., Okeleye, A.A., 2016. Predictive capability evaluation of RSM , ANFIS and ANN : A case of reduction of high free fatty acid of palm kernel oil via esterification process. Energy Conversion and Management 124, 219–230. https://doi.org/10.1016/j.enconman.2016.07.030

Bhowmik, S., Panua, R., Debroy, D., Paul, A., 2017. Artificial Neural Network Prediction of Diesel Engine Performance and Emission Fueled With Diesel–Kerosene–Ethanol Blends: A Fuzzy-Based Optimization. Journal of Energy Resources Technology 139, 042201. https://doi.org/10.1115/1.4035886

Bhowmik, S., Paul, A., Panua, R., Ghosh, S.K., Debroy, D., 2018. Performance-exhaust emission prediction of diesosenol fueled diesel engine: An ANN coupled MORSM based optimization. Energy 153, 212–222. https://doi.org/10.1016/j.energy.2018.04.053

Bliemel, F., 1973. Theil's Forecast Accuracy Coefficient: A Clarification. Journal of Marketing Research 10, No. 4, 444–446. https://doi.org/10.2307/3149394.

Bian, Z. Z. L. Yang, Z.W.L., 2012. Experimental study of ultrasound atomization dehumidifying system with liquid desiccant. J Shanghai Jiao Tong Univ 46, 1604–1608.

Boyacioglu, M.A., Avci, D., 2010. An adaptive network-based fuzzy inference system (ANFIS) for the prediction of stock market return: The case of the Istanbul stock exchange. Expert Systems with Applications 37, 7908–7912. https://doi.org/10.1016/j.eswa.2010.04.045

British Petroleum, 2019. BP Energy Outlook 2019 edition The Energy Outlook explores the forces shaping the global energy transition out to 2040 and the key uncertainties surrounding that. BP Energy Outlook 2019 22–24, 72–76, 144–118.

Buker, M.S., Mempouo, B., Riffat, S.B., 2015. Experimental investigation of a building integrated photovoltaic/thermal roof collector combined with a liquid desiccant enhanced indirect evaporative cooling system. Energy Conversion and Management 101, 239–254. https://doi.org/10.1016/j.enconman.2015.05.026

Buragohain, M., Mahanta, C., 2008. A novel approach for ANFIS modelling based on full factorial design. Applied Soft Computing 8, 609–625. https://doi.org/10.1016/j.asoc.2007.03.010

Camargo, J.R., Godoy, E., Ebinuma, C.D., 2005. An evaporative and desiccant cooling system for air conditioning in humid climates. Journal of the Brazilian Society of Mechanical

Sciences and Engineering 27, 243–247. https://doi.org/10.1590/S1678-58782005000300005

Chau, C.K., Worek, W.M., 2009. Cosorption processes of triethylene glycol in a Packed-Bed liquid desiccant dehumidifier. HVAC and R Research 15, 189–210. https://doi.org/10.1080/10789669.2009.10390833

Chen, L.-F., Soriano, A.N., Li, M.-H., 2009. Vapour pressures and densities of the mixed-solvent desiccants (glycols+ water+ salts). The Journal of Chemical Thermodynamics 41, 724–730.

Chen, X., Riffat, S., Bai, H., Zheng, X., Reay, D., 2020. Recent progress in liquid desiccant dehumidification and air-conditioning: A review. Energy and Built Environment 1, 106–130. https://doi.org/10.1016/j.enbenv.2019.09.001

Chen G, Hoffman A.S., 1995, Graft copolymers that exhibit temperature-induced phase transitions over a wide range of pH. Nature;373:49–52. doi:10.1038/373049a0.

Chen, Z., Yang, Y., 2004. Assessing Forecast Accuracy Measures. Preprint Series 2010 (2004): 2004-10 1–26.

Cheng, Q., Zhang, X.-S., Li, X.-W., 2012. Double-stage photovoltaic/thermal ED regeneration for liquid desiccant cooling system. Energy and Buildings 51, 64–72. https://doi.org/10.1016/j.enbuild.2012.04.017

Chengqin, R., Yi, J., Yianpin, Z., 2006. Simplified analysis of coupled heat and mass transfer processes in packed bed liquid desiccant-air contact system. Solar Energy 80, 121–131.

Cho, H.J., Cheon, S.Y., Jeong, J.W., 2019. Experimental analysis of dehumidification performance of counter and cross-flow liquid desiccant dehumidifiers. Applied Thermal Engineering 150, 210–223. https://doi.org/10.1016/j.applthermaleng.2019.01.006

Chung, T.W., Ghosh, T.K., Hines, A.L., 1996. Comparison between Random and Structured Packings for Dehumidification of Air by Lithium Chloride Solutions in a Packed Column and Their Heat and Mass Transfer Correlations. Industrial and Engineering Chemistry Research 35, 192–198. https://doi.org/10.1021/ie940652u

Chung, T.W., Wu, H., 2000. Comparison between spray towers with and without fin coils for air dehumidification using triethylene glycol solutions and development of the mass-transfer correlations. Industrial and Engineering Chemistry Research 39, 2076–2084. https://doi.org/10.1021/ie990630d

Chung, T.W., Lai, C.H. and Wu, H., 1999. Analysis of mass transfer performance in an air stripping tower. Separation Science and Technology, 34(14), pp.2837-2851.

Cigizoglu, H.K., 2004. Estimation and forecasting of daily suspended sediment data by multi-layer perceptrons. Advances in Water Resources 27, 185–195. https://doi.org/10.1016/j.advwatres.2003.10.003

Cisternas, L.A., Lam, E.J., 1991. An analytic correlation for the vapour pressure of aqueous and non-aqueous solutions of single and mixed electrolytes. Part II. Application and extension. Fluid Phase Equilibria 62, 11–27. https://doi.org/10.1016/0378-3812(91)87002-Q

Conde, M.R., 2004. Properties of aqueous solutions of lithium and calcium chlorides: Formulations for use in air conditioning equipment design. International Journal of Thermal Sciences 43, 367–382. https://doi.org/10.1016/j.ijthermalsci.2003.09.003

Cosenza, F., and G.C.V., 1990. Absorption in falling water/LiBr films on horizontal tubes. ASHRAE Transactions 96.1, 693–701.

Dai, Y.J., Zhang, H.F., 2004. Numerical simulation and theoretical analysis of heat and mass transfer in a cross flow liquid desiccant air dehumidifier packed with honeycomb paper. Energy Conversion and Management 45, 1343–1356. https://doi.org/10.1016/j.enconman.2003.09.006

Das, R.S., Jain, S., 2015. Performance characteristics of cross-flow membrane contactors for liquid desiccant systems. Applied Energy 141, 1–11. https://doi.org/10.1016/j.apenergy.2014.12.014

Davanagere, B.S., Sherif, S.A., Goswami, D.Y., 1999. A feasibility study of a solar desiccant air-conditioning system—Part II: Transient simulation and economics. International Journal of Energy Research 23, 103–116.

De Lucas, A., Donate, M., Rodríguez, J.F., 2008. Applying surfactants to improve the absorption capacity of mixtures of lithium bromide and formates in absorption refrigeration coolers. International Journal of Refrigeration 31, 1073–1080. https://doi.org/10.1016/j.ijrefrig.2007.12.005

Deb, M., Majumder, P., Majumder, A., Roy, S., Banerjee, R., 2016. Application of artificial intelligence (AI) in characterization of the performance–emission profile of a single cylinder CI engine operating with hydrogen in dual fuel mode: An ANN approach with fuzzy-logic based topology optimization. International Journal of Hydrogen Energy 41, 14330–14350. https://doi.org/10.1016/j.ijhydene.2016.07.016

Deng, J., Wang, R.Z., Han, G.Y., 2011. A review of thermally activated cooling technologies for combined cooling, heating and power systems. Progress in Energy and Combustion Science 37, 172–203. https://doi.org/10.1016/j.pecs.2010.05.003

Dhar, P., Tarafder, D., Kumar, A., Katiyar, V., 2015. Effect of cellulose nanocrystal polymorphs on mechanical, barrier and thermal properties of poly(lactic acid) based bionanocomposites. RSC Advances 5, 60426–60440. https://doi.org/10.1039/c5ra06840a

Dharmalingam, K., Bordoloi, D., Kunnumakkara, A.B., Anandalakshmi, R., 2020. Preparation and characterization of cellulose-based nanocomposite hydrogel films containing CuO/Cu2O/Cu with antibacterial activity. Journal of Applied Polymer Science 137, 1–14. https://doi.org/10.1002/app.49216

Dharmalingam K, Anandalakshmi R. 2019, Fabrication, characterization and drug loading efficiency of citric acid crosslinked NaCMC-HPMC hydrogel films for wound healing drug delivery applications. International Journal of Biological Macromolecules;134:815–29. doi:10.1016/j.ijbiomac.2019.05.027.

Diaz, G., 2010. Numerical investigation of transient heat and mass transfer in a parallel-flow liquid-desiccant absorber. Heat and Mass Transfer/Waerme- und Stoffuebertragung 46, 1335–1344. https://doi.org/10.1007/s00231-010-0665-8

Dikmen, E., Ayaz, M., Ezen, H.H., Küçüksille, E.U., Şahin, A.Ş., 2014. Estimation and optimization of thermal performance of evacuated tube solar collector system. Heat and Mass Transfer/Waerme- und Stoffuebertragung 50, 711–719. https://doi.org/10.1007/s00231-013-1282-0

Donate, M., Rodriguez, L., Lucas, A. De, Rodríguez, J.F., 2006. Thermodynamic evaluation of new absorbent mixtures of lithium bromide and organic salts for absorption refrigeration machines. International Journal of Refrigeration 29, 30–35. https://doi.org/10.1016/j.ijrefrig.2005.05.005

Dong H., Cho H., Park J., Jeong J., 2019, Optimum regeneration temperature of a desiccant solution in a packaged liquid desiccant-assisted air conditioning unit 101, 155–166. https://doi.org/10.1016/j.ijrefrig.2019.03.037.

Eberhart, R.C., 2014. Neural Network PC Tools A Practical Guide. Academic Press, elsevier.

Elsarrag, E., Ali, E.E.M., Jain, S., 2005. Design guidelines and performance study on a structured packed liquid desiccant air-conditioning system. HVAC and R Research 11, 319–337. https://doi.org/10.1080/10789669.2005.10391140

Enteria, N., Mizutani, K., 2011. The role of the thermally activated desiccant cooling technologies in the issue of energy and environment. Renewable and Sustainable Energy Reviews 15, 2095–2122. https://doi.org/10.1016/j.rser.2011.01.013

Enteria, N., Yoshino, H., Mochida, A., 2013. Review of the advances in open-cycle absorption air-conditioning systems. Renewable and Sustainable Energy Reviews 28, 265–289. https://doi.org/10.1016/j.rser.2013.07.012

Ertas, A., Anderson, E.E., Kiris, I., 1992. Properties of a new liquid desiccant solution-Lithium chloride and calcium chloride mixture. Solar Energy 49, 205–212. https://doi.org/10.1016/0038-092X(92)90073-J

Ertas, A., Gandhidasan, P., Kiris, I. and Anderson, E.E., 1994. Experimental study on the performance of a regeneration tower for various climatic conditions. Solar energy, 53(1), pp.125-130.

Ertugrul Cihan, Baris Kavasogullari, H.D., 2017. Influence of Surfactant Additive on Performance of Open Liquid Desiccant System. International Sorption Heat Pump Conference 2017, Aug. 7-10, 2017, Tokyo 1–3.

Essa, M.A., Mostafa, N.H., Ibrahim, M.M., 2018. An experimental investigation of the phase change process effects on the system performance for the evacuated tube solar collectors integrated with PCMs. Energy Conversion and Management 177, 1–10. https://doi.org/10.1016/j.enconman.2018.09.045

Factor, H.M., Grossman, G., 1980. A packed bed dehumidifier/regenerator for solar air conditioning with liquid desiccants. Solar energy 24, 541–550. https://doi.org/10.1016/0038-092X(80)90353-9

Fendu, E.M., Oprea, F., 2013. Vapor pressure, density, viscosity, and surface tension of tetrapropylene glycol. Journal of Chemical and Engineering Data 58, 2898–2903. https://doi.org/10.1021/je4004977

Ferreira, C., 2006. Gene Expression Programming Mathematical Modeling by an Artificial Intelligence. Springer. https://doi.org/10.1007/3-540-32849-1

Ferreira, C., 2001. Gene Expression Programming: A New Adaptive Algorithm for Solving Problems. The Ridings, Bristol BS13 8NU, UK 1–22.

Fischer, S., Frey, P., Drück, H., 2012. A comparison between state-of-the-art and neural network modelling of solar collectors. Solar Energy 86, 3268–3277. https://doi.org/10.1016/j.solener.2012.09.002

Fei B, Wach RA, Mitomo H, Yoshii F, Kume T., 2000. Hydrogel of biodegradable cellulose derivatives. I. Radiation-induced crosslinking of CMC. Journal of Applied Polymer Science;78:278–83. doi:10.1002/1097-4628(20001010)78:2<278::AID-APP60>3.0.CO;2-9.

Fu, H.X., Liu, X.H., 2017. Review of the impact of liquid desiccant dehumidification on indoor air quality. Building and Environment 116, 158–172. https://doi.org/10.1016/j.buildenv.2017.02.014

Fumo, N., Goswami, D.Y., 2002. Study of an aqueous lithium chloride desiccant system: Air dehumidification and desiccant regeneration. Solar Energy 72, 351–361. https://doi.org/10.1016/S0038-092X(02)00013-0

Hinton, G;, Salakhutdinov;, R.R., 2006. Reducing the Dimensionality of Data with Neural Networks. Science 313, 504–507. https://doi.org/10.1126/science.1127647

Gandhidasan, P., 2005. Quick performance prediction of liquid desiccant regeneration in a packed bed. Solar Energy 79, 47–55. https://doi.org/10.1016/j.solener.2004.10.002

Gandhidasan, P, 2004. A simplified model for air dehumidification with liquid desiccant. Solar Energy 76, 409–416. https://doi.org/10.1016/j.solener.2003.10.001

Gandhidasan, P., Mohandes, M.A., 2008. Predictions of vapor pressures of aqueous desiccants for cooling applications by using artificial neural networks. Applied Thermal Engineering 28, 126–135.

Gao, W.Z., Liu, J.H., Cheng, Y.P., Zhang, X.L., 2012. Experimental investigation on the heat and mass transfer between air and liquid desiccant in a cross-flow dehumidifier. Renewable Energy 37, 117–123. https://doi.org/10.1016/j.renene.2011.06.006

Gao, Y., Fan, R., Zhang, X.Y., AN, Y.J., Wang, M.X., Gao, Y.K., Yu, Y., 2014. Thermal performance and parameter analysis of a U-pipe evacuated solar tube collector. Solar Energy 107, 714–727. https://doi.org/10.1016/j.solener.2014.05.023

Ghaderian, J., Sidik, N.A.C., 2017. An experimental investigation on the effect of Al2O3/distilled water nanofluid on the energy efficiency of evacuated tube solar collector. International Journal of Heat and Mass Transfer 108, 972–987. https://doi.org/10.1016/j.ijheatmasstransfer.2016.12.101

Ghadiri Moghaddam, D., Besant, R.W., Simonson, C.J., 2014. Solution-side effectiveness for a liquid-to-air membrane energy exchanger used as a dehumidifier/regenerator. Applied Energy 113, 872–882. https://doi.org/10.1016/j.apenergy.2013.08.037

Ghafoor, A., Munir, A., 2015. Worldwide overview of solar thermal cooling technologies. Renewable and Sustainable Energy Reviews 43, 763–774. https://doi.org/10.1016/j.rser.2014.11.073

Ghobadian, B., Rahimi, H., Nikbakht, A.M., Najafi, G., Yusaf, T.F., 2009. Diesel engine performance and exhaust emission analysis using waste cooking biodiesel fuel with an

artificial neural network. Renewable Energy 34, 976–982. https://doi.org/10.1016/j.renene.2008.08.008

Gommed, K., Grossman, G., 2004. A liquid desiccant system for solar cooling and dehumidification. Journal of Solar Energy Engineering 126, 879–885. https://doi.org/10.1115/1.1690284

Gommed, K., Grossman, G., Ziegler, F., 2004a. Experimental investigation of a LiCl-water open absorption system for cooling and dehumidification. Journal of Solar Energy Engineering, Transactions of the ASME 126, 710–715. https://doi.org/10.1115/1.1643075

Gooch, J.W., 2011. Triethylene Glycol. Encyclopedic Dictionary of Polymers 765–765. https://doi.org/10.1007/978-1-4419-6247-8_12115

Gordeeva, L.G., Grekova, A.D., Krieger, T.A., Aristov, Y.I., 2009. Adsorption properties of composite materials (LiCl + LiBr)/silica. Microporous and Mesoporous Materials 126, 262–267. https://doi.org/10.1016/j.micromeso.2009.06.015

Ghorpade VS, Yadav AV, Dias RJ. Citric acid crosslinked β-cyclodextrin/carboxymethylcellulose hydrogel films for controlled delivery of poorly soluble drugs. Carbohydrate Polymers 2017;164:339–48. doi:10.1016/j.carbpol.2017.02.005.

Gu Y., Zhang X., Performance investigation on the liquid desiccant regeneration using rotating packed bed, Int. J. Refrig. 109 (2020) 45–54. https://doi.org/10.1016/j.ijrefrig.2019.09.017.

Hamed, A., Kassem, T.K., Alosaimy, A.S., Fazian, M., 2013. Solar Powered Dehumidification Systems Using Desert Evaporative Coolers: Review.

Harding, G.L., Zhiqiang, Y., Mackey, D.W., 1985. Heat extraction efficiency of a concentric glass tubular evacuated collector. Solar Energy 35, 71–79. https://doi.org/10.1016/0038-092X(85)90038-6

Harriman III, L.G., Plager, D., Kosar, D., 1997. Dehumidification and cooling loads from ventilation air. ASHRAE journal 39, 37-45.

Hassoun, M.H., 1995. fundamentals of artificial neural networks. MIT Press.

Hazami, M., Naili, N., Attar, I., Farhat, A., 2013. Solar water heating systems feasibility for domestic requests in Tunisia: Thermal potential and economic analysis. Energy Conversion and Management 76, 599–608. https://doi.org/10.1016/j.enconman.2013.07.079

Howell, J.R., 1987. A survey of active solar cooling methods. Progress in solar engineering, pp.171-182.

Huang S., Lv Z., Zhang X., Liang C., 2018. Experimental investigation on heat and mass transfer in heating tower solution regeneration using packing tower, Energy Build. 164, 77–86. https://doi.org/10.1016/j.enbuild.2017.12.064.

Hwang, Y., Radermacher, R., Alili, A. Al, Kubo, I., 2008. Review of solar cooling technologies. HVAC and R Research 14, 507–528. https://doi.org/10.1080/10789669.2008.10391022

IEA, 2008. Key world energy statistics.

Jain, S., Dhar, P.L., Kaushik, S.C., 1994. Evaluation of liquid desiccant based evaporative cooling cycles for typical hot and humid climates. Heat Recovery Syst and CHP 621–632. https://doi.org/10.1016/0890-4332(94)90032-9

Jain, S., Tripathi, S., Das, R.S., 2011. Experimental performance of a liquid desiccant dehumidification system under tropical climates. Energy Conversion and Management 52, 2461–2466. https://doi.org/10.1016/j.enconman.2010.12.052

Jain, S., Dhar, P.L. and Kaushik, S.C., 2000. Experimental studies on the dehumidifier and regenerator of a liquid desiccant cooling system. Applied thermal engineering, 20(3), pp.253-267.

Jang, J.R., 1993. ANFIS : Adaptive-Network-Based Fuzzy Inference System. IEEE Transactions On Systems, Man, and Cybernetics 23, 665–685.

Kakati, D., Roy, S., Banerjee, R., 2019. Development of an artificial neural network based virtual sensing platform for the simultaneous prediction of emission-performance-stability parameters of a diesel engine operating in dual fuel mode with port injected methanol. Energy Conversion and Management 184, 488–509. https://doi.org/10.1016/j.enconman.2019.01.087

Kang, C., Hyun, C., Park, M., 2015. Fuzzy logic-based advanced on – off control for thermal comfort in residential buildings. Applied Energy 155, 270–283. https://doi.org/10.1016/j.apenergy.2015.05.119

Kang, H.U., Kim, S.H., Oh, J.M., 2006. Estimation of thermal conductivity of nanofluid using experimental effective particle volume. Experimental Heat Transfer 19, 181–191. https://doi.org/10.1080/08916150600619281

Kang, Y.T., Kim, H.J., Lee, K. Il, 2008. Heat and mass transfer enhancement of binary nanofluids for H2O/LiBr falling film absorption process. International Journal of Refrigeration 31, 850–856. https://doi.org/10.1016/j.ijrefrig.2007.10.008

Katejanekarn, T., Chirarattananon, S., Kumar, S., 2009. An experimental study of a solar-regenerated liquid desiccant ventilation pre-conditioning system. Solar Energy 83, 920–933. https://doi.org/10.1016/j.solener.2008.12.006

Katiyar, P.K., Misra, S., Mondal, K., 2018. Effect of Different Cooling Rates on the Corrosion Behavior of High-Carbon Pearlitic Steel. Journal of Materials Engineering and Performance 27, 1753–1762. https://doi.org/10.1007/s11665-018-3256-3

Kakabaev, A. and Khandurdyev, A., 1969. Absorption solar refrigeration unit with open regeneration of solution. Appl. Solar Energy (USSR)(Engl. Transl.);(United States), 5(4).

Kaya, H., Arslan, K., 2018. Numerical investigation of efficiency and economic analysis of an evacuated U-tube solar collector with different nanofluids. Heat and Mass Transfer/Waerme- und Stoffuebertragung. https://doi.org/10.1007/s00231-018-2442-z

Khan, A.Y., Ball, H.D., 1992. Development of a generalized model for performance evaluation of packed-type liquid sorbent dehumidifiers and regenerators, in: ASHRAE Winter Meeting, Anaheim, CA, USA, 01/25-29/92. pp. 525–533.

Khan, A.Y., Martinez, J.L., 1998. Modelling and parametric analysis of heat and mass transfer performance of a hybrid liquid desiccant absorber. Energy Conversion and Management 39, 1095–1112. https://doi.org/10.1016/S0196-8904(97)00032-0

Kim, H., Jeong, J., Tae, Y., 2011. Heat and mass transfer enhancement for falling film absorption process by SiO2 binary nanofluids. International Journal of Refrigeration 35, 645–651. https://doi.org/10.1016/j.ijrefrig.2011.11.018

Kim, Y., Seo, T., 2007. Thermal performances comparisons of the glass evacuated tube solar collectors with shapes of absorber tube. Renewable Energy 32, 772–795. https://doi.org/10.1016/j.renene.2006.03.016

Kim M.H., Park J.Y., Jeong J.W., 2015. Simplified model for packed-bed tower regenerator in a liquid desiccant system, Appl. Therm. Eng. 89, 717–726. https://doi.org/10.1016/j.applthermaleng.2015.06.057.

Kline, S.J., McClintock, F.A., 1953. Describing uncertainties in single-sample experiments. Mechanical engineering. https://doi.org/10.1016/j.chaos.2005.11.046

Kohavi, R., 1995. A study of cross-validation and bootstrap for accuracy estimation and model selection. Proceedings of the 14th international joint conference on Artificial intelligence - Volume 2 2, 1137–1143.

Koronaki, I.P., Christodoulaki, R.I., Papaefthimiou, V.D., Rogdakis, E.D., 2013. Thermodynamic analysis of a counter flow adiabatic dehumidifier with different liquid

desiccant materials. Applied Thermal Engineering 50, 361–373. https://doi.org/10.1016/j.applthermaleng.2012.06.043

Korres, D.N., Tzivanidis, C., Koronaki, I.P., Nitsas, M.T., 2019. Experimental, numerical and analytical investigation of a U-type evacuated tube collectors' array. Renewable Energy 135, 218–231. https://doi.org/10.1016/j.renene.2018.12.003

Koneru A, Dharmalingam K, Anandalakshmi R. 2020, Cellulose based nanocomposite hydrogel films consisting of sodium carboxymethylcellulose–grapefruit seed extract nanoparticles for potential wound healing applications. International Journal of Biological Macromolecules;148:833–42. doi:10.1016/j.ijbiomac.2020.01.018.

Kök FN, Wilkins RM, Cain RB, Arica MY, Alaeddinoğlu G, Hasirci V., 1999. Controlled release of aldicarb from lignin loaded ionotropic hydrogel microspheres. Journal of Microencapsulation;16:613–23. doi:10.1080/026520499288807.

Kumar R., Asati A.K., 2016, Experimental study on performance of celdek packed liquid desiccant dehumidifier, Heat Mass Transf. 52, 1821–1832. https://doi.org/10.1007/s00231-015-1704-2.

Langmuir, I., 1913. The vapor pressure of metallic tungsten. Physical review 2.5: 329. II, 42–45. https://doi.org/10.1103/PhysRev.2.329

Langroudi, L.O., Pahlavanzadeh, H., Mousavi, S.M., 2014. Statistical evaluation of a liquid desiccant dehumidification system using RSM and theoretical study based on the effectiveness NTU model. Journal of Industrial and Engineering Chemistry 20, 2975–2983. https://doi.org/10.1016/j.jiec.2013.11.031

Li, N., Yang, L., Li, Xiaodong, Li, Xiangdong, Tu, J., Cheung, S.C.P., 2019. Multi-objective optimization for designing of high-speed train cabin ventilation system using particle swarm optimization and multi-fidelity Kriging. Building and Environment 155, 161–174. https://doi.org/10.1016/j.buildenv.2019.03.021

Li, X.-W., Zhang, X.-S., 2009. Photovoltaic–electrodialysis regeneration method for liquid desiccant cooling system. Solar Energy 83, 2195–2204. https://doi.org/10.1016/j.solener.2009.09.001

Li, X., Liu, S., Tan, K.K., Wang, Q.G., Cai, W.J., Xie, L., 2016. Dynamic modeling of a liquid desiccant dehumidifier. Applied Energy 180, 435–445. https://doi.org/10.1016/j.apenergy.2016.07.085

Li, X.W., Zhang, X.S., Quan, S., 2011. Single-stage and double-stage photovoltaic driven regeneration for liquid desiccant cooling system. Applied Energy 88, 4908–4917. https://doi.org/10.1016/j.apenergy.2011.06.052

Liang, R., Ma, L., Zhang, J., Zhao, D., 2011. Theoretical and experimental investigation of the filled-type evacuated tube solar collector with U tube. Solar Energy 85, 1735–1744. https://doi.org/10.1016/j.solener.2011.04.012

Lin Fu, Shigang, Z. S.J.,, 2011. Experimental study on vertical vapor absorption into LiBr solution with and without additive. Applied Thermal Engineering 31, 2850–2854. https://doi.org/10.1016/j.applthermaleng.2011.05.010

Liu, J., Liu, X., Zhang, T., 2020. Performance of heat pump driven internally cooled liquid desiccant dehumidification system. Energy Conversion and Management 205, 112447. https://doi.org/10.1016/j.enconman.2019.112447

Liu, M.S., Ching-Cheng Lin, M., Huang, I. Te, Wang, C.C., 2005. Enhancement of thermal conductivity with carbon nanotube for nanofluids. International Communications in Heat and Mass Transfer 32, 1202–1210. https://doi.org/10.1016/j.icheatmasstransfer.2005.05.005

Liu, X., Jiang, Y., Xia, J., Chang, X., 2007. Analytical solutions of coupled heat and mass transfer processes in liquid desiccant air dehumidifier/regenerator. Energy Conversion and Management 48, 2221–2232.

Liu, X.H., Jiang, Y., Qu, K.Y., 2007. Heat and mass transfer model of cross flow liquid desiccant air dehumidifier/regenerator. Energy Conversion and Management 48, 546–554. https://doi.org/10.1016/j.enconman.2006.06.002

Liu, X.H., Jiang, Y., Yi, X.Q., 2009. Effect of regeneration mode on the performance of liquid desiccant packed bed regenerator. Renewable Energy 34, 209–216. https://doi.org/10.1016/j.renene.2008.03.003

Liu, X.H., Yi, X.Q., Jiang, Y., 2011a. Mass transfer performance comparison of two commonly used liquid desiccants: LiBr and LiCl aqueous solutions. Energy Conversion and Management 52, 180–190. https://doi.org/10.1016/j.enconman.2010.06.057

Liu, X.H., Zhang, Y., Qu, K.Y., Jiang, Y., 2006. Experimental study on mass transfer performances of cross flow dehumidifier using liquid desiccant. Energy Conversion and Management 47, 2682–2692. https://doi.org/10.1016/j.enconman.2005.10.035

Liu, J., Zhang, T., Liu, X., Jiang, J., 2015. Experimental analysis of an internally-cooled/heated liquid desiccant dehumidifier/regenerator made of thermally conductive plastic. Energy and Buildings 99, 75–86. https://doi.org/10.1016/j.enbuild.2015.04.023

Lof, G.O., 1955. Cooling with solar energy. Congress on solar energy 12.

Longo, G.A., Gasparella, A., 2016. Experimental measurement of thermophysical properties of H2O/KCOOH (potassium formate) desiccant. International Journal of Refrigeration 62, 106–113. https://doi.org/10.1016/j.ijrefrig.2015.10.004

Longo, G.A., Gasparella, A., 2005. Experimental and theoretical analysis of heat and mass transfer in a packed column dehumidifier/regenerator with liquid desiccant. International Journal of Heat and Mass Transfer 48, 5240–5254. https://doi.org/10.1016/j.ijheatmasstransfer.2005.07.011

Longo G.A., Gasparella A., 2004. Experimental analysis on chemical dehumidification of air by liquid desiccant and desiccant regeneration in a packed tower Journal of Solar Energy Engineering, Transactions of the ASME, 126 (1), pp. 587-591. https://doi.org/10.1115/1.1637642

Low, M.J.D., 1960. Kinetics of chemisorption of gases on solids. Chemical Reviews 60, 267–312. https://doi.org/10.1021/cr60205a003

Lu, Z.-F., Chen, P.-L., Zhang, X., 2001. Approximate analytical solution of heat and mass transfer processes in packed-type cross-flow liquid desiccant system and its experimental verification. Journal-Tongji University 29.2, 149–153.

Lun, W., Li, K., Liu, B., Zhang, H., Yang, Y., Yang, C., 2018. Experimental analysis of a novel internally-cooled dehumidifier with self-cooled liquid desiccant. Building and Environment 141, 117–126. https://doi.org/10.1016/j.buildenv.2018.05.055

Luo, Y., Shao, S., Xu, H., Tian, C., 2011. Dehumidification performance of [EMIM]BF4. Applied Thermal Engineering 31, 2772–2777. https://doi.org/10.1016/j.applthermaleng.2011.04.050

Lucas A. De, Donate M., Rodríguez J.F., 2008, Applying surfactants to improve the absorption capacity of mixtures of lithium bromide and formates in absorption refrigeration coolers Int. J. Refrig., 31, pp. 1073-1080, 10.1016/j.ijrefrig.2007.12.005

Luo, Y., Yang, H., Lu, L., 2014. Liquid desiccant dehumidifier: Development of a new performance predication model based on CFD. International Journal of Heat and Mass Transfer 69, 408–416. https://doi.org/10.1016/j.ijheatmasstransfer.2013.10.033

Lychnos G., Davies P.A. 2012, Modelling and experimental verification of a solar-powered liquid desiccant cooling system for greenhouse food production in hot climates Energy, 40, pp. 116-130, 10.1016/j.energy.2012.02.021

Ma, L., Zhao, T., Zhang, J., Zhao, D., 2016. Numerical study on the heat transfer characteristics of filled-type solar collector with U-tube. Applied Thermal Engineering 107, 642–652. https://doi.org/10.1016/j.applthermaleng.2016.05.133

Ma J, Li X, Bao Y., 2015, Advances in cellulose-based superabsorbent hydrogels. RSC Advances;5:59745–57. doi:10.1039/c5ra08522e.

Matsumoto K, Sakikawa N, Miyata T. Thermo-responsive gels that absorb moisture and ooze water. Nature Communications 2018;9:1–7. doi:10.1038/s41467-018-04810-8.

Mahbubul, I.M., Khan, M.M.A., Ibrahim, N.I., Ali, H.M., Al-Sulaiman, F.A., Saidur, R., 2018. Carbon nanotube nanofluid in enhancing the efficiency of evacuated tube solar collector. Renewable Energy 121, 36–44. https://doi.org/10.1016/j.renene.2018.01.006

Martin, V. and Goswami, D.Y., 2000. Effectiveness of heat and mass transfer processes in a packed bed liquid desiccant dehumidifier/regenerator. *HVAC &R Research*, *6*(1), pp.21-39. https://doi.org/10.1080/10789669.2000.10391248

Mehla, N., Yadav, A., 2017a. Experimental analysis of thermal performance of evacuated tube solar air collector with phase change material for sunshine and off-sunshine hours. International Journal of Ambient Energy 38, 130–145. https://doi.org/10.1080/01430750.2015.1074612

Mei, L., Dai, Y.J., 2008. A technical review on use of liquid-desiccant dehumidification for air-conditioning application. Renewable and Sustainable Energy Reviews 12, 662–689. https://doi.org/10.1016/j.rser.2006.10.006

Menon, A., 1994. Characterization of a class of sigmoid functions with applications to neural networks 1 Introduction 9, 1–28.

Merkel, F., 1925. Evaporative cooling. Z Verein Deutsch Ingen (VDI) 70, 123–128.

Mehla, N. and Yadav, A., 2017. Experimental analysis of thermal performance of evacuated tube solar air collector with phase change material for sunshine and off-sunshine hours. International Journal of Ambient Energy, 38(2), pp.130-145. https://doi.org/10.1080/01430750.2015.1074612

Milukow, H.A., Binns, A.D., Adamowski, J., Bonakdari, H., Gharabaghi, B., 2019. Estimation of the Darcy–Weisbach friction factor for ungauged streams using Gene Expression Programming and Extreme Learning Machines. Journal of Hydrology 568, 311–321. https://doi.org/10.1016/j.jhydrol.2018.10.073

Misha, S., Mat, S., Ruslan, M.H., Sopian, K., 2012. Review of solid/liquid desiccant in the drying applications and its regeneration methods. Renewable and Sustainable Energy Reviews 16, 4686–4707. https://doi.org/10.1016/j.rser.2012.04.041

Miyata T, Jige M, Nakaminami T, Uragami T., 2006. Tumor marker-responsive behavior of gels prepared by biomolecular imprinting. Proceedings of the National Academy of Sciences of the United States of America;103:1190–3. doi:10.1073/pnas.0506786103.

Miyata T, Asami N, Uragani T. 1999. A reversibly antigen-responsive hydrogen. Nature;399:766–8. doi:10.1038/21619

Mohammad, A.T., Mat, S. Bin, Sopian, K., Al-Abidi, A.A., 2016. Review: Survey of the control strategy of liquid desiccant systems. Renewable and Sustainable Energy Reviews 58, 250–258. https://doi.org/10.1016/j.rser.2015.12.333

Mohandes, M.A., Rehman, S., Halawani, T.O., 1998. A Neural Networks Approach For Wind Speed Prediction. Renewable Energy 145–147. https://doi.org/10.1016/S0960-1481(98)00001-9

Mohaisen A.K., Ma Z., 2015. Development and modelling of a solar assisted liquid desiccant dehumidification air-conditioning system, Build. Simul. 8, 123–135. https://doi.org/10.1007/s12273-014-0196-1.

Moon, C.G., Bansal, P.K., Jain, S., 2009. New mass transfer performance data of a cross-flow liquid desiccant dehumidification system. International Journal of Refrigeration 32, 524–533. https://doi.org/10.1016/j.ijrefrig.2008.06.011

Murad, Y., 2020. Joint shear strength models for exterior RC beam-column connections exposed to biaxial and uniaxial cyclic loading. Journal of Building Engineering 30, 101225. https://doi.org/10.1016/j.jobe.2020.101225

Naik, B.K., Bhowmik, M., Muthukumar, P., 2019. Experimental investigation and numerical modelling on the performance assessments of evacuated U – Tube solar collector systems. Renewable Energy 134. https://doi.org/10.1016/j.renene.2018.09.066

Naik, B.K., Muthukumar, P., 2019. Experimental investigation and parametric studies on structured packing chamber based liquid desiccant dehumidification and regeneration systems. Building and Environment 149, 330–348. https://doi.org/10.1016/j.buildenv.2018.12.028

Naik, B.K., Muthukumar, P., Sunil Kumar, P., 2018. A novel finite difference model coupled with recursive algorithm for analyzing heat and mass transfer processes in a cross flow dehumidifier/regenerator. International Journal of Thermal Sciences 131, 1–13. https://doi.org/10.1016/j.ijthermalsci.2018.05.029

Navneet Walia, H., Singh, A.S., 2015. ANFIS : Adaptive Neuro-Fuzzy Inference System- A Survey. International Journal of Computer Applications 123, 32–38.

Negnevitsky, M., 2005. Artificial intelligence: a guide to intelligent systems. Pearson education.

Nie, X., Zhao, L., Deng, S., Lin, X., 2017. Experimental study on thermal performance of U-type evacuated glass tubular solar collector with low inlet temperature. Solar Energy 150, 192–201. https://doi.org/10.1016/j.solener.2017.04.030

Nkwetta, D.N., Smyth, M., Haghighat, F., Zacharopoulos, A., Hyde, T., 2013. Experimental performance evaluation and comparative analyses of heat pipe and direct flow augmented solar collectors. Applied Thermal Engineering 60, 225–233. https://doi.org/10.1016/j.applthermaleng.2013.06.059

Nottage, H.B., 1941. Merkel's cooling diagram as a performance correlation for air-water evaporative cooling systems. ASHVE Transactions 47, 429.

NSI/ASHRAE55, 1992. Thermal environmental conditions for human occupancy. American Society of Heating: Refrigerating and Air-conditioning Engineers, Atlanta, GA.

Öberg, V., 1998. Heat and mass transfer study of a packed bed absorber/regenerator for solar desiccant cooling. Diss. University of Florida.

Oberg, V., Goswami, D.Y., 2016. Experimental Study of the Heat and Mass Transfer in a Packed Bed Liquid Desiccant Air Dehumidifier. Journal of Solar Energy Engineering 289–297. https://doi.org/10.1115/1.2888133

Oberg, V., Goswami, D.Y., 1998. A review of liquid desiccant cooling. Advances in solar energy 12, 431–470.

Patil, D., Kumar, R., Xiao, F., 2016. Wetting enhancement of polypropylene plate for falling film tower application. Chemical Engineering and Processing: Process Intensification 108, 1–9. https://doi.org/10.1016/j.cep.2016.06.005

Patil, K.R., Tripathi, A.D., Pathak, G., Katti, S.S., 1990. Thermodynamic properties of aqueous electrolyte solutions. 1. Vapor pressure of aqueous solutions of lithium chloride, lithium bromide, and lithium iodide. Journal of Chemical & Engineering Data 35, 166–168. https://doi.org/10.1021/je00060a020

Paul, A., Bhowmik, S., Panua, R., Debroy, D., 2018. Artificial Neural Network-Based Prediction of Performances-Exhaust Emissions of Diesohol Piloted Dual Fuel Diesel Engine Under Varying Compressed Natural Gas Flowrates. Journal of Energy Resources Technology 140, 112201. https://doi.org/10.1115/1.4040380

Park J., D. Yoon, S. Lee, J. Jeong, 2016. Empirical model for predicting the dehumidification effectiveness of a liquid desiccant system, Energy Build. 126, 447–454. https://doi.org/10.1016/j.enbuild.2016.05.050.

Peng, C.S.P., Howell, J.R., 1981. Analysis and design of efficient absorbers for low-temperature desiccant air conditioners. Journal of Solar Energy Engineering, Transactions of the ASME 103, 67–74. https://doi.org/10.1115/1.3266213

Peng, D., Zhang, X., 2009. Modeling and performance analysis of solar air pretreatment collector/regenerator using liquid desiccant. Renewable Energy 34, 699–705. https://doi.org/10.1016/j.renene.2008.05.015

Peng, D., Zhou, J., Luo, D., 2017. Exergy analysis of a liquid desiccant evaporative cooling system Donggen. International Journal of Refrigeration 82, 495–508. https://doi.org/10.1016/j.ijrefrig.2017.06.021

Peng D., Luo D., 2017. Modeling and parametrical analysis on internally-heated liquid desiccant regenerator in liquid desiccant air conditioning, Energy. 141, 461–471. https://doi.org/10.1016/j.energy.2017.09.106.

Pérez-Lombard, L., Ortiz, J., Pout, C., 2008. A review on buildings energy consumption information. Energy and Buildings 40, 394–398. https://doi.org/10.1016/j.enbuild.2007.03.007

Pombeiro, H., Santos, R., Carreira, P., Silva, C., Sousa, J.M.C., 2017. Comparative assessment of low-complexity models to predict electricity consumption in an institutional building: Linear regression vs. fuzzy modeling vs. neural networks. Energy and Buildings 146, 141–151. https://doi.org/10.1016/j.enbuild.2017.04.032

Potnis, S.V. and Lenz, T.G., 1996. Dimensionless mass-transfer correlations for packed-bed liquid-desiccant contactors. Industrial & engineering chemistry research, 35(11), pp.4185-4193.

Price, Duncan M. "Vapor pressure determination by thermogravimetry." Thermochimica acta 367 (2001): 253-262.

Qi, R., Dong, C., Zhang, L.Z., 2020. A review of liquid desiccant air dehumidification: From system to material manipulations. Energy and Buildings 215, 109897. https://doi.org/10.1016/j.enbuild.2020.109897

Qi, R., Lu, L., Yang, H., Qin, F., 2013. Investigation on wetted area and film thickness for falling film liquid desiccant regeneration system. Applied Energy 112, 93–101. https://doi.org/10.1016/j.apenergy.2013.05.083

Qu, M., Abdelaziz, O., Sun, X.G., Yin, H., 2017. Aqueous solution of [EMIM][OAc]: Property formulations for use in air conditioning equipment design. Applied Thermal Engineering 124, 271–278. https://doi.org/10.1016/j.applthermaleng.2017.05.167

Radhwan, A.M., Gari, H.N., Elsayed, M.M., 1993. Parametric study of a packed bed dehumidifier/regenerator using CaCl2 liquid desiccant. Renewable Energy 3, 49–60. https://doi.org/10.1016/0960-1481(93)90130-9

Rafique, M.M., Gandhidasan, P., Bahaidarah, H.M.S., 2016. Liquid desiccant materials and dehumidifiers - A review. Renewable and Sustainable Energy Reviews 56, 179–195. https://doi.org/10.1016/j.rser.2015.11.061

Rafique, M., Gandhidasan, P., Rehman, S., Al-Hadhrami, L.M., 2015. A review on desiccant based evaporative cooling systems. Renewable and Sustainable Energy Reviews 45, 145–159. https://doi.org/10.1016/j.rser.2015.01.051

Ren, H., Ma, Z., Gschwander, S., 2019. Characterisation and evaluation of a new phase change enhanced working solution for liquid desiccant cooling systems. Applied Thermal Engineering 150, 1197–1205. https://doi.org/10.1016/j.applthermaleng.2019.01.096

Rivera, W., Cerezo, J., 2005. Experimental study of the use of additives in the performance of a single-stage heat transformer operating with water-lithium bromide. International Journal of Energy Research 29, 121–130. https://doi.org/10.1002/er.1045

Roy, S., Banerjee, R., Bose, P.K., 2014a. Performance and exhaust emissions prediction of a CRDI assisted single cylinder diesel engine coupled with EGR using artificial neural network. Applied Energy 119, 330–340. https://doi.org/10.1016/j.apenergy.2014.01.044

Roy, S., Banerjee, R., Das, A.K., Bose, P.K., 2014c. Development of an ANN based system identification tool to estimate the performance-emission characteristics of a CRDI assisted CNG dual fuel diesel engine. Journal of Natural Gas Science and Engineering 21, 147–158. https://doi.org/10.1016/j.jngse.2014.08.002

Roy, S., Ghosh, A., Kumar, A., Banerjee, R., 2015. Development and validation of a GEP model to predict the performance and exhaust emission parameters of a CRDI assisted single cylinder diesel engine coupled with EGR. Applied Energy 140, 52–64. https://doi.org/10.1016/j.apenergy.2014.11.065

Roy, S., Ghosh, A., Kumar, A., Banerjee, R., 2014d. A comparative study of GEP and an ANN strategy to model engine performance and emission characteristics of a CRDI assisted single cylinder diesel engine under CNG dual-fuel operation. Journal of Natural Gas Science and Engineering 21, 814–828. https://doi.org/10.1016/j.jngse.2014.10.024

Raucci MG, Alvarez-Perez MA, Demitri C, Giugliano D, De Benedictis V, Sannino A, et al., 2015. Effect of citric acid crosslinking cellulose-based hydrogels on osteogenic differentiation. Journal of Biomedical Materials Research - Part A;103:2045–56. doi:10.1002/jbm.a.35343.

Rajeev S, Michael S, Pandey A, Bhaskar T, 2015. Recent Advances in Thermochemical Conversion of Biomass. Imprint: Elsevier ISBN: 9780.

Saikia, S.S., Nath, S., Bhanja, D., 2019. Effect of vacuum deterioration on thermal performance of coaxial evacuated tube solar collector considering single and two phase flow modelling: A numerical study. Solar Energy 177, 127–143. https://doi.org/10.1016/j.solener.2018.10.089

Sarbu, I., Sebarchievici, C., 2013. Review of solar refrigeration and cooling systems. Energy and Buildings 67, 286–297. https://doi.org/10.1016/j.enbuild.2013.08.022

Schermelleh-Engel, K., Müller, H., 2003. Evaluating the fit of structural equation models: Tests of significance and descriptive goodness-of-fit measures. Methods of Psychological Research 8, 28–74.

Scalabrin, G. and Scaltriti, G., 1990. A liquid sorption-desorption system for air conditioning with heat at lower temperature. J. Sol. Energy Eng., 112(2): 70-75. https://doi.org/10.1115/1.2929649

Sängerlaub, Sven, Esra Kucukpinar, and Kajetan Müller. 2019. Desiccant Films Made of Low-Density Polyethylene with Dispersed Silica Gel—Water Vapor Absorption, Permeability (H2O, N2, O2, CO2), and Mechanical Properties. Materials 12.14, 2304.

Siegel RA. 1993. Hydrophobic weak polyelectrolyte gels: Studies of swelling equilibria and kinetics. Advances in Polymer Science;109:233–67. doi:10.1007/3-540-56791-7_6.

Sharafeldin, M.A., Gróf, G., 2019. Efficiency of evacuated tube solar collector using WO3/Water nanofluid. Renewable Energy 134, 453–460. https://doi.org/10.1016/j.renene.2018.11.010

Shi, Y., Larson, M., Hanjalic, A., 2010. List-wise learning to rank with matrix factorization for collaborative filtering 269. https://doi.org/10.1145/1864708.1864764

Shoaib, N., Aboosadi, Z.A., Esfandiari, N., 2020. Experimental Study of Dehumidification Process by CaCl2 Liquid Desiccant Containing CuO Nanoparticles. International Journal of Air-Conditioning and Refrigeration 28. https://doi.org/10.1142/S2010132520500091

Srivastava, N.C., Eames, I.W., 1998. A review of adsorbents and adsorbates in solid–vapour adsorption heat pump systems. Applied thermal engineering 18, 707–714.

Suzuki A, Tanaka T. 1990. Phase transition in polymer gels induced by visible light. Nature;346:345–7. doi:10.1038/346345a0

Stevens, D.I., Braun, J.E., Klein, S.A., 1989. An effectiveness model of liquid-desiccant system heat/mass exchangers. Solar Energy 42, 449–455. https://doi.org/10.1016/0038-092X(89)90045-5

Theil, H., 1966. Applied economic forecasting. Chicago: Rand McNally;

Timmerman, A., 2003. Neural networks in finance and investing. Using artificial intelligence to improve realworld performance. International Journal of Forecasting. https://doi.org/10.1016/s0169-2070(96)00728-5

Timothy A.Ameel, Kevin G.Gee, B.D.W., 1995. Performance predictions of alternative, low cost absorbents for open-cycle absorption solar cooling. Solar Energy 54, 65–73. https://doi.org/10.1016/0038-092X(94)00103-K

Treybal, R.E., 1980. Mass transfer operations. New York 466.

Ünal, O., Demir, F., Uygunoğlu, T., 2007. Fuzzy logic approach to predict stress-strain curves of steel fiber-reinforced concretes in compression. Building and Environment 42, 3589–3595. https://doi.org/10.1016/j.buildenv.2006.10.023

Wang, L., Li, N., Zhao, B., 2010. Exergy performance and thermodynamic properties of the ideal liquid desiccant dehumidification system. Energy and Buildings 42, 2437–2444. https://doi.org/10.1016/j.enbuild.2010.08.022

Wang, L., Xiao, F., Zhang, X., Kumar, R., 2016. An experimental study on the dehumidification performance of a counter flow liquid desiccant dehumidifier. International Journal of Refrigeration 70, 289–301. https://doi.org/10.1016/j.ijrefrig.2016.06.005

Wang, X., Cai, W., Lu, J., Sun, Y., Ding, X., 2013. A hybrid dehumidifier model for real-time performance monitoring, control and optimization in liquid desiccant dehumidification system. Applied Energy 111, 449–455. https://doi.org/10.1016/j.apenergy.2013.05.026

Wannagosit, C., Sakulchangsatjatai, P., Kammuang-Lue, N., Terdtoon, P., 2018. Validated mathematical models of a solar water heater system with thermosyphon evacuated tube collectors. Case Studies in Thermal Engineering 12, 528–536. https://doi.org/10.1016/j.csite.2018.07.005

Wang, Z.W. Lian, W.W.L., 2011. Analysis of liquid-desiccant dehumidifying system combined with ultrasound atomization technology. J Central South Univ (Science and Technology) 42, 240–246.

Wach RA, Mitomo H, Nagasawa N, Yoshii F. 2003. Radiation crosslinking of carboxymethylcellulose of various degree of substitution at high concentration in aqueous solutions of natural pH. Radiation Physics and Chemistry;68:771–9. doi:10.1016/S0969-806X(03)00403-1.

Wedding, D.K., 2002. Fuzzy sets and fuzzy logic: Theory and applications, Neurocomputing. Prentice Hall P T R Upper Saddle River, New Jersey 07458. https://doi.org/10.1016/s0925-2312(97)88327-0

Wen, T., Lu, L., Dong, C., 2018a. Enhancing the dehumidification performance of LiCl solution with surfactant PVP-K30. Energy and Buildings 171, 183–195. https://doi.org/10.1016/j.enbuild.2018.04.031

Wen, T., Lu, L., Zhong, H., 2018b. Investigation on the dehumidification performance of LiCl/H2O-MWNTs nanofluid in a falling film dehumidifier. Building and Environment 139, 8–16. https://doi.org/10.1016/j.buildenv.2018.05.010

Wen, T., Lu, L., Nie, Y., Zhong, H., 2019. Development and investigation on the dehumidification and corrosion resistance performance of a new mixed liquid desiccant. International Journal of Heat and Mass Transfer 130, 72–82. https://doi.org/10.1016/j.ijheatmasstransfer.2018.10.066

Wen T., Luo Y., Sheng L., 2020. Experimental study on the corrosion behavior and regeneration performance of KCOOH aqueous solution Sol. Energy, 201, pp. 638-648, 10.1016/j.solener.2020.03.044

Wei Xiu-, L., Xiao-Song, Z., Geng, W., Rong-Quan, C., 2008. Research on ratio selection of a mixed liquid desiccant: Mixed LiCl- CaCl2 solution. Solar Energy 82, 1161–1171. https://doi.org/10.1016/j.solener.2008.05.015

Wei Li Xiu, Zhang, X.-S., Wang, F., 2013. A kinetic mass transfer model of liquid dehumidification for liquid desiccant cooling system. Energy and Buildings 61, 93–99. https://doi.org/10.1016/j.enbuild.2013.01.039

Weng L, Zhang L, Ruan D, Shi L, Xu J. 2004. Thermal Gelation of Cellulose in a NaOH/Thiourea Aqueous Solution. Langmuir;20:2086–93. doi:10.1021/la035995o.

Wong, K.I., Wong, P.K., Cheung, C.S., Vong, C.M., 2013. Modeling and optimization of biodiesel engine performance using advanced machine learning methods. Energy 55, 519–528. https://doi.org/10.1016/j.energy.2013.03.057

Wu, Q., Cai, W.J., Shen, S., Wang, X., Ren, H., 2017. A regulation strategy of working concentration in the dehumidifier of liquid desiccant air conditioner. Applied Energy 202, 648–661. https://doi.org/10.1016/j.apenergy.2017.05.128

Xiong Z.Q., Dai Y.J., Wang R.Z., 2009, Investigation on a two-stage solar liquid-desiccant (LiBr) dehumidification system assisted by CaCl2 solution Appl. Therm. Eng., 29, pp. 1209-1215, 10.1016/j.applthermaleng.2008.06.020

Yadigraoglu, G., Pastor, E.J., 1974. Investigation of the accuracy of the Merkel equation for evaporative cooling tower calculations.

Yang, Z., Lian, Z., Tao, R., Ni, H., Zhong, K., 2019. Experimental study on the performance of the internally-heated ultrasonic atomization liquid desiccant regeneration system.

Applied Thermal Engineering 163, 114211. https://doi.org/10.1016/j.applthermaleng.2019.114211

Yang, Z., Lin, B., Zhang, K., Lian, Z., 2015. Experimental study on mass transfer performances of the ultrasonic atomization liquid desiccant dehumidification system. Energy and Buildings 93, 126–136. https://doi.org/10.1016/j.enbuild.2015.02.035

Yao, W., Setterwall, F., Bjuretröm, H., 1991. Surface Tension of Lithium Bromide Solutions with Heat-Transfer Additives. Journal of Chemical and Engineering Data 36, 96–98. https://doi.org/10.1021/je00001a029

Yassin, M.A., Alazba, A.A., Mattar, M.A., 2016. Artificial neural networks versus gene expression programming for estimating reference evapotranspiration in arid climate. Agricultural Water Management 163, 110–124. https://doi.org/10.1016/j.agwat.2015.09.009

Yao, Y.S.L., 2014. Ultrasonic Technology for Desiccant Regeneration, John Wiley & Sons,. John Wiley & Sons,. https://doi.org/10.1002/9781118921616

Yoshida R, Uchida K, Kaneko Y, Sakai K, Kikuchi A, Sakurai Y, et al., 1995. Comb-type grafted hydrogels with rapid deswelling response to temperature changes. Nature;374:240–2. doi:10.1038/374240a0.

Yoshihito Osada; Hidenori Okuzaki; Hirofumi Hori. 1992. A ploymer gel with electrically driven motility. Nature;359:242–4.

Yin, Y., Zhang, X., Chen, Z., 2007. Experimental study on dehumidifier and regenerator of liquid desiccant cooling air conditioning system. Building and Environment 42, 2505–2511. https://doi.org/10.1016/j.buildenv.2006.07.009

Yin, Y., Zhang, X., 2010. Comparative study on internally heated and adiabatic regenerators in liquid desiccant air conditioning system. Building and Environment 45, 1799–1807. https://doi.org/10.1016/j.buildenv.2010.02.008

Yin, Y., Zhang, X., Peng, D., Li, X., 2009. Model validation and case study on internally cooled/heated dehumidifier/regenerator of liquid desiccant systems. International Journal of Thermal Sciences 48, 1664–1671. https://doi.org/10.1016/j.ijthermalsci.2008.12.017

Zalewski, W., Gryglaszewski, P.A., 1997. Mathematical model of heat and mass transfer processes in evaporative fluid coolers. Chemical Engineering and Processing: Process Intensification 36, 271–280. https://doi.org/10.1016/S0255-2701(97)00006-8

Zambolin, E., Del Col, D., 2010. Experimental analysis of thermal performance of flat plate and evacuated tube solar collectors in stationary standard and daily conditions. Solar Energy 84, 1382–1396. https://doi.org/10.1016/j.solener.2010.04.020

Zendehboudi, A., Song, P., Li, X., 2019. Performance investigation of the cross-flow closed-type heat-source tower using experiments and an adaptive neuro-fuzzy inference system model. Energy and Buildings 183, 340–355. https://doi.org/10.1016/j.enbuild.2018.11.003

Zendehboudi, A., Tatar, A., Li, X., 2017. A comparative study and prediction of the liquid desiccant dehumidifiers using intelligent models. Renewable Energy 114, 1023–1035. https://doi.org/10.1016/j.renene.2017.07.078

Zhan, C., Yin, Y., Guo, X., Jin, X., Zhang, X., 2018. Investigation on drying performance and alternative analysis of different liquid desiccants in compressed air drying system. Energy 165, 1–9. https://doi.org/10.1016/j.energy.2018.09.164

Zhang, L., Dang, C., Hihara, E., 2010. Performance analysis of a no-frost hybrid air conditioning system with integrated liquid desiccant dehumidification. International Journal of Refrigeration 33, 116–124. https://doi.org/10.1016/j.ijrefrig.2009.08.007

Zhang, L., Liu, X., Jiang, J., Jiang, Y., 2014. Exergy calculation and analysis of a dehumidification system using liquid desiccant. Energy and Buildings 69, 318–328. https://doi.org/10.1016/j.enbuild.2013.11.025

Zhang, L., Zha, X., Song, X., Zhang, X., 2019. Optimization analysis of a hybrid fresh air handling system based on evaporative cooling and condensation dehumidification. Energy Conversion and Management 180, 83–93. https://doi.org/10.1016/j.enconman.2018.10.100

Zhang, Q., Wu, J., Zhang, G., Zhou, J., Guo, Y., Shen, W., 2012. Calculations on performance characteristics of counterflow Reversibly Used Cooling Towers. International Journal of Refrigeration 35, 424–433. https://doi.org/10.1016/j.ijrefrig.2011.10.016

Zhang, X., You, S., Xu, W., Wang, M., He, T., Zheng, X., 2014. Experimental investigation of the higher coefficient of thermal performance for water-in-glass evacuated tube solar water heaters in China. Energy Conversion and Management 78, 386–392. https://doi.org/10.1016/j.enconman.2013.10.070

Zhao, X., Li, X., Zhang, X., 2016. Selection of optimal mixed liquid desiccants and performance analysis of the liquid desiccant cooling system. Applied Thermal Engineering 94, 622–634. https://doi.org/10.1016/j.applthermaleng.2015.09.037

Zurigat, Y H, Abu-Arabi, M.K., Abdul-Wahab, S.A., 2004. Air dehumidification by triethylene glycol desiccant in a packed column. Energy Conversion and Management 45, 141–155. https://doi.org/10.1016/S0196-8904(03)00109-2

Appendix A

Performance evaluation of developed models

Armstrong and Fildes (1995) suggested that there is no single statistical parameter would measure the model accurately in the sense of capturing necessary complexity of experimental data. Hence, it is necessary to consider multiple criteria to evaluate the model fitness based on various measures simultaneously. Therefore, in the current study, several statistical parameters are calculated based on the experimental and meta-model results for evaluating the performance of developed meta-models Zendehboudi et al. (2019) and Atalay et al. (2019). Certain statistical parameters for performance of regression models are calculated based on regression coefficient (Pearson product-moment correlation coefficient, R), coefficient of determination (absolute fraction of variance, R^2) and some typical statistical errors such as MSE (Mean Square Error) and MAPE (Mean Absolute Percentage Error), wherein the expected values of these parameters are in the range of $R > 0.98$, $R^2 > 0.9999$, $MSE < 0.001$ and $MAPE < 5\%$, and respectively (Bhowmik et al., 2017; Timmerman, 2003). Further, a special category of statistical analysis, such as Mean Square Relative Error (MSRE), Kling–Gupta Efficiency (KGE) and Nash–Sutcliffe coefficient of Efficiency (NSE) are also considered to ascertain how closely the regression model predicted values fit to the actual experimental data (Eqs. A1 -A13). In order to analyze the uncertainty of AI models, a majority of researchers used Theil uncertainty analysis (usually called Theil U2) (Bliemel, 1973; Theil, 1966). Theil U2 can be expressed as a function of average error and variance of the residual between the observed data and the predicted data (Eq. A14). This model uncertainty test is confirming and evaluating the prediction quality, wherein the values should lie between 0 to 1, where 0 represents no forecasting error and 1 a naïve (no change) forecast. Hence, a lower value of Theil U2 indicates a better forecasting capability.

$$R = \sqrt{1 - \left(\frac{\sum_{i=1}^{z} \left(\lambda_{e,i} - \lambda_{p,i} \right)^2}{\sum_{i=1}^{z} \lambda_{e,i}^{\ 2}} \right)} \qquad \text{(A1)}$$

$$R^2 = 1 - \left(\frac{\sum_{i=1}^{z} \left(\lambda_{e,i} - \lambda_{p,i} \right)^2}{\sum_{i=1}^{z} \lambda_{e,i}^2} \right) \tag{A2}$$

$$NSE = \left[1 - \left\{ \frac{\sum_{i=1}^{z} \left(\lambda_{e,i} - \lambda_{p,i} \right)^2}{\sum_{i=1}^{z} \left(\lambda_{e,i} - \bar{\lambda}_{e,i} \right)^2} \right\} \right] \tag{A3}$$

$$KGE = 1 - \sqrt{(R-1)^2 + \left(\frac{SD_{\lambda e}}{SD_{\lambda p}} - 1 \right)^2 + \left(\frac{\bar{\lambda}_e}{\bar{\lambda}_p} - 1 \right)^2} \tag{A4}$$

$$d = 1 - \frac{\sum_{i=1}^{z} \left(\lambda_{ei} - \lambda_{pi} \right)^2}{\sum_{i=1}^{z} \left(\left| \lambda_{pi} - \bar{\lambda}_{ei} \right| + \left| \lambda_{ei} - \bar{\lambda}_{ei} \right| \right)^2} \tag{A5}$$

$$MAPE = \left[\frac{1}{z} \times \sum_{i=1}^{z} \left| \frac{\left(\lambda_{e,i} - \lambda_{p,i} \right)}{\lambda_{e,i}} \right| \right] \times 100\% \tag{A6}$$

$$sMAPE = \left[\frac{1}{z} \times \sum_{i=1}^{z} \left| \frac{2 \left| \lambda_{e,i} - \lambda_{p,i} \right|}{\left| \lambda_{e,i} \right| + \left| \lambda_{p,i} \right|} \right| \right] \times 100\% \tag{A7}$$

$$MAE = \frac{\left[\sum_{i=1}^{z} \left(\lambda_{e,i} - \lambda_{p,i} \right) \right]}{z} \tag{A8}$$

$$MSE = \frac{\left[\sum_{i=1}^{z} \left(\lambda_{e,i} - \lambda_{p,i} \right)^2 \right]}{z} \tag{A9}$$

$$\text{nMSE} = \left[\frac{1}{z} \times \sum_{i=1}^{z} \left| \frac{\left(\lambda_{e,i} - \lambda_{p,i}\right)^2}{\left(\bar{\lambda}_e\right) + \left(\bar{\lambda}_p\right)} \right| \right] \tag{C10}$$

$$\text{RMSE} = \sqrt{\frac{1}{z}\left(\sum_{i=1}^{z} \left(\lambda_{e,i} - \lambda_{p,i}\right)^2 \right)} \tag{A11}$$

$$\text{nRMSE} = \frac{\sqrt{\frac{1}{z}\sum_{z=1}^{n} \left(\lambda_{e,i} - \lambda_{p,i}\right)^2}}{\left(\lambda_{e,\bar{m}ax} - \lambda_{p,max}\right)} \tag{A12}$$

$$\text{MSRE} = \left| \frac{1}{z} \times \left[\sum_{i=1}^{z} \left\{ \frac{\left(\lambda_{e,i} - \lambda_{p,i}\right)^2}{\lambda_{e,i}} \right\} \right] \right| \tag{A13}$$

$$\text{Theil U2} = \left[\frac{\sqrt{\sum_{i=1}^{z} \left(\lambda_{e,i} - \lambda_{p,i}\right)}}{\sqrt{\sum_{i=1}^{z} \left(\lambda_{e,i}\right)^2}} \right] \tag{A14}$$

Where ‘z’ represents the number of run in the data set, ‘λ_e’ represents the experimental output and ‘λ_p’ is the model output value. $SD_{\lambda e}$ is standard deviation of experimental values, and $SD_{\lambda p}$ is standard deviation of model output values and $\bar{\lambda}_e$ is the average of experimental values and $\bar{\lambda}_p$ is the average of predicted results.

Appendix B

Derivation of exergy destruction equations

$$P_a V_a = m_a R_a T_a \quad \text{(B1)}$$

$$P_v V_v = m_v R_v T_v \quad \text{(B2)}$$

As, $V_a = V_v$ and $T_a = T_v$

From the definition of air specific humidity, it can be written as

$$\omega = \frac{m_v}{m_a} \quad \text{(B3)}$$

Using (B1), (B2) in (B3), then Eq. (B3) becomes

$$\omega = \frac{m_v}{m_a} = \frac{R_a P_v}{R_v P_a}$$
$$= \frac{0.287 P_v}{0.461 P_a} \quad \text{(since, } R_a = 0.287 \text{ kJ/kg-K; } R_v = 0.461 \text{ kJ/kg-K)}$$
$$= 0.622 \frac{P_v}{P - P_v} \quad \text{(B4)}$$

Rearranging Eq.(B4)

$$\frac{P_v}{P - P_v} = 1.608\omega \quad \text{(B5)}$$

$$P_v = 1.608 P \frac{\omega}{1 + 1.608\omega} \quad \text{(B6)}$$

Therefore, the vapour pressure of the solution and air becomes

$$P_{v,s}(\xi_s, T_s) = 1.608 P \frac{\omega_e(\xi_s, T_s)}{1 + 1.608\omega_e(\xi_s, T_s)} \quad \text{(B7)}$$

$$P_{v,a}(\xi_a, T_a) = 1.608 P \frac{\omega_a(\xi_a, T_a)}{1 + 1.608\omega_a(\xi_a, T_a)} \quad \text{(B8)}$$

It is also well known that the chemical exergy of air corresponds to the solution, i.e., the amount of moisture transferred from the air to the solution is mainly due to the vapour pressure

difference between them and similarly, chemical exergy destruction happens due to the vapour pressure destruction in the dehumidification chamber. With this concept, the chemical energy destruction (dE_{chem}) in the entire control volume can be written using Eq.(B1), (B5) and (B6), as

$$dE_{chem} = 1.608 m_a R_a T \left(\ln\left(\frac{\omega_e}{1+1.608\omega_e} \right) - \ln\left(\frac{\omega_a}{1+1.608\omega_a} \right) \right) d\omega \quad \text{(B9)}$$

where dω is the mass (humidity) transfer rate between humid air and liquid desiccant in the liquid desiccant dehumidifier.

Now, using Eq.(B6) and (B7) in Eq.(B8), dE becomes

$$dE = 1.608 m_a R_a T \ln\left(\frac{P_{v,s}}{P_{v,a}} \right) d\omega \quad \text{(B10)}$$

The clapeyron equation is

$$\ln P_s = -\frac{h_v}{R_w}\frac{1}{T} + C \quad \text{(B11)}$$

Then, the clapeyron equation for the solution and air becomes

$$\ln P_{v,s} = -\frac{h_v}{R_v}\frac{1}{T_s} + C \quad \text{(B12)}$$

$$\ln P_{v,a} = -\frac{h_v}{R_a}\frac{1}{T_a} + C \quad \text{(B13)}$$

Finally, Eq. (B11) and (B12) can be written as

$$\ln\left(\frac{P_{v,s}}{P_{v,a}} \right) = \frac{h_v}{R_v}\left(\frac{1}{T_a} - \frac{1}{T_s} \right) \quad \text{(B14)}$$

The physical exergy destruction (dE_{phy}) can be derived using Eq.(B9), Eq.(B10) and Eq.(B14), as

$$dE_{phy} = 1.608 m_a T \left(\frac{1}{T_a} - \frac{1}{T_s} \right) dQ \quad \text{(B15)}$$

where dQ is the heat transfer rate between the humid air and the liquid desiccant in the liquid desiccant dehumidifier.

Appendix C

Details of artificial intelligent models

C1. Details about ANN

MLP consists of minimum three layers of nodes, such as an input layer, one or more hidden layers and a set of output layers. Every layer is associated with multiple nodes known as neurons. Neurons are connected directly to the neighbouring layer by weights. The associated weight for each input gradually becomes weaker or stronger. The input and output variables determine the neuron numbers in the input and output layers. In each network, the input data or information are conveyed to the neurons of the hidden layer(s) where transfer functions pattern the behaviour of the information and allocate it to the neurons of the output layer by means of the connecting weights (Negnevitsky, 2005b). The adjustment of weight value for the link between p^{th} neuron in the layer M and q^{th} neuron in the layer (M+1) is written as Eq. (C1).

$$\Delta w_{pq} = \beta \delta_q o_p \tag{C1}$$

where β represents the learning rate, δ_q is the residual error between the q^{th} neuron in layer (M+1) to the p^{th} neuron in layer M, that is elaborated in Eqs. (C2-C3), and o_p is the output value of index p in the Mth layer.

$$\delta_q = o_q\left(d_q - o_q\right)\left(1 - o_q\right)\text{; d= target value of output layer for that neuron.} \tag{C2}$$

$$\delta_q = T_q\left(1 - T_q\right)\sum_k \delta_k w_{kq}\text{ ; T= target value of hidden layer for that neuron.} \tag{C3}$$

Eq. (C2) is used to calculate the residual error of the output layer's neuron while Eq. (C3) is for the hidden layer's neuron, which greatly depends on the change in the weight of the k^{th} neuron in the (M+2) layer that is next to the layer (M+1). The fixing of β is a key factor in the network, as small β values refer to a slow rate of convergence, while too large β generate oscillations. As the literature suggests (Agrawal et al., 2019; Mohandes et al., 1998), the β value can be fixed by introducing a momentum factor in the weight Eq. (C1). Finally, Eq. (C1) becomes Eq. (C4).

$$\Delta w_{qp}(n+1) = \beta \delta_q o_p + \xi \Delta w_{qp}(n) \quad ;\ n = \text{ iteration number} \tag{C4}$$

where ξ is a constant factor (positive) which determines the result of past weight changes on the current direction of movement in weight space.

By supposing 'n' inputs that applied to the network, the net input function 'A' is created by multiplying the values of weights and inputs. Consequently, the output "Y" is determined by translating the generated net function to a transfer function, which can be calculated by Eq. (C5).

By supposing 'n' inputs that applied to the network, the net input function 'A' is created by multiplying the values of weights and inputs. Consequently, the output "Y" is determined by translating the generated net function to a transfer function, which can be calculated by Eq. (C5).

$$Y = F(A) = F\left[\sum_{i=1}^{n} X_i w_i + b\right] \qquad \text{(C5)}$$

where *X*, *w* and b represent the input, weight and bias, respectively.

Moreover, the output of the perceptron model is governed by the activation (transfer) function. The transfer functions can be either linear or non-linear. Three basic activation functions, such as purelin, logsig, and tansig are available in MATLAB® 2015b and these are expressed in Fig. (C1) with corresponding function equation.

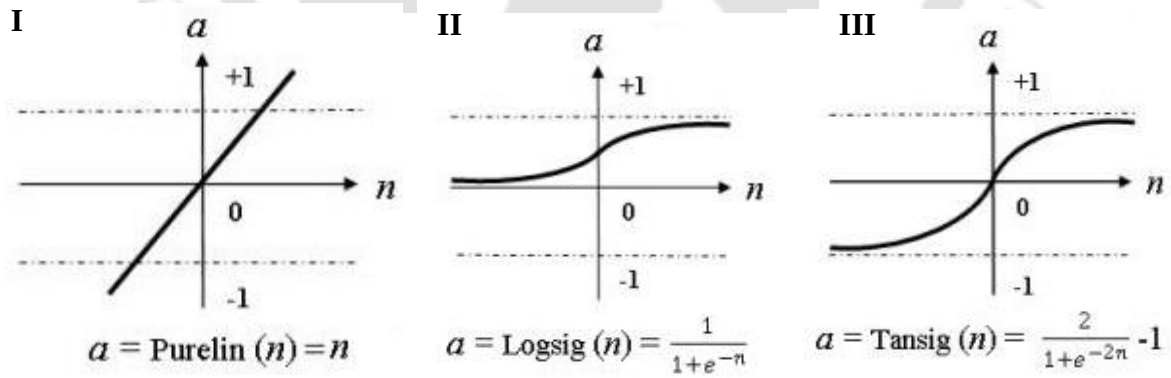

Fig. C1: Different activation function for ANN (I: Purelin, II: Logsig, III: Tansig)

C2. ANFIS model

By considering m inputs ($x_1,\ldots,x_m$), each with n Membership Functions (MFs), a fuzzy rule base of R rules, and one output y. The network, consisting of five layers, is used for training Sugeno-type FIS through learning and adaptation (Walia and Singh, 2015). The number of nodes N in 'layer 1' is the product of the number of inputs m and MFs n for each input, i.e., N = m×n. The number of nodes in 'layers 2–4' is equal to the number of rules R in the fuzzy rule base (Buragohain and Mahanta, 2008).

Layer 1 (fuzzification layer): The key purpose of this step is to transform the crisp inputs x_i to linguistic labels (A_{ij}, such as small, medium, large, etc.) with a degree of membership. The output of node ij is expressed as follows,

$$O_{1,ij} = \mu_{ij}(x_i) \quad \text{for } i = 1, m, \; j=1,n \tag{C6}$$

where μ_{ij} represents the jth membership function for the input x_i. Several types of MFs are used, for example, triangular, trapezoidal, and generalized bell function. The parameters of these MFs are termed premise parameters (Buragohain and Mahanta, 2008).

Layer 2 (product layer): For each node k in this layer, the output represents weighting factor (firing strength) of the rule k. The output w_k is the product of all its inputs as follows,

$$O_{2,i} = \Pi\mu_{ik}(x_i) \qquad \text{for } i =1, m, k=1,R \tag{C7}$$

Layer 3 (normalized layer): The output of each node k in this layer represents the normalized weighting factor w_k of the kth rule as follows,

$$O_{3,k} = \frac{w_k}{\sum_k w_k} \quad \text{for } k = 1, R \tag{C8}$$

Layer 4 (de-fuzzification layer): Each node of this layer gives a weighted output of the first order Sugeno-type fuzzy if-then rule as follows,

$$O_{4,k} = \bar{w}_k f_k ; f_k = \sum_j P_{ki} x_i + r_k \qquad \text{for } i = 1, m; \; k=1,R \tag{C9}$$

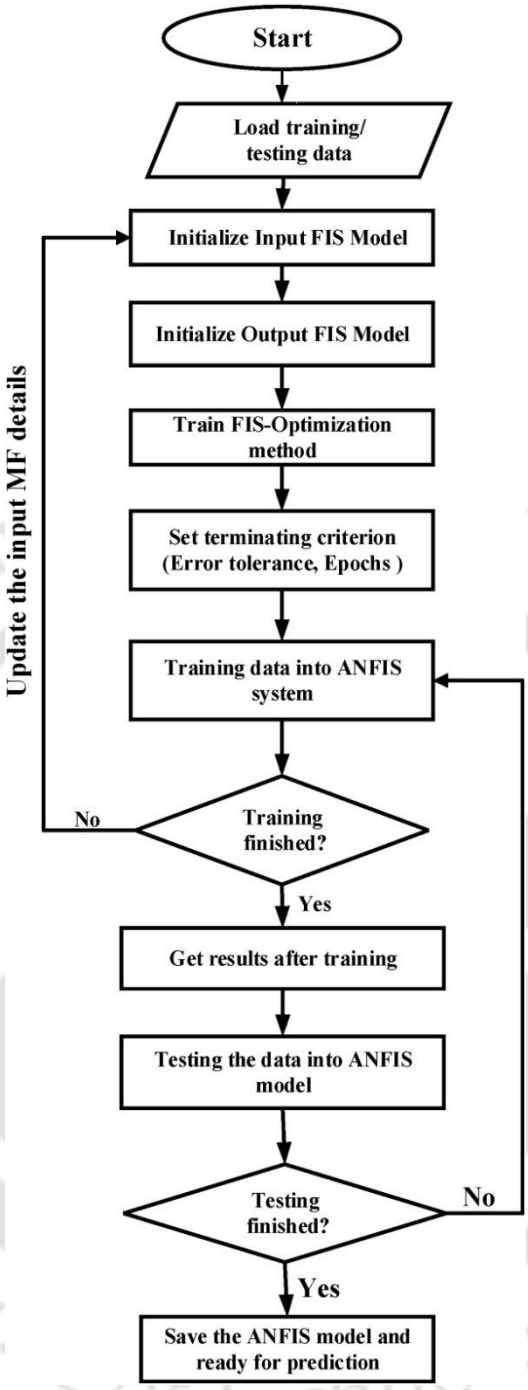

Fig. C2: Flow chart of ANFIS for modeling the desiccant system (MF: membership function; FIS: fuzzy inference system)

where f_k represents the output of the kth rule and parameters p_{ki} and r_k are called consequent parameters.

Layer 5 (output layer): This single–node layer represents the overall output y of the network as the sum of all weighted outputs of the rules,

$$O_{5,k} = \sum_{k} \bar{w}_k f_k \qquad \text{for } k = 1, R \tag{C10}$$

ANFIS requires a training datasets of desired input/output pair (x_1,x_2,…,x_m,y) depicting the target system to be modelled. ANFIS adaptively maps the inputs (x_1,x_2,…,x_m) to the output y through MFs, the rule base, and the related parameters emulating the given training datasets.

C3. GEP Model

GEP comprises of meta-models to express the relation between input and output parameters. In comparison to GP system, GEP programs are much faster (around 100-60,000 times) (Ferreira, 2001; Roy et al., 2015; Ferreira, 2006). In GP, the individuals are expressed as binary strings with a fixed length, which is known as chromosomes. Similarly, in GEP, chromosomes include a series of linear symbolic fixed-length strings which are composed of genes. GEP algorithm comprises of five key components such as terminal set, function set, fitness function, operator(s), and stopping condition. The tree-based structures with different sizes and shapes are commonly referred as an Expression Tree (ET) and every gene composed of the tail part followed by a head. The tail part consists of symbols which represent only terminals (i.e. input variables and constant values), but head part composed of both functions (e.g. +, -, sin, cos, sqrt, etc.) as well as terminals. The tail length can be represented as a function of head size and the no. of arguments within the function, as shown in Eq. (C11) (Roy et al., 2014d).

$$\text{Tail length} = \text{Head length} \times (\text{Number of arguments within the function} - 1) + 1 \tag{C11}$$

The expression of gene in the form sub-ET is relatively simple and straightforward. In GEP, growth can be monitored by simple mathematical operators (e.g., +, −, ×, and ÷) and non-linear functions (e.g., sin, cos, tan, arctan, sqrt etc.) depending on nature of the problem. The flow chart of GEP meta model for modeling the desiccant system is presented in Fig. C3. It is important to note, however, that every gene includes non-linear terms such as Cosine (Cos) or natural logarithm (ln).

Gene expression programming (GEP) is used to develop a relationship between the system independent parameters with its response parameters. The present study deals with the coupled heat and mass transfer phenomena; therefore, all six independent parameters are considered for development of meta-models. Initially, the structural parameters of GEP, i.e., number of genes, head sizes and chromosome numbers, are chosen randomly. The following steps are

summarised and are used to develop the GEP meta-model (Milukow et al., 2019; Ayata et al., 2017; Murad, 2020):

Step 1: Target (response parameters) and model parameters (independent parameters) are selected and the meta-model is developed based on target and model parameters.

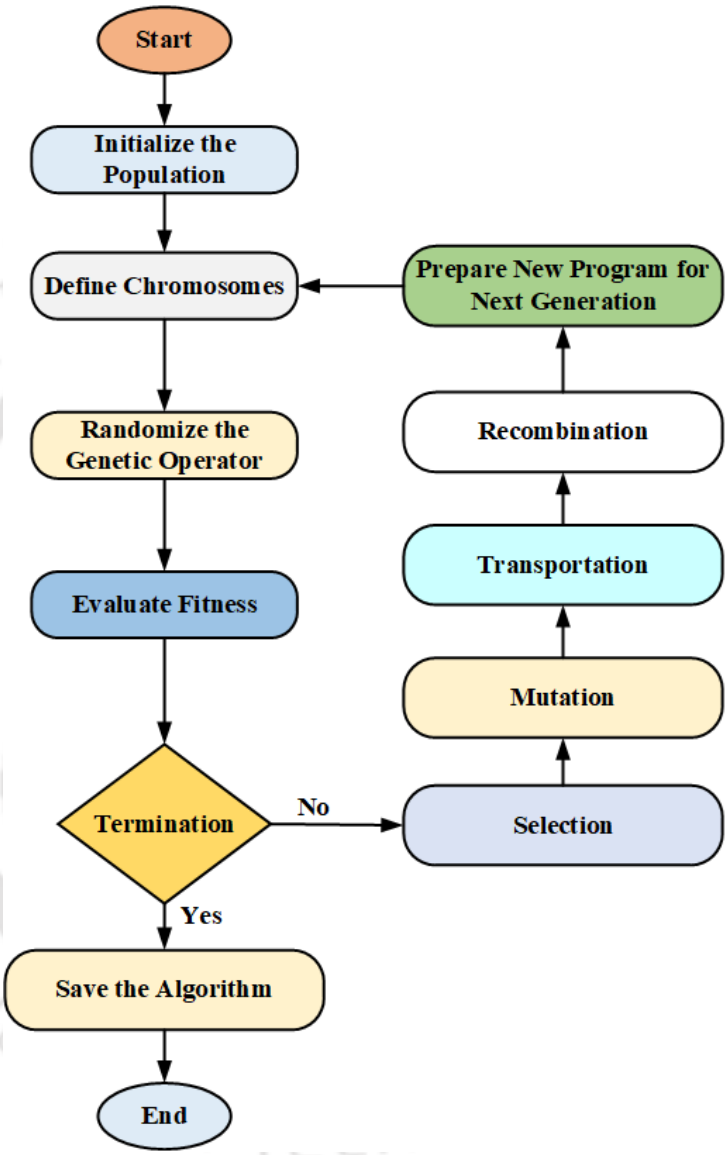

Fig. C3: Flow chart of GEP meta model for modeling the desiccant system

Step 2: Depending on the population size, chromosome numbers, genes and head sizes are chosen randomly.

Step 3: The chromosomes for defined populations are represented as mathematical equations and expression trees (ETs).

Step 4: Fitness function is defined to evaluate the fitness of each chromosome. In the present study, root means square error (RMSE) is chosen as the prevalent fitness function, and the fitness of each chromosome is calculated by Eq. (C12) (Milukow et al., 2019).

$$f_i = \frac{1000}{1+\mathrm{RMSE}} \tag{C12}$$

Fitness (f_i) ranges from 0 to 1000, where 1000 specifies a perfect fit (Milukow et al., 2019). RMSE of zero defines a perfect fit (Milukow et al., 2019).

Step 5: Rate the genetic operators such as inversion, transposition, mutation and recombination for defined chromosomes to reach minimum RMSE value.

Step 6: Again, new generation is formed based on the updated genetic operator values, and this process is repeated in order to reach the desired level of accuracy.

Further, in order to develop GEP meta-models, linking functions (addition (+), subtraction (-), multiplication (*) and division (/)) are needed to be defined to express the linkage between the sub-ETs of a same gene. In the present study, addition (+) and multiplication (*) are chosen as linking functions to link sub-ETs due to higher accuracy compared to other linking functions for this particular problem.

C4. Fuzzy model

In the present study, the fuzzy model comprises of three different input parameters (CR, Ɛm, LHR) and one output (MPCI) parameter, as shown in Fig. 6.5. The linguistic fuzzy input variables are having three linguistic values or memberships namely small (S), medium (M) and high (H). Seven types of linguistic values or memberships namely very very small (VVS), very small (VS), small (S), medium (M), large (L), very large (VL) and very very large (VVL) are used for output variables. The different linguistic values and their fuzzy intervals are shown in Table C1. The membership plots for input and output variables with triangular membership function are depicted in Fig. C5. As a consequence, three input variables and their three membership values are formed using 3^3=27 fuzzy rules (Ünal et al., 2007). These rules are shown in Table C1 and graphically in Fig. C6.

Table C1: Fuzzy rule matrix

Rule No.	CR	ε_{lat}	LHR	Output
IF	**AND**	**AND**	**THEN**	
R1	S	S	S	VVS
R2	S	S	M	VS
R3	S	S	L	S
R4	S	M	S	VS
R5	S	M	M	S
R6	S	M	L	M
R7	S	L	S	S
R8	S	L	M	M
R9	S	L	L	L
R10	M	S	S	VS
R11	M	S	M	S
R12	M	S	L	M
R13	M	M	S	S
R14	M	M	M	M
R15	M	M	L	L
R16	M	L	S	M
R17	M	L	M	L
R18	M	L	L	VL
R19	L	S	S	S
R20	L	S	M	M
R21	L	S	L	L
R22	L	M	S	M
R23	L	M	M	L
R24	L	M	L	VL
R25	L	L	S	L
R26	L	L	M	VL
R27	L	L	L	VVL

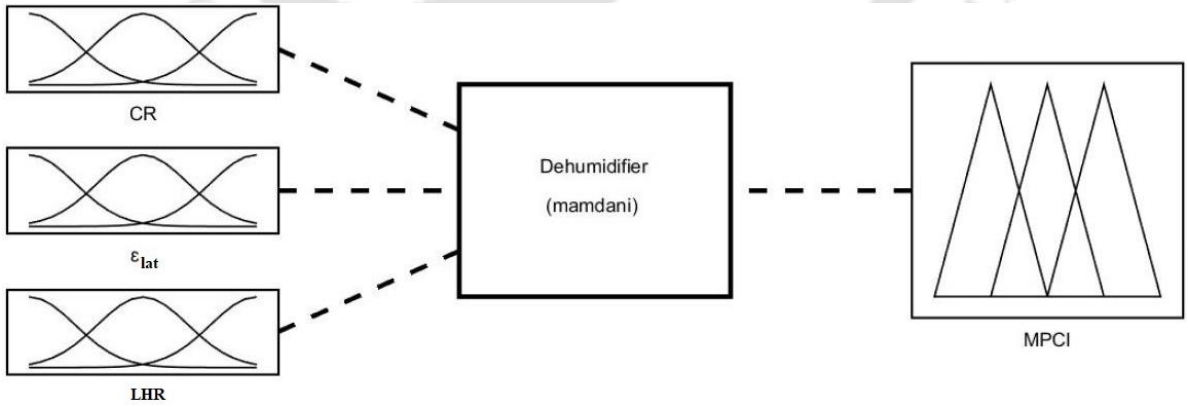

Fig. C4: Membership function plots for MPCI

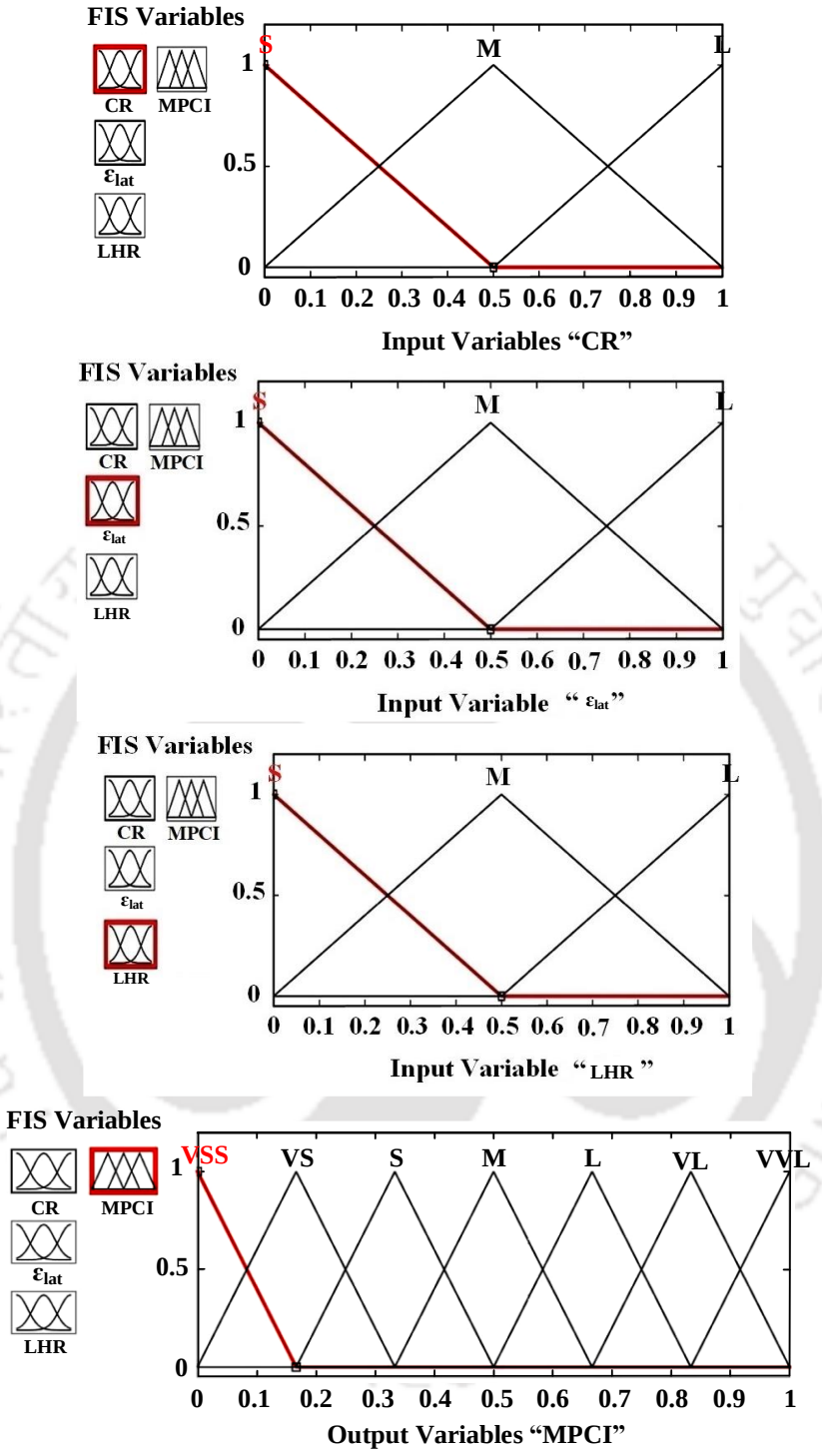

Fig. C5: Schematic diagram of fuzzy membership functions for three input (CR, ε_{lat}, LHR) and one output variables (MPCI)

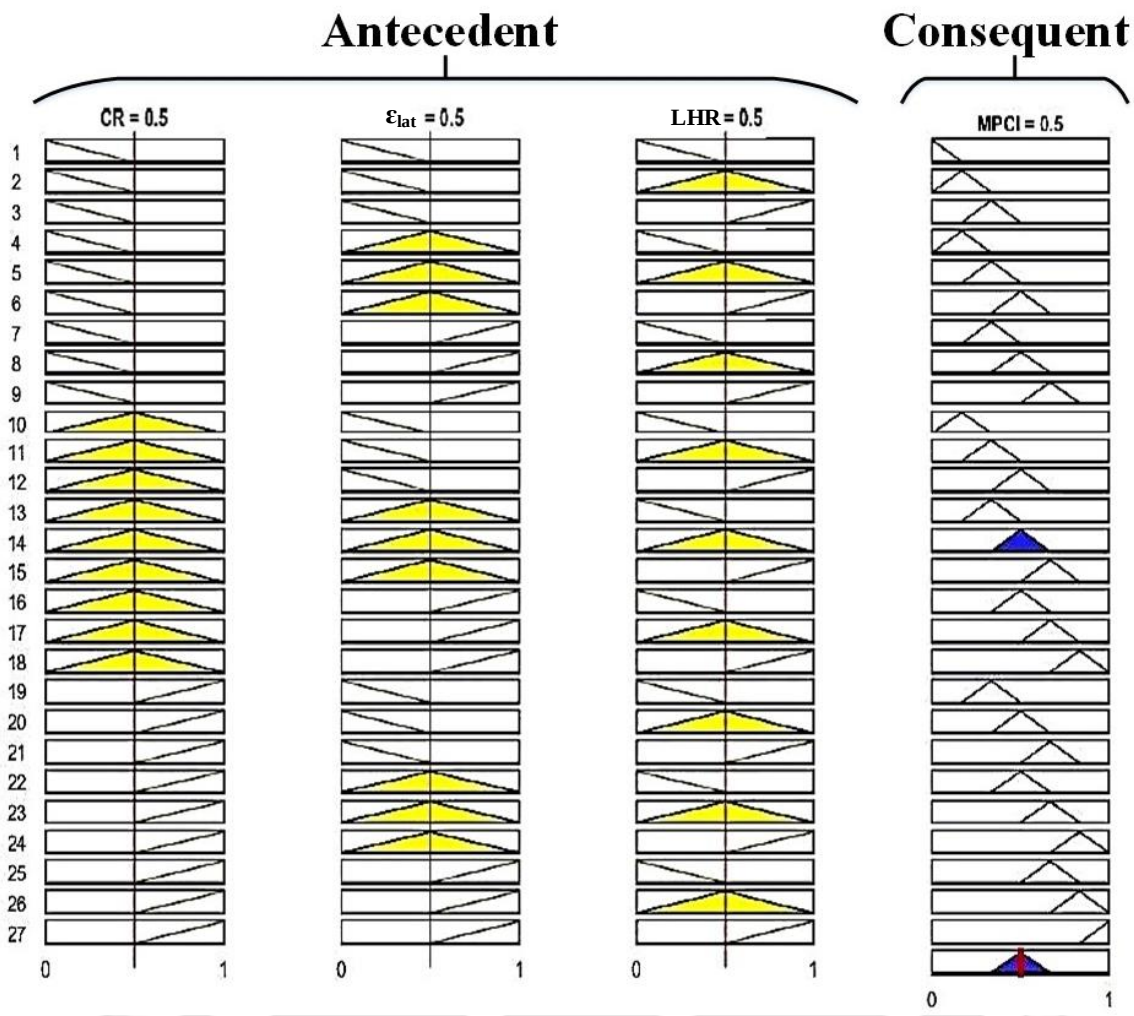

Fig. C6: Fuzzy rule for membership functions to get MPCI

C5. GEP Models Results

The final mathematical correlation in the form of expression trees of each performance parameter is expressed in Figs. (C7-C9). Terminal sets and functions are presented in circles, as shown in Figs. (C7-C9).

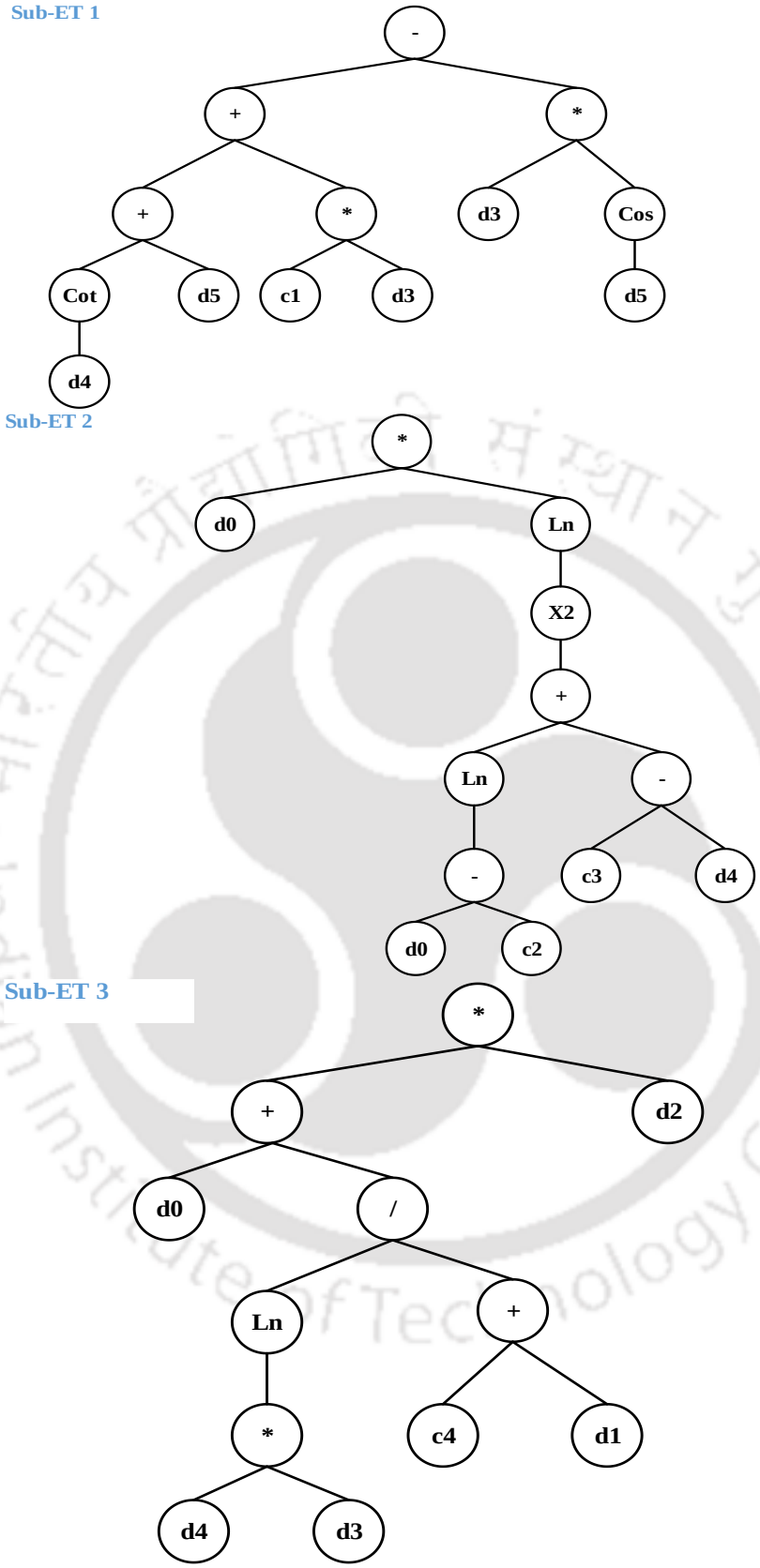

Fig. C7: Expression Trees for CR (C1 = 3.7461; C2 = 0.509581; C3 = 0.4538; C4 = -8.50041) (d0: F_a (kg/m^2-s); d1: T_a (°C); d2: ω_a (kg_{wv}/kg_{da}); d3: F_s (kg/m^2-s); d4: T_s (°C); d5: ζ (%wt.))

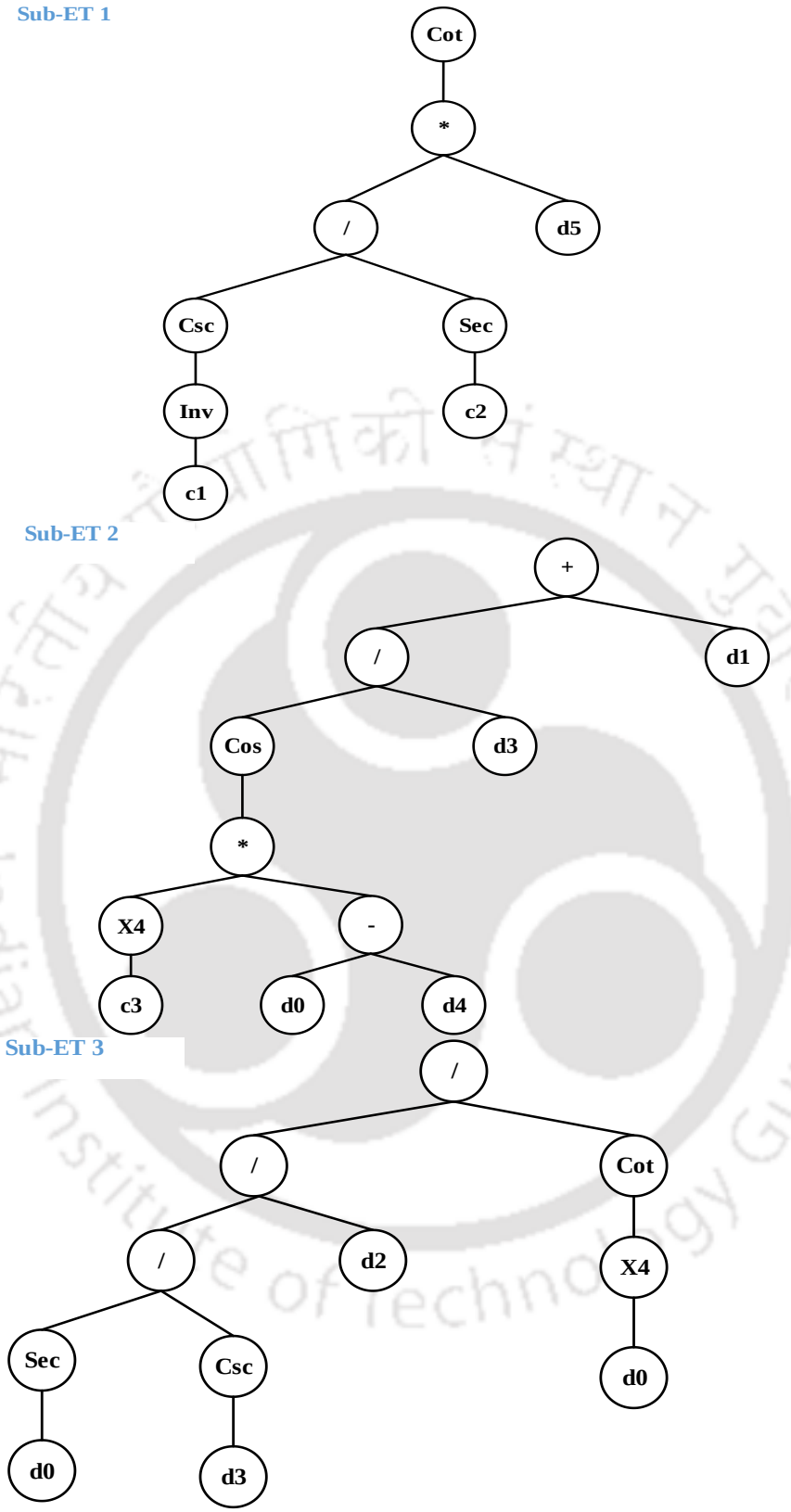

Fig. C8: Expression Trees for ε_{lat} (C1 = 6.93166; C2 = 6.866359; C3 = 1.69729) (d0: F_a (kg/m^2-s); d1: T_a (°C); d2: ω_a (kg_{wv}/kg_{da}); d3: F_s (kg/m^2-s); d4: T_s (°C); d5: ζ (%wt.))

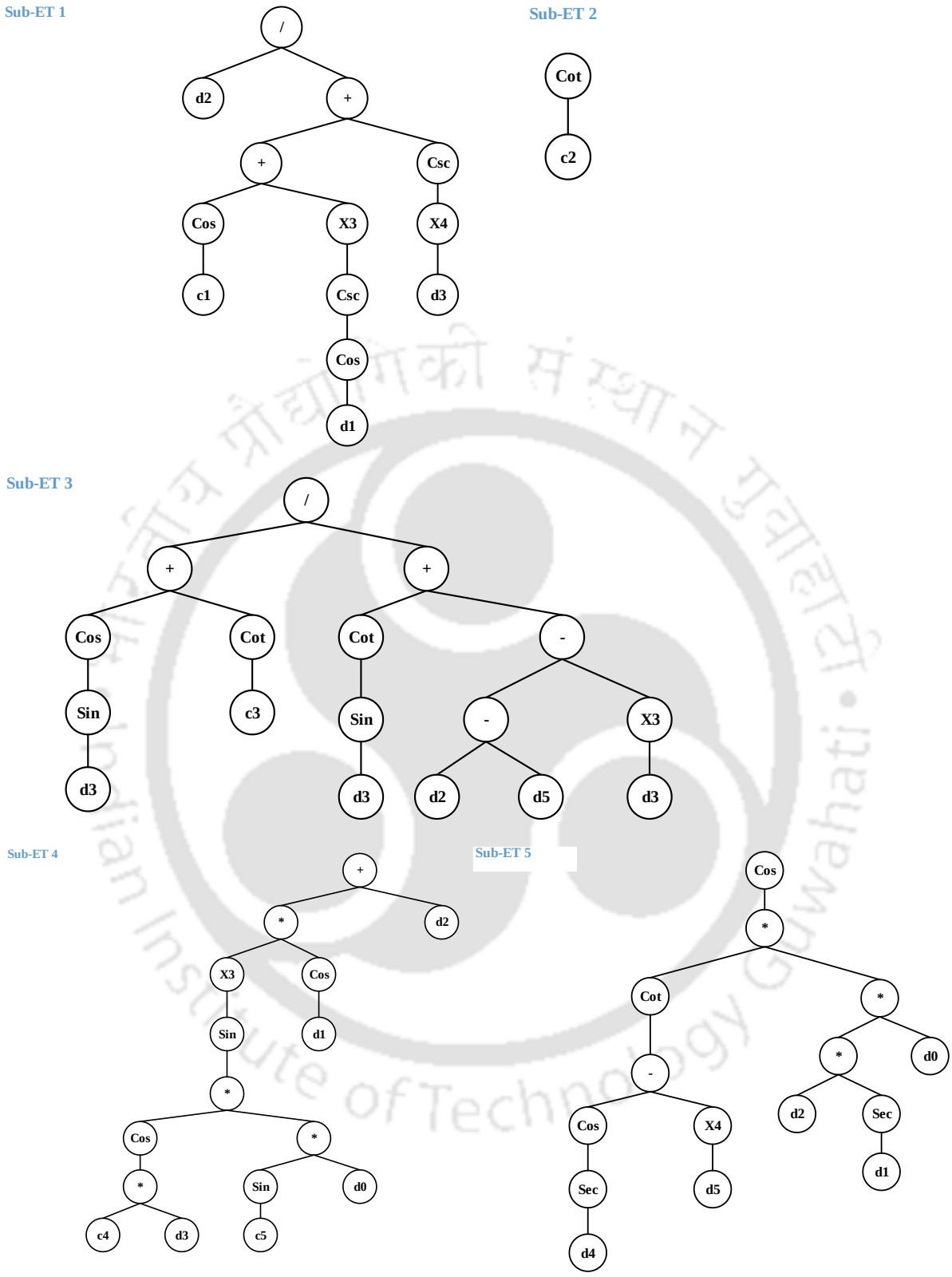

Fig. C9: Expression Trees for LHR. (C1 = 4.09541; C2 = -1.453596; C3 = -2.926419; C4 = -3.28303; C5 = -6.59046) (d0: F_a (kg/m^2-s); d1: T_a (°C); d2: ω_a (kg_{wv}/kg_{da}); d3: F_s (kg/m^2-s); d4: T_s (°C); d5: ζ (%wt.))

Appendix D

Photographic view of desiccant doped hydrogel films

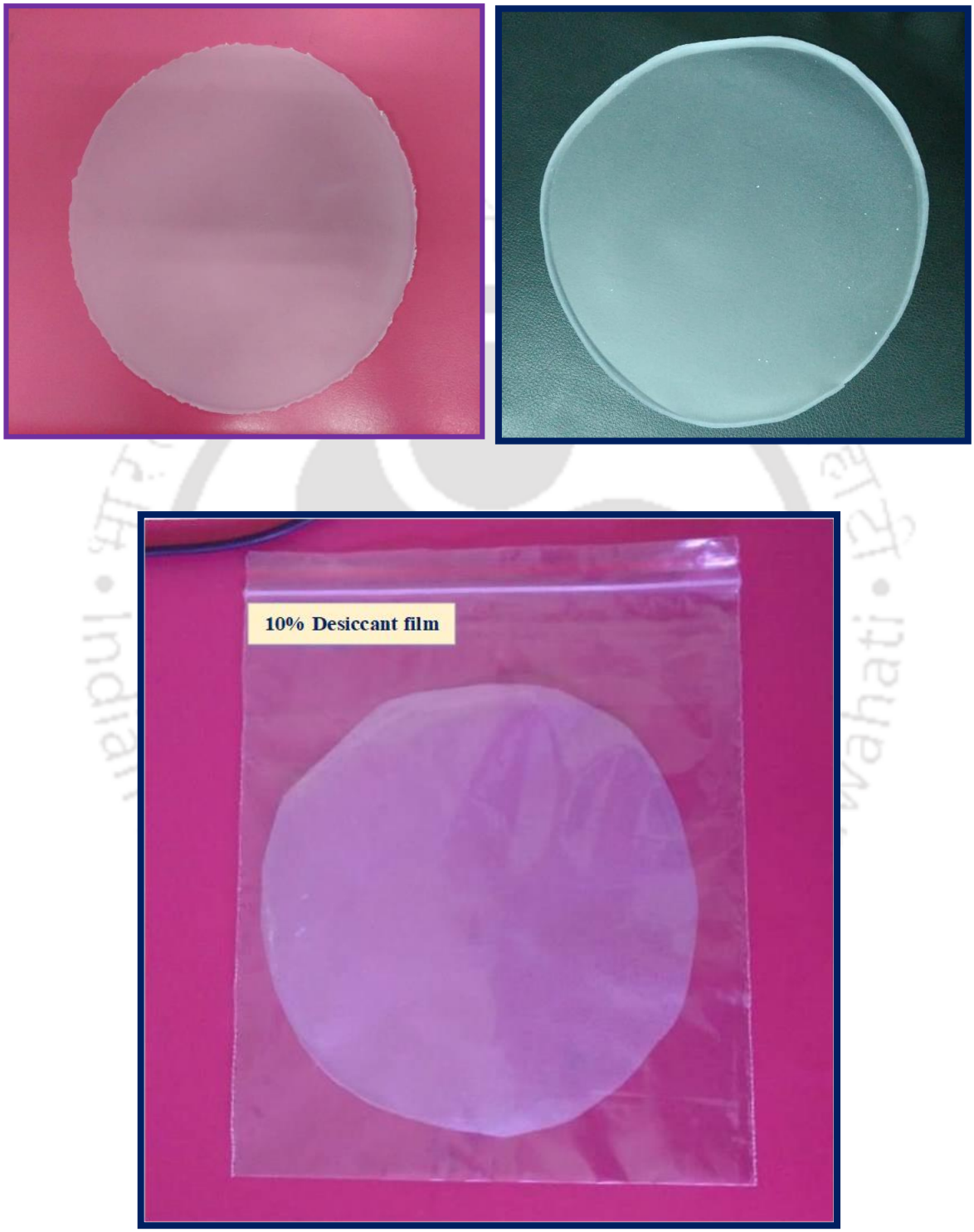

Fig. D1: Photographic view of desiccant doped hydrogel films

LIST OF PUBLICATIONS

Journals:

1. **Mrinal Bhowmik**, P. Muthukumar, R. Anandalakshmi, "Experimental based multilayer perceptron approach for prediction of evacuated solar collector performance in humid subtropical regions", **Renewable Energy**, Elsevier, Volume 143, 2019, Pages 1566-1580, ISSN 0960-1481, DOI: 10.1016/j.renene.2019.05.093 *(Import factor: 6.274)*
2. **Mrinal Bhowmik**, P. Muthukumar, R. Anandalakshmi, "Experimental study of coupled heat and mass transfer phenomena between air and desiccant in a solar-assisted thermal liquid desiccant system", **International Journal of Thermal Sciences**, Volume 162, 2021, 106795, ISSN 1290-0729, DOI: 10.1016/j.ijthermalsci.2020.106795. *(Import factor: 3.476)*
3. **Mrinal Bhowmik**, P. Muthukumar, R. Anandalakshmi, "Experimental investigation on structured packed bed liquid desiccant dehumidifier: An optimal mixture design of experiments strategy", **International Journal of Refrigeration**, Volume 122, 2021, Pages 232-244, ISSN 0140-7007, DOI: 10.1016/j.ijrefrig.2020.11.006 *(Import factor: 3. 461)*
4. **Mrinal Bhowmik**, P. Muthukumar, R. Anandalakshmi, "Experimental based multi-objective optimization for structured packed bed liquid desiccant dehumidification systems", **Journal of Building Engineering**, Elsevier, Volume 32, 2020, 101813, ISSN 2352-7102, DOI: 10.1016/j.jobe.2020.101813 *(Import factor: 3.379)*
5. **Mrinal Bhowmik**, R Anandalakshmi, P. Muthukumar, "Numerical investigation of performance trade-off characteristics of a packed bed dehumidifier using aqueous blends of lithium chloride and calcium chloride". **Heat Mass Transfer**, Springer, Volume *56, Pages 3093–3109*, 2020, DOI: 10.1007/s00231-020-02893-y *(Import factor: 1.867)*
6. **Mrinal Bhowmik**, Sayan Haldar, K. Dharmalingam, P. Muthukumar, R. Anandalakshmi, "Fabrication, Characterization and Evaluation of Desiccant Doped Hydrogel Films for Potential Air-Dehumidification Applications", **Journal of Applied Polymer Science**, Wiley, 2021, Article in press *(Impact factor: 3.125)*
7. **Mrinal Bhowmik**, Sayan Haldar, K. Dharmalingam, P. Muthukumar, R. Anandalakshmi, "Evaluation of thermo-kinetic and absorption characteristics of pure desiccants and desiccant mixtures", **Materials Today: Proceedings**, Elsevier, Volume 26, Part 2, 2020, Pages 1967-1971, ISSN 2214-7853, DOI: 10.1016/j.matpr.2020.02.430 *(Cite Score: 1.3)*
8. **Mrinal Bhowmik**, B. Kiran Naik, P. Muthukumar, R. Anandalakshmi, "Implementation of Artificial Intelligent Models for Liquid Desiccant Dehumidifier Performance Prediction and Optimization – A Metaheuristic Approach", (**Applied Energy**, Under review)

Book chapter:

1. **Mrinal Bhowmik**, P. Muthukumar, R. Anandalakshmi, "Modelling and Trade-Off Analysis of Performance Parameters for Counter Flow Packed Bed Liquid Desiccant Air Dehumidifier" Lecture Notes in Mechanical Engineering, **Springer**, 2021, Theoretical, Computational, and Experimental Solutions to Thermo-Fluid Systems, DOI: 10.1007/978-981-33-4165-4_29

Conferences:

1. **Mrinal Bhowmik**, R. Anandalakshmi and P. Muthukumar, "Numerical Study on Dehumidification Performance of a Cross-Flow Liquid Desiccant Adiabatic Dehumidifier with Various Halide Salt Desiccants", 5th International Conference on Computational Methods for Thermal Problems, ThermaComp-2018, July 9-11, 2018, Indian Institute of Science, Bangalore, India *(Scopus index)*
2. **Mrinal Bhowmik**, B. Kiran Naik, R. Anandalakshmi and P. Muthukumar, "An Experimental Investigation of the Dehumidifier Performance Evaluation using Aqueous Desiccant Blends", International Conference on Polygeneration, ICP 2019, May 15-17,2019, Kyushu University, Japan.
3. **Mrinal Bhowmik**, M. Joshi, R. Anandalakshmi and P. Muthukumar, "Performance Investigations on Twist Tape Based U-Tube Solar Evacuated Tube Collector for Humid Subtropical Region", 25th National and 3rd International ISHMT-ASTFE Heat and Mass Transfer Conference, IHMTC-2019, December 28-31, 2019, IIT Roorkee, India.
4. **Mrinal Bhowmik**, R. Anandalakshmi, P. Muthukumar "Modelling and Validation of Performance Parameters of a Counter Flow Dehumidifier with LiCl Solution" International Conference on Innovations in Thermo-Fluid Engineering and Sciences (ICITFES – 2020) 10-12 February 2020, NIT Rourkela, India.
5. **Mrinal Bhowmik**, Juri Sonowal, P. Muthukumar, R. Anandalakshmi, "Experimental Investigations on a Solar Assisted Packed Bed Regeneration Systems Using a Binary Desiccant Solution" International Conference On Polygeneration, 4 - 6 October 2021 (accepted)

Awards:

1. **Speaker of the day award** received from IISc Bangalore, India, for "Numerical study on dehumidification performance of a cross-flow liquid desiccant adiabatic dehumidifier with various halide salt desiccants", in 5th International Conference on Computational Methods for Thermal Problems, July 9-11, 2018 *(ThermaComp 2018).*